UNIVERSITY OF CALIFORNIA,
IRVINE

Nucleation and Growth Mechanisms of Protein@Metal-Organic Frameworks

DISSERTATION

submitted in partial satisfaction of the requirements
for the degree of

DOCTOR OF PHILOSOPHY

in Chemistry

by

Brooke Payne Carpenter

Dissertation Committee:
Assistant Professor Joseph P. Patterson, Chair
Professor Rachel W. Martin
Professor Andy S. Borovik

2023

DEDICATION

To Josh, who was by my side and supported me throughout this entire journey.

To Riley, who is my greatest source of joy and motivation.

TABLE OF CONTENTS

LIST OF FIGURES

LIST OF TABLES

ACKNOWLEDGEMENTS

No words can express my gratitude to my advisor, Joe Patterson, whose belief in my potential led him to accept me as one of his first graduate students. His mentorship and unwavering encouragement have forever shaped my life and instilled in me confidence not only in my research but also in myself. His selflessness and dedication as a mentor were beyond measure, and I will always treasure the privilege of working for him. He allowed me to explore my professional interests, even if they diverged from our research, and his support was instrumental in my growth as a researcher and individual. Thank you for being a dream mentor.

I extend my heartfelt thanks to my lab mates, Aoon and Paul, who were there with me from the beginning of the Patterson Lab. They have been my biggest supporters in the lab and have become more than just colleagues; they are cherished friends. Their unwavering friendship, trust, and constant push to excel have made me a better researcher and a better person.

I would like to express my sincere appreciation to Dr. Alana Ogata, a postdoc during my first year, who has made a profound and lasting impact on my academic journey. Alana's patience and dedication were invaluable as we started up our project. She invested her time in teaching me scientific and professional skills. Throughout graduate school, she remained a constant source of support, and I will always look up to her as a role model.

My sincere gratitude also goes to the members of my dissertation committee. I am indebted to Professor Rachel Martin, who played a pivotal role in my academic path. Taking a chance on me as a junior undergraduate, she allowed me to work in her lab during the summer of 2017. Her mentorship inspired me to pursue graduate school and become a part of UCI's academic community. I truly would not be here without her. Additionally, I am grateful for my opportunities to continue to collaborate with her and members of the Martin group throughout graduate school.

I am equally thankful to Professor Andy Borovik, whose generosity in sharing knowledge and expertise were instrumental in my growth as a researcher. As a first-year graduate student with no background in inorganic chemistry, he welcomed me into his group meetings and patiently answered my questions, breaking down complex concepts in a way that I could grasp.

I would like to express my deepest gratitude to my collaborators in graduate school, Professor Jennifer Prescher and Mariana Navarro. Their invaluable contributions and expertise have enriched my understanding of enzyme kinetics and have been instrumental in the success of this research. Special thanks go to Mariana for her tireless efforts in performing many of the kinetic experiments and for her dedication in breaking down complex enzyme kinetic issues. Her contributions have been indispensable in shaping the outcomes of this dissertation.

Thank you to my undergraduate advisor, Dr. Sarah Morgan from Southern Miss, and my chemistry teacher, Ms. Amy Denson from East Central Community College. Their mentorship and unwavering support prepared me for graduate school and inspired me throughout this journey. They were always just a phone call or email away, offering wisdom and encouragement.

I am incredibly grateful to my dear friends, either from the Class of 2018 or from the Patterson Lab, whom I had the privilege of meeting during my time at UC Irvine. Their unwavering support and friendship have been a guiding light throughout every major life stage, from getting married to becoming a mom. Their presence provided me with a strong support system and a nurturing community that profoundly impacted my experience at UC Irvine.

My heartfelt appreciation goes out to my family, who has been an unwavering pillar of support throughout my entire academic journey. Specifically, I want to thank my husband, Josh, for his boundless love, encouragement, and belief in my abilities. He has been a constant source of motivation, always there to provide the support I needed to persevere through challenges and complete this journey. Josh's dedication as a partner and father made my experience in graduate school far better than I could have ever imagined.

I am also deeply grateful to my son, Riley, who has been a constant source of inspiration. He taught me the true meaning of love and motivated me to strive for excellence not only for myself but also for our family's future.

To my family as a whole, thank you for understanding the demands of graduate school and for being by my side through thick and thin. Your love, patience, and belief in me have been the foundation upon which I built my academic success.

I also want to acknowledge that much of the material in this thesis is a reprint of material as it appears in the *Journal of American Chemical Society* and *Chemistry of Materials*. It has been properly used with permission according to guidelines.

VITA
Brooke Payne Carpenter

Education

East Central Community College	August 2014-May 2016
University of Southern Mississippi	August 2016-May 2018
University of California, Irvine	August 2018-August 2023

Publications

1. **Carpenter, B.P.;** Talosig, A.R.; Palma G.D.; Rose, B. Patterson J.P. "Nucleation and Growth Mechanisms of Metal-Organic Frameworks." *Under review with Chem. Soc. Rev.*
2. Hopstock, K.S.;**Carpenter B.P**.; Patterson J.P.; Al-Abadleh H.A.; and Nizkorodov S.A.; Formation of insoluble brown carbon through iron-catalyzed reaction of biomass burning organics. *Environ. Sci. Atmos*. 2023,3, 207-220.
3. Palma G.D.; Geels S.; **Carpenter B.P**.; Talosig, A.R., Chen C.; Marangoni, F.; Patterson, J.P. Cyclodextrin metal-organic framework-based protein biocomposites. Biomater. Sci, 2022, 10, 6749-6754.
4. **Carpenter, B.P**., Talosig, A.R.; Mulvey, J.T.; Merham, J.; Rose, B. "Role of Protein Folding and Molecular Modifications and Protein Folding in the Nucleation and Growth of Protein-Metal-Organic Frameworks. *Chem. Mater.* 2022, 34, 8336-8334
5. Rizvi, A. Mulvey, J.T., **Carpenter B.P.**, Talosig, A.R., Patterson, J.P. A Close Look at Molecular Self-Assembly with the Transmission Electron Microscope. *Chem. Rev. 2021, 121, 22, 14232–14280.*
6. Ogata, A. F.; Rakowski, A. M.; **Carpenter, B. P**.; Fishman, D. A.; Merham, J. G.; Hurst, P. J., Patterson, J. P. Direct Observation of Amorphous Precursor Phases in the Nucleation of Protein–Metal–Organic Frameworks. *J. Am. Chem. Soc.* **2020**, *142* (3), 1433–1442.
7. Bristol, A. N.; **Carpenter, B.P**.; Davis, A.N.; Kemp, L.K.; Rangachari V.; Karim S. Morgan, S.E. Aqueous RAFT Synthesis of Low Molecular Weight Anionic Polymers for Determination of Structure/Binding Interactions with Gliadin. Macromol Biosci. 2020. 20 (8), e200125.
8. Sprague-Piercy, M.A.; Bierma, J.C.; Crosby, M.G.; **Carpenter B.P**.; Takahashi, G.R.; Paulino J.; Hung I.; Zhang R.; Kelly, J.E.; Kozlyuk, N.; Chen, X.; Butts, C.T.; Martin, R.W. The Droserasin 1 PSI: A Membrane-Interacting Antimicrobial Peptide from the Carnivorous Plant *Drosera capensis. Biomolecules.* 2020. 10 (7), 1069.

Fellowships and Awards

1. **Diversity Fellowship**
   Offered by the School of Physical Sciences to fund students who have a passion for and commitment to improving DEI efforts within their department.
2. **Graduate Recruitment Fellowship**
   Offered stipend for assisting the Chemistry Department in recruiting perspective students and serving as contact person for the Department staff and prospective students.
3. **Science Communication Fellowship**
   Fellows serve on the communication team for the School of Physical Sciences where they are tasked with delivering engaging emails, news briefs, and social media content to increase visibility of research breakthroughs, departmental events, novel teaching strategies, and outreach opportunities through the school.

4. **Undergraduate Honors College Alumni**
   Graduated with honors (Magna cum laude) from the University of Southern Mississippi

Conferences and Presentations

1. Oral Presentation - 263rd ACS National Meeting and Exposition (San Diego, CA). "Protein Molecular Modification alters Structural Properties of Protein-Metal-Organic Frameworks." Brooke Carpenter, Rain Talosig, Jamie Esquivel, Alana Ogata, Dmitry Fishman, Joseph Patterson. March 2022.
2. Virtual Oral Presentation - MOF 2020 Young Investigators Symposium. "Nucleation and Growth Mechanisms of Protein-Metal-Organic Frameworks." Brooke Carpenter, Rain Talosig, Jamie Esquivel, Alana Ogata, Dmitry Fishman, Joseph Patterson. March 2020.
3. Poster Presentation - 258th Annual ACS National Meeting and Exposition (San Diego, CA) "Analysis of the Growth Mechanism of Encapsulated Biomolecules in Metal Organic Frameworks (MOF) and of the Catalytic Efficiency of Enzyme MOFs (eMOFs)." Brooke Carpenter, Alana Ogata, Kyle Roskamp, Rachel, Martin, Joseph Patterson. August 2019.
4. Poster Presentation - 255th Annual ACS National Meeting and Exposition (New
5. Orleans, LA) "Synthesis of Anionic Acrylamide-based Polymers for Determination of Interactions with Food-based Proteins." Brooke Payne, Ashley Davis, Ashleigh Bristol, and Sarah Morgan. March 2018
6. Oral Presentation - Honors College Prospectus Presentation (Hattiesburg, MS). "Synthesis of Poly(3-Acrylamido-3-Methylbutonate) for Determination of Binding Selectivity with Food Proteins." Brooke Payne, Ashleigh Bristol, and Sarah Morgan. April 27th, 2017.
7. Poster Presentation – The University of California, Irvine Summer Undergraduate Research Symposium (Irvine, California). "Characterization of D1 PSI from Carnivorous Plant Drosera capensis." Brooke Payne, Jan Bierma, Natalia Kozyluk, and Rachel Martin. August 17th, 2017.
8. Oral Presentation – Semi-finalist for UCI Grad Slam Competition (Irvine, CA)
9. Poster Presentation – The University of California, Irvine Summer Undergraduate Research Symposium (Irvine, California). "Characterization of D1 PSI from Carnivorous Plant Drosera capensis." Brooke Payne, Jan Bierma, Natalia Kozyluk, and Rachel Martin. August 17th, 2017.

Leadership and Service

1. **ChemUNITY Events Coordinator**
   Abstracted and budgeted events for ChemUNITY, a peer mentorship program for incoming Chemistry graduate students
2. **Homecoming Booth Organizer**
   Organized and performed demonstration experiments for the School of Physical Sciences Homecoming Booth
3. **Chemistry Diversity Fellow**
   Initiated DEI work and cultivated a more inclusive environment for the Chemistry Department through serving on faculty interview panels and meeting regularly with the Office of Inclusion and Excellence and with the Faculty Chair of DEI.

SISTERs Outreach (UCR Chapter)
Organized and presented a chapter meeting on my career path and research

4. **Events and Outreach Coordinator (Santiago Canyon College)**
   Organized the visit of local community college to UC Irvine where I provided tours of research facility and a lecture on my research.

Mentorship

1. **Departmental Mentor (ChemUNITY)**
   Mentored first-year graduate students to navigate common obstacles during first year and provided outlook on graduate school and career paths.
2. **Graduate Student Mentor**
   Mentored first and second year graduate students in the Patterson lab on laboratory practices and instrumental techniques for research projects.
3. **Undergraduate Student Mentor**
   Mentored undergraduate students in the Patterson lab on laboratory practices and instrumental techniques for research projects.

Teaching

1. **Organic Chemistry Laboratory Assistant**
   Taught and demonstrated proper laboratory practices for organic chemistry experiments. Provided office hours and student evaluations.
2. **General Chemistry Teaching Assistant**
   Held office hours, created practice worksheets, and facilitated class discussions.
3. **Chemical Biology Laboratory Assistant**
   Taught and demonstrated proper laboratory practices for chemical biology experiments. Provided office hours and student evaluations.

Certificates

1. **Activate to Captivate:** UCI, Winter 2019
   8-week speaking certificate focused on content creation and content delivery techniques. Learned to deliver research in an engaging way and techniques to maintain audience interest.
2. **Peer Mentorship Excellence Program:** UCI, Spring 2020
   Quarter-long mentorship certificate focused on developing and strengthening strategies and techniques used to mentor peers.

ABSTRACT OF THE DISSERTATION

Nucleation and Growth of Protein-Metal-Organic Frameworks

by

Brooke Payne Carpenter

Doctor of Philosophy in Chemistry

University of California, Irvine, 2023

Professor Joseph Patterson, Chair

Protein-Metal-Organic Frameworks (MOFs) present a diverse array of building blocks for designing high-performance materials with applications spanning numerous industries including drug delivery, catalysis, and gas storage. However, the intricate crystallization mechanisms involving various pathways and intermediates complicate their understanding, stalling the implementation of the materials. Fundamental crystallization studies have been pivotal in advancing both biological and synthetic systems, and MOFs are no exception. This dissertation delves into how proteins exert control over the nucleation and growth of MOFs, influencing final crystal properties such as topology, morphology, and encapsulation efficiency. Advanced microscopy and scattering techniques, such as cryogenic transmission electron microscopy (cryoTEM) and powder x-ray diffraction (PXRD), are employed to conduct these studies. The investigation commences with zeolitic imidazolate framework-8 (ZIF-8) as a model MOF system and bovine serum albumin (BSA) as a model protein. Synthetic protocols are established to explore the impact of BSA concentration and ligand-to-metal ratios on ZIF-8 formation. Notably, the use of cryoTEM allows for the direct observation of MOFs, uncovering the role of transient amorphous phases in ZIF-8 nucleation and growth. Furthermore, it was discovered how protein folding

influences the stability of these amorphous phases, enabling modulation of key physical properties such as crystal size, morphology, and encapsulation efficiency. Moving beyond BSA, subsequent investigations aim to connect nucleation and growth mechanisms to the final enzymatic performance of MOFs using catalytically active proteins, namely glucose oxidase (GOx) and catalase (CAT). The results underscore the significance of protein folding in the initial complexes with MOF precursors, pivotal in designing active materials. To further tailor the extent of enzyme activity, the accessibility of the enzyme to substrates and its diffusion barrier can be controlled through final crystal properties, including size, topology, defects, and porosity. Generalizing these findings, the dissertation introduces two novel, catalytically active proteins into ZIF-8 for the first time, main protease (M^{pro}) of SARS-CoV-2 and Nanoluciferase (NanoLuc). In summary, this work provides valuable insights into how protein folding influences MOF nucleation and growth mechanisms and, consequently, their final crystal properties. The research contributes to the broader understanding of MOFs as versatile materials and paves the way for high-performance hybrid materials.

Chapter 1: Introduction

A portion of this chapter is under review for publication in Chemical Society Reviews and has been adapted for this thesis:

Brooke P. Carpenter, A. Rain Talosig, Ben Rose, Giuseppe Di Palma, and Joseph P. Patterson. "Nucleation and Growth of Metal-Organic Frameworks." Under review with *Chem. Soc. Rev.*

Chapter 1: Introduction

1.1 Metal-Organic Frameworks

Metal-organic frameworks (MOFs) have become one of the largest and fastest growing research fields since the material was first introduced in the late 1990's.[1] Composed of metal nodes connected with organic ligands, MOFs have attracted popularity due to their incredibly high surface area, with some obtaining surface areas greater than the area of a football field per gram of material (~7800 m^2/g).[2] These high surface areas make MOFs perfect for storage of large amounts of gaseous guest species such as hydrogen,[3] or carbon dioxide.[4] MOFs also exhibit greater synthetic flexibility when compared to other porous materials like zeolites, which are currently used in many applications but have limited catalytic usage due to a narrow range of synthetic precursors.[5] In contrast, MOF coordination networks can be synthesized from many different transition metals and linkers and can be easily tuned to obtain crystals with varying chemical functionality and porosity, allowing small molecules and biomolecules to be selectively adsorbed or encapsulated.[6–8] Because of this synthetic diversity and ease of tunability, MOFs are now being studied for applications in almost every major industry, including catalysis,[9] gas storage,[10] sensors,[11] and drug delivery.[12,13]

While high throughput screening methods can be credited for accelerating the synthesis of new MOFs (>90,000 recorded MOFs),[14] currently only a limited number of MOFs are actually in industrial usage due to limited knowledge in how synthetic scaling and how high temperature and pressure processing techniques affect MOF formation and final structure.[15] The zeolite community – which has exploded in catalysis applications in the past two decades – has demonstrated that mechanistic studies on how a material forms enables its advancement, even with the limited catalytic applications this material has when compared to MOFs.[16–18] Additionally, the

commercialization of most pharmaceutical drugs can be largely credited to mechanistic studies of drug formation as the studies were used to tailor drugs with specific surface chemistries and properties.[19,20] Extensive mechanistic studies have been performed only on a limited number of MOF systems, but through those limited studies, the general consensus is that MOFs formations are often complex, not fitting conventional crystallization models.[21,22] Large-scale studies need to be performed to generalize these findings, which is challenging due to multiple intermediate phases occurring for each MOF synthetic condition. These phases need to be identified and characterized to better predict dominant MOF pathways. Additionally, how the reaction solution influences the formation and dynamics of the various intermediate phases has yet to be fully realized. Thus, a combination of ex-situ and in situ studies are essential to gain a holistic understanding of the reaction dynamics and mechanisms of MOF synthesis on both the molecular and bulk scale. Such mechanistic studies will enable tighter control of MOF synthetic conditions and provide translatable findings for other materials. Chapter 1 of this thesis encompasses how we currently understand, control, and monitor MOF crystallization mechanisms, specifically focusing on zeolitic imidazolate frameworks (ZIFs), a class of MOFs which are structurally like zeolites and are widely studied.

1.2 Nucleation and Growth Theories and Models

Crystallization studies have proven to be an important area of research in synthetic materials such as MOFs and across many natural systems occurring in biology and geology. Through these studies, scientists have extracted key thermodynamic and kinetic factors that unlock how atoms, ions, and molecules can pack to obtain final crystals with targeted properties. Since the early 20th century, classical nucleation theory (CNT) has served as a theoretical framework

for understanding the rates and mechanisms during crystallization.[23–25] The theory breaks crystallization down into two main categories: nucleation and crystal growth. Nucleation describes the assembly of monomers (atoms, ions, or molecules) into the smallest thermodynamically stable structure which possesses a crystalline lattice, known as a crystal nucleus. The key principle for nucleation is that a significant energy barrier must be overcome to form a stable nucleus. This barrier is determined by two competing factors: Surface or interfacial energy and bulk energy.[26] The interfacial energy is always a positive term as it is the origin of the nucleation barrier since it requires energy to make an interface. The bulk energy is always a negative term as it denotes a release in energy or stabilization of the nuclei. By utilizing enthalpic and entropic strategies, such as manipulating bond strengths and degrees of freedom of MOF precursors, the interfacial energy term can be minimized, and crystal growth can proceed. Otherwise, if the interfacial energy is too high, a nucleus cannot be formed, and precursors remain in solution or bulk phase. Crystal growth then occurs on the downhill slope of the energy barrier and involves the addition of monomers to the surface of the growing crystal lattice. The key principle for crystal growth is that monomers will tend to add to different crystal faces at different rates, which controls the morphology of the crystal as it grows.[27,28] This growth often occurs through Ostwald Ripening, which refers to a phenomenon in which smaller particles of MOF precursors dissolve and add onto the surface of the growing crystalline phase.[29]

While CNT is essential to understanding how MOFs form, it has only been able to describe a few MOF systems.[30–32] Most MOF crystallizations are categorized as non-classical, as they include intermediates and irregular final crystal structures and morphologies that cannot be explained with CNT. Additionally, MOF crystals often form metastable phases, which are a local energy minima in the MOF formation reaction (Figure 1.1).[21,33] These metastable phases have

broad definitions as they can be characterized as molecular clusters,[34] crystalline nanoparticles,[32] liquids,[21] kinetic polymorphs (which later evolve to a more thermodynamically stable, often nonporous polymorph),[35] and amorphous species.[22] The behavior of this metastable phase has significant consequences of the final MOF's characteristics, as it aids in establishing a degree of local supersaturation for the critical nucleus to form and start the nucleation process. Metastable phases have been observed to form when precursors concentrate, and phases separate from the bulk solution to form solute-rich and solvent-poor areas. The solute-rich area then condenses into species such as amorphous particles and/or dense-liquid phases,[22] which serve as the metastable phase. Once the metastable phase is formed, an energy barrier must be overcome for the metastable phase to transition into a critical nucleus for the final crystalline phase. While this transition is challenging to probe, the critical nucleus can form through the aggregation of the metastable phase, which is based on attractive forces of phases at close distances. If the metastable phase is of amorphous character, this transition is often called the amorphous-to-crystalline (ATC) pathway, which is a common mechanism observed in zeolites,[36] biomimetic polymers,[37] and magnetite.[38] In this case, nucleation occurs within the rearrangement of the previously disordered Metal-Ligand-Metal bonds.

Once a critical nucleus has been reached, MOFs have been observed to grow through particle attachment,[22] where amorphous particles attach to the growing crystal in no orientated preference. Additionally, they can grow through oriented attachment (OA),[32] where crystalline precursors attach to the critical nucleus through alignment of their lattices to the growing crystal.[39]

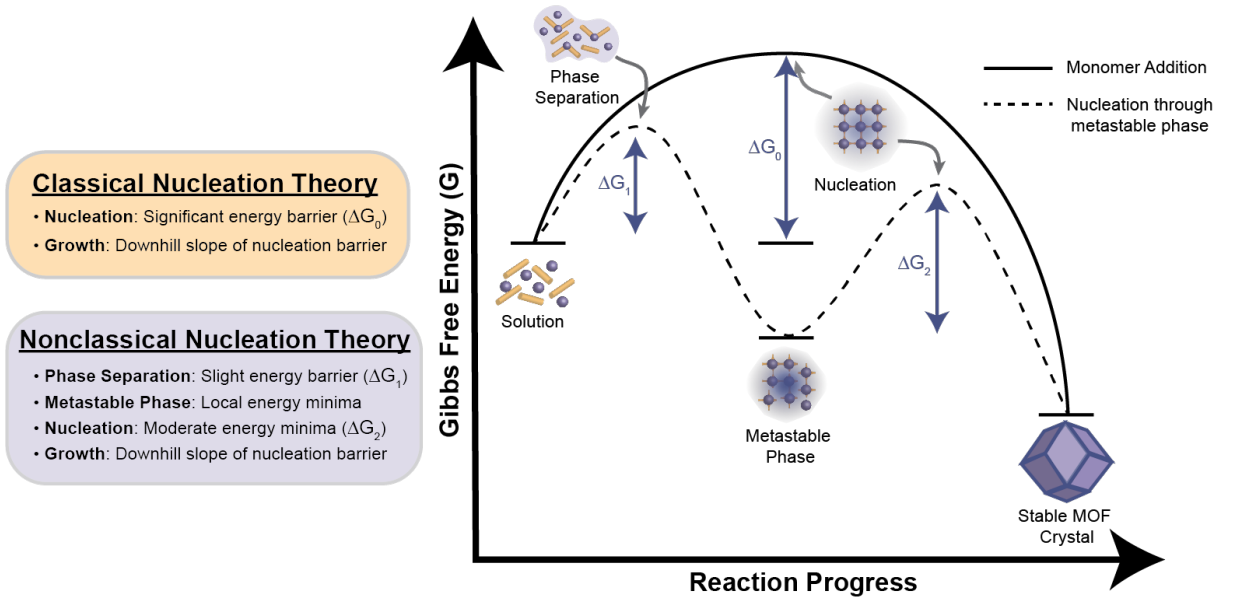

Figure 1.1: Free energy diagram comparing monomer addition (classical nucleation theory) and nucleation through metastable phase (nonclassical nucleation theory) mechanisms.

The nucleation and growth of MOFs can also be described by the secondary building unit (SBU) approach.[40–42] A SBU consists of building units, which are the "bricks" or smallest possible assembly of MOF precursors.[43] SBUs arrange into larger complexes that form the basis of the network topology. The growth of SBUs into MOFs can be categorized similarly to polymerization where the SBUs can either undergo chain or step growth mechanisms.[32] In chain growth mechanisms, single SBUs add like monomers to the growing ends of a crystal. In step growth mechanisms, SBU dimers, longer oligomers, and/or smaller crystals add to each other through oriented attachment. SBUs can arrange into a large library of rigid geometries, which have direct implications on the structural properties of a crystal.[42] Thus, through the design of SBUs with appropriate geometries and sizes, the final network topology, and final physical properties, such as stability and porosity, can be predicted for MOF crystals.

1.3 Controlling MOF Nucleation and Growth

The MOF nucleation and growth reaction can be controlled through manipulating phase changes during synthesis. Phase change of a system occurs when the total free energy of the proceeding phase is less than the total free energies of the prior phase. Intrinsic and extrinsic parameters can dictate whether a phase transformation is energetically favorable through increasing or decreasing the free energy barrier to nucleate a particular phase. Intrinsic factors refer to the internal properties within a MOF system, such as the chemical composition and concentration of the precursors, along with temperature and reaction medium. Extrinsic factors include the presence of foreign surfaces, small molecule modulators, and confinement, which can directly affect the surface energy barrier to nucleation. Extrinsic factors frequently control the rates and mechanisms of MOF by favoring a type of nucleation called heterogeneous nucleation, which occurs outside of the bulk solution such as on a foreign surface. Heterogeneous nucleation enables nucleation to occur at lower supersaturation conditions, resulting in increased rates of nucleation compared to nucleation occurring in the bulk solution (homogeneous nucleation).[44] Much has been written about the effects of different synthetic conditions on final MOF size and quality. In this section, we use these final properties to extrapolate information about MOF nucleation and growth mechanisms. Some properties mentioned in this review which can be tied to nucleation and growth include metal-ligand bond strength (which can relate to nucleation probability and to growth),[45] crystal size (which can relate to crystal growth),[46] crystalline defects (which indicate errors in SBU formation and/or arrested growth), and crystal polymorph (which can be used to tell whether a reaction is thermodynamically or kinetically controlled).[22] Both intrinsic and extrinsic factors will be discussed in more detail in this subsection.

Chemical composition and medium

Both MOF composition and solvent play significant roles in both the nucleation and growth of MOFs. The strength of the metal-ligand bond, which is essential to the assembly of stable SBUs, can be modulated based on electron sharing between the ligand and metal. When choosing a ligand, factors to consider are the electron- withdrawing and electron-donating effects. For example, ZIF-8 has a stronger Zn-N coordination than ZIF-108, as the ligand in ZIF-108, 2-nitroimidazole, has a greater electron-withdrawing effect on the imidazole ring, and thus greater Zn-N bond length than the ligand in ZIF-8, 2-methylimidazole.[47] The different strength of the Zn-N bond in different Zn-based imidazolate MOFs provides different applications for the materials; while stronger Zn-N bonds are desired for storage applications, weaker bonds can facilitate reversible phase transformation, which broadens the material's applicability.[48] Indeed, ZIF-108 undergoes metal substitution much easier than ZIF-8 does, the latter of which requires a base to prevent phase transformation during this process.[47,49] This suggests that the rate of growth should be higher for ZIF-8, as hydrolysis-resistant metal-ligand bonds lead to higher crystal growth rates. When choosing a metal ion, the Irving-Williams series can be used to determine the strength of divalent metal complexes in water.[50,51] This series is often explained based on the ionic radius of a divalent metal and the crystal field stabilization energy of a complex. For example, Cu^{2+} is expected to form a more stable metal complex than Zn^{2+} based on the smaller ionic radius of Cu^{2+}.

Of course, to measure MOF nucleation and growth, a given metal and linker must be able to form a MOF. While this may seem obvious, many metal-ligand combinations will not produce MOFs, meaning selection of a linker for a corresponding metal node must be done with care. When designing the metal-ligand combination for a MOF, Pearsons's hard-soft acids and bases (HSAB) theory must be utilized, as the binding strength and stability of the metal and ligand bond drives

the self-assembly process and dictates the final performance of a MOF.[52] Hard metal ions such as Zr^{4+} form strong metal-ligand complexes with strong bases such as carboxylate ligands, and soft metals such as Zn^{2+} form strong metal-ligand complexes with weak bases such as azolate ligands.[53] Borderline metal ions such as Cu^{2+} can interact with both strong and weak bases, examples being benzene-1,3,5-tricarboxylate, a strong base, and 2,2'-dipyridyl, a weak base, in the case of HKUST-1 and $[Cu(4,4'\text{-}DP)_{0.5}Cl]_n$ respectively.[54–56] Different linkers and metals will display different nucleation and growth kinetics, the understanding of which varies between MOF system.

As metal-ligand bond strength cannot be discussed in a vacuum, the reaction solution, specifically the solvent, is critical for dictating the metal and ligand coordination environments.[57] Furthermore, MOF's can only self-assemble into crystalline units if the metal-ligand bond formation is more energetically favorable than the solvent-ligand exchange rate. Solvent can play various roles in the self-assembly process. It can govern the rate and pathway of crystal formation, be incorporated into the MOF by coordinating with the metal ions, or both. In the case of water-stable ZIFs, the ΔG of hydrolysis must be a positive value, meaning that metal-ligand binding is more energetically favorable than the metal or ligand binding with water.[53] By modulating the hydrophobicity of the ligand, the rate of ligand/solvent binding can further be tuned, as hydrophobic ligands have a lower rate of binding with water molecules.

The solubility of the ligand in the reaction medium plays an important role in the crystallization rate as a more soluble ligand facilitates increased nucleation and growth rate. For example, a study demonstrated this concept by using a ligand more soluble in DMF than in water and showed how the MOF crystallized much faster in DMF than water due to the ligand's high solubility in DMF.[58] The solubility of the ligand also can impact the network dimension of a MOF as it influences the binding affinity of the solvent molecules to the metal centers. For example, a

study showed that through increasing ligand solubility, the solvent-metal binding consequently decreased, which resulted in an increase of the crystal dimensionality (i.e. 1D, 2D, 3D).[59]

The rate and extent of deprotonation of the ligand further affects the self-assembly and final MOF structure and size. A study by Kim et al. observed larger particles formed in more polar solvents as more polar solvents have higher proton acceptance power.[60] As a result, the interfacial energy of the system decreases as the concentration of available ligands for metal coordination increases. With a higher concentration of available ligands, larger MOFs with high crystallinity can form.

In addition to solvent polarity, the purity and ionic strength of a solvent affects the arrangement and size of the initial assembled clusters. For example, a pure aqueous solvent has been shown to facilitate fast nucleation and produce larger clusters compared to an aqueous solution with ions.[34] Additionally, free ions, such as Na^+ and F^-, in solution can dictate the extent of defects in a crystal structure.[61] This occurs as a result of the ions interacting with the MOF building units during growth, preventing ligands from rotating and consequently forming defects. Defect formation is most prominent at lower ion concentrations. As ion concentration increases, the probability of crystalline unit formation is decreased, due to an increased stability between the metal and counterion. Ions also can stabilize complexes during growth, raising the energy barrier to add more monomers or SBUs, which leads to defects and trapping of kinetic products. Ions can also add themselves into the crystal lattice of a MOF, as is the case with ZIF-C–where carbonate ions incorporate themselves into the ZIF-8 lattice during formation–changing the nucleation and growth mechanism in a way that is still not understood. The concentration of precursors and ratio of ligand to metal is further key in MOF self-assembly mechanisms. Excess ligand drives nucleation in some ZIF systems through the deprotonation of building units, reducing the rate of

hydrolysis. Increasing the extent of excess ligands speeds up the reaction rate, producing smaller kinetic products with low dispersity.

Surfaces

Surface substrates have shown great potential for nanoscale control of crystal formation,[64] aiding in the discovery of new types of materials for CO_2 separation,[65] water splitting,[66] and field-effect transistors.[67] Surfaces control the self-assembly pathway of crystal formation by modifying the interfacial free energy barrier and offering a site for crystals to nucleate (Figure 1.2).[68] The effects of surfaces themselves on crystal growth are usually not as pronounced, although confinement by surfaces can noticeably affect growth of MOFs. The extent of which a surface can modify crystal nucleation is largely dependent on two factors: 1.) atomic structure of the surface and 2.) the strength of the bonds formed by the MOF precursors and the surface. By matching the atomic structure of a surface to a desired lattice place of a crystal, surfaces can be used to control the orientation of the crystal lattice by minimizing the lattice strain in a desired orientation. Planar substrates include flat, smooth surfaces such as alumina[69] and silica[70,71] and provide a uniform surface for MOFs to grow. These substrates often include self-assembled monolayers (SAMs),[72,73] that can be functionalized with different terminating groups to dictate the orientation of the MOF crystal. In a study by Shekhah et al., the authors describe studying the formation of metal-organic frameworks (MOFs) in a sequential fashion on a functionalized SAMs.[74] The surface of the SAMs was functionalized with mercaptohexadecanoic acid (MHDA) as the carboxylic acid groups matched with the (100) plane in the crystal lattice. As a result, the orientation and growth of the crystal could be controlled, resulting in homogeneous crystalline films. Furthermore, SAMs can be functionalized with multiple different terminating groups which promotes nucleation of

different lattice orientations. Such control of the nucleation enables the engineering of novel MOF structures with finely tuned lattice patterns.[75]

Another aspect to consider when choosing a surface is the chemical composition of the surface interface. The interfacial chemistry can be used to modulate the binding strength of the MOF precursors to the surface and consequently, the probability of nucleation. By the MOF precursors forming stronger bonds with the surface rather than with the solvent molecules, the interfacial energy barrier required for nucleation decreases.[26] The available surface area for strong bonds to form can also impact the probability of nucleation. Non-planar substrates, which are surfaces that are more complex and have three-dimensional structures, provide a larger surface area for the MOFs to grow on, leading to faster formation and higher yields.[76–78] Examples of non-planar substrates include foams,[79] fibers,[80] nanowires,[81] proteins,[7,78,82,83] and porous metals.[84,85] The ability for a protein to drive crystal formation of ZIF-8 (sod) is strictly dependent on its negatively charged surface as studies have shown that biomolecules with high isoelectric points (>7) cannot promote crystal formation.[78] With this insight, molecular modifications were shown to be promising methods for tailoring the surface chemistry to promote nucleation and growth of a particular MOF phase. Furthermore, proteins are believed to add to the growing crystal through particle addition. Through addition, the proteins create defects in the crystal as they are too complex to match the lattice planes of the MOF.[22,83] By controlling the size and concentration of protein particles, such defects can be tailored.

In summary, each type of surface has its own benefits for tailoring the nucleation and growth of MOF formation. For example, if a planar substrate is being used, a fabrication method may be developed that takes advantage of the flat and smooth surface of the substrate to help control the growth and formation of the MOFs in a precise and uniform manner. On the other hand,

if a non-planar substrate is being used, a fabrication method may be developed that can adequately grow the MOFs on the more complex surface of the substrate, potentially leading to faster formation, higher yields, and trapping of kinetic products (Figure 1.2).

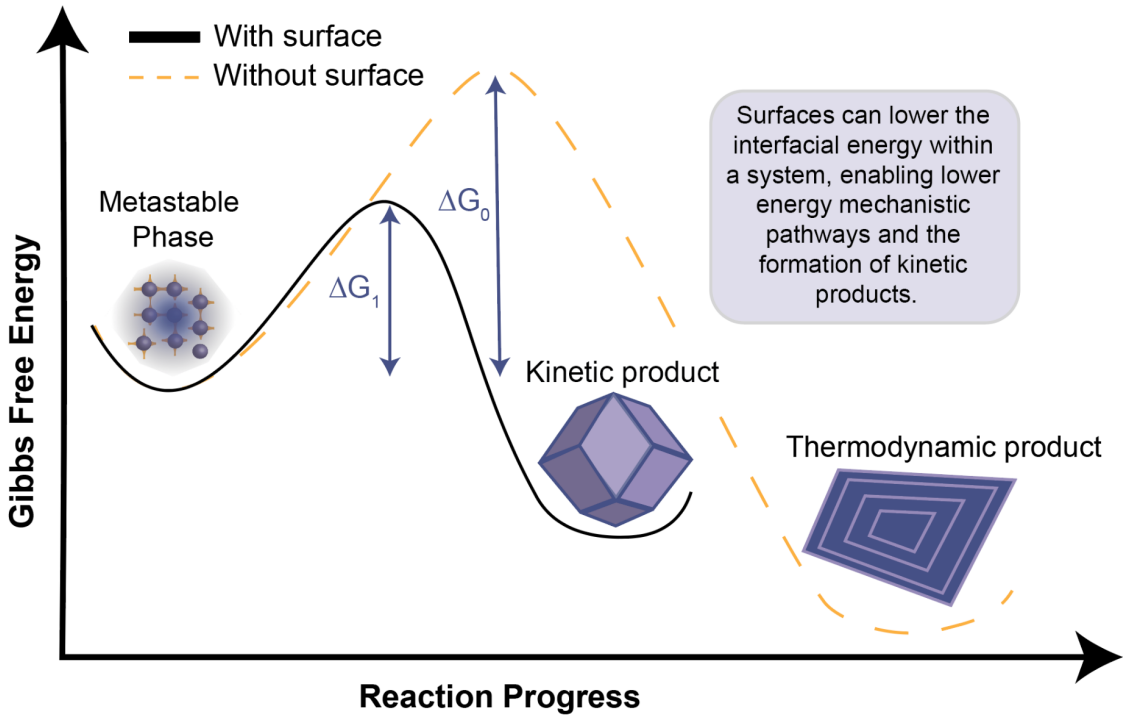

Figure 1.2: Comparison of free energy barrier in homogeneous (without surface) and heterogeneous crystallization (with surface).

1.4 Monitoring MOF Nucleation and Growth

The complexity of MOF nucleation and growth requires strategic experimental and instrumental methods to obtain a thorough understanding of the mechanisms and kinetics driving each intermediate and final phase. While no single instrumentation method can capture the broad spectrum of the crystallization process from initial building units to final bulk crystal, each instrument has its own strength as some instrumental techniques enable characterization of a specific, localized region and provide qualitative insight into individual crystal size and

morphology, while other techniques may provide ensemble information and quantitative insight into the crystallization kinetics. Thus, multiple complementary instrumentation methods are required to obtain a holistic overview of the crystallization by providing descriptions of each phase and phase transition. Each instrument will be discussed in more detail in this section, and examples of how each technique can be used to monitor MOF nucleation and growth will be provided.

Mass Spectrometry

Mass spectrometry (MS) provides compositional and structural information of the initial building units in solutions that occur prenucleation. Such studies enable a molecular understanding into the mechanisms and dynamics in which metastable phases such as particles form. Electrospray ionization (ESI) is a soft ionization technique that is frequently paired with MS (i.e. ESI-MS) to minimize damages, such as fragmentation, to the prenucleation species. In a study by Filez et al., ESI-MS was used to determine the composition of the prenucleation clusters in ZIF-67, which allowed for a greater understanding of the quantity and composition of the initial building units.[87] By taking measurements of sample aliquots, the mechanism in which these building units evolve to form a stable nucleus was determined to be through monomer-by-monomer addition. In a different study by Salionov et al., high resolution ESI-MS was used to monitor the growth of MIL-53 (Al), which revealed how solvent byproducts play a role in the nuclei formation.[88] The study further uncovered the crystallization mechanism to occur through nuclei aggregation.

Spectroscopy Techniques

Infrared (IR) and Raman spectroscopies both provide information on the molecular bindings occurring in solution and in various phases in MOF formation through measurement, by

means of either scattering or absorption of the vibrational modes of the chemical bonds. Thus, influences by intrinsic or extrinsic factors can be monitored through changes in the vibration mode. IR spectroscopy relies on atoms being free to vibrate to detect different functional groups with known absorptions. Atoms in MOFs are locked in a crystal lattice, having different IR absorption than the free atoms. Time-resolved fourier transform infrared spectroscopy (FTIR) has been used to measure the folding of enzymes within ZIF-8, specifically the amide I, II, and III peaks.[89] FTIR measurements can be used to determine the presence of enzymes in a p-MOF, as well as presence of CO_2, in the case of ZIF-C.[89,90]

Whereas IR is based on absorption of IR light, Raman spectroscopy measures vibrational modes by means of photon scattering. Raman is particularly useful for studying MOF-guest interactions in aqueous solutions, as Raman is not sensitive to water vibration which could overlap the MOF-guest vibrations.[91] In situ Raman has been used to study how temperature plays a role in molecular packing and, consequently, ability to integrate guest molecules. Furthermore, a study by Kumari et al. found that lower temperatures promoted greater gas adsorption in ZIF-8 due to larger windows between the methyl-imidazole rings in the MOF building blocks.[92] Using a combination of both Raman and IR spectroscopies is most impactful, as each is sensitive to different vibrations, providing greater insight into the chemical reactions occurring in solution, and this is applicable to all MOFs. Embrechts et al. used in situ Raman and FTIR spectroscopies to study the nucleation and growth of MIL-53 (Al) in DMF through evolution in the vibrational bands.[93] Through this study, the transformation of the atomic ordering in the metastable phase to the stable crystalline nucleus could be probed.

Scattering Techniques

Scattering techniques can be performed on MOFs to obtain averaged ensemble data pertaining to the nucleation and growth kinetics of a crystallization as well as the evolution of particle size, morphology, and distribution. Data of a sample is obtained through collecting scattered radiation off a sample as a function of angle and/or time. Based on the radiation wavelength, different length scales can be obtained.

Dynamic light scattering (DLS) and static light scattering (SLS) use light or photon radiation sources, allowing for nanometer resolution, of initial MOF species.[94] DLS measures the scattering of light at a single angle to determine the hydrodynamic radius (R_h), which relates the diffusion of a particle in solution to the diameter of a sphere. SLS measures radiation at several angles to obtain the radius of gyration (R_g), or the radius based on a particle's center of mass. R_g allows the molecular weight of particles to be determined. Using a mathematical approximation, Saha and coworkers fit time-resolved SLS data from the growth of ZIF-71 nanoparticles to a nucleation and growth model.[95,96] By determining the mass values of the intermediates, the NG model then provided information on how the mass of the nanoparticles evolve over time. Additionally, by using the ratio of R_g/R_h, particle morphology and shape evolution of MOF particles can be studied.[96]

Light scattering techniques can further be used to measure solution turbidity by measuring the scattering intensity, enabling the rate of particle formation to be determined.[22] Zeta potential, which measures the surface charge of particles, measurements can be performed with light scattering techniques. Surface charge measurements are particularly important to understanding the electrostatics driving heterogeneous nucleation on surfaces such as biomolecules[78] and zeolites.[97] It is important to note that light scattering techniques are limited in that they cannot

obtain accurate particle or intensity measurements in very heterogeneous and/or turbid MOF solutions. Thus, controls are needed for all lights scattering methods to determine the best working concentrations of MOF samples.

X-ray scattering techniques use x-rays as radiation sources, enabling higher resolution than previously mentioned light scattering techniques due to the short wavelengths of X-rays compared to visible light. These methods can provide insight into the nucleation and growth mechanisms of MOFs through morphological and structural evolution studies of the amorphous and crystalline phases. X-ray diffraction is a subclass of X-ray scattering where the scattered radiation is elastic (i.e the same energy as the incident X-rays) and is limited to measuring crystalline structures. While the arrangement of amorphous species cannot be determined with XRD, the presence of the species can still be determined through broad peaks occurring in the spectra background. The rate of crystallinity can then be monitored through changes in peak intensities over time, as it gives insight into reaction pathways and observes intermediate crystalline and amorphous phases. A study by Katsensis and coworkers used in situ XRD to monitor the structural evolution of ZIF-8 while applying a mechanical stress (i.e. mechanochemical synthesis).[98] By monitoring the XRD peaks, they were able to discover new metastable phases and a deeper understanding of how structural density plays a role in polymorph transformation.

Small angle X-ray scattering (SAXS) and wide-angle X-ray scattering (WAXS) are both types of X-ray scattering techniques which can identify crystallographic information as well as information pertaining to particle shape and size. SAXS is extremely versatile and can monitor the size and shape of initial MOF phases during nucleation and growth of MOF in the 1-100 nm range. Samples can be amorphous, semi crystalline, or crystalline, allowing for information on the initial stages of nucleation and growth that are not typically observed in XRD to be collected. SAXS

applications are not limited to identification of crystalline size and shape; this technique can also be used to understand the shape and function of enzymes when they are encapsulated in MOFs.[99] In a recent study, SAXS was used to track the microstructural changes of hollowed MOFs to hold different enzymes and showed that the microporous region would shrink, allowing for the macropores to expand to hold the enzymes.

WAXS measurements are taken with the detector in a closer position than with SAXS, so larger diffraction angles can be monitored, which is used to look at crystalline phases.[100,101] WAXS has been utilized to studying the change and formation of transitory MOF structures and monitor the kinetics of MOF crystallization and growth. MOF synthesis reactions often absorb significant amounts of X-rays, limiting the amount and accuracy of data that can be collected via X-ray scattering techniques. Additionally, many laboratory X-ray sources lack the brilliance, beam coherence, and tunable wavelength ideal for studying material formation kinetics *in situ.* SAXS and WAXS also suffer from poor temporal resolution, as laboratory X-ray source measurements–especially ones with low signal-to-noise–often take minutes to hours, during which important kinetic information can become lost. While synchrotron sources can and have mitigated these issues, obtaining experiment time at these sources is difficult, and consequently, few studies of this type have been conducted. WAXS has been used mainly to monitor the growth of characteristic crystalline peaks and measure the kinetic growth. For example, it has been used to understand the formation mechanisms of a multicomponent MOFs, revealing phase transitions throughout the synthesis.[102] The kinetic information gained from these experiments are crucial in the development of scaled up reactions and optimization of the synthesis.

Electron Microscopy Techniques

Microscopy methods provide images of localized regions of a sample enabling phases that occur simultaneously to be distinguished. Additionally, information on the dynamics and character of individual phases and crystals can be obtained. The resolution or viewing range of a sample is dependent on the wavelength of the beam source and the voltage at which the beam is emitted. For example, microscopes that use photons (a.k.a. visible light) rather than electrons for a beam source have lower resolution as photons have a longer de Broglie wavelength than electrons.

Electron microscopes utilize beams of electrons to image samples, allowing atomic scale resolution. The two main categories of electron microscopes are transmission electron microscopes (TEM) and scanning electron microscopes (SEM). These microscopes are largely differentiated based on the energy of electrons emitted. Transmission electron microscopy uses high energy electrons to pass through the sample and provide internal information such as pores and defects in the crystal structure. TEM is unique among all techniques because the lattice structure of individual phases and products can be imaged using high resolution TEM (HRTEM).[103] This allows amorphous phases to be distinguished from crystalline phases and provide insight into the evolution of the system.[22] While high resolution provides crystal structure in real-space imaging, micro electron diffraction (microED) images a sample in reciprocal space and obtains diffraction patterns, similar to that in x-ray diffraction, on selected phases of interest.

MOFs can be a challenge to image with TEM, especially at high resolution, as the high electron energy can damage the crystal structure.[104,105] To combat the beam sensitivity of MOFs, cryogenic TEM (cryoTEM) has been used to improve beam stability of the specimen. In this technique, aliquots of samples are brought to cryogenic temperatures, providing a snapshot of the reaction at certain time points.[104] To provide further information into the kinetics and dynamics

of a crystallization in real-time, liquid phase TEM (LPTEM) can been used to visualize the growth of MOFs while in their native, solution.[106] Using LPTEM, Liu et al. captured three key nucleation steps during the formation of MOF nanocrystals.[21] The LPTEM videos display a homogeneous solution of MOF precursors that phase separate to form a dense liquid phase. The dense liquid phase then condenses into an amorphous cluster that then undergoes crystallization. The direct observation in this study provides insight into how to better control crystallization and should be generalizable to many other MOF systems.

Scanning electron microscopy (SEM) uses lower energy electrons compared to TEM, allowing external features such as the surface morphology of the MOF crystals to be imaged, with resolution as low as 1 nm.[107] SEM has proved to be particularly useful for studying how the size, shape, and morphology of metastable and stable phases evolve over time. A study by Jian et al. demonstrated that by modulating the rate of nucleation through precursor concentration, the shape and size of ZIF-8 crystals could be controlled.[108] At a set concentration, the authors monitored the morphological evolution over the course of 24 hours and observed crystal growth through Ostwald ripening as small ZIF-8 crystals disappeared overtime while larger crystals appeared. Because MOFs are not conductive materials, electrons often build up on the surface of the crystals, called "charging", producing blurry images.[109] To reduce charging, thin coatings of conductive elements such as iridium or gold are coated onto the sample using a plasma sputter coater.[110]

1.5 Dissertation Overview

In this dissertation, the nucleation and growth mechanisms of MOFs are probed with a particular focus on how proteins control the kinetics and thermodynamics of the crystal formation. Such studies are essential to the prediction and development of biocomposites with finely tuned

sizes, morphologies, topologies, and surface chemistries. In each chapter, electron microscopy and X-ray diffraction are used as complementary techniques to characterize intermediate phases and/or final crystal topologies. Products from this dissertation work have resulted in two research chapters, **Chapter 2** and **Chapter 3,** being published in peer-reviewed journals. Additionally, **Chapter 1** has been submitted for peer-review and awaiting acceptance. **Chapter 4** is in preparation for peer-review and anticipated to be submitted during the Fall of 2023. **Chapter 5** is intended as a stand-alone chapter for this dissertation.

Chapter 1 introduces the field of MOFs and provides an overview of the current theories and fundamental chemistry used to decipher MOF crystallization. The discussion explores using intrinsic and extrinsic synthetic parameters as tools to modulate the crystallization pathway for creating MOF crystals with precisely customized physical and chemical properties. Experimental and computational methods are provided to guide the probing of MOF crystal formation on the molecular and bulk scale.

Chapter 2 describes the initial screening of synthetic conditions for protein-MOFs. Furthermore, the structural evolution of p-MOFs was probed, revealing nonclassical pathways via dissolution–recrystallization of highly hydrated amorphous particles and solid-state transformation of a protein-rich amorphous phase. With this data, we propose a general description of protein-MOF crystallization which is best characterized by particle aggregation and colloidal theory for future synthetic strategies.

Chapter 3 investigates how a molecular modification of proteins can affect the folding of a protein. Protein folding was further found to have a direct effect on the MOF formation mechanism, and consequently, the final crystal properties, including size, morphology, topology, and encapsulation efficiency.

Chapter 4 continues to build onto the concepts obtained from the previous chapters with introduction of catalytically active proteins, enzymes. Here, a guide is presented to designing high-performance enzyme-MOFs. This guide encourages others in the field to give specific attention towards both the initial enzyme folding with MOF precursors as well as the defects and extent of crystallinity in the final crystals.

Chapter 5 introduces two novel proteins, SARS-CoV-2 main protease (M^{pro}) and Nanoluciferase (Nanoluc), into ZIF-8 for the first time. Here, structure/function relationships are extrapolated from the data based on concepts learned from previous chapters in this dissertation.

Chapter 6 summarizes the major findings from this dissertation and provides an outlook on the exciting future of protein-MOF crystallization.

1.6 References

(1) Li, H.; Eddaoudi, M.; O'Keeffe, M.; Yaghi, O. M. Design and Synthesis of an Exceptionally Stable and Highly Porous Metal-Organic Framework. *Nature* **1999**, *402* (6759), 276–279. https://doi.org/10.1038/46248.

(2) Hönicke, I. M.; Senkovska, I.; Bon, V.; Baburin, I. A.; Bönisch, N.; Raschke, S.; Evans, J. D.; Kaskel, S. Balancing Mechanical Stability and Ultrahigh Porosity in Crystalline Framework Materials. *Angewandte Chemie International Edition* **2018**, *57* (42), 13780–13783. https://doi.org/10.1002/anie.201808240.

(3) Suh, M. P.; Park, H. J.; Prasad, T. K.; Lim, D.-W. Hydrogen Storage in Metal–Organic Frameworks. *Chem. Rev.* **2012**, *112* (2), 782–835. https://doi.org/10.1021/cr200274s.

(4) Aniruddha, R.; Sreedhar, I.; Reddy, B. M. MOFs in Carbon Capture-Past, Present and Future. *Journal of CO2 Utilization* **2020**, *42*, 101297. https://doi.org/10.1016/j.jcou.2020.101297.

(5) Park, K. S.; Ni, Z.; Côté, A. P.; Choi, J. Y.; Huang, R.; Uribe-Romo, F. J.; Chae, H. K.; O'Keeffe, M.; Yaghi, O. M. Exceptional Chemical and Thermal Stability of Zeolitic Imidazolate Frameworks. *Proceedings of the National Academy of Sciences* **2006**, *103* (27), 10186–10191. https://doi.org/10.1073/pnas.0602439103.

(6) Zheng, H.; Zhang, Y.; Liu, L.; Wan, W.; Guo, P.; Nyström, A. M.; Zou, X. One-Pot Synthesis of Metal–Organic Frameworks with Encapsulated Target Molecules and Their Applications for Controlled Drug Delivery. *J. Am. Chem. Soc.* **2016**, *138* (3), 962–968. https://doi.org/10.1021/jacs.5b11720.

(7) Liang, K.; Ricco, R.; Doherty, C. M.; Styles, M. J.; Bell, S.; Kirby, N.; Mudie, S.; Haylock, D.; Hill, A. J.; Doonan, C. J.; Falcaro, P. Biomimetic Mineralization of Metal-Organic Frameworks as Protective Coatings for Biomacromolecules. *Nat Commun* **2015**, *6* (1), 7240.

https://doi.org/10.1038/ncomms8240.
(8) Lyu, F.; Zhang, Y.; Zare, R. N.; Ge, J.; Liu, Z. One-Pot Synthesis of Protein-Embedded Metal–Organic Frameworks with Enhanced Biological Activities. *Nano Lett.* **2014**, *14* (10), 5761–5765. https://doi.org/10.1021/nl5026419.
(9) Lee, J.; Farha, O. K.; Roberts, J.; Scheidt, K. A.; Nguyen, S. T.; Hupp, J. T. Metal–Organic Framework Materials as Catalysts. *Chem. Soc. Rev.* **2009**, *38* (5), 1450–1459. https://doi.org/10.1039/B807080F.
(10) Getman, R. B.; Bae, Y.-S.; Wilmer, C. E.; Snurr, R. Q. Review and Analysis of Molecular Simulations of Methane, Hydrogen, and Acetylene Storage in Metal–Organic Frameworks. *Chem. Rev.* **2012**, *112* (2), 703–723. https://doi.org/10.1021/cr200217c.
(11) Lu, G.; Hupp, J. T. Metal−Organic Frameworks as Sensors: A ZIF-8 Based Fabry−Pérot Device as a Selective Sensor for Chemical Vapors and Gases. *J. Am. Chem. Soc.* **2010**, *132* (23), 7832–7833. https://doi.org/10.1021/ja101415b.
(12) Wang, Q.; Sun, Y.; Li, S.; Zhang, P.; Yao, Q. Synthesis and Modification of ZIF-8 and Its Application in Drug Delivery and Tumor Therapy. *RSC Advances* **2020**, *10* (62), 37600–37620. https://doi.org/10.1039/D0RA07950B.
(13) Peng, S.; Bie, B.; Sun, Y.; Liu, M.; Cong, H.; Zhou, W.; Xia, Y.; Tang, H.; Deng, H.; Zhou, X. Metal-Organic Frameworks for Precise Inclusion of Single-Stranded DNA and Transfection in Immune Cells. *Nat Commun* **2018**, *9* (1), 1293. https://doi.org/10.1038/s41467-018-03650-w.
(14) Moosavi, S. M.; Nandy, A.; Jablonka, K. M.; Ongari, D.; Janet, J. P.; Boyd, P. G.; Lee, Y.; Smit, B.; Kulik, H. J. Understanding the Diversity of the Metal-Organic Framework Ecosystem. *Nat Commun* **2020**, *11* (1), 4068. https://doi.org/10.1038/s41467-020-17755-8.
(15) Zuliani, A.; Khiar, N.; Carrillo-Carrión, C. Recent Progress of Metal–Organic Frameworks as Sensors in (Bio)Analytical Fields: Towards Real-World Applications. *Anal Bioanal Chem* **2023**, 1–19. https://doi.org/10.1007/s00216-022-04493-7.
(16) Li, Y.; Yu, J. Emerging Applications of Zeolites in Catalysis, Separation and Host–Guest Assembly. *Nat Rev Mater* **2021**, *6* (12), 1156–1174. https://doi.org/10.1038/s41578-021-00347-3.
(17) Li, Y.; Cao, H.; Yu, J. Toward a New Era of Designed Synthesis of Nanoporous Zeolitic Materials. *ACS Nano* **2018**, *12* (5), 4096–4104. https://doi.org/10.1021/acsnano.8b02625.
(18) Yu, J.; Xu, R. Rational Approaches toward the Design and Synthesis of Zeolitic Inorganic Open-Framework Materials. *Acc. Chem. Res.* **2010**, *43* (9), 1195–1204. https://doi.org/10.1021/ar900293m.
(19) Budiman, A.; Citraloka, Z. G.; Muchtaridi, M.; Sriwidodo, S.; Aulifa, D. L.; Rusdin, A. Inhibition of Crystal Nucleation and Growth in Aqueous Drug Solutions: Impact of Different Polymers on the Supersaturation Profiles of Amorphous Drugs—The Case of Alpha-Mangostin. *Pharmaceutics* **2022**, *14* (11), 2386. https://doi.org/10.3390/pharmaceutics14112386.
(20) Artusio, F.; Fumagalli, F.; Valsesia, A.; Ceccone, G.; Pisano, R. Role of Self-Assembled Surface Functionalization on Nucleation Kinetics and Oriented Crystallization of a Small-Molecule Drug: Batch and Thin-Film Growth of Aspirin as a Case Study. *ACS Appl Mater Interfaces* **2021**, *13* (13), 15847–15856. https://doi.org/10.1021/acsami.1c00460.
(21) Liu, X.; Chee, S. W.; Raj, S.; Sawczyk, M.; Král, P.; Mirsaidov, U. Three-Step Nucleation of Metal–Organic Framework Nanocrystals. *PNAS* **2021**, *118* (10). https://doi.org/10.1073/pnas.2008880118.

(22) Ogata, A. F.; Rakowski, A. M.; Carpenter, B. P.; Fishman, D. A.; Merham, J. G.; Hurst, P. J.; Patterson, J. P. Direct Observation of Amorphous Precursor Phases in the Nucleation of Protein–Metal–Organic Frameworks. *J. Am. Chem. Soc.* **2020**, *142* (3), 1433–1442. https://doi.org/10.1021/jacs.9b11371.
(23) De Yoreo, J. J.; Gilbert, P. U. P. A.; Sommerdijk, N. A. J. M.; Penn, R. L.; Whitelam, S.; Joester, D.; Zhang, H.; Rimer, J. D.; Navrotsky, A.; Banfield, J. F.; Wallace, A. F.; Michel, F. M.; Meldrum, F. C.; Cölfen, H.; Dove, P. M. Crystallization by Particle Attachment in Synthetic, Biogenic, and Geologic Environments. *Science* **2015**, *349* (6247), aaa6760. https://doi.org/10.1126/science.aaa6760.
(24) Kashchiev, D. Thermodynamically Consistent Description of the Work to Form a Nucleus of Any Size. *J. Chem. Phys.* **2003**, *118* (4), 1837–1851. https://doi.org/10.1063/1.1531614.
(25) Vlachos, D. G.; Jensen, K. F. The Roles of Supersaturation, Terrace Width, and Impurities on the Formation of Macrosteps on Crystal Surfaces Using the Terrace-Ledge-Kink Model. *Surface Science* **1992**, *262* (3), 359–370. https://doi.org/10.1016/0039-6028(92)90132-P.
(26) De Yoreo, J. J.; Vekilov, P. G. Principles of Crystal Nucleation and Growth. *Reviews in Mineralogy and Geochemistry* **2003**, *54* (1), 57–93. https://doi.org/10.2113/0540057.
(27) Wulff, G. XXV. Zur Frage der Geschwindigkeit des Wachsthums und der Auflösung der Krystallflächen. *Zeitschrift für Kristallographie - Crystalline Materials* **1901**, *34* (1–6), 449–530. https://doi.org/10.1524/zkri.1901.34.1.449.
(28) Barmparis, G. D.; Lodziana, Z.; Lopez, N.; Remediakis, I. N. Nanoparticle Shapes by Using Wulff Constructions and First-Principles Calculations. *Beilstein J. Nanotechnol.* **2015**, *6* (1), 361–368. https://doi.org/10.3762/bjnano.6.35.
(29) Liu, Y.; Yang, Y.; Sun, Y.; Song, J.; Rudawski, N. G.; Chen, X.; Tan, W. Ostwald Ripening-Mediated Grafting of Metal–Organic Frameworks on a Single Colloidal Nanocrystal to Form Uniform and Controllable MXF. *J. Am. Chem. Soc.* **2019**, *141* (18), 7407–7413. https://doi.org/10.1021/jacs.9b01563.
(30) Millange, F.; Medina, M. I.; Guillou, N.; Férey, G.; Golden, K. M.; Walton, R. I. Time-Resolved In Situ Diffraction Study of the Solvothermal Crystallization of Some Prototypical Metal-Organic Frameworks. *Angewandte Chemie International Edition* **2010**, *49* (4), 763–766. https://doi.org/10.1002/anie.200905627.
(31) Wang, X.-G.; Cheng, Q.; Yu, Y.; Zhang, X.-Z. Controlled Nucleation and Controlled Growth for Size Predicable Synthesis of Nanoscale Metal–Organic Frameworks (MOFs): A General and Scalable Approach. *Angewandte Chemie International Edition* **2018**, *57* (26), 7836–7840. https://doi.org/10.1002/anie.201803766.
(32) Dighe, A. V.; Huelsenbeck, L.; Bhawnani, R. R.; Verma, P.; Stone, K. H.; Singh, M. R.; Giri, G. Autocatalysis and Oriented Attachment Direct the Synthesis of a Metal–Organic Framework. *JACS Au* **2022**, *2* (2), 453–462. https://doi.org/10.1021/jacsau.1c00494.
(33) Anderson, S. L.; Gładysiak, A.; Boyd, P. G.; Ireland, C. P.; Miéville, P.; Tiana, D.; Vlaisavljevich, B.; Schouwink, P.; Beek, W. van; Gagnon, K. J.; Smit, B.; Stylianou, K. C. Formation Pathways of Metal–Organic Frameworks Proceeding through Partial Dissolution of the Metastable Phase. *CrystEngComm* **2017**, *19* (25), 3407–3413. https://doi.org/10.1039/C7CE00589J.
(34) Kollias, L.; Rousseau, R.; Glezakou, V.-A.; Salvalaglio, M. Understanding Metal–Organic Framework Nucleation from a Solution with Evolving Graphs. *J. Am. Chem. Soc.* **2022**, *144* (25), 11099–11109. https://doi.org/10.1021/jacs.1c13508.
(35) Katsenis, A. D.; Puškarić, A.; Štrukil, V.; Mottillo, C.; Julien, P. A.; Užarević, K.; Pham, M.-

H.; Do, T.-O.; Kimber, S. A. J.; Lazić, P.; Magdysyuk, O.; Dinnebier, R. E.; Halasz, I.; Friščić, T. In Situ X-Ray Diffraction Monitoring of a Mechanochemical Reaction Reveals a Unique Topology Metal-Organic Framework. *Nat Commun* **2015**, *6* (1), 6662. https://doi.org/10.1038/ncomms7662.

(36) Burkett, S. L.; Davis, M. E. Mechanism of Structure Direction in the Synthesis of Si-ZSM-5: An Investigation by Intermolecular 1H-29Si CP MAS NMR. *J. Phys. Chem.* **1994**, *98* (17), 4647–4653. https://doi.org/10.1021/j100068a027.

(37) Gower, L. B.; Odom, D. J. Deposition of Calcium Carbonate Films by a Polymer-Induced Liquid-Precursor (PILP) Process. *Journal of Crystal Growth* **2000**, *210* (4), 719–734. https://doi.org/10.1016/S0022-0248(99)00749-6.

(38) Kuhrts, L.; Prévost, S.; Chevrier, D. M.; Pekker, P.; Spaeker, O.; Egglseder, M.; Baumgartner, J.; Pósfai, M.; Faivre, D. Wettability of Magnetite Nanoparticles Guides Growth from Stabilized Amorphous Ferrihydrite. *J. Am. Chem. Soc.* **2021**, *143* (29), 10963–10969. https://doi.org/10.1021/jacs.1c02687.

(39) Penn, R. L.; Banfield, J. F. Imperfect Oriented Attachment: Dislocation Generation in Defect-Free Nanocrystals. *Science* **1998**. https://doi.org/10.1126/science.281.5379.969.

(40) Aerts, A.; Kirschhock, C. E. A.; Martens, J. A. Methods for in Situ Spectroscopic Probing of the Synthesis of a Zeolite. *Chem. Soc. Rev.* **2010**, *39* (12), 4626–4642. https://doi.org/10.1039/B919704B.

(41) Eddaoudi, M.; Moler, D. B.; Li, H.; Chen, B.; Reineke, T. M.; O'Keeffe, M.; Yaghi, O. M. Modular Chemistry: Secondary Building Units as a Basis for the Design of Highly Porous and Robust Metal−Organic Carboxylate Frameworks. *Acc. Chem. Res.* **2001**, *34* (4), 319–330. https://doi.org/10.1021/ar000034b.

(42) Kalmutzki, M. J.; Hanikel, N.; Yaghi, O. M. Secondary Building Units as the Turning Point in the Development of the Reticular Chemistry of MOFs. *Science Advances* **2018**, *4* (10), eaat9180. https://doi.org/10.1126/sciadv.aat9180.

(43) Férey, G. Building Units Design and Scale Chemistry. *Journal of Solid State Chemistry* **2000**, *152* (1), 37–48. https://doi.org/10.1006/jssc.2000.8667.

(44) Karthika, S.; Radhakrishnan, T. K.; Kalaichelvi, P. A Review of Classical and Nonclassical Nucleation Theories. *Crystal Growth & Design* **2016**, *16* (11), 6663–6681. https://doi.org/10.1021/acs.cgd.6b00794.

(45) Yuan, S.; Feng, L.; Wang, K.; Pang, J.; Bosch, M.; Lollar, C.; Sun, Y.; Qin, J.; Yang, X.; Zhang, P.; Wang, Q.; Zou, L.; Zhang, Y.; Zhang, L.; Fang, Y.; Li, J.; Zhou, H.-C. Stable Metal–Organic Frameworks: Stable Metal–Organic Frameworks: Design, Synthesis, and Applications (Adv. Mater. 37/2018). *Advanced Materials* **2018**, *30* (37), 1870277. https://doi.org/10.1002/adma.201870277.

(46) Mitrović, M. M.; Žekić, A. A.; Napijalo, M. M. Correlation between the Crystal Size and Crystal Growth Rate of KDP and Rochelle Salt Crystals. *Journal of Crystal Growth* **2000**, *216* (1), 437–442. https://doi.org/10.1016/S0022-0248(00)00423-1.

(47) Ban, Y.; Li, Y.; Peng, Y.; Jin, H.; Jiao, W.; Liu, X.; Yang, W. Metal-Substituted Zeolitic Imidazolate Framework ZIF-108: Gas-Sorption and Membrane-Separation Properties. *Chemistry – A European Journal* **2014**, *20* (36), 11402–11409. https://doi.org/10.1002/chem.201402287.

(48) Zhou, Y.; Ban, Y.; Yang, W. Reversibly Phase-Transformative Zeolitic Imidazolate Framework-108 and the Membrane Separation Utility. *Inorg. Chem.* **2022**, *61* (43), 17342–17352. https://doi.org/10.1021/acs.inorgchem.2c02978.

(49) Sun, J.; Semenchenko, L.; Lim, W. T.; Ballesteros Rivas, M. F.; Varela-Guerrero, V.; Jeong, H.-K. Facile Synthesis of Cd-Substituted Zeolitic-Imidazolate Framework Cd-ZIF-8 and Mixed-Metal CdZn-ZIF-8. *Microporous and Mesoporous Materials* **2018**, *264*, 35–42. https://doi.org/10.1016/j.micromeso.2017.12.032.
(50) Irving, H.; Williams, R. J. P. 637. The Stability of Transition-Metal Complexes. *J. Chem. Soc.* **1953**, No. 0, 3192–3210. https://doi.org/10.1039/JR9530003192.
(51) Irving, H.; Williams, R. J. P. Order of Stability of Metal Complexes. *Nature* **1948**, *162* (4123), 746–747. https://doi.org/10.1038/162746a0.
(52) Pearson, R. G. Hard and Soft Acids and Bases. *J. Am. Chem. Soc.* **1963**, *85* (22), 3533–3539. https://doi.org/10.1021/ja00905a001.
(53) Zhang, X.; Wang, B.; Alsalme, A.; Xiang, S.; Zhang, Z.; Chen, B. Design and Applications of Water-Stable Metal-Organic Frameworks: Status and Challenges. *Coordination Chemistry Reviews* **2020**, *423*, 213507. https://doi.org/10.1016/j.ccr.2020.213507.
(54) Ahrland, S.; Chatt, J.; Davies, N. R. The Relative Affinities of Ligand Atoms for Acceptor Molecules and Ions. *Q. Rev. Chem. Soc.* **1958**, *12* (3), 265–276. https://doi.org/10.1039/QR9581200265.
(55) Sharma, D.; Rasaily, S.; Pradhan, S.; Baruah, K.; Tamang, S.; Pariyar, A. HKUST-1 Metal Organic Framework as an Efficient Dual-Function Catalyst: Aziridination and One-Pot Ring-Opening Transformation for Formation of β-Aryl Sulfonamides with C–C, C–N, C–S, and C–O Bonds. *Inorg. Chem.* **2021**, *60* (11), 7794–7802. https://doi.org/10.1021/acs.inorgchem.1c00201.
(56) Ahamad, M. N.; Shahid, M.; Ahmad, M.; Sama, F. Cu(II) MOFs Based on Bipyridyls: Topology, Magnetism, and Exploring Sensing Ability toward Multiple Nitroaromatic Explosives. *ACS Omega* **2019**, *4* (4), 7738–7749. https://doi.org/10.1021/acsomega.9b00715.
(57) Moh, P. Y.; Cubillas, P.; Anderson, M. W.; Attfield, M. P. Revelation of the Molecular Assembly of the Nanoporous Metal Organic Framework ZIF-8. *J. Am. Chem. Soc.* **2011**, *133* (34), 13304–13307. https://doi.org/10.1021/ja205900f.
(58) Ragon, F.; Chevreau, H.; Devic, T.; Serre, C.; Horcajada, P. Impact of the Nature of the Organic Spacer on the Crystallization Kinetics of UiO-66(Zr)-Type MOFs. *Chemistry – A European Journal* **2015**, *21* (19), 7135–7143. https://doi.org/10.1002/chem.201406119.
(59) Banerjee, D.; Finkelstein, J.; Smirnov, A.; Forster, P. M.; Borkowski, L. A.; Teat, S. J.; Parise, J. B. Synthesis and Structural Characterization of Magnesium Based Coordination Networks in Different Solvents. *Crystal Growth & Design* **2011**, *11* (6), 2572–2579. https://doi.org/10.1021/cg200327y.
(60) Kim, Y. J.; Kim, M.-Z.; Alam, S. F.; Rehman, A. ur; Devipriyanka, A.; Sharma, P.; Lee, H. R.; Cho, C.-H. Polarity-Dependent Particle Size of Zeolitic Imidazolate Framework Synthesized in Various Solvents. *Materials Chemistry and Physics* **2021**, *259*, 124021. https://doi.org/10.1016/j.matchemphys.2020.124021.
(61) Kollias, L.; Cantu, D. C.; Glezakou, V.-A.; Rousseau, R.; Salvalaglio, M. On the Role of Enthalpic and Entropic Contributions to the Conformational Free Energy Landscape of MIL-101(Cr) Secondary Building Units. *Advanced Theory and Simulations* **2020**, *3* (12), 2000092. https://doi.org/10.1002/adts.202000092.
(62) Liang, W.; Ricco, R.; Maddigan, N. K.; Dickinson, R. P.; Xu, H.; Li, Q.; Sumby, C. J.; Bell, S. G.; Falcaro, P.; Doonan, C. J. Control of Structure Topology and Spatial Distribution of Biomacromolecules in Protein@ZIF-8 Biocomposites. *Chem. Mater.* **2018**, *30* (3), 1069–

1077. https://doi.org/10.1021/acs.chemmater.7b04977.
(63) Malekmohammadi, M.; Fatemi, S.; Razavian, M.; Nouralishahi, A. A Comparative Study on ZIF-8 Synthesis in Aqueous and Methanolic Solutions: Effect of Temperature and Ligand Content. *Solid State Sciences* **2019**, *91*, 108–112. https://doi.org/10.1016/j.solidstatesciences.2019.03.022.
(64) Lewis, D. J.; Zornberg, L. Z.; Carter, D. J. D.; Macfarlane, R. J. Single-Crystal Winterbottom Constructions of Nanoparticle Superlattices. *Nat. Mater.* **2020**, *19* (7), 719–724. https://doi.org/10.1038/s41563-020-0643-6.
(65) Venna, S. R.; Carreon, M. A. Metal Organic Framework Membranes for Carbon Dioxide Separation. *Chemical Engineering Science* **2015**, *124*, 3–19. https://doi.org/10.1016/j.ces.2014.10.007.
(66) Liu, S.; Xiao, W.; Jin, C.; Xia, S.; Wang, W.; Jiang, X.; Li, L.; Wang, S.; Chen, C. MOFs Derived CdS/CdO Heterojunction Photoanode for High-Efficient Water Splitting. *Applied Surface Science* **2022**, *605*, 154697. https://doi.org/10.1016/j.apsusc.2022.154697.
(67) Kumar, S.; Pramudya, Y.; Müller, K.; Chandresh, A.; Dehm, S.; Heidrich, S.; Fediai, A.; Parmar, D.; Perera, D.; Rommel, M.; Heinke, L.; Wenzel, W.; Wöll, C.; Krupke, R. Sensing Molecules with Metal–Organic Framework Functionalized Graphene Transistors. *Advanced Materials* **2021**, *33* (43), 2103316. https://doi.org/10.1002/adma.202103316.
(68) Altintas, C.; Keskin, S. Molecular Simulations of MOF Membranes and Performance Predictions of MOF/Polymer Mixed Matrix Membranes for CO2/CH4 Separations. *ACS Sustainable Chem. Eng.* **2019**, *7* (2), 2739–2750. https://doi.org/10.1021/acssuschemeng.8b05832.
(69) Zhao, X.; Fang, X.; Wu, B.; Zheng, L.; Zheng, N. Facile Synthesis of Size-Tunable ZIF-8 Nanocrystals Using Reverse Micelles as Nanoreactors. *Sci. China Chem.* **2014**, *57* (1), 141–146. https://doi.org/10.1007/s11426-013-5008-4.
(70) Horcajada, P.; Serre, C.; Grosso, D.; Boissière, C.; Perruchas, S.; Sanchez, C.; Férey, G. Colloidal Route for Preparing Optical Thin Films of Nanoporous Metal–Organic Frameworks. *Advanced Materials* **2009**, *21* (19), 1931–1935. https://doi.org/10.1002/adma.200801851.
(71) Makiura, R.; Motoyama, S.; Umemura, Y.; Yamanaka, H.; Sakata, O.; Kitagawa, H. Surface Nano-Architecture of a Metal–Organic Framework. *Nature Mater* **2010**, *9* (7), 565–571. https://doi.org/10.1038/nmat2769.
(72) Biemmi, E.; Scherb, C.; Bein, T. Oriented Growth of the Metal Organic Framework Cu3(BTC)2(H2O)3·xH2O Tunable with Functionalized Self-Assembled Monolayers. *J. Am. Chem. Soc.* **2007**, *129* (26), 8054–8055. https://doi.org/10.1021/ja0701208.
(73) Vello, T. P.; Strauss, M.; Costa, C. A. R.; Corrêa, C. C.; Bof Bufon, C. C. Deterministic Control of Surface Mounted Metal–Organic Framework Growth Orientation on Metallic and Insulating Surfaces. *Phys. Chem. Chem. Phys.* **2020**, *22* (10), 5839–5846. https://doi.org/10.1039/C9CP05717J.
(74) Shekhah, O.; Wang, H.; Kowarik, S.; Schreiber, F.; Paulus, M.; Tolan, M.; Sternemann, C.; Evers, F.; Zacher, D.; Fischer, R. A.; Wöll, C. Step-by-Step Route for the Synthesis of Metal−Organic Frameworks. *J. Am. Chem. Soc.* **2007**, *129* (49), 15118–15119. https://doi.org/10.1021/ja076210u.
(75) Khalil, I. E.; Fonseca, J.; Reithofer, M. R.; Eder, T.; Chin, J. M. Tackling Orientation of Metal-Organic Frameworks (MOFs): The Quest to Enhance MOF Performance. *Coordination Chemistry Reviews* **2023**, *481*, 215043.

https://doi.org/10.1016/j.ccr.2023.215043.
(76) Liu, J.; Wöll, C. Surface-Supported Metal–Organic Framework Thin Films: Fabrication Methods, Applications, and Challenges. *Chem. Soc. Rev.* **2017**, *46* (19), 5730–5770. https://doi.org/10.1039/C7CS00315C.
(77) Lv, M.; Sun, M.; Wu, M.; Zhang, F.; Yin, H.; Sun, Y.; Liu, R.; Fan, Z.; Du, J. Tryptophan-Modulated Nanoscale Metal–Organic Framework for Coordinated Loading of Biomolecules for Cascade Production of Reactive Oxygen and Nitrogen Species. *Nano Lett.* **2022**, *22* (23), 9621–9629. https://doi.org/10.1021/acs.nanolett.2c03778.
(78) Maddigan, N. K.; Tarzia, A.; Huang, D. M.; Sumby, C. J.; Bell, S. G.; Falcaro, P.; Doonan, C. J. Protein Surface Functionalisation as a General Strategy for Facilitating Biomimetic Mineralisation of ZIF-8. *Chem. Sci.* **2018**, *9* (18), 4217–4223. https://doi.org/10.1039/C8SC00825F.
(79) Shekhah, O.; Fu, L.; Sougrat, R.; Belmabkhout, Y.; Cairns, A. J.; Giannelis, E. P.; Eddaoudi, M. Successful Implementation of the Stepwise Layer-by-Layer Growth of MOF Thin Films on Confined Surfaces: Mesoporous Silica Foam as a First Case Study. *Chem. Commun.* **2012**, *48* (93), 11434–11436. https://doi.org/10.1039/C2CC36233C.
(80) Liu, F.; Xu, H. Development of a Novel Polystyrene/Metal-Organic Framework-199 Electrospun Nanofiber Adsorbent for Thin Film Microextraction of Aldehydes in Human Urine. *Talanta* **2017**, *162*, 261–267. https://doi.org/10.1016/j.talanta.2016.09.065.
(81) Yao, M.-S.; Tang, W.-X.; Wang, G.-E.; Nath, B.; Xu, G. MOF Thin Film-Coated Metal Oxide Nanowire Array: Significantly Improved Chemiresistor Sensor Performance. *Advanced Materials* **2016**, *28* (26), 5229–5234. https://doi.org/10.1002/adma.201506457.
(82) Bim-Junior, O.; Alania, Y.; Tabatabaei, F. S.; Frem, R.; Bedran-Russo, A. K.; Lisboa-Filho, P. N. Biomimetic Growth of Metal–Organic Frameworks for the Stabilization of the Dentin Matrix and Control of Collagenolysis. *Langmuir* **2022**, *38* (4), 1600–1610. https://doi.org/10.1021/acs.langmuir.1c03073.
(83) Tong, L.; Huang, S.; Shen, Y.; Liu, S.; Ma, X.; Zhu, F.; Chen, G.; Ouyang, G. Atomically Unveiling the Structure-Activity Relationship of Biomacromolecule-Metal-Organic Frameworks Symbiotic Crystal. *Nat Commun* **2022**, *13* (1), 951. https://doi.org/10.1038/s41467-022-28615-y.
(84) Huang, A.; Bux, H.; Steinbach, F.; Caro, J. Molecular-Sieve Membrane with Hydrogen Permselectivity: ZIF-22 in LTA Topology Prepared with 3-Aminopropyltriethoxysilane as Covalent Linker. *Angewandte Chemie International Edition* **2010**, *49* (29), 4958–4961. https://doi.org/10.1002/anie.201001919.
(85) Kwon, H. T.; Jeong, H.-K.; Lee, A. S.; An, H. S.; Lee, J. S. Heteroepitaxially Grown Zeolitic Imidazolate Framework Membranes with Unprecedented Propylene/Propane Separation Performances. *J. Am. Chem. Soc.* **2015**, *137* (38), 12304–12311. https://doi.org/10.1021/jacs.5b06730.
(86) Carpenter, B. P.; Talosig, A. R.; Mulvey, J. T.; Merham, J.; Patterson, J. P. The Role of Molecular Modification and Protein Folding in the Nucleation and Growth of Protein-Metal-Organic Frameworks. *Chemistry of Materials* **2022**.
(87) Filez, M.; Caratelli, C.; Rivera-Torrente, M.; Muniz-Miranda, F.; Hoek, M.; Altelaar, M.; Heck, A. J. R.; Van Speybroeck, V.; Weckhuysen, B. M. Elucidation of the Pre-Nucleation Phase Directing Metal-Organic Framework Formation. *Cell Reports Physical Science* **2021**, *2* (12), 100680. https://doi.org/10.1016/j.xcrp.2021.100680.
(88) Salionov, D.; Semivrazhskaya, O. O.; Casati, N. P. M.; Ranocchiari, M.; Bjelić, S.; Verel,

R.; van Bokhoven, J. A.; Sushkevich, V. L. Unraveling the Molecular Mechanism of MIL-53(Al) Crystallization. *Nat Commun* **2022**, *13* (1), 3762. https://doi.org/10.1038/s41467-022-31294-4.

(89) Liang, W.; Xu, H.; Carraro, F.; Maddigan, N. K.; Li, Q.; Bell, S. G.; Huang, D. M.; Tarzia, A.; Solomon, M. B.; Amenitsch, H.; Vaccari, L.; Sumby, C. J.; Falcaro, P.; Doonan, C. J. Enhanced Activity of Enzymes Encapsulated in Hydrophilic Metal–Organic Frameworks. *J. Am. Chem. Soc.* **2019**, *141* (6), 2348–2355. https://doi.org/10.1021/jacs.8b10302.

(90) Carraro, F.; Velásquez-Hernández, M. de J.; Astria, E.; Liang, W.; Twight, L.; Parise, C.; Ge, M.; Huang, Z.; Ricco, R.; Zou, X.; Villanova, L.; Kappe, C. O.; Doonan, C.; Falcaro, P. Phase Dependent Encapsulation and Release Profile of ZIF-Based Biocomposites. *Chem. Sci.* **2020**, *11* (13), 3397–3404. https://doi.org/10.1039/C9SC05433B.

(91) Hadjiivanov, K. I.; Panayotov, D. A.; Mihaylov, M. Y.; Ivanova, E. Z.; Chakarova, K. K.; Andonova, S. M.; Drenchev, N. L. Power of Infrared and Raman Spectroscopies to Characterize Metal-Organic Frameworks and Investigate Their Interaction with Guest Molecules. *Chem. Rev.* **2021**, *121* (3), 1286–1424. https://doi.org/10.1021/acs.chemrev.0c00487.

(92) Kumari, G.; Jayaramulu, K.; Maji, T. K.; Narayana, C. Temperature Induced Structural Transformations and Gas Adsorption in the Zeolitic Imidazolate Framework ZIF-8: A Raman Study. *J. Phys. Chem. A* **2013**, *117* (43), 11006–11012. https://doi.org/10.1021/jp407792a.

(93) Embrechts, H.; Kriesten, M.; Hoffmann, K.; Peukert, W.; Hartmann, M.; Distaso, M. Elucidation of the Formation Mechanism of Metal–Organic Frameworks via in-Situ Raman and FTIR Spectroscopy under Solvothermal Conditions. *J. Phys. Chem. C* **2018**, *122* (23), 12267–12278. https://doi.org/10.1021/acs.jpcc.8b02484.

(94) Cravillon, J.; Münzer, S.; Lohmeier, S.-J.; Feldhoff, A.; Huber, K.; Wiebcke, M. Rapid Room-Temperature Synthesis and Characterization of Nanocrystals of a Prototypical Zeolitic Imidazolate Framework. *Chem. Mater.* **2009**, *21* (8), 1410–1412. https://doi.org/10.1021/cm900166h.

(95) Saha, S.; Wiebcke, M.; Huber, K. Insight into Fast Nucleation and Growth of Zeolitic Imidazolate Framework-71 by In Situ Static Light Scattering at Variable Temperature and Kinetic Modeling. *Crystal Growth & Design* **2018**, *18* (8), 4653–4661. https://doi.org/10.1021/acs.cgd.8b00626.

(96) Saha, S.; Springer, S.; Schweinefuß, M. E.; Pontoni, D.; Wiebcke, M.; Huber, K. Insight into Fast Nucleation and Growth of Zeolitic Imidazolate Framework-71 by In Situ Time-Resolved Light and X-Ray Scattering Experiments. *Crystal Growth & Design* **2016**, *16* (4), 2002–2010. https://doi.org/10.1021/acs.cgd.5b01594.

(97) Netzsch, P.; Ettlinger, R.; Morris, R. E. Controllable Surfactant-Directed Zeolitic-Imidazolate-8 Growth on Swollen 2D Zeolites. *APL Materials* **2023**, *11* (3), 031115. https://doi.org/10.1063/5.0139673.

(98) Katsenis, A. D.; Puškarić, A.; Štrukil, V.; Mottillo, C.; Julien, P. A.; Užarević, K.; Pham, M.-H.; Do, T.-O.; Kimber, S. A. J.; Lazić, P.; Magdysyuk, O.; Dinnebier, R. E.; Halasz, I.; Friščić, T. In Situ X-Ray Diffraction Monitoring of a Mechanochemical Reaction Reveals a Unique Topology Metal-Organic Framework. *Nat Commun* **2015**, *6*, 6662. https://doi.org/10.1038/ncomms7662.

(99) Chen, S.-Y.; Lo, W.-S.; Huang, Y.-D.; Si, X.; Liao, F.-S.; Lin, S.-W.; Williams, B. P.; Sun, T.-Q.; Lin, H.-W.; An, Y.; Sun, T.; Ma, Y.; Yang, H.-C.; Chou, L.-Y.; Shieh, F.-K.; Tsung, C.-K. Probing Interactions between Metal–Organic Frameworks and Freestanding Enzymes

in a Hollow Structure. *Nano Lett.* **2020**, *20* (9), 6630–6635. https://doi.org/10.1021/acs.nanolett.0c02265.

(100) Cravillon, J.; Schröder, C. A.; Nayuk, R.; Gummel, J.; Huber, K.; Wiebcke, M. Fast Nucleation and Growth of ZIF-8 Nanocrystals Monitored by Time-Resolved In Situ Small-Angle and Wide-Angle X-Ray Scattering. *Angewandte Chemie International Edition* **2011**, *50* (35), 8067–8071. https://doi.org/10.1002/anie.201102071.

(101) Stavitski, E.; Goesten, M.; Juan-Alcañiz, J.; Martinez-Joaristi, A.; Serra-Crespo, P.; Petukhov, A. V.; Gascon, J.; Kapteijn, F. Kinetic Control of Metal–Organic Framework Crystallization Investigated by Time-Resolved In Situ X-Ray Scattering. *Angewandte Chemie International Edition* **2011**, *50* (41), 9624–9628. https://doi.org/10.1002/anie.201101757.

(102) He, B.; Macreadie, L. K.; Gardiner, J.; Telfer, S. G.; Hill, M. R. In Situ Investigation of Multicomponent MOF Crystallization during Rapid Continuous Flow Synthesis. *ACS Appl Mater Interfaces* **2021**, *13* (45), 54284–54293. https://doi.org/10.1021/acsami.1c04920.

(103) Gong, X.; Noh, H.; Gianneschi, N. C.; Farha, O. K. Interrogating Kinetic versus Thermodynamic Topologies of Metal–Organic Frameworks via Combined Transmission Electron Microscopy and X-Ray Diffraction Analysis. *J. Am. Chem. Soc.* **2019**, *141* (15), 6146–6151. https://doi.org/10.1021/jacs.9b01789.

(104) Liu, L.; Zhang, D.; Zhu, Y.; Han, Y. Bulk and Local Structures of Metal–Organic Frameworks Unravelled by High-Resolution Electron Microscopy. *Commun Chem* **2020**, *3* (1), 1–14. https://doi.org/10.1038/s42004-020-00361-6.

(105) Wiktor, C.; Meledina, M.; Turner, S.; Lebedev, O. I.; Fischer, R. A. Transmission Electron Microscopy on Metal–Organic Frameworks – a Review. *J. Mater. Chem. A* **2017**, *5* (29), 14969–14989. https://doi.org/10.1039/C7TA00194K.

(106) Patterson, J. P.; Abellan, P.; Denny, M. S.; Park, C.; Browning, N. D.; Cohen, S. M.; Evans, J. E.; Gianneschi, N. C. Observing the Growth of Metal–Organic Frameworks by in Situ Liquid Cell Transmission Electron Microscopy. *J. Am. Chem. Soc.* **2015**, *137* (23), 7322–7328. https://doi.org/10.1021/jacs.5b00817.

(107) Vladár, A. E.; Postek, M. T.; Ming, B. On the Sub-Nanometer Resolution of Scanning Electron and Helium Ion Microscopes. *Microscopy Today* **2009**, *17* (2), 6–13. https://doi.org/10.1017/S1551929500054420.

(108) Jian, M.; Liu, B.; Liu, R.; Qu, J.; Wang, H.; Zhang, X. Water-Based Synthesis of Zeolitic Imidazolate Framework-8 with High Morphology Level at Room Temperature. *RSC Adv.* **2015**, *5* (60), 48433–48441. https://doi.org/10.1039/C5RA04033G.

(109) Rizvi, A.; Mulvey, J. T.; Carpenter, B. P.; Talosig, R.; Patterson, J. P. A Close Look at Molecular Self-Assembly with the Transmission Electron Microscope. *Chem. Rev.* **2021**, *121* (22), 14232–14280. https://doi.org/10.1021/acs.chemrev.1c00189.

(110) Goldstein, J. I.; Newbury, D. E.; Echlin, P.; Joy, D. C.; Romig, A. D.; Lyman, C. E.; Fiori, C.; Lifshin, E. Coating and Conductivity Techniques for SEM and Microanalysis. In *Scanning Electron Microscopy and X-Ray Microanalysis*; Springer US: Boston, MA, 1992; pp 671–740. https://doi.org/10.1007/978-1-4613-0491-3_13.

Chapter 2.

Investigating Synthetic Parameters and Protein Interactions in Protein-Metal-Organic Frameworks

This work appears in the following publication and has been re-formatted for this thesis:

Ogata, A.F.; Rakowski A.M.; **Carpenter B.P**. Fishman, D.A.; Merham, J.G.; Hurst, P.J.; Patterson, J.P. Direct Observation of Amorphous Precursor Phases in the Nucleation of Protein-Metal-Organic Frameworks. *J. Am. Chem. Soc*, 2020. 142 (3), 1433-1442.

Chapter 2. Investigating Synthetic Parameters and Protein Interactions in Protein-Metal-Organic Frameworks.

2.1 Introduction

In biological systems, crystal formation is precisely controlled through the process of biomineralization, whereby macromolecules direct nucleation and growth mechanisms to create highly ordered and optimized structures.[1] Analogous to biomineralization, biomolecules can be incorporated into synthetic crystals such as metal–organic frameworks (MOFs), forming a new class of synthetic biological nanomaterials.[2–7] During protein–MOF (p-MOF) crystallization, proteins are encapsulated into the MOF framework and exhibit enhanced bioactivity and stability[8–10] that is desired for the development of next-generation materials in drug delivery,[2,11–13] chemical and biological sensing,[11,14–16] and catalysis.[17,18] Synthetic conditions largely affect the performance of the final p-MOF product, as a result of various nucleation rates (rapid[19] vs unchanged[20]), crystal morphologies (protein dependent[8] vs MOF dependent[21]), and protein loading mechanisms (homogeneous encapsulation[8] vs surface encapsulation[22]). Synthetic parameters such as ligand:metal ratio, ZIF-8 precursor concentrations, and choice of biomolecule offer a large landscape from which to design p-MOFs with desired properties. However, the large p-MOF parameter space has resulted in a wide range of reported synthesis conditions and final crystal products.[4,8,9,17,21,22]

Despite the heterogeneity in p-MOF products, a compelling argument for studying p-MOF systems is the simplicity with which the materials can be synthesized. Mixing the metal, ligand, and protein precursors in water at room temperature will induce crystallization over a period of 24 hr. It is hypothesized that proteins with negatively charged surfaces can concentrate positively charged metal ions and ligands to a local region, resulting in a localized supersaturation that

promotes MOF nucleation and crystallization.[2,4,8,19,23] This hypothesized mechanism is analogous to biomineralization processes, where biomolecules alter the energy barriers to nucleation and promote crystal growth pathways.[24] Progress in predictive models for p-MOF synthesis has been demonstrated by controlling the surface charge of proteins[25] or hydrophilicity[26] of MOFs, indicating that the formation of p-MOFs is highly dependent on interactions between biomolecules and MOF precursors. However, direct observations of the underlying p-MOF crystallization mechanisms have not been reported, likely due to the difficulties associated with characterizing the transient, nanoscale hybrid precursors present in solution.

In this study, synthetic and instrumental protocols are established for studying p-MOFs, specifically the model system ZIF-8 and bovine serum albumin (BSA), that are vital for future studies in this thesis. Additionally, light scattering, zeta potential, and FTIR studies were performed to understand the crystallization kinetics, electrostatic interactions between the protein and MOF precursors, and incorporation of biomolecule in the MOF. Cryogenic transmission electron microscopy studies by Dr. Alana Ogata demonstrated that amorphous phases are vital in determining local supersaturation and, therefore, controlling the crystallization mechanism. We identify two key amorphous phases: (1) 2-methylimidazole/zinc (HmIm/Zn) amorphous particles and (2) protein/HmIm/Zn particles. We also identify two distinct mechanisms dependent on the HmIm:Zn precursor ratios. At high ligand:metal ratios (~35:1), ZIF-8 crystals nucleate from the HmIm/Zn amorphous phase and the protein/HmIm/Zn particles undergo a solid-state transformation at the growing ZIF-8 crystal surface through heterogeneous crystallization. At low ligand:metal ratios (~4:1), the HmIm/Zn amorphous phase is unable to crystallize, and the protein/HmIm/Zn phase promotes ZIF-8 nucleation directly.

2.2 Experimental methods

Materials

Chemical reagents for ZIF-8 and BSA-ZIF-8 syntheses were obtained from Sigma-Aldrich and used as received unless otherwise stated. 2-Methylimidazole (HmIm), zinc acetate dihydrate, bovine serum albumin, and bovine serum albumin fluorescein isothiocyanate conjugate. Milli-Q water ($\rho > 18$ MΩ cm) was used as the solvent for all aqueous solutions.

ZIF-8 and BSA/ZIF-8 Synthesis

Separate aqueous solutions of 2-methylimidazole (1400 mM, 1 mL) and zinc acetate (40 mM, 1 mL) were prepared for a final concentration of HmIm:Zn = 700:20 mM upon mixing. These two solutions were combined and aged for 24 h without stirring. The resulting precipitate was recovered by centrifugation at 6000 rpm for 5 min, washed with water, and centrifuged twice more. For synthesis of BSA/ZIF-8, BSA was added into a solution of HmIm for a final concentration of 5 mg/mL BSA in a HmIm aqueous solution (1400 mL, 1 mL) and subsequently mixed with a separate solution of zinc acetate (40 mM, 1 mL). Solutions were aged for 24 h without stirring, and a precipitate was obtained as described for ZIF-8. All samples described here were synthesized by adding BSA (5 mg/mL) to aqueous solutions of HmIm (1400 mM) and subsequently mixing with zinc acetate (40 mM). However, we determined that adding BSA to either zinc acetate or 2-methylimidazole solutions produced the same final product upon mixing (Figure 2.1).

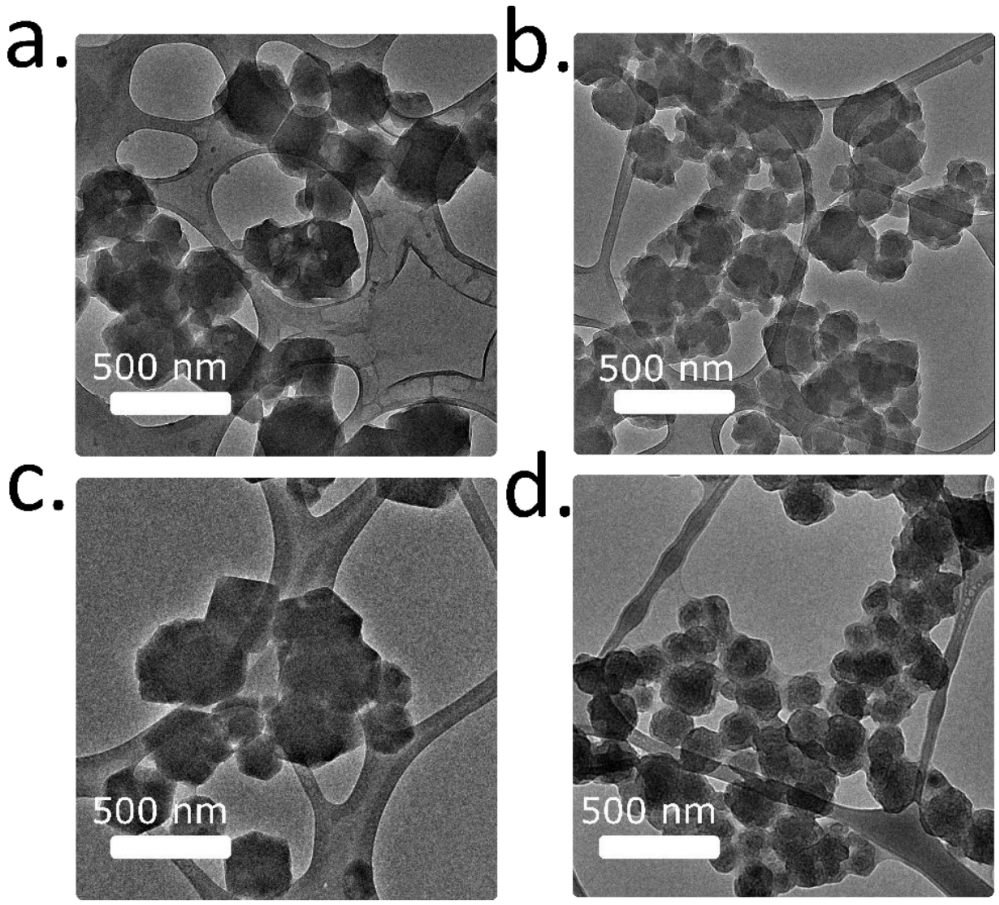

Figure 2.1: TEM micrographs of final crystal products for BSA-ZIF-8 synthesis. BSA was added to aqueous solutions of 2-methylimidizole for a final solution of (a) 1.25 mg/mL BSA and (b) 5 mg/mL BSA in 1 mL of 1400 mM HmIm and mixed with a separate solution of zinc acetate (40 mM, 1 mL). As a comparative synthesis, BSA was added to aqueous solutions of zinc acetate for a final solution of (c) 1.25 mg/mL BSA and (d) 5 mg/mL BSA in 1 mL of 40 mM Zn and mixed with a separate solution of 2-methylimidazole (1400 mM, 1 mL). All solutions were aged for 24 hrs and washed twice by centrifugation.

TEM

Lacey Carbon grids were purchased from Electron Microscopy Sciences and used as received. Precipitates were adsorbed from 10x diluted ZIF-8 solutions for 5 min and blotted with Kimwipe paper. Transmission electron micrographs were obtained on a JEOL-2100F TEM using a Schottky type field emission gun operating at 200 kV. Images were recorded using Serial EM software and collected using Gatan Oneview, Gatan K2 and Gatan K3 cameras.

CryoTEM

CryoTEM Quantifoil R2/2 Holey Carbon Films were purchased from Electron Microscopy Sciences. Grids were glow discharged for 70 s to increase hydrophilicity prior to sample preparation. Samples were taken from reaction solutions at time points ranging 4 s to 4 h. Vitrification was carried out by an Automatic Plunge Freezer ME GP2 (Leica Microsystems) where sample preparation onto cryoTEM grids was carried out at 95% humidity to prevent evaporation and blotted for 4 s before autoplunging into liquid propane. Vitrified samples were studied on a JEOL-2100F TEM using a Schottky type field emission gun operating at 200 kV. Images were recorded using Serial EM software and a Gatan OneView CMOS camera at 4k × 4k resolution. BSA-ZIF-8 reaction solutions taken at >1 min were centrifuged for 5 s immediately prior to vitrification and samples were taken from the supernatant to minimize the material build up on cryoTEM grids. Analysis times of 4 s were achieved by placing two separate drops of 2-methylimidazolate solution and zinc acetate solution on the grid and initiating mixing upon contact with blotting paper for 4 s.

Structural Characterization

Samples analyzed by SEM were sputter-coated with ∼5 nm of iridium (Quorum Q150T) and imaged by a FEI Magellan 400 XHR system. Secondary electron images were acquired with an accelerating voltage of 10 kV, using a through lens detector operating in immersion mode. PXRD patterns were acquired using a Rigaku SmartLab X-ray diffractometer utilizing X-rays generated at 40 kV and 44 mA with Cu Kα irradiation.

Fluorescence Imaging

All-optical transmission and single photon fluorescence imaging was performed using an Olympus FluoView 1000 laser scanning microscopy system based on an Olympus IX81 inverted microscope frame. A femtosecond oscillator (MaiTai HP, SpectraPhysics) was tuned to produce 960 nm pulses (80 fs, 80 MHz) that were then converted to 480 nm pulses via second harmonic generation in 0.5 mm β-barium borate crystal. Excitation pulses at 480 nm were focused on to the sample with 60× NA = 1.41 oil-immersion objective lens (Olympus). Transmitted light was collected via an optical condenser in the forward channel to produce an all-optical image for correlation with TEM images. Fluorescence signal was collected in backscattering geometry, and fundamental light was filtered with a dichroic beam splitter and set of bandpass filters optimized for fluorescence emission. Both forward and backward detection channels were equipped with photomultiplier tubes (Hamamatsu). Imaging was performed at various fields of view with resolution 800 × 800 and 2048 × 2048 pixels while keeping galvanometric mirror scanning speed at 2 μs/pixel. All images were acquired using a Kalman filter utilizing two images.

Zeta Potential and Light Scattering Turbidity Measurements

Measurements were taken with a Malvern Zetasizer ZS Nano dynamic light scattering instrument. Zeta potential samples were measured in a disposable capillary cell from Malvern Panalytical. For each sample measurement, the instrument was set to automatic runs (ranging from 10 to 100) to ensure the instrument achieved sufficient signal, and averages of three measurements were taken. Turbidity measurements were made using the SOP Player window and set to automatic runs (ranging from 10 to 100) with 60 s pauses for over the course of 12 h.

2.3 Results

Crystallization of ZIF-8

ZIF-8 is a MOF widely employed for the encapsulation of various biomolecules, as summarized in Table A1. Major advances in in situ analytical techniques have enabled direct observation of ZIF-8 formation in methanol,[27–32] revealing intermediate states such as amorphous particles,[28] gel phases,[33] and amorphous phases.[29] Studies of MOF formation in aqueous systems are limited.[34–36] but crucial for understanding p-MOF systems which are typically synthesized in water. The synthesis of ZIF-8 under aqueous conditions can produce a wide range of ZIF-8 crystal polymorphs from sodalite (sod) to diamondoid (dia) topologies.[20] Studies provide evidence of nonclassical phases such as nanocrystals, stable clusters, and an amorphous intermediate in the ZIF-8 formation in aqueous systems.[29] However, the morphology, interactions, and nature of these phases (amorphous or crystalline) has yet to be directly probed.

TEM enables direct observation of morphological changes with atomic scale resolution to probe crystal growth.[37] Although MOF crystals are stable under the high vacuum conditions of an electron microscope, the precursor phases to all crystalline structures synthesized in solution involve the formation of hydrated transient species. These hydrated species are incompatible with standard TEM experiments, and we consequently utilized cryoTEM to monitor ZIF-8 formation in the absence and presence of BSA. BSA serves as an inexpensive model protein that rapidly promotes the biomineralization of ZIF-8 and is widely studied for understanding p-MOF nucleation and growth.[19,22,38] CryoTEM preparation enables high control of synthetic conditions, an advantage utilized here by initiation of ZIF-8 reactions upon mixing Zn and HmIm aqueous solutions, followed by vitrification of the resulting crystallization solutions at various time points (>4 s). Based on previous literature,[8,20] we screened several ligand:metal ratios (HmIm:Zn) for the

synthesis of ZIF-8 and observed a wide range of crystal structures and sizes (Figure 2.2).

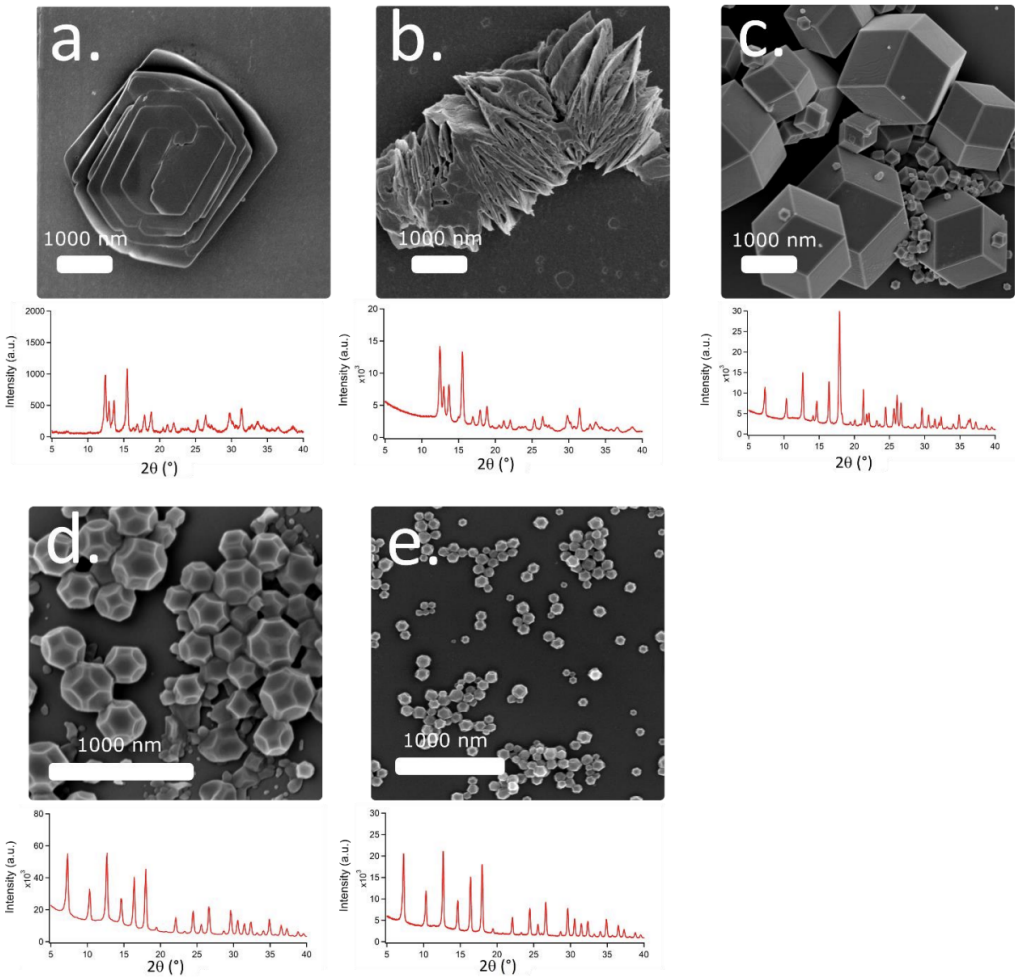

Figure 2.2: Final crystal products for ZIF synthesis carried out at various HmIm:Zn ratios. SEM micrographs and corresponding PXRD patterns (below) characterized for ZIF crystal synthesized from HmIm:Zn ratios (a) 4:1, (b) 10:1, (c) 35:1, (d) 100:1, and e) 270:1. Zinc acetate concentrations were kept constant at 20 mM for all reactions.

In agreement with previous reports,[22] low ZIF-8 precursor concentrations or low HmIm:Zn molar ratio conditions favor the formation of ZIF-8 (dia) topology or an amorphous material.[38] In contrast, sufficiently high ratios of ZIF-8 precursors result in the formation of ZIF-8 (sod) crystals. ZIF-8 (sod) is extensively studied in p-MOF literature, and therefore, we chose to focus our initial

analysis on the HmIm:Zn ratio of 35:1 which spontaneously produces ZIF-8 (sod) with good reproducibility and crystal purity. HmIm:Zn ratios above 35:1, which also produce ZIF-8 (sod), formed too rapidly for the early stages to be captured by cryoTEM. To probe the kinetics of ZIF-8 formation, we performed static light scattering measurements at one angle (Figure 2.3) to measure the change in solution turbidity with time.

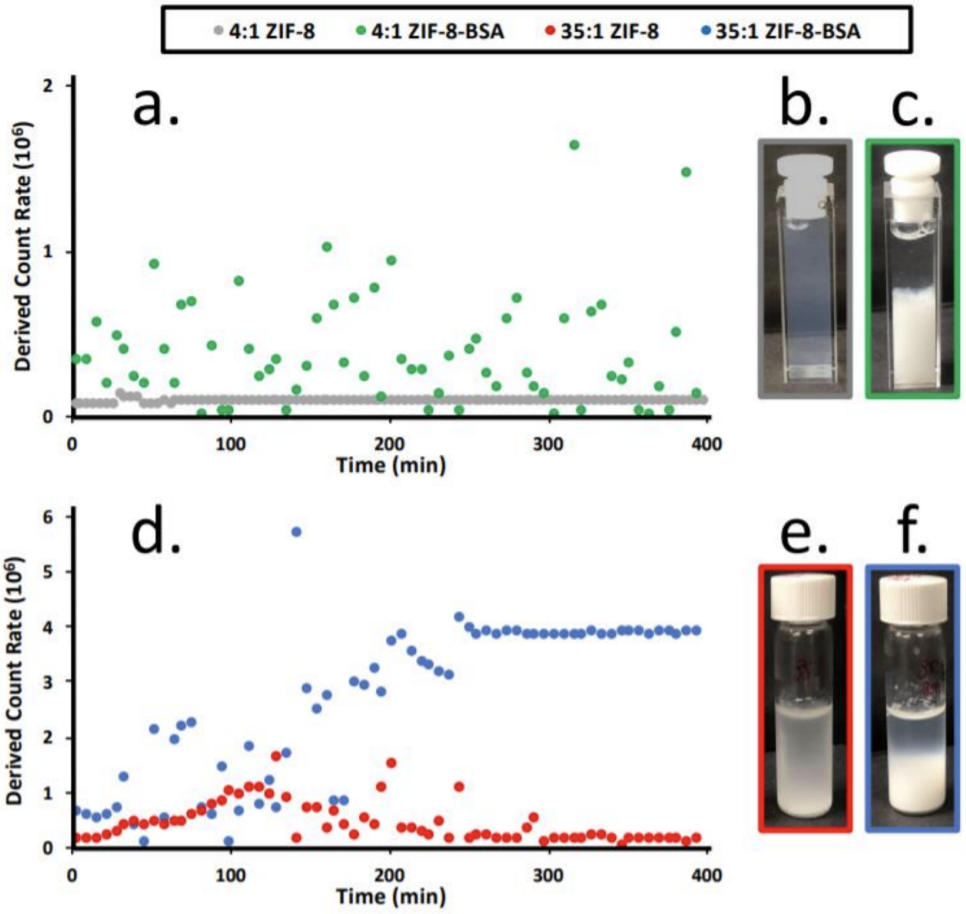

Figure 2.3: (a) Turbidity measurements over 6 hours of ZIF-8 solutions at HmIm:Zn ratio of 4:1 in the (green) presence and (grey) absence of BSA. Photos of (b) 80 mM HmIm : 20 mM Zn (c) 80 mM HmIm: 20 mM Zn with 5 mg/ml BSA solutions after 6 hours. (d) Turbidity measurements over 6 hours of ZIF-8 solutions at HmIm:Zn ratio of 35:1 in the (blue) presence and (red) absence of BSA. Photos of (e) 700 mM HmIm : 20 mM Zn and (f) 700 mM HmIm : 20 mM Zn with 5 mg/ml BSA solutions after 6 hours.

ZIF-8 solutions at a HmIm:Zn ratio of 4:1 showed no signal without BSA and a very noisy

signal with BSA. ZIF-8 solutions at a HmIm:Zn ratio of 35:1 showed an increase in turbidity without BSA within the first 100 min of the reaction followed by a decrease in turbidity. With BSA, the ZIF-8 solutions at a HmIm:Zn ratio of 35:1 showed initial noisy data that gradually increased, followed by a plateau. We hypothesize that ZIF-8 crystals at 35:1 nucleate and grow during increase in turbidity and precipitate out either above (with BSA) or below (without BSA) the area of detection upon reaching large crystal sizes.

We aim to elucidate this mechanism by cryoTEM. MOFs are notoriously sensitive to the electron beam,[25,27,39] and consequently, cryoTEM images were recorded with a 5 s exposure time and a low electron dose rate of $1e^{-}Å^{-2}s^{-1}$ to minimize beam damage on ZIF-8 crystals. These conditions yielded a total dose below the recently cited thresholds of 25 and 90 e^{-} $Å^{-2}$ for ZIF-8 at room temperature[25] and dry-cryo conditions,[39] respectively. Despite the low dose constraints, lattice-resolution images were readily obtained (Figure A1) in both dry- and cryo-state conditions, enabling a direct view of p-MOF crystal growth mechanisms. Figure 2.4 shows a time series of ZIF-8 synthesis imaged by cryoTEM. Within 4 s of the reaction, we observe the formation of ~7 nm amorphous particles with a narrow size distribution of 7 ±1 nm (Figure 2.4a, c and 2.5).

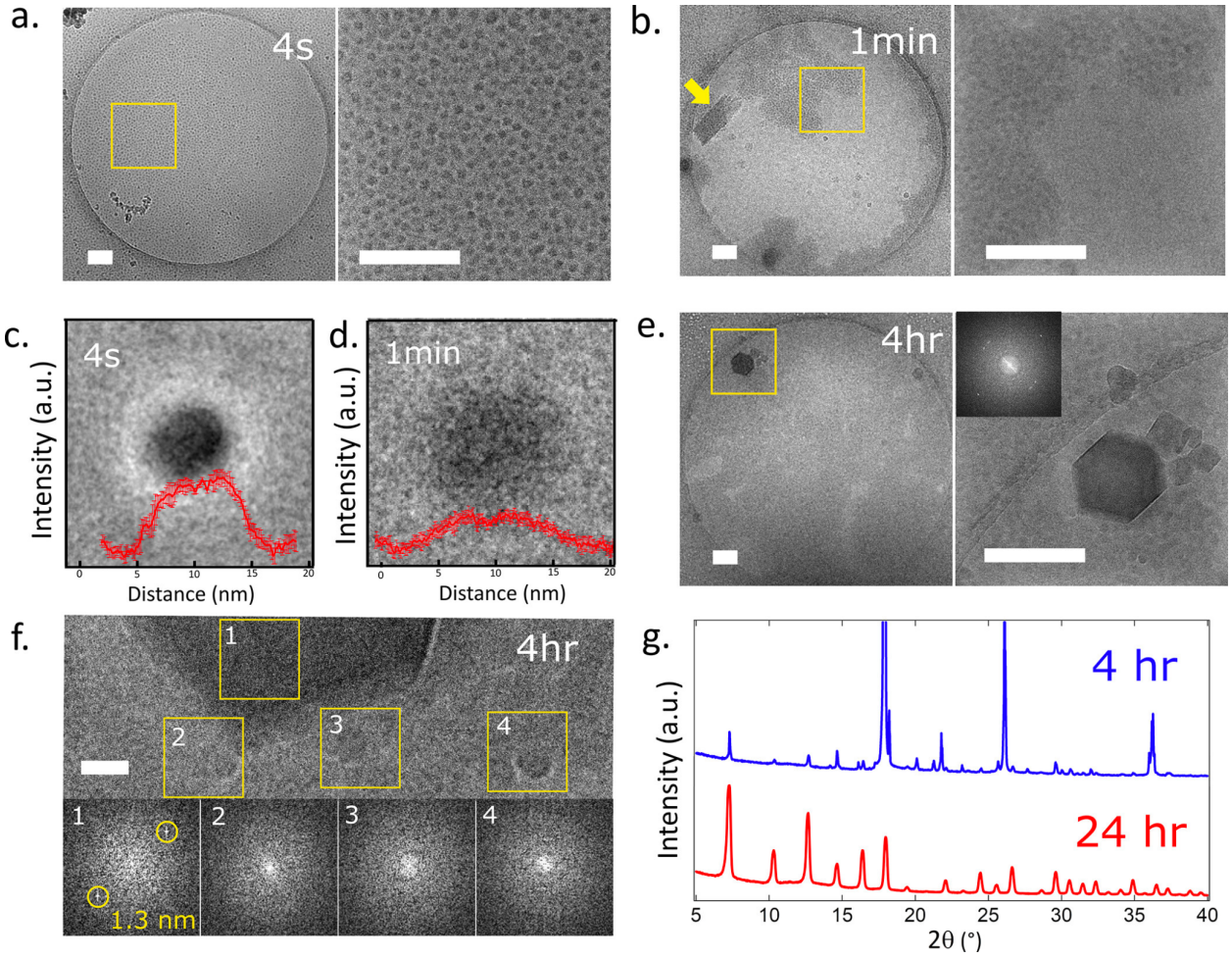

Figure 2.4: Representative cryoTEM images of nucleation and growth processes of ZIF-8 in water. Scale bars are 200 nm unless otherwise noted. (a, b, e) Time series of amorphous particles at (left) low and (right) high magnification during ZIF-8 crystal formation after (a) 4 s, (b) 1 min, and (e) 4 h. Yellow boxes indicate regions imaged at higher magnification. (c, d) Images of aligned and stacked micrographs for particles at (c) 4 s and (d) 1 min at 5 µm defocus used for line profile analysis. Overlaid are the corresponding averaged line profile analyses from 93 (4 s) and 45 (1 min) particles. (e) CryoTEM images of ZIF-8 crystal formation after 4 h reaction time. Yellow boxes indicate regions imaged at higher magnification with inset of fast Fourier transform. (f) Lattice-resolution cryoTEM image of a ZIF-8 crystal found in (e) after 4 h reaction time. Yellow boxes indicate four regions with corresponding fast Fourier transform. Scale bar, 10 nm. (g) PXRD patterns for ZIF-8 precipitate isolated after 4 h (blue) and 24 h (red) reaction time.

Formation of nanometer-sized particles was previously observed by small angle X-ray scattering[28] and dynamic light scattering studies,[31] although it was unclear whether these particles

were amorphous or crystalline. Here, we observe amorphous particles, defined by the lack of crystallinity observed in real space imaging, and hypothesize that each particle is composed of both the zinc and imidazole precursors. After 1 min, the amorphous particles aggregate and begin to lose definition as a second amorphous phase appears exclusively in regions containing a high density of aggregated particles (Figure 2.4b). This amorphous phase was not observed in isolation, suggesting that it originates from the amorphous particles. Images recorded under similar recording conditions were compared for particles at 4 s and 1 min to assess the observed morphological changes. Averaging >40 images of individual particles (see Appendix A.1 and Figure A.5) and measuring the line profiles provide a high signal-to-noise average structure of each species. Line profiles of the particles at 4 s show a sharp contrast between the particle and background (Figure 2.4c) with a diameter ∼7 nm. In comparison, particles analyzed at 1 min (Figure 2.4d) exhibit lower contrast and a diameter ∼15 nm. We hypothesize that particles become solvated at 1 min, resulting in a highly hydrated amorphous phase. The bright halo around particles found at 4 s are Fresnel fringes which occur at particle/compositional phase boundaries when images are recorded with significant defocus values (in this case, approximately −5 μm). The absence of these Fresnel fringes in particles found at 1 min is evidence that the compositional difference between the particles and the background has decreased, as the region becomes a homogeneous amorphous phase. Previous studies of ZIF-8 reporting multiple amorphous phases posed the question as to how these phases interacted.[28,29] Here, we propose that amorphous particles dissolve to form an amorphous phase of highly concentrated precursors. This is similar to dissolution−recrystallization mechanisms observed in calcium carbonate formation which can result in more than one crystal polymorph.[40] We note the presence of 2D sheet-like structures found in Figure 2.3b (indicated by yellow arrow) that were observed in several cryoTEM images

for ZIF-8 synthesis times 1 min to 4 h (Figure A2). These 2D structures are indicative of a second crystallization pathway and can be attributed to mechanisms described by Katsenis et al., who demonstrated that the transformation of ZIF-8 (sod) to other ZIF-8 polymorphs proceeds through an intermediate amorphous phase.[41] Under conditions reported here, the 2D structures exist as a transient species and do not appear to be directly involved in the ZIF-8 formation. After 4 h of ZIF-8 reaction time, we observe hexagonally shaped particles ~100 nm in diameter (Figure 2.4e) that exhibit lattice fringes that extend uniformly throughout the crystal with spacings (1.3 nm) in agreement with ZIF-8 (sod) crystalline structure.[42] These early stage ZIF-8 crystals were exclusively found within the amorphous phase and suggest that crystal nucleation originates from the amorphous phase by one of the following pathways: (1) Classical nucleation from within the amorphous phase, (2) Solid-state transformation of the particles within the amorphous phase, (3) Heterogeneous nucleation on the surface of the amorphous particle or amorphous phases. We acquired lattice-resolution cryoTEM images of early stage ZIF-8 crystals in the presence of the amorphous phase (Figure 4f) showing that crystallinity is confined to the ~100 nm particles. Amorphous particles found in proximity and on the ZIF-8 crystal surfaces show no lattice fringes, suggesting that crystal growth by particle aggregation is unlikely. This is in accordance with in situ TEM studies of ZIF-8 growth in methanol, which showed no evidence of particle aggregation.[27] Ensemble analysis was carried out by ex situ PXRD, where precipitate from the same 4 h aged ZIF-8 solutions were collected by centrifugation (Figure 2.4g). We observe diffraction peaks at a 2θ of 7°, 10.3°, and 12.7° attributable to ZIF-8 (sod) and identify the 1.3 nm d-spacing found in cryoTEM as the (011) plane.[42] Three additional peaks at a 2θ 17°, 26°, and 36° are not in agreement with ZIF8 (sod) diffraction patterns and indicate a second transient crystal structure present in the crystallization solution at 4 h reaction time. These additional peaks are not

identified as other ZIF-8 polymorphs, and we hypothesize that they are related to the 2D sheets observed by cryoTEM (Figure A2). The PXRD pattern showed no amorphous peak, indicating that amorphous phases observed by cryoTEM are highly solvated and remain in solution during centrifugation. One limitation of cryoTEM is that particles >500 nm in diameter are often removed during the blotting step or obscured by thick ice layers.[43] Time-resolved dry state TEM analysis on samples synthesized <4 h showed that ZIF-8 crystals are observed as early as 30 min into the reaction with average diameters of 580 ± 130 nm (Figure 2.5). The large crystal size distribution suggests slow nucleation and fast growth mechanisms that are further supported by our observation of ZIF-8 crystals and amorphous phases coexisting at multiple time points. Final ZIF-8 products, aged for 24 h, show fully resolved ZIF-8 (sod) peaks in PXRD (Figure 2.4g) and continue to exhibit a broad size distribution (average diameter ~2 μm) consistent with our proposed mechanism of slow nucleation and fast growth (Figure 2.5).

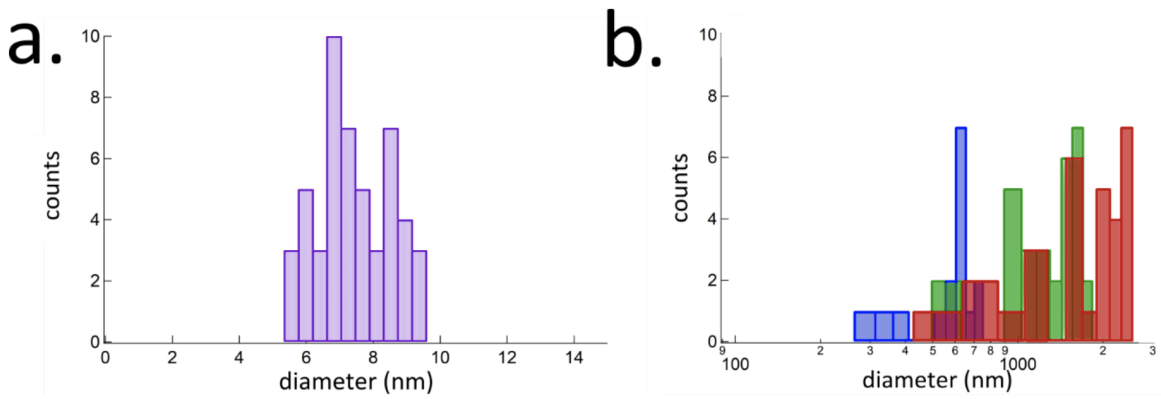

Figure 2.5: Size distribution plots for (a) amorphous particles found at 4 s synthesis time and (b) ZIF-8 crystals found at (blue) 30 min, (green) 4 hr, and (red) 24 hr synthesis time. Average crystal diameters for 30 min, 4 hr, and 24 hr synthesis times. Average crystal diameters for 30 min, 4 hr, and 24 hr synthesis times were 580 nm ± 130 nm, 1290 nm ± 350 nm, and 1750 nm ± 580 nm, respectively.

Single-crystalline ZIF-8 is observed at early stages (Figure A3a) and throughout synthesis

up to 24 h (Figure A3b). We therefore propose crystal growth by monomer addition, where the amorphous phase serves as a reservoir for Zn and HmIm precursors. Classical growth is further supported by the surface morphology of final ZIF-8 crystals, which exhibit well-defined crystal facets (Figure 2.2c). Such features are indicative of monomer addition, which enables single units to rearrange on the crystal surface and produce morphologies with the most thermodynamically favored surface energy, which for ZIF-8 is the rhombic dodecahedron.[44]

Crystallization of BSA-ZIF-8

With an initial understanding of ZIF-8 formation in aqueous systems, we next monitored the influence of BSA on ZIF-8 crystallization and the protein interactions with the amorphous phases described above. We explored a range of BSA concentrations for BSA-ZIF-8 synthesis based on previous literature (0.05−5 mg/mL, Figure 2.6 and Tables A1 and A2,) and selected to study ZIF-8 with 5 mg/mL of BSA.

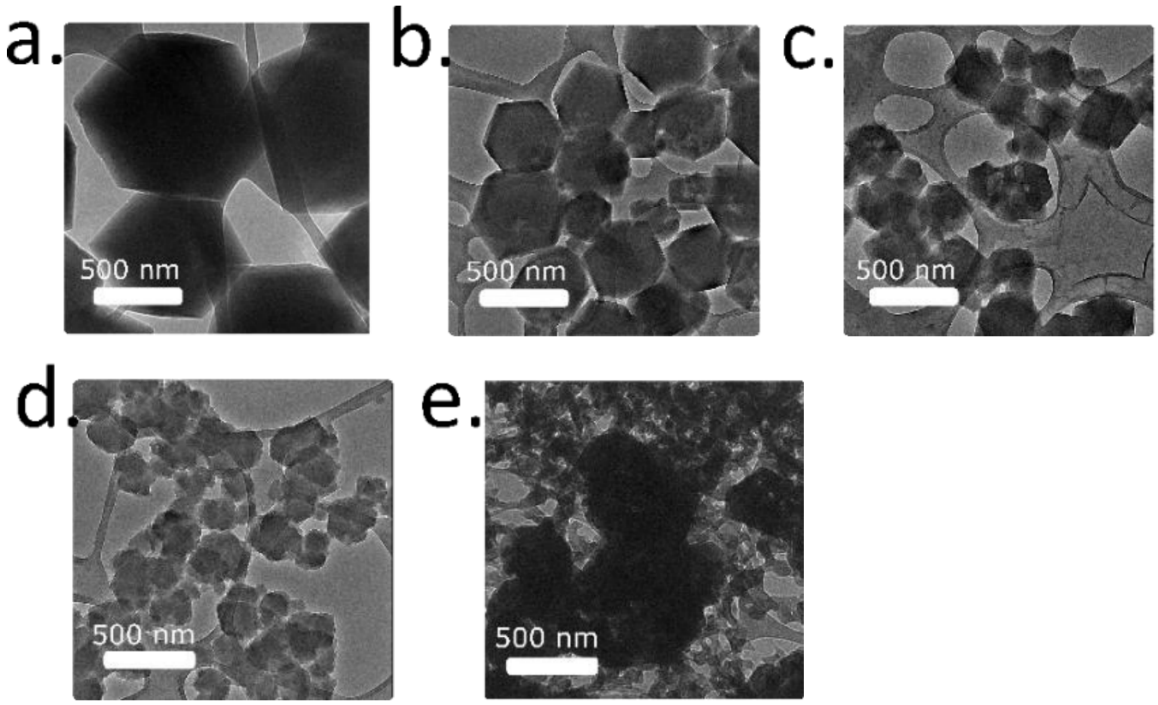

Figure 2.6: TEM analysis of BSA-ZIF-8 crystal morphology dependence on BSA concentration. (a) 0.05 mg/mL, (b) 0.5 mg/mL, (c) 1.25 mg/mL, (d) 5 mg/mL, and (e) 10 mg/mL BSA was added to HmIm solutions for a final ZIF-8 synthesis at HmIm : Zn ratio = 35 : 1 (1400 mM : 40 mM), aged for 24 hrs, and washed by centrifugation for TEM samples.

BSA-ZIF-8 crystals synthesized with 5 mg/mL BSA displayed a significantly different morphology to ZIF-8 alone, enabling identification of the role of BSA in the crystallization process. Fourier transform infrared spectroscopic analysis for BSA-ZIF-8 crystals confirms the encapsulation of protein into the ZIF-8 framework, in agreement with previous studies (Figure 2.7).

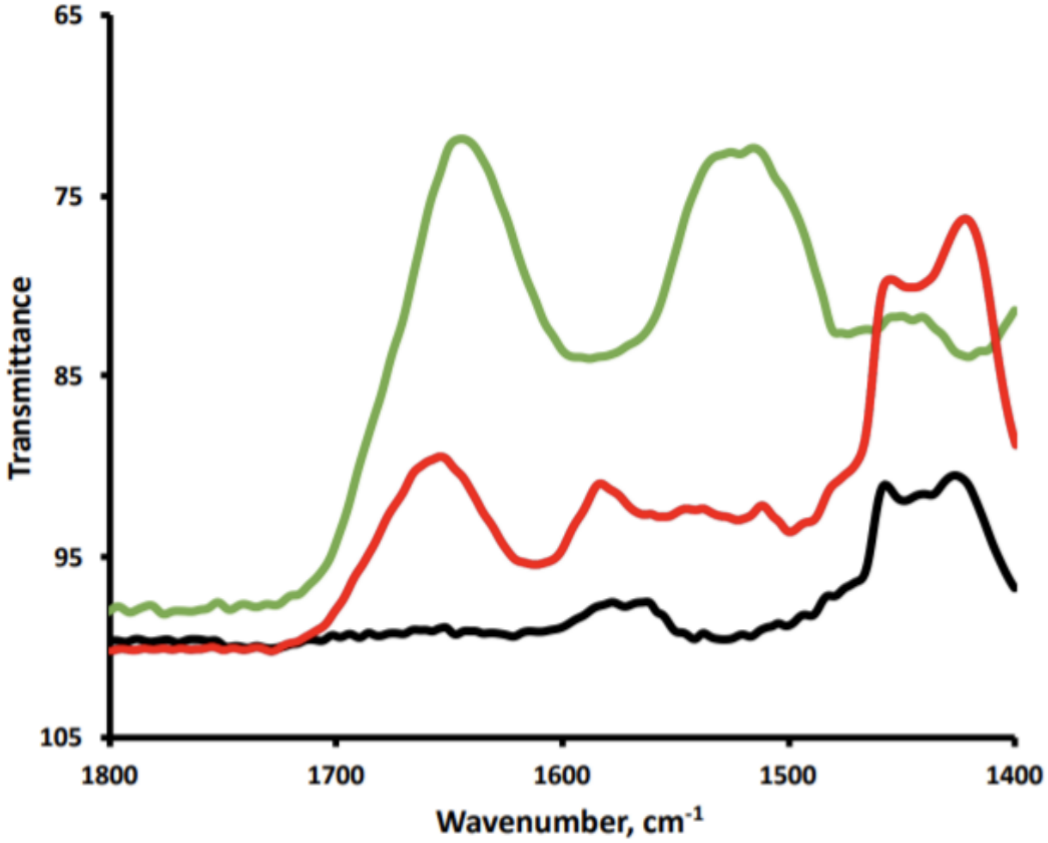

Figure 2.7: FTIR spectra of (green) BSA, (red) BSA@ZIF-8, and (black) ZIF-8. ZIF-8 and BSA-ZIF-8 samples were centrifuged for 10 minutes at 10,000 rpm. The precipitant was washed 3x with nanopure water and once with 1x SDS buffer. Washed precipitant was then analyzed with Jasco V-670 spectrometer. Peaks characteristic to BSA include the C=O stretch at 1,660 cm-1 and C=N stretch mode at 1,582 cm-1 corresponding to the amide bond.[8]

Static light scattering measurements of BSA-ZIF-8 solutions show an increase in the rate of particle formation within the first 100 min compared to the ZIF-8 only samples (Figure 2.3). Additionally, the turbid phase remains in solution for the entirety of the measurement, indicating the formation of smaller particles. CryoTEM images reveal that within 4 s, amorphous particles and an amorphous phase appear as observed for ZIF-8 formation (Figure A4). More notably, an additional amorphous phase composed of ~8 nm sized particles attributable to BSA molecules

(~7 nm molecular diameter, Figure 2.8a) forms simultaneously. This protein amorphous phase aggregates into branched networks composed of many BSA particles (Figure 2.8b) after 1 min and shows no spatial preference for the ZIF-8 amorphous phase.

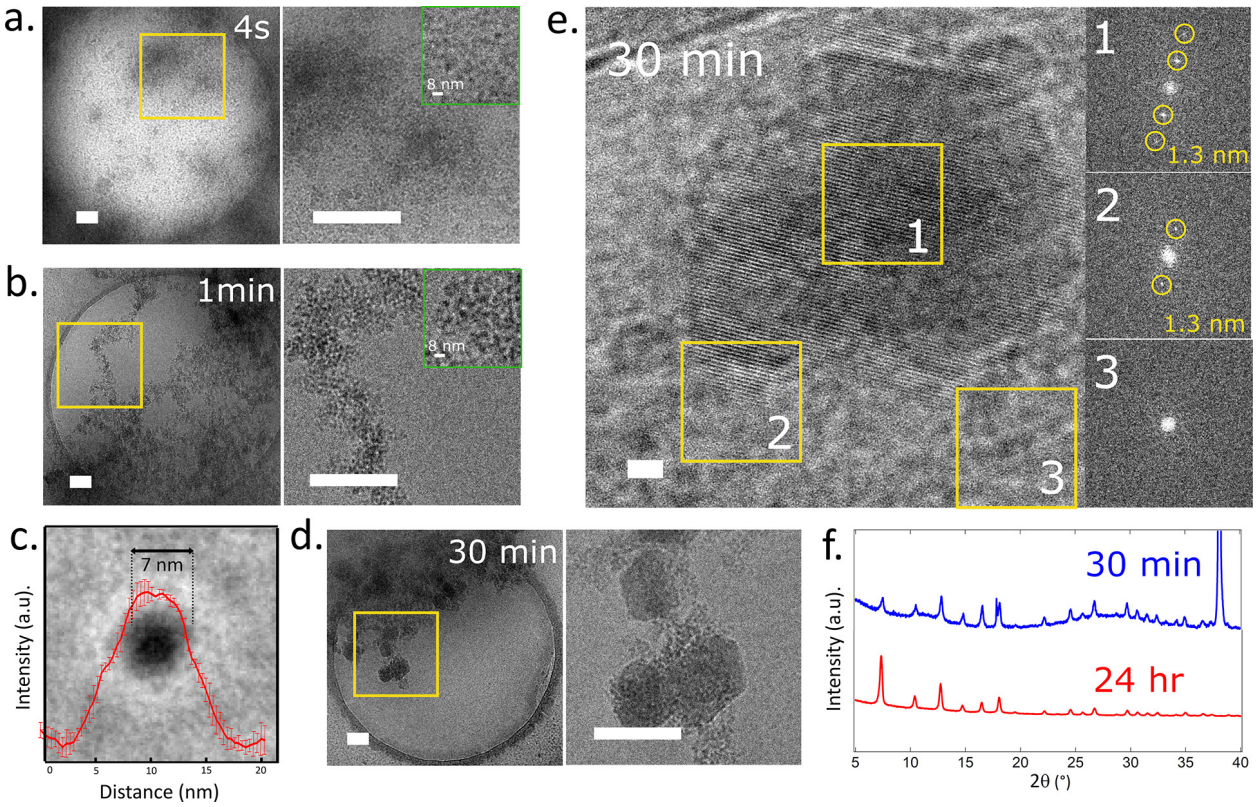

Figure 2.8: Representative CryoTEM images of nucleation and growth process of BSA-ZIF-8 in water at (left) low and (right) high magnification. Scale bars are 200 nm unless otherwise noted. (a, b, d) Time series of formation BSA-induced amorphous phases throughout BSA-ZIF-8 evolution after (a) 4 s, (b) 1 min, and (c) 30 min. Yellow boxes indicate regions imaged at higher magnification. Insets are high magnification images revealing 8 nm particles attributed to BSA molecules. (c) Averaged line profile analysis of BSA particles in (b) overlaid on corresponding aligned and stacked images from 59 particles used for line profile analysis. (d) CryoTEM image of BSA-ZIF-8 at 30 min reaction time. (e) Lattice-resolution cryoTEM of a 100 nm particle within protein-aggregated networks after 30 min reaction. Scale bar, 10 nm. Yellow boxes indicate three regions with corresponding unfiltered fast Fourier transform. This image is processed using an average background subtraction filter (f) PXRD patterns for BSA-ZIF-8 precipitate isolated after 30 min (blue) and 24 h (red) aging.

As a control experiment, we prepared solutions of BSA-Zn and BSA-HmIm. CryoTEM of BSA-Zn and BSA-HmIm solutions showed two distinct aggregated networks with both amorphous and crystalline features (Figure 2.9).

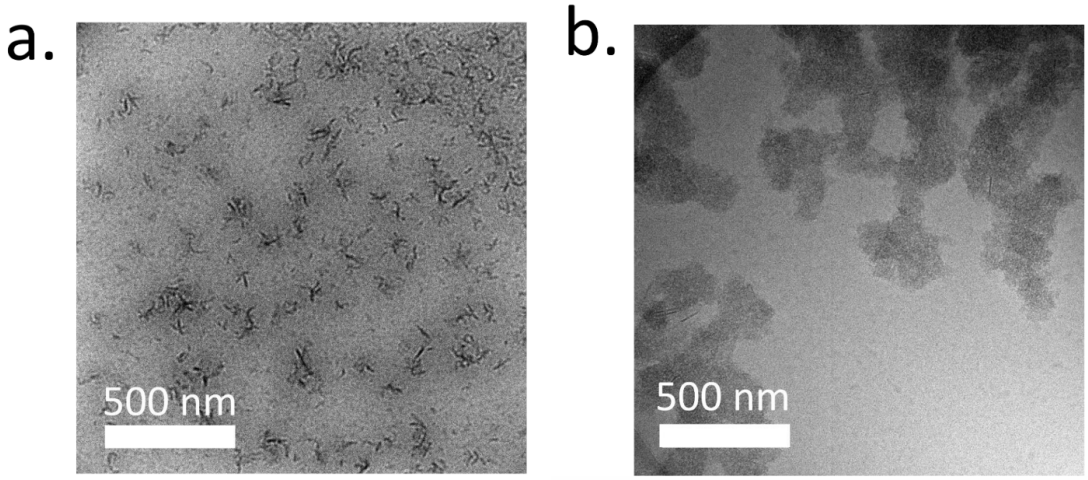

Figure 2.9: CryoTEM micrographs of (a) BSA-HmIm and (b) BSA-Zn solutions as described in the full methods. Structures observed are unique to each solution and suggests that BSA can complex and form a secondary structure with both Zn and HmIm alone.

However, the structures are markedly different from the protein-branched networks in Figure 2.8b, indicating that during the BSA-ZIF-8 synthesis, BSA forms an amorphous network with both Zn and HmIm. Line-profile analysis of the BSA network shows that each particle, ∼13 nm in diameter, has a core−shell structure (Figure 2.8c). The core diameter (∼7 nm) is consistent with the diameter of a single BSA molecule, resulting in an estimated ∼3 nm HmIm/Zn shell that surrounds each BSA molecule. After 30 min of the BSA-ZIF-8 reaction, ZIF-8 crystals ∼100 nm in diameter are found exclusively within the protein aggregated networks (Figure 2.8d), and no crystals were observed in isolation. Lattice-resolution cryoTEM shows that ZIF-8 particles exhibit

lattice fringes which extend past the 100 nm particle boundary overlapping protein particles from the aggregated networks (Figure 2.8e). Fast Fourier transforms of the image areas where BSA particles are in the center or at the surface of the ZIF-8 crystal show long-range crystal structure. In comparison, a fast Fourier transform of the image area where the protein aggregated networks are at a 10−20 nm distance from the crystal surface shows no crystalline structure. We therefore hypothesize that crystallization of the protein aggregated networks occurs through a solid-state transformation process on the ZIF-8 surface. Further evidence of the amorphous nature of the protein-aggregated networks was provided by PXRD. Ex situ PXRD confirms that there is ZIF-8 (sod) crystallinity at 30 min synthesis time and, in contrast to ZIF-8 formation without BSA, a broad diffraction peak is observed at high 2θ, indicating the presence of a highly amorphous material (Figure 2.8f). Therefore, precipitate collected by centrifugation at 30 min reaction time was a mixture of crystalline and amorphous solid material, suggesting that BSA stabilizes an amorphous phase that can crash out upon centrifugation. This conclusion is further supported by observation of an amorphous solid product obtained after 24 h of reaction time when BSA-ZIF-8 was synthesized with a high (10 mg/mL) BSA concentration (Figure 2.6e). Interestingly, a second transient crystal phase was not observed during the formation of BSA-ZIF-8 in cryoTEM images or in PXRD. CryoTEM images of BSA-ZIF-8 formed after 24 h no longer show protein-aggregated networks. Final BSA-ZIF-8 crystals grow to ∼250 nm in diameter with rough, spherical morphologies (Figure 2.10a).

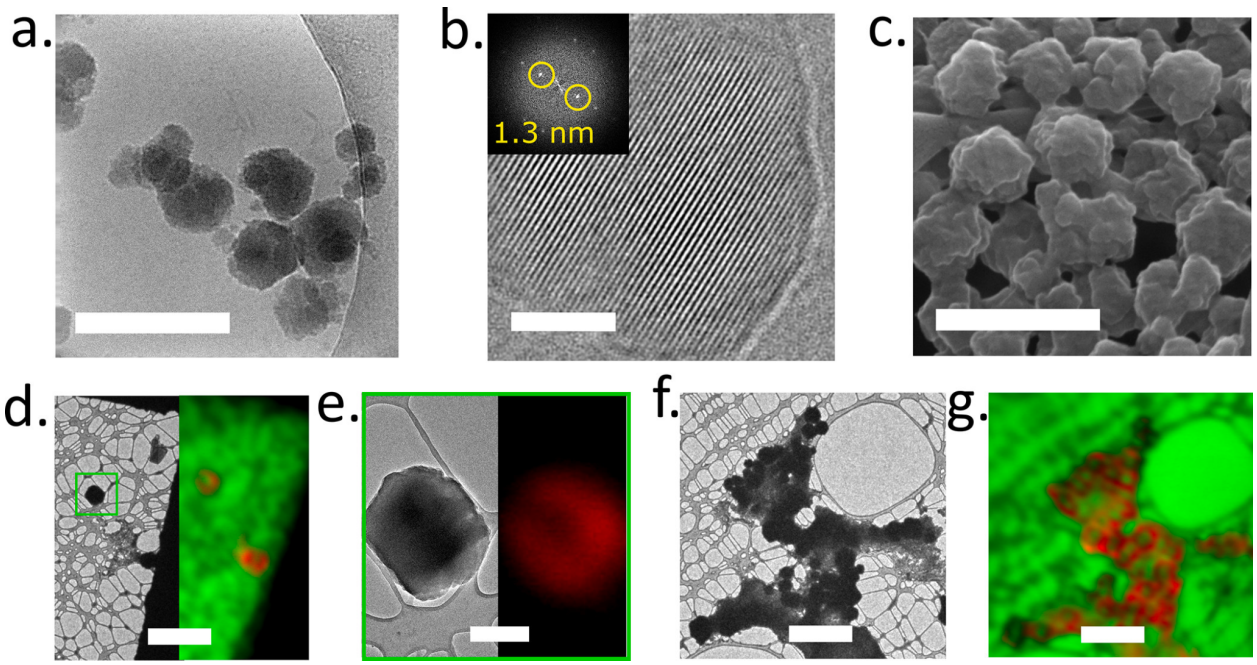

Figure 2.10: Characterization of final BSA-ZIF-8 crystals. (a) CryoTEM of BSA-ZIF-8 crystals after 24 h. Scale bar, 500 nm. (b) Dry-state TEM micrograph of final ZIF-8 product with inset of unfiltered fast Fourier transform indicating single crystalline lattice fringes. Scale bar, 20 nm. This image is processed using an average background subtraction filter. (c) SEM of final BSA-ZIF-8 products. Scale bar, 500 nm. (d–g) Correlative TEM and fluorescence microscopy of FITC-BSA-ZIF-8. (d) TEM (left) and fluorescence micrograph (right) of single FITC-BSA-ZIF-8 crystal at low magnification. All scale bars are 2 μm unless otherwise noted. (e) High magnification TEM (left) and fluorescence micrograph (right) of single crystal outlined in panel a. Scale bar, 500 nm. (f) TEM at low magnification of FITC-BSA-ZIF-8 crystals. (g) Crystals in panel f observed by fluorescence imaging showing subsurface protein encapsulation.

Each particle exhibits single crystal lattice fringes (Figure 2.10b) with ZIF-8 (sod) crystal structure as characterized by PXRD (Figure 2.8f). The single crystalline structure of BSA-ZIF-8 provides further evidence that amorphous protein clusters crystallize upon contact with the ZIF-8 crystal surface to form a single crystal. SEM images reveal a rough surface morphology (Figure 2.10c) that no longer resembles the equilibrium shape of a rhombic dodecahedron for pure ZIF-8 crystals (Figure A3c), supporting aggregate mediated crystal growth originating from the protein aggregated networks. To probe the location of protein molecules encapsulated within ZIF-8

crystals, we performed ZIF-8 synthesis with fluorescein-tagged BSA (FITC-BSA) and imaged FITC-BSA-ZIF-8 crystals by single photon fluorescence microscopy. Correlative TEM and fluorescent micrographs (Figure 2.10d) of a FITC-BSA-ZIF-8 crystal demonstrate a hollow morphology by fluorescence microscopy in contrast to a homogeneous single crystal by TEM. At higher magnification (Figure 2.10e), fluorescence signals overlay the surface regions of the single particle. The hollow morphology shown by fluorescence microscopy is consistent across all FBSA-ZIF-8 crystals (Figure 2.10f, g). The observation that FITC-BSA molecules are predominantly encapsulated in the outer shell of ZIF-8 crystals agrees with protein incorporation after the initial formation of ZIF-8 alone, as observed by cryoTEM. Control experiments performed by incubating fully formed ZIF-8 crystals in FBSA show no fluorescence (Figure A5) and discount FITC-BSA adsorption to the crystal surface as a source of fluorescence. These data support previously reported BSA-ZIF-8 structures which exhibited subsurface encapsulation of FITC- BSA into ZIF-8 crystals resulting in (ZIF-8)−core−(BSA/ZIF-8)−shell morphologies.[22]

Crystallization of BSA-ZIF-8 at Low HmIm:Zn Conditions

We next explored the scope of amorphous phases in p-MOF nucleation by studying the crystallization of ZIF-8 at a low HmIm:Zn ratio of 4:1. Synthesis at a HmIm:Zn ratio of 4:1 does not spontaneously form ZIF-8 (sod) and results in the formation of flat-spiralized plate structures (Figure 2.11) identified as ZIF-8 (dia) by PXRD (Figure 2.12a).[38]

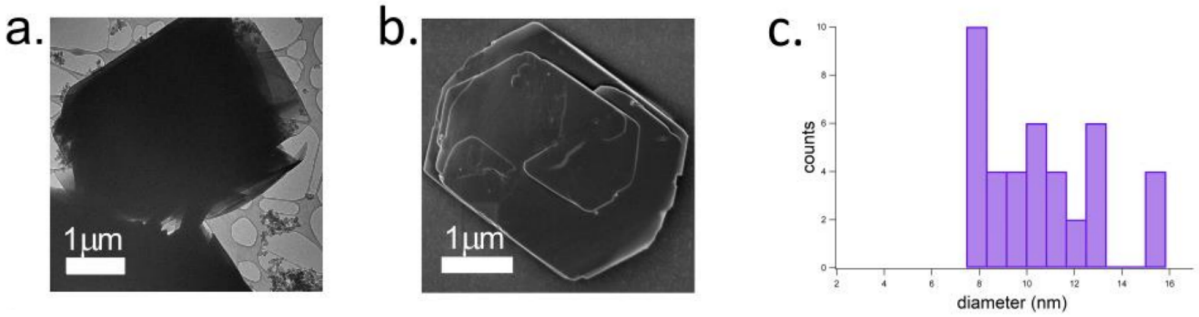

Figure 2.11: (a) SEM and (b) TEM of ZIF-8 at a HmIm:Zn ratio of 4:1 after 24 hrs reaction time (c) Size distribution plots for amorphous particles found at 1 hr synthesis time for ZIF-8 synthesis at HmIm:Zn ratio of 4:1.

Nucleation and growth kinetics at HmIm:Zn = 4:1 conditions are significantly slower compared to HmIm:Zn = 35:1 conditions as probed by static light scattering measurements (Figure 2.3). CryoTEM images of crystallization solutions at a HmIm:Zn ratio of 4:1 imaged after 1 min (Figure 2.5b) and 1 h (Figure 2.5c) show amorphous particles with an average size of 10 ± 2 nm (Figure 2.11 and Figure 2.12a).

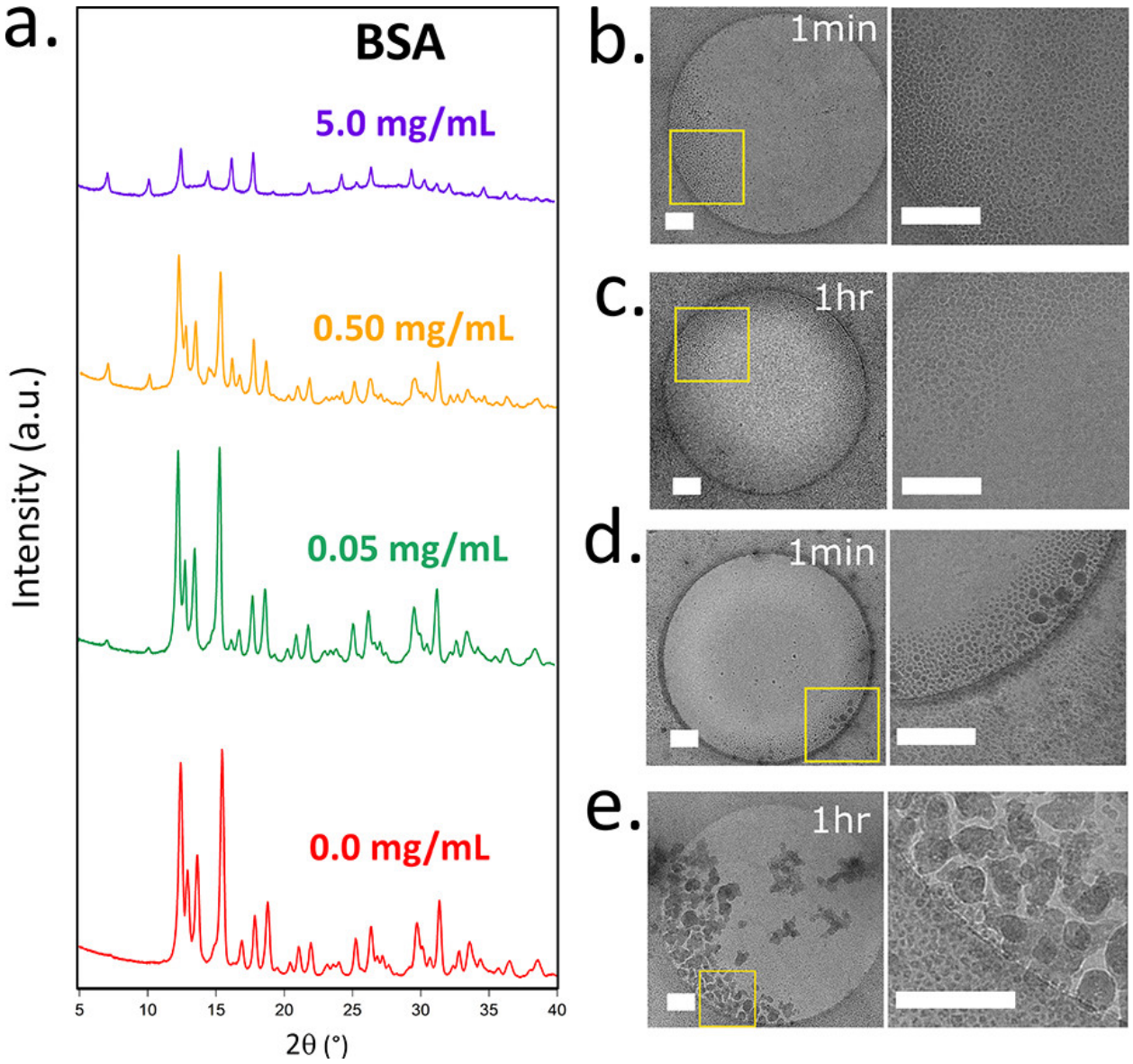

Figure 2.12. Characterization of ZIF-8 and BSA-ZIF-8 at low HmIm:Zn ratios. (a) PXRD patterns for BSA-ZIF-8 precipitate isolated after 24 h reaction time for the addition of (purple) 5.0 mg/mL, (yellow) 0.50 mg/mL, (green) 0.05 mg/mL, and (red) 0.0 mg/ mL BSA. (b, c) CryoTEM images of ZIF-8 (HmIm:Zn = 4:1) after (b) 1 min and (c) 1 h synthesis time at left (low) and (right) high magnification. Scale bars are 200 nm unless otherwise noted. Yellow box indicates region imaged at higher magnification. (d, e) CryoTEM images of BSA-ZIF-8 (HmIm:Znm BSA = 4:1, 5.0 mg/mL) after (d) 1 min and (e) 1 h reaction time at (left) low (left) and (right) high magnification. Scale bars are 200 nm unless otherwise noted. The yellow box indicates the region imaged at higher magnification.

The particles are like those observed at 1 s in the HmIm:Zn ratio of 35:1; however, they appear to be stable and do not show evidence of aggregation and dissolution. The absence of

particle aggregation at early reaction times can explain the slow crystallization kinetics observed by bulk scattering techniques. This provides further evidence that the formation of amorphous precursors is a key step in the crystallization of ZIF-8. Future work will focus on the mechanism by which these stable amorphous particles convert into the ZIF-8 (dia) crystals. Here, we focus on the influence of BSA on amorphous particles. The addition of BSA (5 mg/mL) to the HmIm:Zn ratio of 4:1 solution results in the formation of ZIF-8 (sod) crystals with ~68 nm pores (Figure A6), consistent with previously reported cytochrome-c-ZIF-8 biocomposites.[17] This shows that at low HmIm:Zn ratios, BSA directly influences the nucleation of ZIF-8 crystals and provides control over the ZIF-8 polymorph. Due to the rapid nucleation in these samples, it was challenging to capture the prenucleation state by cryoTEM. Addition of 0.5 mg/mL BSA shows a slower nucleation rate and results in a mixture of ZIF8 (dia) and ZIF-8 (sod) (Figure 2.12c). Resulting ZIF-8 (sod) crystals show ~25 nm pores (Figure A6) like 5 mg/mL BSA-ZIF-8 crystals. Static light scattering measurements show increased formation of precipitate compared to ZIF-8 only at HmIm:Zn = 4:1 (Figure 2.3), and suggest that BSA directly influences the formation of a second phase. CryoTEM analysis of the 0.5 mg/ mL BSA-ZIF-8 sample after 1 min (Figure 2.12d) shows a mixture of ~10 nm spherical particles and larger irregularly shaped amorphous particles that appear to result from aggregation of the spheres. The amorphous phase grows and quantity after 1 h. As the presence of this amorphous phase was not found in the absence of BSA, we hypothesize that the biomolecule is interacting with amorphous HmIm/Zn particles, promoting their aggregation and the formation of a protein-induced amorphous phase that results in nucleation of ZIF-8 (sod). We also hypothesize that the pores in the final BSA-ZIF-8 crystals are related to the aggregation and crystallization of the irregularly shaped amorphous phase; however, more work is needed to confirm this.

2.4 Discussion

These data demonstrate the importance of amorphous phases and particle−particle interactions in the formation of ZIF-8 and BSA-ZIF-8 composites. Aggregation of colloidal particles, such as the observed amorphous particles during ZIF-8 formation, is largely dependent on the electrostatic interactions between particles. Therefore, differences in nucleation and growth mechanisms can be explained by changes in interactions between the two types of amorphous particles: (1) the HmIm/Zn amorphous particles and (2) the protein/ HmIm/Zn particles. The main challenges here are that both particles form transiently in solution and that at any single time point a crystallization sample can contain a mixture of the different species present. Consequently, interpretation of bulk data based on scattering or zeta potential measurements is challenging. Nonetheless, we further investigated the interactions between particles by cryoTEM in combination with light scattering methods. We propose that a key step in ZIF-8 formation is the aggregation of amorphous particles in driving the dissolution− recrystallization process. To test this hypothesis, we studied amorphous particles formed under low ZIF-8 precursor concentration conditions, as decreasing concentrations is expected to reduce the aggregation kinetics. CryoTEM images of serially diluted ZIF-8 precursor solutions (700:20, 350:10, 140:4, and 70:2 mM) show that higher dilution conditions increase particle size from 7 ± 1 nm to 15 ± 1, 47 ± 6, and 106 ± 14 nm (Figure 2.13 and Figure A7).

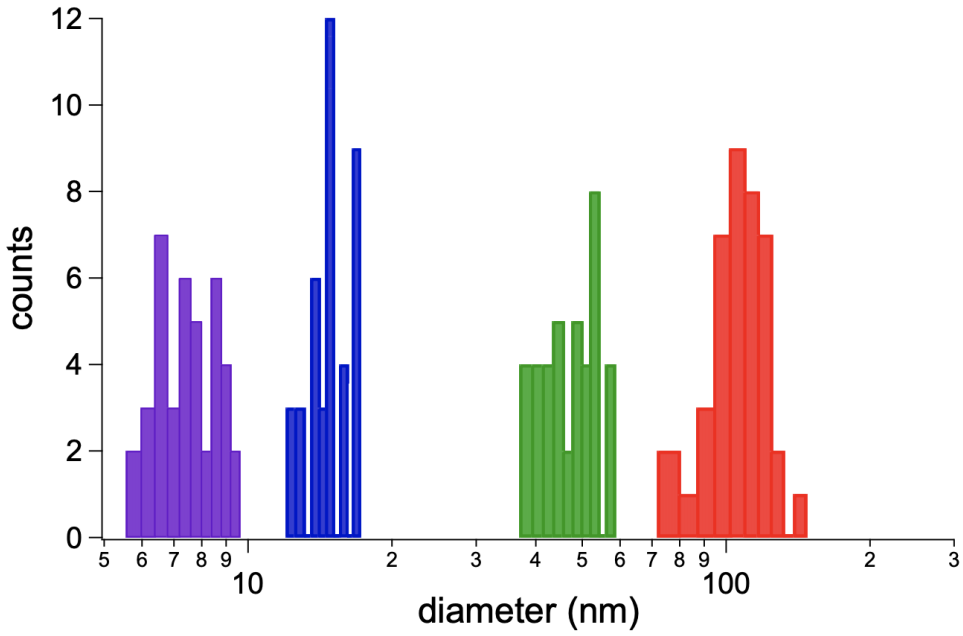

Figure 2.13: Size distribution plots for amorphous particles found at 1 min synthesis time for ZIF-8 synthesis at HmIm:Zn ratio of (purple) 700 mM : 20 mM, (blue) 350 mM : 10 mM, (green) 140 mM : 4 mM, (red) 70 mM : 2 mM.

The HmIm/Zn solution diluted 10-fold from the ZIF-8 synthesis forms stable 106 ± 14 nm amorphous particles with a zeta potential value of 34.6 ± 7.0 mV. Interestingly, the 10-fold diluted HmIm/Zn solutions show no evidence of aggregation or crystallization after 24 h. The stability of these particles is attributed to a high electrical potential at the particle surface that enhances repulsion forces and prevents aggregation. These data support our hypothesis that aggregation of amorphous particles is key to the dissolution−recrystallization mechanism that results in ZIF-8 formation. The incorporation of biomolecules into ZIF-8 crystals also occurs through a particle aggregation-mediated process. This can occur either at the surface of a growing ZIF-8 crystal or through the aggregation of amorphous precursor particles. To provide further evidence for the formation of the transient particle specifies and the role of zeta potential in controlling particle

aggregation we studied mixtures of BSA with either HmIm or Zn. The zeta potential measurement for BSA is −18.8 ± 9.6 mV (pH 7.2). When BSA is added to imidazolate solutions, the zeta potential becomes even higher in magnitude at −27.5 ± 4.8 mV (pH 10.7). Structures observed by cryoTEM (Figure 2.9) are likely driven by hydrogen bonding but do not aggregate into larger networks due to electrostatic repulsion. In contrast, BSA-Zn solutions show a small zeta potential of 2.2 ± 4.1 mV (pH 6.7) and result in a highly aggregated phase due to the shielding effects of positively charged zinc ions on the negatively charged BSA surface. This is further supported by BSA-Zn solutions becoming turbid (Figure A8) and the observation of large, aggregated structures in cryoTEM micrographs (Figure 2.9).

Although these data do not allow us to probe the transient BSA/Zn/HmIm amorphous particles seen in Figures 2.4a and 2.12e directly, they demonstrate that the electrostatics and aggregation state of the BSA/Zn/HmIm amorphous particles will be dependent on the relative ratios of the precursors. To provide evidence of the generality of transient biomolecule/Zn/HmIm intermediates, we performed the same precursor studies on alternative proteins that enable formation of ZIF-8 biocomposites:[19] pepsin and lipase (Table 2.1).

Table 2.1: Zeta potential values for protein-ZIF precursor solutions. 5mg/mL of protein was mixed with 700 mM HmIm solutions or 20 mM Zn solutions.

	Protein only (mV)	**Protein-Zn (mV)**	**Protein-HmIm (mV)**
BSA	-18.8 ±9.6 (pH 7.2)	2.2 ±4.1 (pH 6.7)	-27.5 ± 4.8(pH 10.7)
Lipase	-17.1 ± 4.5(pH 7.2)	-0.56 ±5.7 (pH 6.1)	-22.2 ±10.3 (pH 10.4)
Pepsin	-8.8 ±5.8 (pH 5.2)	-5.7 ±4.0 (pH 6.0)	-25.1 ± 10.2 (pH 10.3)

Each protein shows changes in zeta potential upon mixing with either Zn or HmIm, indicating interaction between the protein and ZIF precursors. Furthermore, the pepsin/Zn and lipase/Zn samples show a low zeta potential and become significantly turbid, forming large, aggregated structures observed by cryoTEM (Figure A9). CryoTEM images of biomolecule/HmIm and biomolecule/Zn solutions show that interactions between the biomolecule and precursors manifest into unique aggregated structures. Therefore, we propose that the formation of transient protein/HmIm/Zn precursors will be a general phenomenon in the formation of p-MOFs for low isoelectric-point (PI < 7) proteins, which make up most reported p-MOF systems. The size and charge of these prenucleated species will be dependent on the specific protein, the concentrations of the protein and ZIF-8 precursors, and the time after mixing.

2.5 Conclusions

By employing cryoTEM analysis to BSA-ZIF-8 crystal formation, we show the role of transient amorphous phases and their interactions with proteins that is reminiscent of biomineralization processes. ZIF-8 crystallization is described in two categories for formation at (1) high HmIm:Zn ratios and (2) low HmIm:Zn ratios. At high HmIm:Zn ratios, ZIF-8 crystallization is driven by the formation of amorphous particles that undergo a dissolution–recrystallization mechanism. Dissolution of amorphous particles forms an amorphous phase with local regions of high supersaturation, enabling ZIF-8 (sod) nucleation. Characterization of ZIF-8 formation in the presence of BSA reveals that the dissolution–recrystallization mechanism occurs simultaneously with the formation of a protein-induced amorphous phase. Large, aggregated networks of BSA-Zn-HmIm particles interact with the ZIF-8 crystals and undergo heterogeneous crystallization to form the final BSA-ZIF-8 (sod) composite. At low HmIm:Zn ratios, amorphous

particles form and do not proceed through dissolution–recrystallization. An alternative nucleation and growth mechanism results in the formation of ZIF-8 (dia). Upon addition of BSA, complexation of ZIF-8 precursor ions to the protein surface drives local supersaturation that favors ZIF-8 (sod) formation around protein particles. Crystal growth incorporates BSA particles, resulting in a final BSA-ZIF-8 (sod) crystal with nanometer-sized pores. A schematic of the crystallization of ZIF-8 and BSA-ZIF-8 according to the four pathways described is given in Figure 2.14. Based on these data, we believe that controlling how proteins are encapsulated into p-MOFs may be most successful when approached from a colloidal organization perspective, emphasizing the electrostatic interactions that occur between precursor particles in solution.[45,46]

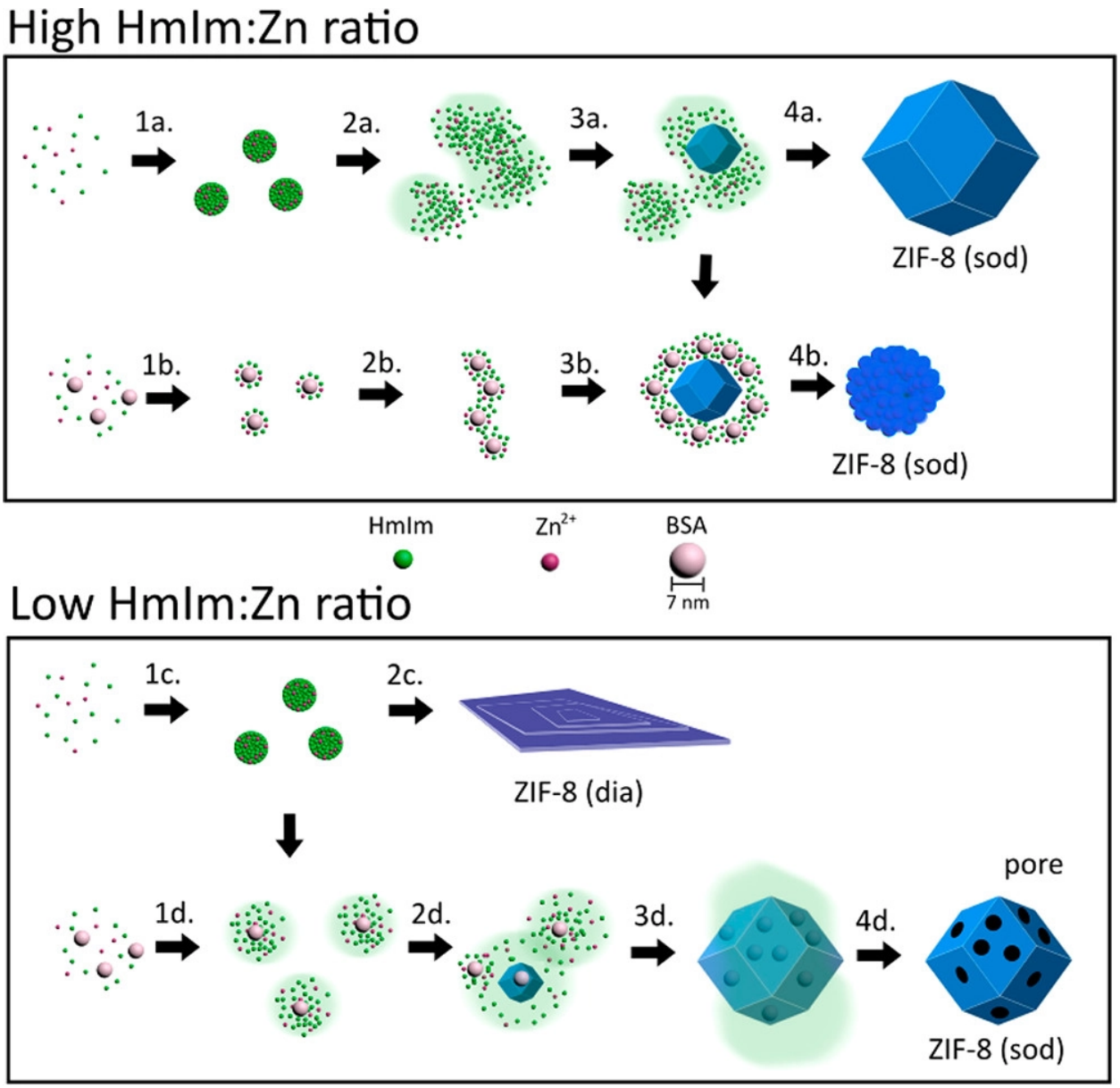

Figure 2.14: Proposed schematic of ZIF-8 formation with and without BSA. At high HmIm:Zn ratios, ZIF-8 crystal growth follows steps 1a–3a and reaches completion through 4a. In the presence of BSA, steps 1a–3a occur in parallel with a second process outlined in 1b–3b. At low HmIm:Zn ratios, ZIF-8 (dia) forms in the absence of BSA through the formation of amorphous particles outline in 1c–2c. Upon addition of BSA, HmIm and Zn ions complex at the protein surface and form a protein-induced amorphous phase that promotes ZIF-8 (sod) nucleation and growth outlined in 1d–4d.

2.6 References

(1) Veis, A. A Window on Biomineralization. *Science* **2005**, *307* (5714), 1419–1420. https://doi.org/10.1126/science.1109440.

(2) Chen, T.-T.; Yi, J.-T.; Zhao, Y.-Y.; Chu, X. Biomineralized Metal–Organic Framework Nanoparticles Enable Intracellular Delivery and Endo-Lysosomal Release of Native Active Proteins. *J. Am. Chem. Soc.* **2018**, *140* (31), 9912–9920. https://doi.org/10.1021/jacs.8b04457.

(3) Lian, X.; Fang, Y.; Joseph, E.; Wang, Q.; Li, J.; Banerjee, S.; Lollar, C.; Wang, X.; Zhou, H.-C. Enzyme–MOF (Metal–Organic Framework) Composites. *Chem. Soc. Rev.* **2017**, *46* (11), 3386–3401. https://doi.org/10.1039/C7CS00058H.

(4) Li, S.; Dharmarwardana, M.; Welch, R. P.; Benjamin, C. E.; Shamir, A. M.; Nielsen, S. O.; Gassensmith, J. J. Investigation of Controlled Growth of Metal–Organic Frameworks on Anisotropic Virus Particles. *ACS Appl. Mater. Interfaces* **2018**, *10* (21), 18161–18169. https://doi.org/10.1021/acsami.8b01369.

(5) Riccò, R.; Liang, W.; Li, S.; Gassensmith, J. J.; Caruso, F.; Doonan, C.; Falcaro, P. Metal–Organic Frameworks for Cell and Virus Biology: A Perspective. *ACS Nano* **2018**, *12* (1), 13–23. https://doi.org/10.1021/acsnano.7b08056.

(6) Asadi, V.; Kardanpour, R.; Tangestaninejad, S.; Moghadam, M.; Mirkhani, V.; Mohammadpoor-Baltork, I. Novel Bovine Carbonic Anhydrase Encapsulated in a Metal–Organic Framework: A New Platform for Biomimetic Sequestration of CO2. *RSC Adv.* **2019**, *9* (49), 28460–28469. https://doi.org/10.1039/C9RA04603H.

(7) Peng, S.; Liu, J.; Qin, Y.; Wang, H.; Cao, B.; Lu, L.; Yu, X. Metal–Organic Framework Encapsulating Hemoglobin as a High-Stable and Long-Circulating Oxygen Carriers to Treat Hemorrhagic Shock. *ACS Appl. Mater. Interfaces* **2019**, *11* (39), 35604–35612. https://doi.org/10.1021/acsami.9b15037.

(8) Liang, K.; Ricco, R.; Doherty, C. M.; Styles, M. J.; Bell, S.; Kirby, N.; Mudie, S.; Haylock, D.; Hill, A. J.; Doonan, C. J.; Falcaro, P. Biomimetic Mineralization of Metal-Organic Frameworks as Protective Coatings for Biomacromolecules. *Nature Communications* **2015**, *6* (1), 7240. https://doi.org/10.1038/ncomms8240.

(9) Wu, X.; Ge, J.; Yang, C.; Hou, M.; Liu, Z. Facile Synthesis of Multiple Enzyme-Containing Metal–Organic Frameworks in a Biomolecule-Friendly Environment. *Chem. Commun.* **2015**, *51* (69), 13408–13411. https://doi.org/10.1039/C5CC05136C.

(10) Lian, X.; Erazo-Oliveras, A.; Pellois, J.-P.; Zhou, H.-C. High Efficiency and Long-Term Intracellular Activity of an Enzymatic Nanofactory Based on Metal-Organic Frameworks. *Nat Commun* **2017**, *8* (1), 2075. https://doi.org/10.1038/s41467-017-02103-0.

(11) Liu, B.; Hu, F.; Zhang, J.; Wang, C.; Li, L. A Biomimetic Coordination Nanoplatform for Controlled Encapsulation and Delivery of Drug–Gene Combinations. *Angewandte Chemie International Edition* **2019**, *58* (26), 8804–8808. https://doi.org/10.1002/anie.201903417.

(12) Peng, S.; Bie, B.; Sun, Y.; Liu, M.; Cong, H.; Zhou, W.; Xia, Y.; Tang, H.; Deng, H.; Zhou, X. Metal-Organic Frameworks for Precise Inclusion of Single-Stranded DNA and Transfection in Immune Cells. *Nat Commun* **2018**, *9* (1), 1293. https://doi.org/10.1038/s41467-018-03650-w.

(13) Zhang, Y.; Wang, F.; Ju, E.; Liu, Z.; Chen, Z.; Ren, J.; Qu, X. Metal-Organic-Framework-Based Vaccine Platforms for Enhanced Systemic Immune and Memory Response. *Advanced Functional Materials* **2016**, *26* (35), 6454–6461.

https://doi.org/10.1002/adfm.201600650.
(14) Chen, W.-H.; Luo, G.-F.; Vázquez-González, M.; Cazelles, R.; Sohn, Y. S.; Nechushtai, R.; Mandel, Y.; Willner, I. Glucose-Responsive Metal–Organic-Framework Nanoparticles Act as "Smart" Sense-and-Treat Carriers. *ACS Nano* **2018**, *12* (8), 7538–7545. https://doi.org/10.1021/acsnano.8b03417.
(15) Wang, Q.; Zhang, X.; Huang, L.; Zhang, Z.; Dong, S. GOx@ZIF-8(NiPd) Nanoflower: An Artificial Enzyme System for Tandem Catalysis. *Angewandte Chemie International Edition* **2017**, *56* (50), 16082–16085. https://doi.org/10.1002/anie.201710418.
(16) Li, P.; Moon, S.-Y.; Guelta, M. A.; Lin, L.; Gómez-Gualdrón, D. A.; Snurr, R. Q.; Harvey, S. P.; Hupp, J. T.; Farha, O. K. Nanosizing a Metal–Organic Framework Enzyme Carrier for Accelerating Nerve Agent Hydrolysis. *ACS Nano* **2016**, *10* (10), 9174–9182. https://doi.org/10.1021/acsnano.6b04996.
(17) Zheng, H.; Zhang, Y.; Liu, L.; Wan, W.; Guo, P.; Nyström, A. M.; Zou, X. One-Pot Synthesis of Metal–Organic Frameworks with Encapsulated Target Molecules and Their Applications for Controlled Drug Delivery. *J. Am. Chem. Soc.* **2016**, *138* (3), 962–968. https://doi.org/10.1021/jacs.5b11720.
(18) Chen, Y.; Lykourinou, V.; Hoang, T.; Ming, L.-J.; Ma, S. Size-Selective Biocatalysis of Myoglobin Immobilized into a Mesoporous Metal–Organic Framework with Hierarchical Pore Sizes. *Inorg. Chem.* **2012**, *51* (17), 9156–9158. https://doi.org/10.1021/ic301280n.
(19) Maddigan, N. K.; Tarzia, A.; Huang, D. M.; Sumby, C. J.; Bell, S. G.; Falcaro, P.; Doonan, C. J. Protein Surface Functionalisation as a General Strategy for Facilitating Biomimetic Mineralisation of ZIF-8. *Chem. Sci.* **2018**, *9* (18), 4217–4223. https://doi.org/10.1039/C8SC00825F.
(20) Jian, M.; Liu, B.; Liu, R.; Qu, J.; Wang, H.; Zhang, X. Water-Based Synthesis of Zeolitic Imidazolate Framework-8 with High Morphology Level at Room Temperature. *RSC Adv.* **2015**, *5* (60), 48433–48441. https://doi.org/10.1039/C5RA04033G.
(21) Cui, J.; Feng, Y.; Lin, T.; Tan, Z.; Zhong, C.; Jia, S. Mesoporous Metal–Organic Framework with Well-Defined Cruciate Flower-Like Morphology for Enzyme Immobilization. *ACS Appl. Mater. Interfaces* **2017**, *9* (12), 10587–10594. https://doi.org/10.1021/acsami.7b00512.
(22) Liang, W.; Ricco, R.; Maddigan, N. K.; Dickinson, R. P.; Xu, H.; Li, Q.; Sumby, C. J.; Bell, S. G.; Falcaro, P.; Doonan, C. J. Control of Structure Topology and Spatial Distribution of Biomacromolecules in Protein@ZIF-8 Biocomposites. *Chem. Mater.* **2018**, *30* (3), 1069–1077. https://doi.org/10.1021/acs.chemmater.7b04977.
(23) Pan, Y.; Li, H.; Farmakes, J.; Xiao, F.; Chen, B.; Ma, S.; Yang, Z. How Do Enzymes Orient When Trapped on Metal–Organic Framework (MOF) Surfaces? *J. Am. Chem. Soc.* **2018**, *140* (47), 16032–16036. https://doi.org/10.1021/jacs.8b09257.
(24) De Yoreo, J. J.; Vekilov, P. G. Principles of Crystal Nucleation and Growth. *Reviews in Mineralogy and Geochemistry* **2003**, *54* (1), 57–93. https://doi.org/10.2113/0540057.
(25) Zhu, Y.; Ciston, J.; Zheng, B.; Miao, X.; Czarnik, C.; Pan, Y.; Sougrat, R.; Lai, Z.; Hsiung, C.-E.; Yao, K.; Pinnau, I.; Pan, M.; Han, Y. Unravelling Surface and Interfacial Structures of a Metal–Organic Framework by Transmission Electron Microscopy. *Nature Mater* **2017**, *16* (5), 532–536. https://doi.org/10.1038/nmat4852.
(26) Liang, W.; Xu, H.; Carraro, F.; Maddigan, N. K.; Li, Q.; Bell, S. G.; Huang, D. M.; Tarzia, A.; Solomon, M. B.; Amenitsch, H.; Vaccari, L.; Sumby, C. J.; Falcaro, P.; Doonan, C. J. Enhanced Activity of Enzymes Encapsulated in Hydrophilic Metal–Organic Frameworks.

J. Am. Chem. Soc. **2019**, *141* (6), 2348–2355. https://doi.org/10.1021/jacs.8b10302.
(27) Patterson, J. P.; Abellan, P.; Denny, M. S.; Park, C.; Browning, N. D.; Cohen, S. M.; Evans, J. E.; Gianneschi, N. C. Observing the Growth of Metal–Organic Frameworks by in Situ Liquid Cell Transmission Electron Microscopy. *J. Am. Chem. Soc.* **2015**, *137* (23), 7322–7328. https://doi.org/10.1021/jacs.5b00817.
(28) Cravillon, J.; Schröder, C. A.; Nayuk, R.; Gummel, J.; Huber, K.; Wiebcke, M. Fast Nucleation and Growth of ZIF-8 Nanocrystals Monitored by Time-Resolved In Situ Small-Angle and Wide-Angle X-Ray Scattering. *Angewandte Chemie International Edition* **2011**, *50* (35), 8067–8071. https://doi.org/10.1002/anie.201102071.
(29) Terban, M. W.; Banerjee, D.; Ghose, S.; Medasani, B.; Shukla, A.; Legg, B. A.; Zhou, Y.; Zhu, Z.; Sushko, M. L.; Yoreo, J. J. D.; Liu, J.; Thallapally, P. K.; Billinge, S. J. L. Early Stage Structural Development of Prototypical Zeolitic Imidazolate Framework (ZIF) in Solution. *Nanoscale* **2018**, *10* (9), 4291–4300. https://doi.org/10.1039/C7NR07949D.
(30) Cravillon, J.; Nayuk, R.; Springer, S.; Feldhoff, A.; Huber, K.; Wiebcke, M. Controlling Zeolitic Imidazolate Framework Nano- and Microcrystal Formation: Insight into Crystal Growth by Time-Resolved In Situ Static Light Scattering. *Chem. Mater.* **2011**, *23* (8), 2130–2141. https://doi.org/10.1021/cm103571y.
(31) Hikov, T.; Schröder, C. A.; Cravillon, J.; Wiebcke, M.; Huber, K. In Situ Static and Dynamic Light Scattering and Scanning Electron Microscopy Study on the Crystallization of the Dense Zinc Imidazolate Framework ZIF-Zni. *Phys. Chem. Chem. Phys.* **2011**, *14* (2), 511–521. https://doi.org/10.1039/C1CP22855B.
(32) Van Vleet, M. J.; Weng, T.; Li, X.; Schmidt, J. R. In Situ, Time-Resolved, and Mechanistic Studies of Metal–Organic Framework Nucleation and Growth. *Chem. Rev.* **2018**, *118* (7), 3681–3721. https://doi.org/10.1021/acs.chemrev.7b00582.
(33) Venna, S. R.; Jasinski, J. B.; Carreon, M. A. Structural Evolution of Zeolitic Imidazolate Framework-8. *J. Am. Chem. Soc.* **2010**, *132* (51), 18030–18033. https://doi.org/10.1021/ja109268m.
(34) Pan, Y.; Liu, Y.; Zeng, G.; Zhao, L.; Lai, Z. Rapid Synthesis of Zeolitic Imidazolate Framework-8 (ZIF-8) Nanocrystals in an Aqueous System. *Chem. Commun.* **2011**, *47* (7), 2071–2073. https://doi.org/10.1039/C0CC05002D.
(35) Kida, K.; Okita, M.; Fujita, K.; Tanaka, S.; Miyake, Y. Formation of High Crystalline ZIF-8 in an Aqueous Solution. *CrystEngComm* **2013**, *15* (9), 1794–1801. https://doi.org/10.1039/C2CE26847G.
(36) Low, Z.-X.; Yao, J.; Liu, Q.; He, M.; Wang, Z.; Suresh, A. K.; Bellare, J.; Wang, H. Crystal Transformation in Zeolitic-Imidazolate Framework. *Crystal Growth & Design* **2014**, *14* (12), 6589–6598. https://doi.org/10.1021/cg501502r.
(37) Nielsen, M. H.; Aloni, S.; Yoreo, J. J. D. In Situ TEM Imaging of CaCO3 Nucleation Reveals Coexistence of Direct and Indirect Pathways. *Science* **2014**. https://doi.org/10.1126/science.1254051.
(38) Carraro, F.; Velásquez-Hernández, M. de J.; Astria, E.; Liang, W.; Twight, L.; Parise, C.; Ge, M.; Huang, Z.; Ricco, R.; Zou, X.; Villanova, L.; Kappe, C. O.; Doonan, C.; Falcaro, P. Phase Dependent Encapsulation and Release Profile of ZIF-Based Biocomposites. *Chem. Sci.* **2020**, *11* (13), 3397–3404. https://doi.org/10.1039/C9SC05433B.
(39) Li, Y.; Wang, K.; Zhou, W.; Li, Y.; Vila, R.; Huang, W.; Wang, H.; Chen, G.; Wu, G.-H.; Tsao, Y.; Wang, H.; Sinclair, R.; Chiu, W.; Cui, Y. Cryo-EM Structures of Atomic Surfaces and Host-Guest Chemistry in Metal-Organic Frameworks. *Matter* **2019**, *1* (2), 428–438.

https://doi.org/10.1016/j.matt.2019.06.001.
(40) Du, H.; Amstad, E. Water: How Does It Influence the CaCO3 Formation? *Angewandte Chemie International Edition* **2020**, *59* (5), 1798–1816. https://doi.org/10.1002/anie.201903662.
(41) Katsenis, A. D.; Puškarić, A.; Štrukil, V.; Mottillo, C.; Julien, P. A.; Užarević, K.; Pham, M.-H.; Do, T.-O.; Kimber, S. A. J.; Lazić, P.; Magdysyuk, O.; Dinnebier, R. E.; Halasz, I.; Friščić, T. In Situ X-Ray Diffraction Monitoring of a Mechanochemical Reaction Reveals a Unique Topology Metal-Organic Framework. *Nature Communications* **2015**, *6* (1), 6662. https://doi.org/10.1038/ncomms7662.
(42) Park, K. S.; Ni, Z.; Côté, A. P.; Choi, J. Y.; Huang, R.; Uribe-Romo, F. J.; Chae, H. K.; O'Keeffe, M.; Yaghi, O. M. Exceptional Chemical and Thermal Stability of Zeolitic Imidazolate Frameworks. *Proceedings of the National Academy of Sciences* **2006**, *103* (27), 10186–10191. https://doi.org/10.1073/pnas.0602439103.
(43) Thompson, R. F.; Walker, M.; Siebert, C. A.; Muench, S. P.; Ranson, N. A. An Introduction to Sample Preparation and Imaging by Cryo-Electron Microscopy for Structural Biology. *Methods* **2016**, *100*, 3–15. https://doi.org/10.1016/j.ymeth.2016.02.017.
(44) Pan, Y.; Heryadi, D.; Zhou, F.; Zhao, L.; Lestari, G.; Su, H.; Lai, Z. Tuning the Crystal Morphology and Size of Zeolitic Imidazolate Framework-8 in Aqueous Solution by Surfactants. *CrystEngComm* **2011**, *13* (23), 6937–6940. https://doi.org/10.1039/C1CE05780D.
(45) Smallenburg, F.; Boon, N.; Kater, M.; Dijkstra, M.; van Roij, R. Phase Diagrams of Colloidal Spheres with a Constant Zeta-Potential. *The Journal of Chemical Physics* **2011**, *134* (7), 074505. https://doi.org/10.1063/1.3555627.
(46) Ofir, E.; Oren, Y.; Adin, A. Electroflocculation: The Effect of Zeta-Potential on Particle Size. *Desalination* **2007**, *204* (1), 33–38. https://doi.org/10.1016/j.desal.2006.03.533.

Chapter 3.

Role of Molecular Modification and Protein Folding in the Nucleation and Growth of Protein-Metal-Organic Frameworks

This work appears in the following publication and has been re-formatted for this thesis:
Carpenter, B.P.; Talosig, A.R.; Mulvey, J.T.; Merham, J.G.; Esquivel, J.; Rose, B.; Ogata, A.F.; Fishman, D.A.; Patterson, J.P. Role of Molecular Modification and Protein Folding in the Nucleation and Growth of Protein-Metal-Organic Frameworks. Chem Mater. 2022, 24 (18), 8336-8344.

Chapter 3. The Role of Molecular Modification and Protein Folding in the Nucleation and Growth of Protein-Metal-Organic Frameworks

3.1 Introduction

Living systems have evolved enzymes to have remarkable catalytic efficiency and stereoselectivity.[1] However, most enzymes evolved in specific environments that did not promote enzymes with high thermal or chemical stability. Consequently, the implementation of enzymes into industrial applications, which are typically performed in non-physiological environments, has been limited by enzyme stability.[2,3] Enormous efforts have been devoted to enhancing stability and recyclability of enzymes by immobilizing them onto supported structures to significantly reduce the energy and economic cost of the chemical industry.[4,5] One promising support strategy utilizes metal-organic frameworks (MOFs) due to their large surface area, simplistic synthetic conditions, and tunable pore and crystal sizes.[5–9] MOFs consist of coordinated metal ions and organic ligands building blocks that form protective frameworks for biomolecules.[10–12]

Enzymes can be integrated into MOF systems through in situ approaches in which the crystal forms in the presence of a protein,[6,7] or post synthetic approaches, where the protein is incorporated after crystallization by surface attachment,[13] pore entrapment,[14] or covalent linkage.[15,16] In situ approaches are advantageous due to their mild synthetic conditions, simplistic synthetic procedures, and typically higher encapsulation efficiencies (EE%).[7,17] The primary challenge with the in situ approach is understanding how the biomolecules affect the nucleation and growth of the MOF crystals and become incorporated into frameworks. Low isoelectric point (pI) (< 7) proteins have been shown to effectively initiate the nucleation of zeolitic imidazole framework-8 (ZIF-8) when precursors are below supersaturation conditions.[18] High pI (>7) proteins cannot initiate nucleation, but molecular modifications of proteins can be used to lower

the pI and promote nucleation.[18] However, the role molecular modification and protein folding plays in controlling crystal properties such as size and morphology has not been established. These properties are essential for catalytic performance of protein@MOFs as they determine accessibility of enzymes to substrates. For example, when an enzyme is located throughout the crystal, smaller crystal sizes are desired to reduce the diffusion barrier and allow the substrate to reach the internal enzymes.[19] Furthermore, a recent study demonstrated that variation in protein@MOF crystal structure directly affects enzymatic activity, which supports the need for understanding nucleation and growth mechanisms to optimize protein@MOFs properties.[20]

Here, we demonstrate how molecular modification of a protein affects encapsulation efficiency, crystal size, and morphology of protein@MOFs. One of the most common molecular modifications for proteins in MOF systems is a fluorescent tag such as fluorescein isothiocyanate (FITC), which aids in determining the encapsulation efficiency and location of protein in crystal.[6,17] In our studies, bovine serum albumin (BSA) and FITC-BSA are used as model proteins as they have been well studied and are inexpensive.[21–23] Biophysical characterization of the proteins were performed using electrospray ionization mass spectrometry (ESI-MS), circular dichroism, and zeta potential measurements. To compare final protein@MOF crystals, scanning electron microscopy (SEM), transmission electron microscopy (TEM), fluorescent microscopy, powder X-ray diffraction (PXRD) and fluorescence spectroscopy are used. Encapsulation efficiencies of BSA and FITC-BSA are determined using a developed procedure to measure intrinsic tryptophan fluorescence by accounting for potential interaction between protein and MOF precursors. To evaluate how the FITC modification affects the nucleation and growth mechanism, cryogenic TEM (cryoTEM) and in situ XRD are performed.

3.2 Results

BSA@ZIF-8 and FITC-BSA@ZIF-8 synthesis

Stock solutions of 2-methylimidazole (HmIm)(5600 mm, 2800 mM, 1400 mM, 700 mM, and 320 mM, 0.5 mL), zinc acetate (40 mM, 1 ml) and protein (10 mg/ml, 5 mg/ml, and 2.5 mg/ml, 0.5 mL) were prepared with Milli-Q water (18 MΩ). Stock solutions were used to prepare a series of MOF crystallization experiments with variation in HmIm:Zn ratio (70:1, 35:1, 17.5:1, 4:1), and protein concentration (2.5 mg/ml 1.25 mg/ml, and 0.625 mg/ml) (Table 3.1). Protein solutions were added to 2-methylimidazole solutions, and crystallization was initiated by addition of zinc acetate solution. Solutions were aged for 24 hours without stirring. Precipitate was obtained via centrifugation at 10,000 rpm for 10 min where the supernatant was kept for EE% measurements.[6,24,25] Precipitates were then washed with water three times prior to electron microscopy and PXRD analysis.

Protein Characterization

BSA and FITC-BSA underwent biophysical characterization using mass spectrometry techniques, circular dichroism, and zeta potential measurements. Mass spectra of FITC-BSA indicates heterogeneous FITC tagging as by the poor signal-to-noise in the raw spectra and the multiple peaks found in the deconvoluted spectra (Figure 3.1a). Charge state deconvolution was performed on the data and determined the center of mass for BSA to be 66,955 g/mol, which aligns with the reported mass in literature,[26] and the center of mass for FITC-BSA to be 72,433 g/mol. FITC-BSA was found to have 12-18 FITC tags per biomolecule. To determine how FITC affects surface charge, zeta potential measurements were performed on BSA and FITC-BSA at pH ranges from 2-11 (Figure 3.1b). Measurements revealed that both proteins have similar isoelectric points

(~4-4.5) and that both were highly negatively charged in the pH conditions that occur during MOF synthesis. Circular dichroism was used to measure the secondary protein structure of the tagged and untagged protein in the absence and presence of zinc acetate to understand how ZIF-8 precursors affect the protein structures (Figure 3.1c). All samples were performed at the same protein concentration of 1 mg/ml. Studies were attempted in the presence of HmIm, but the quantum yield of HmIm was too high for the instrument detector as HmIm absorbs in the UV wavelength range. However, HmIm is believed to also affect protein folding.[27] BSA is a globular protein that consists of predominantly α-helical content. The CD band for α-helical proteins has characteristic peak dips at ~210 nm and ~220 nm.[28] A reduction of ellipticity (Δε) at these peak dips is representative of protein unfolding. It was found that the α-helical character of BSA was reduced when modified with FITC or when in the presence of zinc acetate. When FITC-BSA is in the presence of zinc acetate, the α-helical character significantly decreases compared to all other samples. Intrinsic tryptophan fluorescence further confirms the unfolding of BSA when tagged with FITC (Figure B1). A blueshift can be observed for FITC-BSA compared to BSA as the center of mass changes from 345 nm to 310 nm. While we also see a blueshift (~5-10 nm) for BSA@ZIF-8, the shift is more significant for FITC-BSA where the center of mass shifts from 310 to 380 nm. We can associate these changes with structural changes of protein molecules that influence the position of energy states as well as transition probability.[29] While protein unfolding has been shown to occur in the presence of zinc acetate and when encapsulated in ZIF-8, refolding of the protein upon release from ZIF-8 is possible.[30]

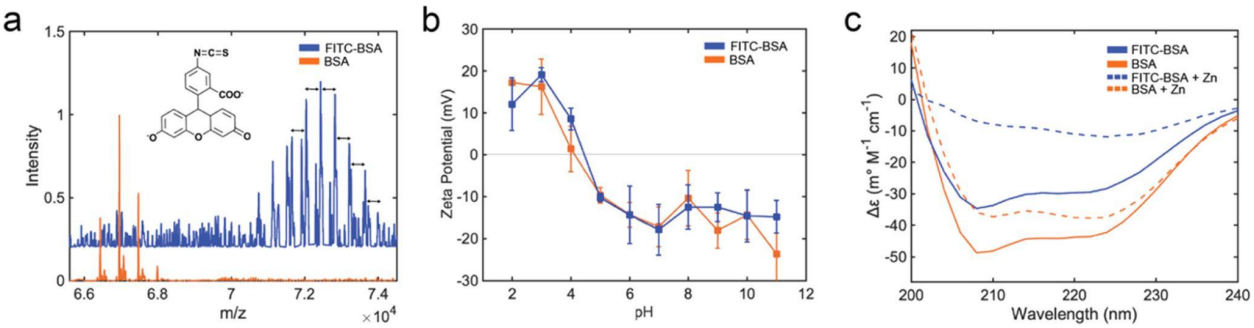

Figure 3.1: Biophysical characterization of FITC-BSA (blue) and BSA (orange) using (a.) ESI-MS where the black arrows are indicative of FITC-tag spacing, (b.) zeta potential, and (c.) circular dichroism in the absence (solid line) and presence (dashed line) of zinc.

Crystal Structure

ZIF-8 crystals can form various polymorphs with diamondoid (dia) and sodalite (sod) being the most widely studied.[31,32] Polymorph control can be obtained by altering the HmIm:Zn ratio, changing the precursor concentrations, or by integrating a nucleation and growth driving agent (i.e. surfaces or biomolecules).[33,34] PXRD was used to analyze isolated ZIF-8, BSA@ZIF-8 and FITC-BSA@ZIF-8 crystals. At low HmIm:Zn ratios (4:1), ZIF-8 crystals form the diamondoid (dia) structure (Figure B2a).[35] As HmIm:Zn ratio gradually increases (17.5:1), a mixture of dia and sod can be obtained (Figure B2b) followed by exclusively sod formation at 35:1 and 70:1 (Figure B2c, B2d). The sod polymorph is also formed exclusively for all HmIm:Zn ratios except 4:1 in the presence of BSA and FITC-BSA (Figure 3.2, B3, B4).[21] For 1.25 mg/ml and 0.625 mg/ml at 4:1, a mixture of sod and ZIF-CO_3-1 (ZIF-C) can be observed for both protein@MOFs (B3a, B4a), This is not surprising as it has been recently found that ZIF-C forms as the weight percent of BSA is decreased.[22]

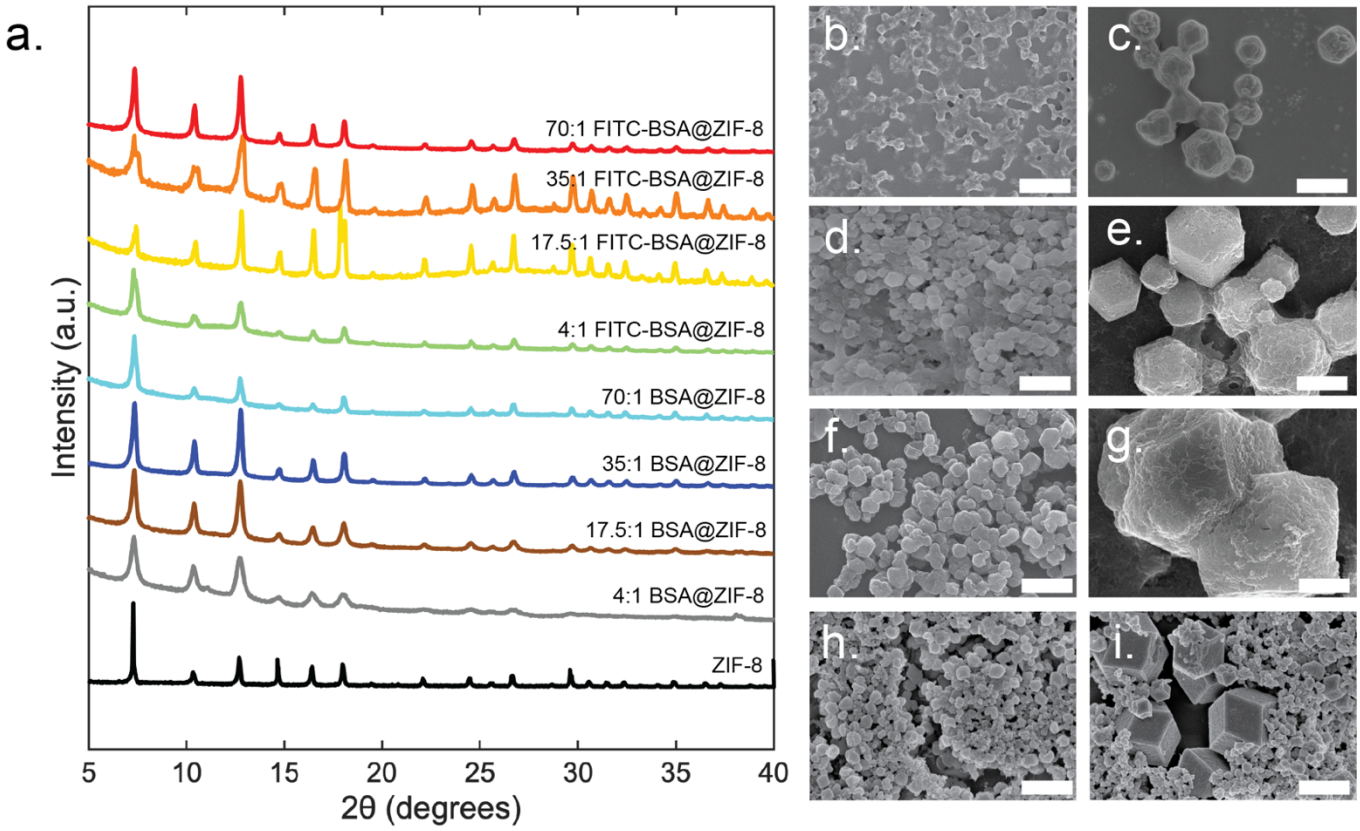

Figure 3.2: (a.) PXRD patterns of protein@MOFs at varying HmIm:Zn ratios. SEM images of (b.) 4:1 BSA@ZIF-8, (c.) 4:1 FITC-BSA@ZIF-8, (d.), 17.5:1 BSA@ZIF-8, (e.) 17.5:1 FITC-BSA@ZIF-8, (f.) 35:1 BSA@ZIF-8, (g.) 35:1 FITC-BSA@ZIF-8 (h.) 70:1 BSA@ZIF-8, (i.) 70:1 FITC-BSA@ZIF-8, at final protein concentrations of 2.5 mg/ml. Scale bar is 1 µm.

Crystal Size

ZIF-8 (sod) crystals form large crystals with a large particle size distribution. For example, with 35:1, crystal sizes range from 710 nm to 3.7 µm with an average mean diameter of 2.1 µm and average standard deviation of ~800 nm (Figure 3.3). By integrating BSA into a ZIF-8 system, the crystal size and standard deviation decrease with an average crystal size of 245 nm and average standard deviation of 50 nm. At all HmIm:Zn conditions, the crystal size gradually decreases as the BSA concentration increases (Figure 3.3c, B6a). For example, with 4:1, the average crystal

size with 0.625 mg/ml BSA is 229 nm, and the average crystal size with 2.5 mg/ml BSA is 184 nm. For all synthetic conditions with FITC-BSA, the average mean size of crystals (1.3 µm) is larger than BSA@ZIF-8 crystals (245 nm) but smaller than ZIF-8 crystals (1.4 µm) (Table 3.1). In addition, the average standard deviation for FITC-BSA is 194 nm, which is greater than the average standard deviation of BSA@ZIF-8 (50 nm) but smaller than that of ZIF-8 (800 nm). Except for the 4:1 condition (Figure B6b), size trends related to protein concentration or HmIm:Zn cannot be observed for FITC-BSA@ZIF-8 (Figure 3.3b, 3.3d).

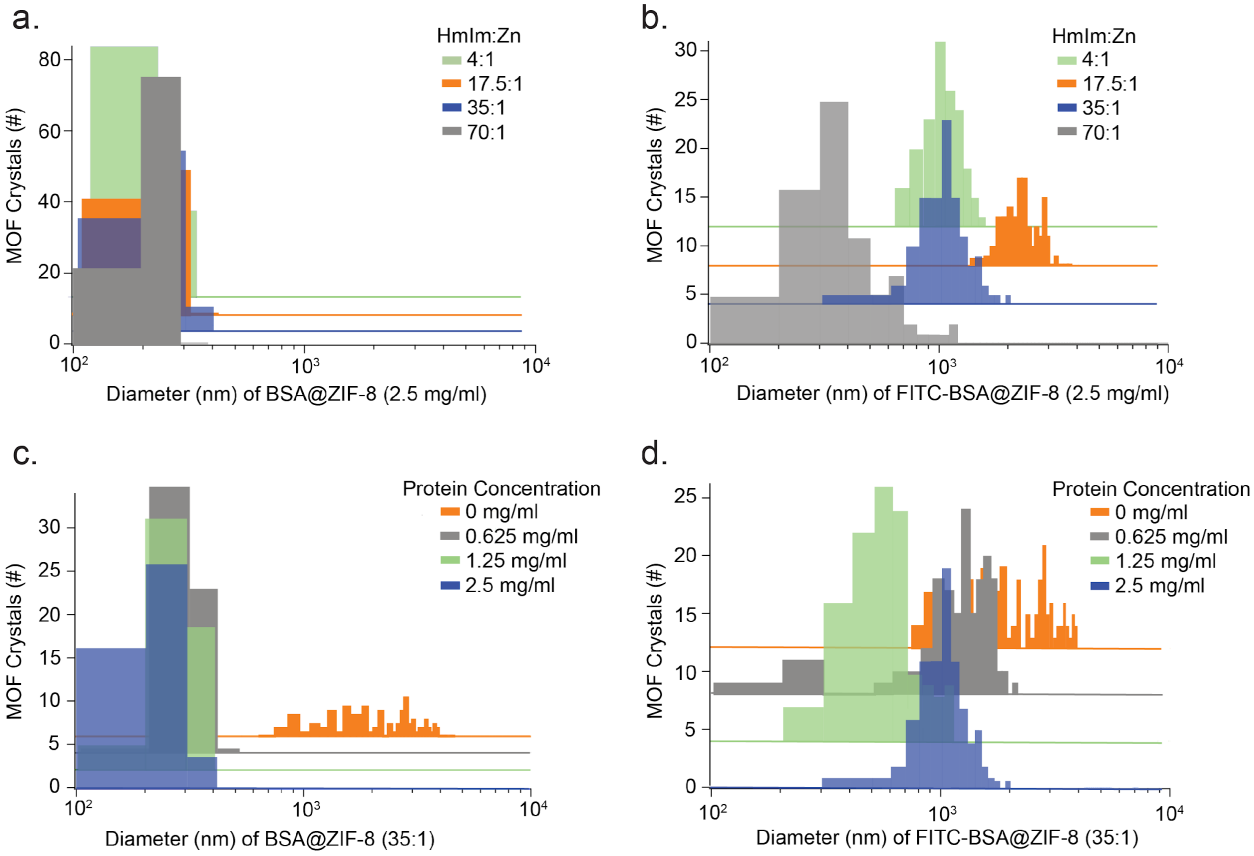

Figure 3.3: Size distribution histograms of (a) BSA@ZIF-8 and (b) FITC-BSA@ZIF-8 at constant protein concentrations of 2.5 mg/ml and HmIm:Zinc ratios of 4:1 (green), 17.5:1 (orange), 35:1 (blue) and 70:1 (grey) and (c) BSA@ZIF-8 and (d) FITC-BSA at a constant HmIm:Zinc ratio of 35:1 with final protein concentrations of 2.5 mg/ml (blue), 1.25 mg/ml (green), 0.625 mg/ml (grey), and 0 mg/ml (orange).

Table 3.1: Summary of crystal sizes for BSA@ZIF-8 and FITC-BSA@ZIF-8 at four different HmIm:Zn ratios (4:1, 17.5:1, 35:1, 70:1) with final protein concentrations of 2.5 mg/ml, 1.25 mg/ml, and 0.625 mg/ml.

			crystal size (nm)	
HmIm/Zn (mM:mM)	**ratio HmIm/Zn**	**final protein concentrations (mg/mL)**	**BSA**	**FITC-BSA**
80:20	4:1	2.5	184 ± 31	944 ± 197
		1.25	187 ± 45	1317 ± 214
		0.625	229 ± 41	2065 ± 282
700:20	17.5:1	2.5	203 ± 42	2215 ± 391
		1.25	296 ± 63	403 ± 51
		0.625	292 ± 94	389 ± 52
1400:20	35:1	2.5	228 ± 57	1183 ± 334
		1.25	270 ± 50	585 ± 189
		0.625	291 ± 40	1281 ± 301
2800:20	70:1	2.5	215 ± 33	486 ± 212
		1.25	229 ± 49	402 ± 51
		0.625	316 ± 61	389 ± 51

Crystal Morphology

In the absence of protein, ZIF-8 crystals exhibit smooth surfaces for both sod and dia polymorphs (Figure B2). Introduction of BSA at all HmIm:Zn ratios results in the formation of spheroid crystals with rough surfaces (Figure 3.2b, 3.2d, 3.2f, 3.2h). As the ratio of HmIm:Zn increases, BSA@ZIF-8 crystals become more faceted and have smoother surfaces (Figure B3). In the presence of FITC-BSA, crystals retain truncated rhombic dodecahedral morphology, displaying rough surfaces at low HmIm:Zn ratios (Figure 3.2c, 3.2e) and smoother surfaces at high ratios (Figure 3.2g, 3.2i). The 70:1 FITC-BSA@ZIF-8 crystals form three different types of

crystals that can be described as large smooth surfaced crystals, mid-sized crystals with rougher surfaces, and small spheroid crystals with rough surfaces (Figure 3.2i). All MOF crystals were washed three times with water to remove excess precursors, yet significant amorphous peaks in PXRD patterns can be observed in the 17.5:1 with 1.25 mg/ml of BSA as well as with 17.5:1 and 35:1 with 2.5 mg/ml FITC (Figure 3.2a). A comparison of BSA@ZIF-8 and FITC-BSA@ZIF-8 crystals (35:1, 2.5 mg/ml) by TEM indicates that the FITC-BSA@ZIF-8 sample contains large regions of undefined material (Figure B8). We hypothesize this undefined material contributes to the amorphous peak seen in PXRD.

Encapsulation Efficiency

Protein incorporation into BSA@ZIF-8 and FITC-BSA@ZIF-8 was confirmed with FTIR as amide I peaks at 1654 cm^{-1} can be observed in both MOF samples (Figure B9).[36,37] Additionally, intrinsic tryptophan fluorescence was performed on the protein@MOFs (Figure B1). For both protein@MOFs, samples were excited at 280 nm and emission peaks can be observed between 310-380 nm which can be linked to tryptophan amino acids, and thus protein, being incorporated into the MOFs. The encapsulation efficiency for FITC-BSA@ZIF-8 and BSA@ZIF-8 was determined by measuring the concentration of protein in the supernatant,[6,17,18] which is the liquid obtained after the first centrifugation cycle prior to washes. EE% is calculated by quantifying remaining protein concentration in supernatant to calculate protein concentration in MOF precipitate. EE% was measured using fluorescence spectroscopy where the emission intensity of fluorescein (~520 nm) and tryptophan (~340 nm) was measured for FITC-BSA@ZIF-8 and BSA@ZIF-8, respectively (Figure 3.4). Tryptophan fluorescence intensity is sensitive to solution pH and metal binding; thus, supernatants for BSA@ZIF-8 and FITC-BSA@ZIF-8 were diluted in

a phosphate buffer (~pH 6.7) containing excess tetrasodium ethylenediaminetetraacetic acid (EDTA) to ensure the protein conformation remained a constant. (Figure B11).

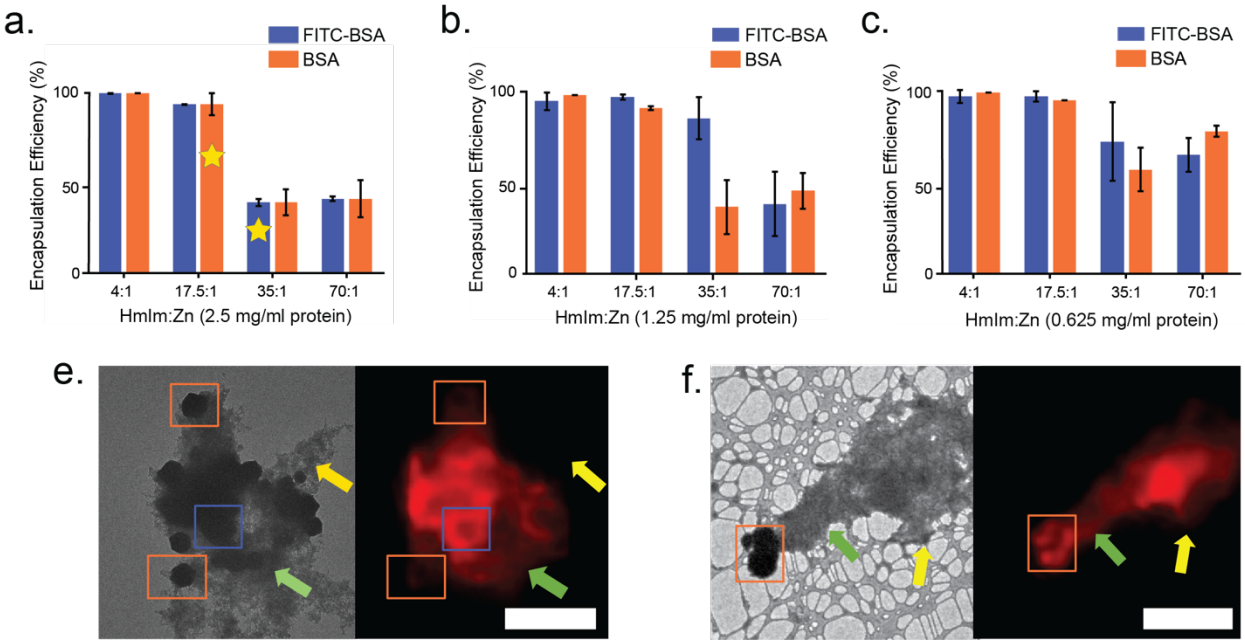

Figure 3.4: Encapsulation efficiency of protein@MOFs at final protein concentrations of (a.) 2.5 mg/ml, (b.) 1.25 mg/ml, and (c.) 0.625 mg/ml. (e,f) Correlative TEM (left) and Fluorescence microscopy (right) images of FITC-BSA@ZIF-8 crystals at a 35:1 with 2.5 mg/ml FITC-BSA. (e.) and (f.) show two different regions of the same sample. Scale bars are 10 µm. A strong, uniform signal can be viewed around the outside edges of some crystals (blue box) whereas a weak, nonuniform signal can be seen in other crystals (orange box). Green arrows denote amorphous phase with clear fluorescent signal whereas the yellow arrow denotes amorphous region that has little to no fluorescence.

Protein EE% measurements of BSA@ZIF-8 systems were also measured using the Bradford assay, which validated results from the fluorescent measurements (Figure B14). When HmIm:Zn ratios of 4:1 or 17.5:1 are used, both BSA@ZIF-8 and FITC-BSA@ZIF-8 have ~100% encapsulation for all protein concentrations studied. The most significant difference was observed in the 35:1 samples at protein concentrations of 2.5 mg/ml and 1.25 mg/ml where the EE% of FITC-BSA@ZIF-8 was ~90% and the BSA@ZIF-8 was ~40%. These EE% method for these results is notable because EE% is measured through protein quantification of the supernatant;

therefore, the protein concentration in the MOF precipitate, which could potentially contain both MOF crystals and MOF amorphous phases, is the calculated EE% value. The 35:1 crystals were then imaged with fluorescent microscopy, which revealed that FITC-BSA is located in both crystals and in the amorphous material (Figure 3.4e, 3.4f). Crystals with little to no fluorescence can also be observed in the fluorescent microscopy data. Thus, samples that contain a significant amorphous background, based on PXRD patterns, are indicated with a star. Future work will focus on methods to distinguish between proteins that are encapsulated into crystals and that are precipitated into an amorphous phase.

Mechanistic studies

In situ measurements were performed on the crystallization of FITC-BSA@ZIF-8 using XRD and cryoTEM. Based on the data in the previous sections, the 35:1 BSA@ZIF8 and FITC-BSA@ZIF-8 with protein concentrations of 2.5 mg/ml were chosen to study as the systems have the largest variance in crystal size, morphology, and encapsulation efficiency. In situ XRD data was analyzed by measuring the area under the (011) peak over 8 hours to measure the extent of crystallinity (Figure 3.5a). As the reaction progresses, more amorphous species crystallize which can be quantified by an increase in area under the (011) peak (Figure B15). Distinct differences between the growth of BSA@ZIF-8 and FITC-BSA@ZIF-8 can be observed between 10 minutes to 110 minutes. During this time, BSA@ZIF-8 is observed to have a greater extent of crystallinity and to grow at a greater crystallization rate. ZIF-8 in the absence of protein was also measured and crystallized at a similar rate as FITC-BSA@ZIF-8. Time point measurements for cryoTEM were chosen based on differences in the in situ XRD data. At initial timepoints (~1 min) all cryoTEM images of FITC-BSA@ZIF-8 reveal similar Zn/HmIm amorphous and protein/Zn/HmIm

amorphous phases (Figure 3.5b). Particle picking and averaging of individual particles was used to determine average particle diameters (see Appendix B.2 for details). The full width at half maximum (FWHM) of BSA@ZIF8 particles line profile was 6.8 +/- 1 nm (Figure 3.5c) and the FITC-BSA@ZIF8 particles line profile was 12.0 +/- 0.55 nm (Figure 3.5b). Note: the data used for Figure 5a were collected in our previous paper.[21] After 1 hour, the particulate amorphous phase disappears for BSA@ZIF-8 and is replaced with predominantly BSA@ZIF-8 crystals (Figure 3.5d). Meanwhile, at 1 hour, the FITC-BSA@ZIF-8 sample still contains the particulate amorphous phase, which is observed both isolated or in the presence of crystals (Figure 3.5e). Particle picking and averaging was attempted for the FITC-BSA@ZIF-8 amorphous particles at 1 hour. However, the resulting image did not reveal a well-defined particle, which we believe is due to the heterogeneity of the particles within the amorphous phase (Figure B16). After 24 hours, the BSA@ZIF-8 sample solely consists of crystals, whereas particulate amorphous phases can still be observed in the FITC-BSA@ZIF-8 samples (Figure B8b).

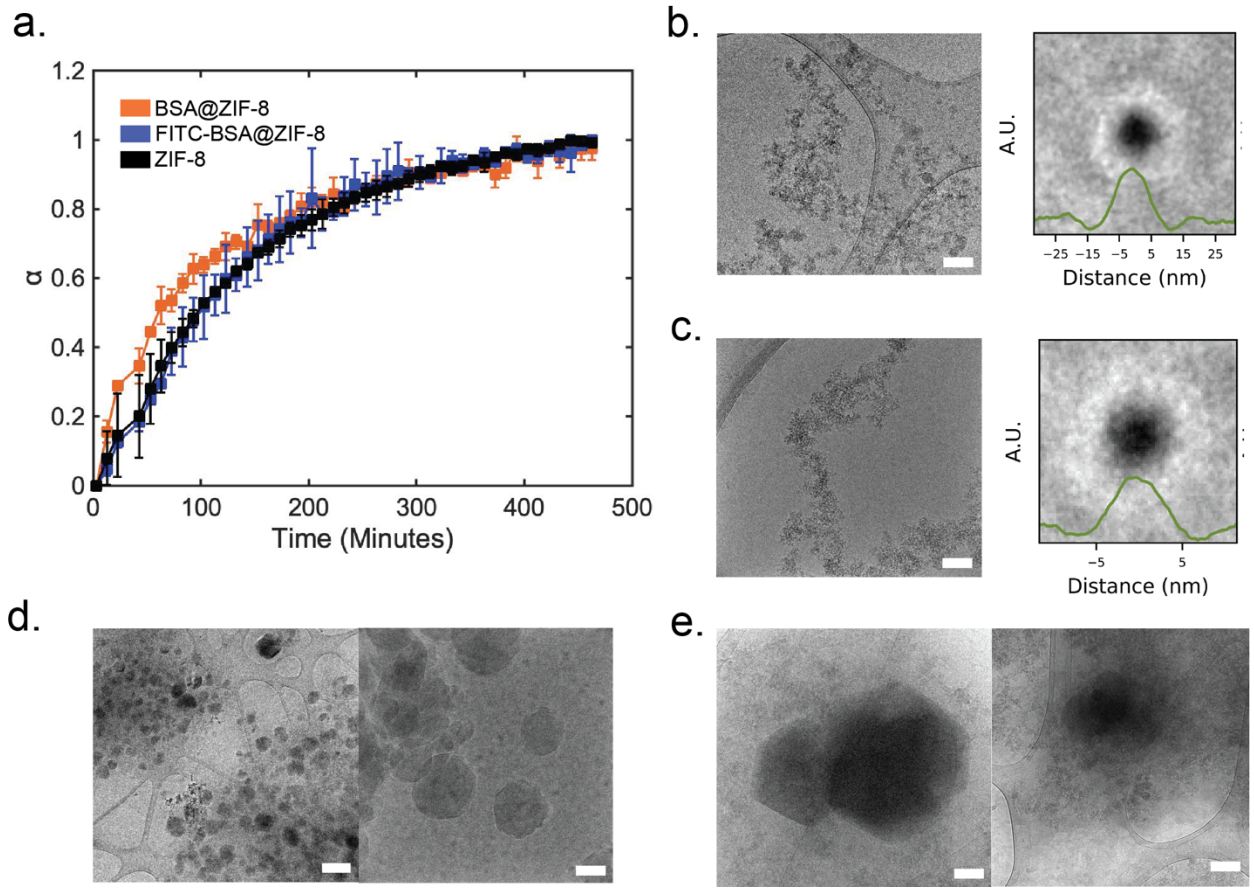

Figure 3.5: In situ measurements of protein@MOFs. (a.) Insitu XRD of BSA@ZIF-8 (orange), FITC-BSA@ZIF-8(blue), and ZIF-8(black). The data is displayed as extent of crystallinity (α) over time. (b.) CryoTEM image of FITC-BSA@ZIF-8 at 1 minute (scale bar 100 nm). (c.) CryoTEM image of BSA@ZIF-8 at 1 min. Low magnification image (scale bar 100 nm)(left) and averaged particles (right) Note: the data used for Figure 5a were collected in our previous paper.[21] (d.) Low magnification cryoTEM image (scale bar 1 µm) (left) and high magnification image (scale bar 100 nm)(right) of BSA@ZIF-8 at 1 hour. (e.) CryoTEM of FITC-BSA@ZIF-8 at 1 hour showing appearance of crystal (left) and amorphous particles (right). Scale bar is 100 nm.

3.3 Discussion

Previous research has demonstrated that BSA can be incorporated into ZIF-8 crystals via two different mechanisms that are dependent on HmIm:Zn ratios.[21] At low ratios, BSA binds with Zn and HmIm, forming an amorphous precursor phase, which increases local supersaturation and promotes nucleation of ZIF-8 (sod). At high ratios, ZIF-8 crystals can form independently, and

BSA is incorporated when amorphous particles of BSA/HmIm/Zn attach to the surface of growing crystals and undergo crystallization by particle attachment. The mechanism of particle attachment results in rough surfaces observed for BSA@ZIF-8 crystals. Although these are described as separate mechanisms, both mechanisms likely occur simultaneously under certain conditions. With this understanding, this chapter aims to determine how molecular modifications affect the mechanisms through observation of in situ experiments and final crystal sizes and morphologies. In the case where proteins directly promote nucleation (low HmIm:Zn ratios), large mean crystal sizes and large size distributions indicate that nucleation from the protein/HmIm/Zn amorphous phase is slower with FITC-BSA@ZIF-8 than BSA@ZIF-8 (Figure 3.3, Table 3.1). When proteins are incorporated by particle attachment (high HmIm:Zn ratios), the collective data indicate that FITC-BSA can readily form an amorphous phase with HmIm and Zn (Figure 3.6.2a-3.6.2b). Moreover, the larger FITC-BSA@ZIF-8 crystals (Table 3.1) indicate a slower rate of particle nucleation on the surface of growing ZIF-8 crystals (Figure 3.6.2c). The SEM images further support this as FITC-BSA@ZIF-8 crystals have smoother surfaces compared to the BSA@ZIF-8 crystals (Figure 3.2).

EE% provides information on how efficiently particular growth mechanisms incorporate biomolecules into the final MOF products. At low HmIm:Zn ratios EE% measurements suggest both FITC-BSA and BSA are successful in promoting ZIF-8 (sod) growth as both are fully incorporated into the MOF crystals. At high HmIm:Zn ratios (70:1 and 35:1), the EE% measurements suggest FITC modification can increase the encapsulation of BSA into ZIF-8. However, the XRD and fluorescent microscopy data show FITC-BSA@ZIF-8 products consist of both amorphous and crystalline phases, in contrast to BSA@ZIF-8 products, which almost

exclusively consist of crystalline phases (Figure 3.2 and 3.4). This also supports our hypothesis that nucleation from the amorphous phase is inhibited by FITC-BSA.

To further test this hypothesis, in situ XRD and cryoTEM measurements on the 35:1 protein@MOF at 2.5 mg/ml protein concentration were performed to understand how FITC-BSA mechanistically alters the final MOF crystal properties and phases. The cryoTEM data shows that particulate amorphous phase form for both BSA@ZIF-8 and FITC-BSA within one minute. Some of the particles within the phases appear to consist of a protein core and HmIm/Zn shell (Figure 5a). We further believe that HmIm and Zn are bound throughout the protein cores and that the zinc bound atoms are responsible for the dark contrast of the particles. These FITC-BSA/HmIm/Zn particles persist for the remaining duration of the FITC-BSA@ZIF-8 synthesis, as supported by the cryoTEM, whereas the BSA/HmIm/Zn particles adsorb and crystallize onto a growing ZIF-8 crystal. In addition, the rate of crystallinity development for FITC-BSA@ZIF-8 in the 10-100 min is slow compared to BSA@ZIF-8. This provides direct evidence for the inability for the FITC-BSA/HmIm/Zn particles to grow by particle attachment. Instead, this suggests a monomer addition mechanism is favored.[21]

The collective data strongly supports that FITC-BSA has a different nucleation and growth mechanism compared to BSA. Despite the size of fluorescent dyes being relatively small in comparison to proteins, research has found that fluorescent tags such as FITC can affect physicochemical characteristics of biomolecules such as size, secondary protein structure, and surface charge.[31,32] Our initial hypothesis was that protein charge would be the main factor enabling particle addition crystallization.[18,38] However, zeta potential measurements revealed similar pI (+/- 0.5) for FITC-BSA and BSA (Figure 3.1b). Instead, circular dichroism studies suggest variation in protein folding, especially within the amorphous precursor phase, to be the

cause of the deviation in protein@MOF formation mechanisms. In general, protein unfolding causes hydrophobic amino acid groups to become exposed and protein aggregation to occur.[39] In the case of FITC-BSA@ZIF-8 and BSA@ZIF-8, we hypothesize that unfolding is caused by the high binding affinity of the zinc ion to the electrophilic groups on the amino acids and FITC tag. While unfolding of BSA is minimal in the presence of zinc, as supported by recent literature,[40] FITC tagging increases the extent of unfolding of BSA with zinc (Figure 3.1c). Unfolding of FITC-BSA in the amorphous phase explains the large heterogeneity of amorphous particles at 1 hour (Figure B16). To further validate the effect of protein unfolding in the growth mechanisms, BSA@ZIF-8 crystals were synthesized using a partially unfolded BSA (Figure B17). Crystals produced with partially-unfolded BSA had a similar morphology as FITC-BSA@ZIF-8 crystals (Figure B17b) and were ~800 nm – much larger than BSA@ZIF-8 crystals (Figure B18). This supports that protein folding is the dominant factor behind the differences observed between BSA and FITC-BSA@ZIF-8 crystals.

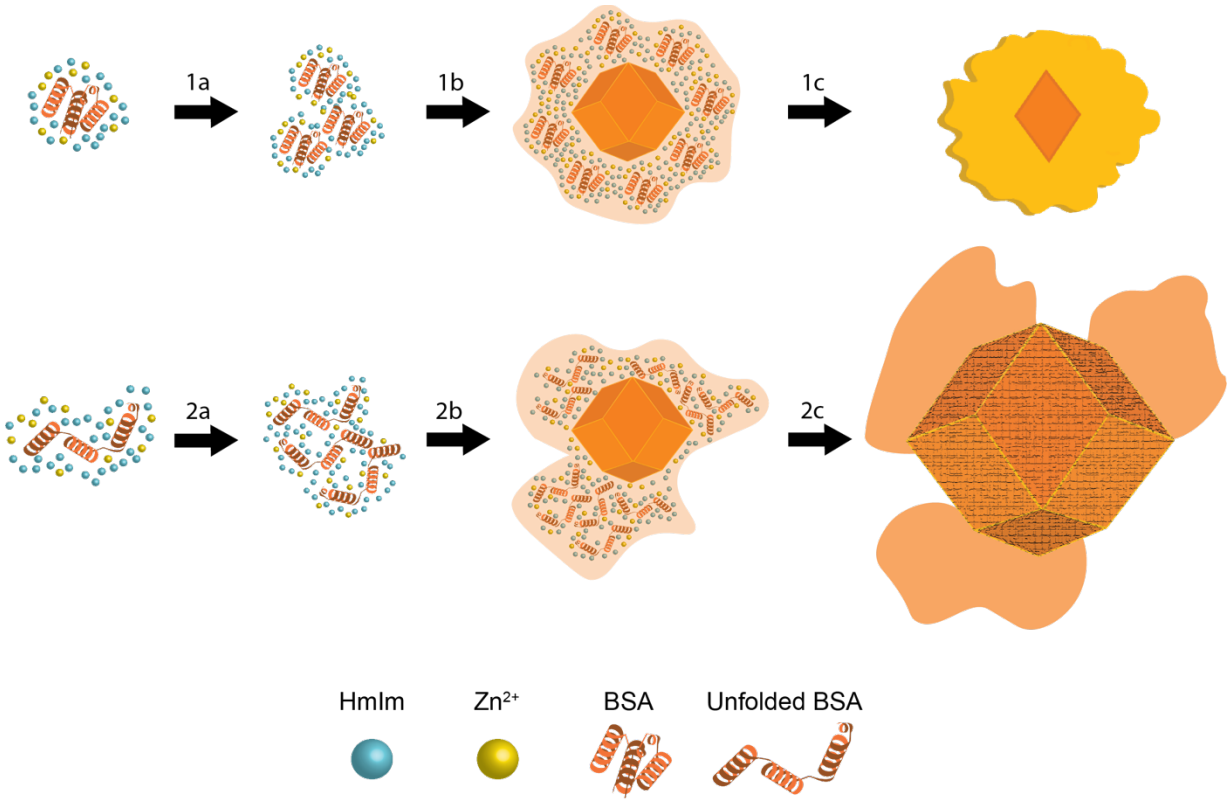

Figure 3.6: Proposed schematic of the formation mechanism of BSA@ZIF-8 at high HmIm:Zn ratios when BSA is (1a.-1c.) Folded vs (2a.-2c.) Unfolded. Both mechanisms initially form particulate amorphous intermediates consisting of protein/HmIm/Zn (a.-b.). The folded BSA/HmIm/Zn intermediate are then able to adsorb and crystallize onto the growing ZIF-8 surface (1c) whereas the unfolded BSA/HmIm/Zn intermediate cannot (2c.).

3.4 Conclusion

In conclusion, we have demonstrated that modification of BSA with FITC molecules significantly alters the crystal growth mechanism affecting the encapsulation efficiency, crystal size and crystal morphology. Circular dichroism studies indicate this is predominantly driven by protein folding within the amorphous precursor phase, and fluorescent spectroscopy studies confirm that proteins remain unfolded in the final MOF crystals. The data also show that different HmIm:Zn ratios will modulate how molecular modification can affect these properties. For example, the effect of modification on the 35:1, 1.25 mg/ml system is that EE% increases from ~40% to 90%, and mean crystal diameter increases from 270 nm +/- 50 nm to 580 nm +/-189 nm.

However, the effect of modification for the 4:1, 1.25 mg/ml system is that EE% remains the same (~100%) while mean crystal diameter increases from 187 nm to 1317 nm. These data show that the mechanisms that govern protein EE% and crystal size are at least partially decoupled, which presents a challenge as the role of a protein during crystallization processes is complex. However, these results also present an opportunity to use molecular modifications of proteins to independently tune the structural features and properties of protein@MOFs. Tuning of protein@MOFs requires a deep understanding of non-classical nucleation pathways and protein folding and aggregation in these pathways. Although each biomolecule will behave differently, we believe the general mechanisms and tunability with molecular modifications and protein folding should be generalizable to all biomolecules. Future work with other proteins and molecular modifications is needed to confirm this generalizability.

3.5 Experimental

Materials

All chemical reagents used for FITC-BSA@ZIF-8 and BSA@ZIF-8 were obtained from Sigma Aldrich unless stated otherwise. FITC-BSA was purchased from Sigma Aldrich post-tagging and purification. Stock solutions of bovine serum albumin, bovine serum albumin fluorescein isothiocyanate, 2-methylimidazole (HmIm), and zinc acetate (Zn) were made using Milli-Q water ($\rho > 18 M\Omega$ cm).

TEM

TEM samples were prepared by pipetting 10x diluted solutions onto TEM grids for ~5-10 min and were then blotted with Kimwipe paper. 400 Mesh Carbon grids were used and purchased

from TedPella. Images were obtained using a JOEL-2800 TEM with a Schottky field type field emission gun at 200 kV in convergent beam mode using a Gatan OneView Camera.

CryoTEM

CryoTEM samples were prepared using Quantifoil R2/2 Holey Carbon Films from Electron Microscopy Sciences or 400 Mesh Carbon grids from TedPella. Prior to sample application, glow discharge was applied to the grids for 70 seconds. Reaction solutions at various time points were centrifuged for ~2 seconds, and 3 μL of each sample was taken from the reaction solutions and underwent vitrification using an Automatic Plunge Freezer ME GP2 (Leica Microsystems). Vitrification was performed at ~95% humidity with blot times of 4 seconds, and samples were plunged into liquid propane. Samples were then analyzed using the JOEL-2100 TEM with a Schottky field type emission gun set to 200 kV. Images were obtained using Serial EM software or Gatan OneView Camera.

SEM

Samples were prepared by pipetting 10 uL of sample onto 1mm thick glass slides which were then coated with 5 nm Iridium (Quorum Q150T) to reduce charging. Samples were imaged with a Magellan 400 XRH system with secondary electron images taken at an accelerating voltage ranging from 2-3 keV.

PXRD

After removing all liquid from the top of centrifuged crystal precipitates and allowing samples to air dry, a Rigaku SmartLab X-ray diffractometer was used to obtain PXRD patterns at

40 kV and 44 mA while in Bragg-Brentano mode. Results were plotted with background subtraction using IGOR software.

In Situ XRD

Samples were initially mixed in glass vials and immediately transferred into 10 mm glass capillaries. Samples were scanned every 10 minutes for 8 hours using a Rigaku Smartlab. The instrument was set to 40 kV and 44 mA and measured in parallel beam/ parallel slit analyzer mode. Results were plotted with background subtraction using IGOR software.

Fluorescence Microscopy

Fluorescence imaging and microscopy were performed as described in previous manuscript.[18] Second harmonic of 960 nm femtosecond pulse radiation (480 nm, 76 MHz, 5 mW) has been coupled into Olympus FluoView 1000 laser scanning microscopy system based on an Olympus IX81 inverted microscope frame. Fluorescence has been collected using 60× NA = 1.41 oil-immersion objective lens (Olympus) in epi geometry. Transmitted light has been used for simple morphology mapping and correlation with TEM images. Imaging was performed at various fields of view with resolution 800 × 800 and 2048 × 2048 pixels with scanning speed 2 μs/pixel. All images were processed to be displayed in RGB (100,0,0) coordinates.

Mass Spectrometry

MALDI-TOF-MS measurements were performed using a Brûker Ultra Flex Extreme in linear positive mode. Samples were spotted in water and ran in saturated sinapic acid in a 50:50 water/acetonitrile with 0.1% TFA (trifluoracetic acid). Intact mass measurements were also

performed using a Xevo G2-XS Qtof after desalting thru Phenyl-Hexyl Column BEH guard column. The measurements were performed in positive mode from 400-4,000 da. The charge state series were deconvoluted using Waters' Masslynx MaxEnt1 algorithm with ranges of 50,000:80,000 g/mol. Baseline subtraction was then performed.

Circular Dichroism: Circular dichroism samples were diluted to 1 mg/ml using water and were analyzed between 200 nm and 240 nm in a 10 mm quartz cuvette. Five accumulations for each sample was performed.

Zeta Potential

Zeta potential measurements of samples were performed with a Malvern Zetasizer ZS Nano dynamic light scattering instrument. The instrument was set to automatic runs (ranging from 10-100), and triplicate measurements were averaged for each sample. Measurements were performed with samples in a disposable capillary cell from Malvern Panalytical.

3.6 References

(1) Cooper, G. M., *The Cell: A Molecular Approach. 2nd edition,* Sinauer Associates*,* **2000**.
(2) Lian, X.; Fang, Y.; Joseph, E.; Wang, Q.; Li, J.; Banerjee, S.; Lollar, C.; Wang, X.; Zhou, H.-C. Enzyme–MOF (Metal–Organic Framework) Composites. *Chem. Soc. Rev.* **2017**, *46* (11), 3386–3401. https://doi.org/10.1039/C7CS00058H.
(3) Franssen, M. C. R.; Steunenberg, P.; Scott, E. L.; Zuilhof, H.; Sanders, J. P. M. Immobilised Enzymes in Biorenewables Production. *Chem. Soc. Rev.* **2013**, *42* (15), 6491–6533. https://doi.org/10.1039/C3CS00004D.
(4) Sheldon, R. A. Cross-Linked Enzyme Aggregates (CLEA®s): Stable and Recyclable Biocatalysts. *Biochem Soc Trans* **2007**, *35* (6), 1583–1587. https://doi.org/10.1042/BST0351583.
(5) Wang, X.; Lan, P. C.; Ma, S. Metal–Organic Frameworks for Enzyme Immobilization: Beyond Host Matrix Materials. *ACS Cent. Sci.* **2020**. https://doi.org/10.1021/acscentsci.0c00687.
(6) Liang, K.; Ricco, R.; Doherty, C. M.; Styles, M. J.; Bell, S.; Kirby, N.; Mudie, S.; Haylock, D.; Hill, A. J.; Doonan, C. J.; Falcaro, P. Biomimetic Mineralization of Metal-Organic Frameworks as Protective Coatings for Biomacromolecules. *Nature Communications* **2015**, *6* (1), 7240. https://doi.org/10.1038/ncomms8240.

(7) Zheng, H.; Zhang, Y.; Liu, L.; Wan, W.; Guo, P.; Nyström, A. M.; Zou, X. One-Pot Synthesis of Metal–Organic Frameworks with Encapsulated Target Molecules and Their Applications for Controlled Drug Delivery. *J. Am. Chem. Soc.* **2016**, *138* (3), 962–968. https://doi.org/10.1021/jacs.5b11720.
(8) Xia, H.; Li, N.; Zhong, X.; Jiang, Y. Metal-Organic Frameworks: A Potential Platform for Enzyme Immobilization and Related Applications. *Front Bioeng Biotechnol* **2020**, *8*. https://doi.org/10.3389/fbioe.2020.00695.
(9) Zhuang, J.; Kuo, C.-H.; Chou, L.-Y.; Liu, D.-Y.; Weerapana, E.; Tsung, C.-K. Optimized Metal-Organic-Framework Nanospheres for Drug Delivery: Evaluation of Small-Molecule Encapsulation. *ACS Nano* **2014**, *8* (3), 2812–2819. https://doi.org/10.1021/nn406590q.
(10) An, H.; Li, M.; Gao, J.; Zhang, Z.; Ma, S.; Chen, Y. Incorporation of Biomolecules in Metal-Organic Frameworks for Advanced Applications. *Coordination Chemistry Reviews* **2019**, *384*, 90–106. https://doi.org/10.1016/j.ccr.2019.01.001.
(11) Zhuang, J.; Young, A. P.; Tsung, C.-K. Integration of Biomolecules with Metal–Organic Frameworks. *Small* **2017**, *13* (32), 1700880. https://doi.org/10.1002/smll.201700880.
(12) Riccò, R.; Liang, W.; Li, S.; Gassensmith, J. J.; Caruso, F.; Doonan, C.; Falcaro, P. Metal–Organic Frameworks for Cell and Virus Biology: A Perspective. *ACS Nano* **2018**, *12* (1), 13–23. https://doi.org/10.1021/acsnano.7b08056.
(13) Liu, W.-L.; Yang, N.-S.; Chen, Y.-T.; Lirio, S.; Wu, C.-Y.; Lin, C.-H.; Huang, H.-Y. Lipase-Supported Metal–Organic Framework Bioreactor Catalyzes Warfarin Synthesis. *Chemistry – A European Journal* **2015**, *21* (1), 115–119. https://doi.org/10.1002/chem.201405252.
(14) Pisklak, T. J.; Macías, M.; Coutinho, D. H.; Huang, R. S.; Balkus, K. J. Hybrid Materials for Immobilization of MP-11 Catalyst. *Top Catal* **2006**, *38* (4), 269–278. https://doi.org/10.1007/s11244-006-0025-6.
(15) Jung, S.; Kim, Y.; Kim, S.-J.; Kwon, T.-H.; Huh, S.; Park, S. Bio-Functionalization of Metal–Organic Frameworks by Covalent Protein Conjugation. *Chem. Commun.* **2011**, *47* (10), 2904–2906. https://doi.org/10.1039/C0CC03288C.
(16) Shih, Y.-H.; Lo, S.-H.; Yang, N.-S.; Singco, B.; Cheng, Y.-J.; Wu, C.-Y.; Chang, I.-H.; Huang, H.-Y.; Lin, C.-H. Trypsin-Immobilized Metal–Organic Framework as a Biocatalyst In Proteomics Analysis. *ChemPlusChem* **2012**, *77* (11), 982–986. https://doi.org/10.1002/cplu.201200186.
(17) Wu, X.; Ge, J.; Yang, C.; Hou, M.; Liu, Z. Facile Synthesis of Multiple Enzyme-Containing Metal–Organic Frameworks in a Biomolecule-Friendly Environment. *Chem. Commun.* **2015**, *51* (69), 13408–13411. https://doi.org/10.1039/C5CC05136C.
(18) Maddigan, N. K.; Tarzia, A.; Huang, D. M.; Sumby, C. J.; Bell, S. G.; Falcaro, P.; Doonan, C. J. Protein Surface Functionalisation as a General Strategy for Facilitating Biomimetic Mineralisation of ZIF-8. *Chem. Sci.* **2018**, *9* (18), 4217–4223. https://doi.org/10.1039/C8SC00825F.
(19) Li, P.; Moon, S.-Y.; Guelta, M. A.; Lin, L.; Gómez-Gualdrón, D. A.; Snurr, R. Q.; Harvey, S. P.; Hupp, J. T.; Farha, O. K. Nanosizing a Metal–Organic Framework Enzyme Carrier for Accelerating Nerve Agent Hydrolysis. *ACS Nano* **2016**, *10* (10), 9174–9182. https://doi.org/10.1021/acsnano.6b04996.
(20) Tong, L.; Huang, S.; Shen, Y.; Liu, S.; Ma, X.; Zhu, F.; Chen, G.; Ouyang, G. Atomically Unveiling the Structure-Activity Relationship of Biomacromolecule-Metal-Organic

Frameworks Symbiotic Crystal. *Nat Commun* **2022**, *13* (1), 951. https://doi.org/10.1038/s41467-022-28615-y.
(21) Ogata, A. F.; Rakowski, A. M.; Carpenter, B. P.; Fishman, D. A.; Merham, J. G.; Hurst, P. J.; Patterson, J. P. Direct Observation of Amorphous Precursor Phases in the Nucleation of Protein–Metal–Organic Frameworks. *J. Am. Chem. Soc.* **2020**, *142* (3), 1433–1442. https://doi.org/10.1021/jacs.9b11371.
(22) Carraro, F.; Velásquez-Hernández, M. de J.; Astria, E.; Liang, W.; Twight, L.; Parise, C.; Ge, M.; Huang, Z.; Ricco, R.; Zou, X.; Villanova, L.; Kappe, C. O.; Doonan, C.; Falcaro, P. Phase Dependent Encapsulation and Release Profile of ZIF-Based Biocomposites. *Chem. Sci.* **2020**, *11* (13), 3397–3404. https://doi.org/10.1039/C9SC05433B.
(23) Liang, W.; Ricco, R.; Maddigan, N. K.; Dickinson, R. P.; Xu, H.; Li, Q.; Sumby, C. J.; Bell, S. G.; Falcaro, P.; Doonan, C. J. Control of Structure Topology and Spatial Distribution of Biomacromolecules in Protein@ZIF-8 Biocomposites. *Chem. Mater.* **2018**, *30* (3), 1069–1077. https://doi.org/10.1021/acs.chemmater.7b04977.
(24) Liang, J.; Mazur, F.; Tang, C.; Ning, X.; Chandrawati, R.; Liang, K. Peptide-Induced Super-Assembly of Biocatalytic Metal–Organic Frameworks for Programmed Enzyme Cascades. *Chem. Sci.* **2019**, *10* (34), 7852–7858. https://doi.org/10.1039/C9SC02021G.
(25) Phipps, J.; Chen, H.; Donovan, C.; Dominguez, D.; Morgan, S.; Weidman, B.; Fan, C.; Beyzavi, H. Catalytic Activity, Stability, and Loading Trends of Alcohol Dehydrogenase Enzyme Encapsulated in a Metal–Organic Framework. *ACS Appl. Mater. Interfaces* **2020**, *12* (23), 26084–26094. https://doi.org/10.1021/acsami.0c06964.
(26) Carter, D. C.; Ho, J. X. Structure of Serum Albumin. In *Advances in Protein Chemistry*; Anfinsen, C. B., Edsall, J. T., Richards, F. M., Eisenberg, D. S., Eds.; Lipoproteins, Apolipoproteins, and Lipases; Academic Press, 1994; Vol. 45, pp 153–203. https://doi.org/10.1016/S0065-3233(08)60640-3.
(27) Chen, G.; Kou, X.; Huang, S.; Tong, L.; Shen, Y.; Zhu, W.; Zhu, F.; Ouyang, G. Modulating the Biofunctionality of Metal–Organic-Framework-Encapsulated Enzymes through Controllable Embedding Patterns. *Angewandte Chemie International Edition* **2020**, *59* (7), 2867–2874. https://doi.org/10.1002/anie.201913231.
(28) Greenfield, N. J. Using Circular Dichroism Collected as a Function of Temperature to Determine the Thermodynamics of Protein Unfolding and Binding Interactions. *Nat Protoc* **2006**, *1* (6), 2527–2535. https://doi.org/10.1038/nprot.2006.204.
(29) Vivian, J. T.; Callis, P. R. Mechanisms of Tryptophan Fluorescence Shifts in Proteins. *Biophys J* **2001**, *80* (5), 2093–2109. https://doi.org/10.1016/S0006-3495(01)76183-8.
(30) Kumar, D. 2.54 - Protein Refolding/Renaturation. In *Comprehensive Biotechnology (Second Edition)*; Moo-Young, M., Ed.; Academic Press: Burlington, 2011; pp 765–784. https://doi.org/10.1016/B978-0-08-088504-9.00136-7.
(31) Yin, L.; Wang, W.; Wang, S.; Zhang, F.; Zhang, S.; Tao, N. How Does Fluorescent Labeling Affect the Binding Kinetics of Proteins with Intact Cells? *Biosensors and Bioelectronics* **2015**, *66*, 412–416. https://doi.org/10.1016/j.bios.2014.11.036.
(32) Bingaman, S.; Huxley, V. H.; Rumbaut, R. E. Fluorescent Dyes Modify Properties of Proteins Used in Microvascular Research. *Microcirculation* **2003**, *10* (2), 221–231. https://doi.org/10.1038/sj.mn.7800186.
(33) Hernandez, K.; Fernandez-Lafuente, R. Control of Protein Immobilization: Coupling Immobilization and Site-Directed Mutagenesis to Improve Biocatalyst or Biosensor

Performance. *Enzyme and Microbial Technology* **2011**, *48* (2), 107–122. https://doi.org/10.1016/j.enzmictec.2010.10.003.
(34) Yoreo, J. J. D.; Gilbert, P. U. P. A.; Sommerdijk, N. A. J. M.; Penn, R. L.; Whitelam, S.; Joester, D.; Zhang, H.; Rimer, J. D.; Navrotsky, A.; Banfield, J. F.; Wallace, A. F.; Michel, F. M.; Meldrum, F. C.; Cölfen, H.; Dove, P. M. Crystallization by Particle Attachment in Synthetic, Biogenic, and Geologic Environments. *Science* **2015**, *349* (6247). https://doi.org/10.1126/science.aaa6760.
(35) Katsenis, A. D.; Puškarić, A.; Štrukil, V.; Mottillo, C.; Julien, P. A.; Užarević, K.; Pham, M.-H.; Do, T.-O.; Kimber, S. A. J.; Lazić, P.; Magdysyuk, O.; Dinnebier, R. E.; Halasz, I.; Friščić, T. In Situ X-Ray Diffraction Monitoring of a Mechanochemical Reaction Reveals a Unique Topology Metal-Organic Framework. *Nature Communications* **2015**, *6* (1), 6662. https://doi.org/10.1038/ncomms7662.
(36) Jackson, M.; Mantsch, H. H. The Use and Misuse of FTIR Spectroscopy in the Determination of Protein Structure. *Critical Reviews in Biochemistry and Molecular Biology* **1995**, *30* (2), 95–120. https://doi.org/10.3109/10409239509085140.
(37) Liang, W.; Xu, H.; Carraro, F.; Maddigan, N. K.; Li, Q.; Bell, S. G.; Huang, D. M.; Tarzia, A.; Solomon, M. B.; Amenitsch, H.; Vaccari, L.; Sumby, C. J.; Falcaro, P.; Doonan, C. J. Enhanced Activity of Enzymes Encapsulated in Hydrophilic Metal–Organic Frameworks. *J. Am. Chem. Soc.* **2019**, *141* (6), 2348–2355. https://doi.org/10.1021/jacs.8b10302.
(38) Liang, K.; Ricco, R.; M. Doherty, C.; J. Styles, M.; Falcaro, P. Amino Acids as Biomimetic Crystallization Agents for the Synthesis of ZIF-8 Particles. *CrystEngComm* **2016**, *18* (23), 4264–4267. https://doi.org/10.1039/C5CE02549D.
(39) March, D.; Bianco, V.; Franzese, G. Protein Unfolding and Aggregation near a Hydrophobic Interface. *Polymers (Basel)* **2021**, *13* (1), 156. https://doi.org/10.3390/polym13010156.
(40) Jing, P. P.; Li, Y. X.; Su, Y. H.; Liang, W. L.; Leng, Y. X. The Role of Metal Ions in the Behavior of Bovine Serum Albumin Molecules under Physiological Environment. *Spectrochimica Acta Part A: Molecular and Biomolecular Spectroscopy* **2022**, *267*, 120604. https://doi.org/10.1016/j.saa.2021.120604.

Chapter 4.

A Guide to Achieving High Performance Protein@Metal-Organic Frameworks

This chapter is in preparation for submission to a peer-review journal

4.1 Introduction

Enzymes are highly efficient and selective biological catalysts that hold immense potential in various industries, including drug delivery,[1,2] bioremediation,[3] and CO_2 reduction.[4] However, the widespread application of these biomolecules is limited due to susceptibility to denaturation and inability to withstand harsh industrial conditions. Metal-organic frameworks (MOFs), consisting of metal nodes and organic linkers, offer a promising solution by protecting and immobilizing enzymes in their active conformations.[5–7] Unlike other protein immobilization methods, MOFs provide a wide range of metal and ligand building units, allowing customization of crystal size, structure, and porosity, enabling optimization for different enzymes and applications.[8] MOFs enable one-pot integration of enzymes in aqueous synthetic conditions that favor protein stability and retained activity in the composite.[6,7] While little is known related to the enzyme environment and its conformation during MOF formation, other studies have shown that factors such as the tertiary structure, location, and orientation of the enzyme within the crystal play a key role in whether an enzyme remains active in an enzyme@MOF.[9–11] In previous research, we demonstrated that the folding of the enzyme, when synthesized in situ, affects the crystallization mechanism and kinetics, which determine final structural properties.[12] This study also found that the initial protein folding can be influenced by the MOF precursors, specifically zinc. Other studies have shown that the hydrophilicity of the ligand further plays a role in the folding, and thus activity, of the enzyme in the MOF.[13]

Furthermore, the structural factors of the crystal such as network topology,[14] morphology, defects,[15] and size[16] play an important role in designing high performance biocomposites.[17,18] Zeolitic Imidazolate Framework-8 (ZIF-8) has emerged as a widely studied MOF for enzyme encapsulation due to its precursor availability, ease of synthesis, and environmentally friendly

characteristics. ZIF-8 forms a sodalite (sod) topology consisting of zinc metal nodes connected by 2-methylimidazole (HmIm) ligands. Variations in its synthetic conditions, particularly the ligand to metal ratio (ligand:metal), have commonly been used to tune crystal formation and final crystal porosity to achieve high enzyme activity and encapsulation efficiency.[15] At low ratios of HmIm:Zn, enzymes with low isoelectric points (<7) drive nucleation through attraction of the positively charged metal ions to the negatively charged enzyme surface. [7,19,20] This mechanism has been coined *biomimetic mineralization* and yields high enzyme encapsulation. The biomimetic mineralization approach has yielded the formation of other ZIF-8 topologies and crystal structures–the combination of which is known as a polymorph–such as ZIF-C and ZIF-L,[14] but also the sodalite topology found in most synthesized ZIF-8 composites.[7] Often, mixtures of different ZIF-8 polymorphs can be obtained in the same sample through the biomimetic mineralization process, and the exact polymorphs obtained vary enzyme to enzyme, suggesting the biomolecule aids in polymorph determination. ZIF-8 polymorphism is important for enzyme activity, as amorphous MOFs have been found to have the highest enzyme activity in the case of glucose oxidase (GOx) ZIF-8 composites, which has been proposed to be due to interconnected mesopores found within the amorphous crystal structure.[17]

In this study, we demonstrate that the enzymatic interactions with both initial building blocks and the final MOF crystal are two main key components in designing a successful biocomposite system. More specifically, the enzyme interactions with MOF precursors, particularly upon formation of prenucleation clusters consisting of enzymes and MOF precursors, are shown to influence the folding, encapsulation efficiency, and activity of the enzymes GOx and catalase (CAT) within the ZIF-8 system. To exhibit enzyme activity, we show that building units must form with minimal enzyme denaturation. If this requirement is met, the physical properties

of the crystal must still be optimized for high activity, as crystallinity and structure influence the diffusion and accessibility of the substrate to the immobilized enzyme. To study the formation process of active biocomposites, we use time-resolved cryogenic-transmission electron microscopy (cryoTEM) to elucidate two distinct mechanisms resulting in either highly or poorly active enzyme@ZIF-8 biocomposites.

4.2 Results

Enzyme@MOF synthesis and structural characterization

Glucose oxidase and catalase were each encapsulated into ZIF-8 by varying the HmIm: Zn ratio to achieve two different mechanistic pathways: biomimetic mineralization and solid-state transformation.[19] To synthesize the biocomposites, separate stock solutions of the enzymes (5 mg/ml, 0.75 mL), 2-methylimidazole (HmIm) (320 mM and 2800 mM, 0.75 mL), and zinc acetate (40 mM, 1.50 mL) were prepared in nanopure water. The different concentrations of HmIm were combined with each of the enzymes and zinc acetate solutions to produce systems with ligand:metal ratios of 4:1 (biomineralization approach) and 35:1 (solid-state transformation approach) with final enzyme concentrations of 1.25 mg/ml. After solutions were combined and aged for 24 hours without mixing, the samples were centrifuged and washed 3x with either water or methanol. Fourier transform-infrared spectroscopy (FTIR) confirmed the encapsulation of each enzyme for all CAT and GOx biocomposites through the presence of the amide carbonyl (amide I) stretch at 1,660 cm^{-1} (Figure C1).[7]

At 4:1 GOx@ZIF-8 synthesis conditions with water washes, crystals have an encapsulation efficiency (EE%) of ~100% (Figure C22). Powder X-Ray Diffraction (P-XRD) verifies the product to be a heterogeneous mixture of both an amorphous phase, which can be observed in the broad peak around 14˚, and crystalline ZIF-CO_3-1 (ZIF-C). ZIF-C is a ZIF-8 polymorph which

incorporates CO_2 into its crystal structure as carbonate ion.[14,21] Dry state TEM shows small, ~20 nm, spherical particles along with sheets for 4:1 GOx@ZIF-8 (Figure 4.1b). At 4:1 GOx@ZIF-8 synthesis conditions with methanol washes, P-XRD verifies phase transformation of the ZIF-C crystals to ZIF-8 (sod) with no obvious amorphous phase present in the pattern. Dry state TEM images indicate multiple phases in the final product, as rhombic dodecahedron morphology and amorphous spherical particles are present (Figure 4.1b). We believe that this phase transformation occurs as a result of methanol being a stronger coordinating solvent and displacing the carbonate ligands in ZIF-C.[21,22] As the carbonate ligands are displaced, the coordination environment around the metal nodes changes, causing the structural rearrangement to sodalite topology with very little coordination defects. At 35:1 GOx@ZIF-8 synthesis conditions, crystals have a low EE% of 30%. P-XRD verifies no amorphous phase present and only sodalite (sod) crystal structure with coordination defects; this is seen in the lower relative intensity of the first peak (visible around 7˚) compared to the higher angle peaks. This contrasts with pure sod, where the first peak is significantly more intense than all subsequent peaks. (Figure 4.1a). Dry-state TEM images show biocomposites with rhombic dodecahedron morphology, which is characteristic of sod, while also indicating the presence of both defects and polycrystallinity (Figure 4.1d, Figure C8),

At 4:1 CAT@ZIF-8 conditions with water washes, crystals have an EE% of 100%. P-XRD verifies the product to be ZIF-C with a slight amorphous peak present. Dry-state TEM images show a continuous film for CAT@ZIF-8 along with stacked sheets found throughout the film (Figure 4.1e). At 4:1 CAT@ZIF-8 with methanol washes, P-XRD verifies phase transformation of ZIF-C crystals to ZIF-8 (sod) with no obvious amorphous phase present in the pattern. Dry-state TEM shows multiple phases with concentrated regions of amorphous particles surrounding crystals with rhombic dodecahedron morphology. (Figure 4.1f). At 35:1 CAT@ZIF-8, crystals

have an EE% of 100%. P-XRD confirms no amorphous phase present and only sodalite (sod) crystal structure. Dry-state TEM images show biocomposites with rhombic dodecahedron morphology, and confirm the presence of coordination defects (Figure 4.1g).

In summary, both CAT and GOx drive similar final crystal structures when varying the HmIm:Zn ratios. Both enzymes have low isoelectric points (<7); thus, the ability for each enzyme to drive the formation of a kinetic product when below the normal supersaturation conditions for ZIF-8 is expected. However, each enzyme, at 4:1 conditions with water washes, drives the formation of kinetic products with different morphologies. Additionally, only CAT consistently becomes encapsulated into ZIF-8 at any HmIm:Zn ratio whereas the EE% for GOx decreases with increasing HmIm:Zn.

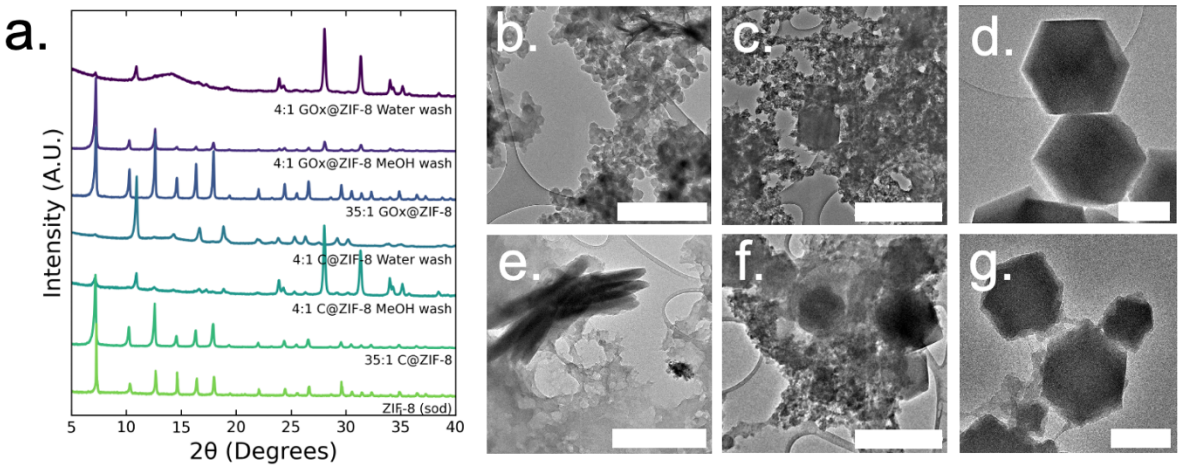

Figure 4.1: (a.) P-XRD patterns of CAT@MOFs and GOx@MOFs at 4:1 HmIm:Zn ratios with either water or methanol washes and at 35:1 HmIm:Zn. Dry-state TEM images of (b.) 4:1 GOx@ZIF-8 with 3x water washes, (c) 4:1 GOx@ZIF-8 with 3x methanol washes, (d.) 35:1 GOx@ZIF-8, (e.) 4:1 CAT@ZIF-8 with 3x water only washes, (f) 4:1 CAT@ZIF-8 with 3x methanol washes, (g.) 35:1 CAT@ZIF-8. Scale bars are 500 nm.

Enzyme activity in MOFs

Enzymatic activity assays were performed on GOx@ZIF-8 systems. The 4:1 GOx@ZIF-8 was observed to have a slightly lower activity compared to the free enzyme (Figure 3.2a), and the activity of GOx decreased even further when synthesized at 35:1 synthetic conditions. These results are supported by literature, which have found either amorphous MOFs or MOFs with large defects to have greater activity than highly crystalline sod crystals.[15,17] To investigate how phase transformation affects activity, activity measurements were then performed on the 4:1 GOx@ZIF-8 with methanol washes; however, no activity was observed. Enzymatic activity assays were then performed on CAT@ZIF-8 systems. No enzymatic activity could be observed in any of the experimented synthetic conditions for CAT@ZIF-8 (Figure 3.2b, Figure C4).

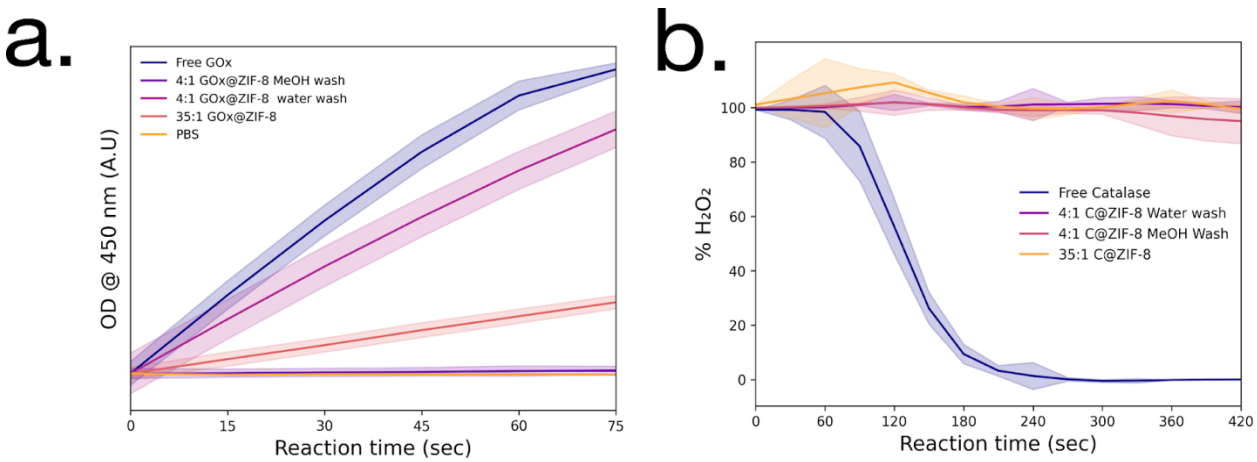

Figure 4.2: Enzyme activity assays of (a.) GOx@ZIF-8 and (b.) Catalase@ZIF-8 at a variety of synthetic conditions. Standard deviations are shown as highlighted sections.

Enzyme folding and activity relationship

To gain insight into the lack of enzymatic activity in CAT@ZIF-8 systems, protein folding studies were undertaken. Characterization of the protein folding within MOF prenucleation clusters is challenging, as the species are transient and advanced spectroscopic techniques often require long scan times, which often surpass the lifespan of a given transient species, to achieve

sufficient resolution. Additionally, imidazole rings absorb light at 280 nm, at the same wavelength as proteins, making it impossible to utilize light absorption techniques like UV-Visible spectroscopy and Circular Dichroism (CD) to probe protein folding in the presence of HmIm. Here, using CD, we examine enzyme folding when enzymes are incubated with zinc, as previous studies have found that proteins can form stable complexes with each of the precursors.[19] When CD was performed on GOx/Zn solutions, a slight reduction on the alpha helical character was observed (Figure 4.3a). In contrast, when CD was performed on CAT/Zn solutions, a dramatic decrease in alpha helical character was observed, indicating general denaturation of the biomolecule (Figure 4.3b).

To support that stability of catalase was dependent on the specific metal cation and not the presence of any counterion, potassium acetate was employed as a control. Potassium is a common biological cation found in high concentrations in most living systems, unlike zinc which is usually found in small amounts; potassium is expected to facilitate little denaturation.[23] Furthermore, activity of catalase has been reported in a potassium based MOF system.[24] Indeed, the folding of catalase was examined when incubated with zinc acetate and potassium acetate via CD, and it was found that potassium acetate altered the secondary structure of catalase minimally compared to zinc acetate (Figure 4.3b). Based on these results, we propose that it is the metal cation itself, and not the counterion, that causes unfolding in prenucleation clusters.

While circular dichroism studies are insightful to determine transitions in specific enzymatic secondary structural elements, these structural changes do not necessarily correspond to changes in activity. To gain a better understanding of the effects of MOF precursors on catalase activity, enzymatic assays were performed with CAT incubated with HmIm or zinc acetate, with potassium acetate used as a control. CAT incubated with potassium acetate had the best activity,

followed by CAT incubated with HmIm, then finally zinc acetate (Figure 4.3c). While we note that these studies only involve clusters and not the whole MOF, our findings support previous studies which have shown that catalase exhibits excellent activity when confined in a potassium-based MOF.[24] Furthermore, the activity and folding of catalase with MAF-7 – which shares the zinc metal ion and sodalite topology of ZIF-8, but uses a more hydrophilic linker, 3-methyl-1H-1,2,4 triazole (HmTz) – precursors were also investigated. [13] MAF-7 was investigated specifically because it shares many features with ZIF-8, yet encapsulated catalase shows activity (Figure C9). While MAF-7 and ZIF-8 share zinc metal ions, in our synthesis, the metal salts used are different, with ZIF-8 being commonly made with zinc acetate and MAF-7 being commonly made with zinc nitrate. Activity assays confirmed catalase incubated with either salt to have similar activity (Figure 4.3c). Catalase was then incubated with either ligand, HmIm or HmTz, and the activity of catalase was also similar with each ligand.

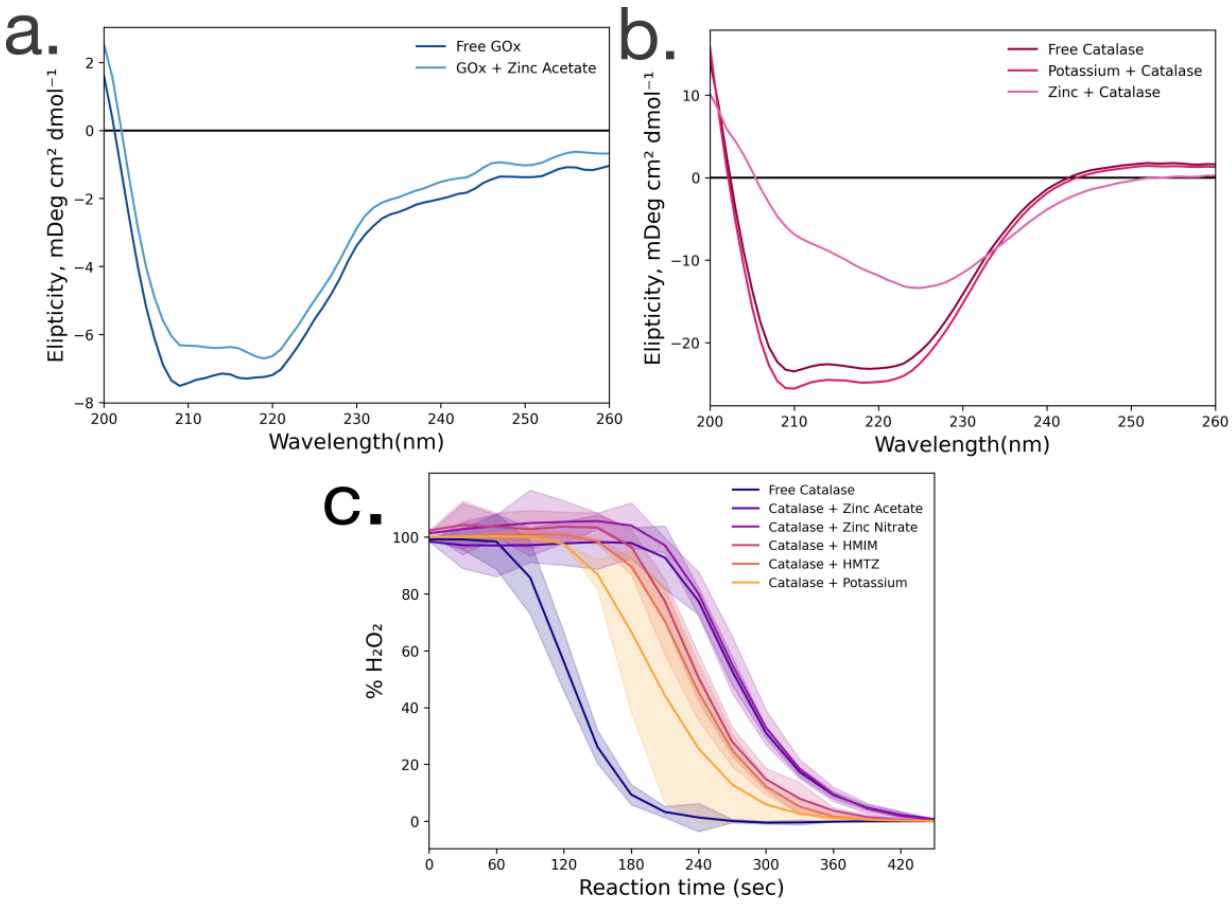

Figure 4.3: (a.) Circular Dichroism spectroscopy performed of glucose oxidase both alone and in the presence of zinc, (b.) and catalase alone, in the presence of zinc, and in the presence of potassium. (c.) Catalase activity in the presence of MOF precursors and various ions.

Mechanistic and structural relationships to enzyme activity

To gain a deeper understanding of the evolution of each enzyme@metal-organic framework (MOF) and to eventually customize their properties, time-resolved cryoTEM analysis was conducted on the GOx@ZIF-8 system during the initial hour of crystallization. The choice of GOx@ZIF-8 systems was motivated by the fact that each synthetic condition yields a distinct enzymatic outcome, unlike CAT@ZIF-8, which exhibits no activity at any synthetic condition. In situ time-resolved cryoTEM was utilized to image the crystal formation reaction and found small irregular amorphous aggregate networks at 1 minute (Figure 4.4a). The aggregates then evolved

into larger particulates by 30 minutes (Figure 4.4b). The particles appear to be stable at 1 hour (Figure 4.4c) and remain in the sample after 24 hours (Figure 4.4d,g). Through particle size analysis, the particles at 1 min averaged ~10 +/- 7 nm while the particles at 30 min, 1 hour, and 24 hours averaged ~20 +/- 10 nm (Figure 4.4d, Figure C6). While these particles are hypothesized to be amorphous based on the large amorphous backbone in the P-XRD, the ZIF-C region is believed to be the dense sheet-like region surrounded by the amorphous particles.[14]

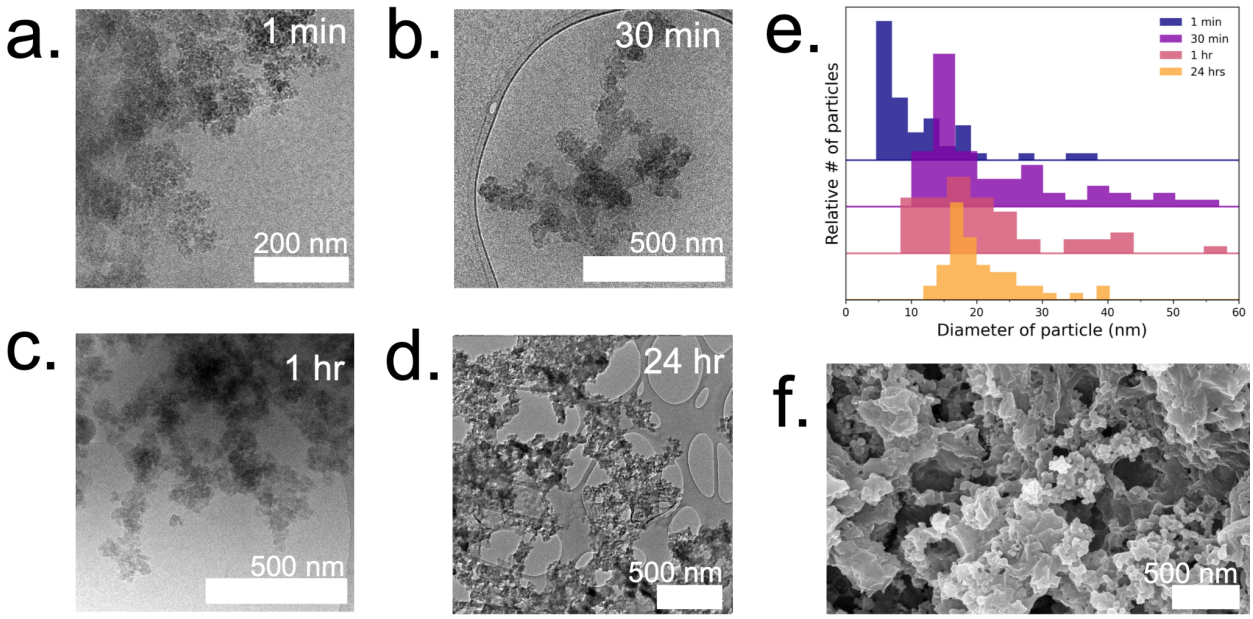

Figure 4.4: Time resolved cryoTEM of 4:1 GOx@ZIF-8 at a.) 1 min, b.) 30 min, and c.) 1 hour. d.) Dry-state TEM of 4:1 GOx@ZIF-8 after washes with water. (e.) Particle size analysis at 1 min (blue), 30 min (purple), 1 hour (pink), and 24 hours (orange). SEM of 4:1 GOx@ZIF-8 after washes with water.

To understand how the mechanistic and structural properties of the 35:1 GOx@ZIF-8 differentiated from the previous system, we performed similar in situ time-resolved cryoTEM studies. CryoTEM images reveal that at 1 minute, aggregates like the structure found in the 4:1 system form and are surrounded by individual particles that are 12 +/- 2 nm (Figure 4.5a). These

particles continue to grow and double in size (21 +/- 4 nm) by 10 min (Figure 4.5b). At 10 minutes, these particles are localized and surround a highly concentrated region. The amorphous phases continue to aggregate and condense to form dense phases surrounded by a cloud, which is hypothesized to serve as a rich reservoir of MOF precursors for the growing dense phase (Figure 4.5c). Outlines of irregular crystals can be observed within these clouds and closer inspection into the regions with high-resolution TEM reveals crystallinity as indicated by the lattice spacing (Figure 4.5e) and the Fast Fourier Transform (FFT) (Figure 4.5f). The crystal appears poorly crystalline at 30 min with lattices appearing in multiple directions along with gaps of lattices (Figure 4.5g). These gaps in the lattice are believed to be coordination defects containing enzymes. By 1-hour, well-defined rhombic dodecahedron crystals that are believed to be monocrystalline can be observed along with branched networks of aggregates dispersed throughout the sample (Figure 4.5d, Figure C7). As commonly observed with this system, amorphous phases contributing to the crystal growth undergo solid-state transformation to achieve a monocrystalline structure. While topological and structural characteristics of ZIF-8 (sod) are observed after 24 hours, indentions and pores can also be observed on the surface of the crystals (Figure 4.5h). Highly porous, irregular crystals can also be observed after 24 hours in addition to the lesser porous, regular crystals (Figure C8).

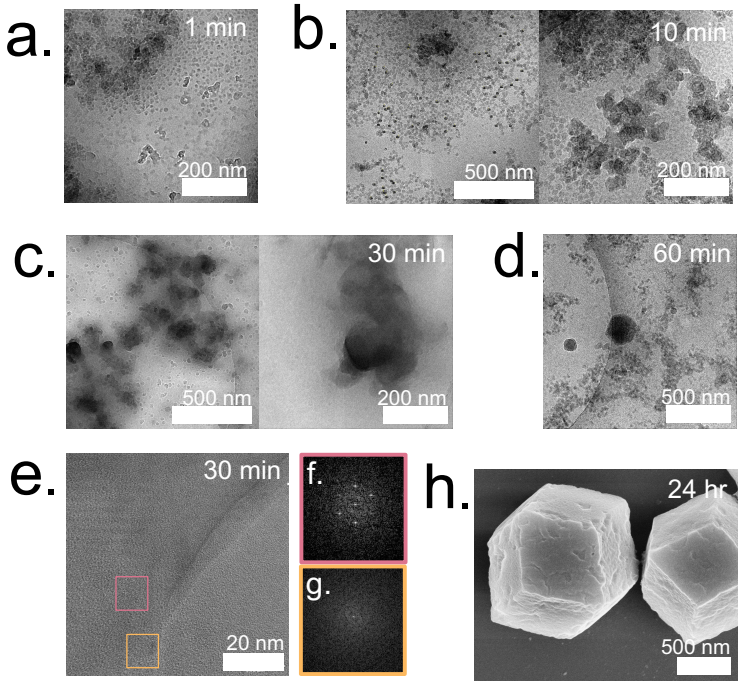

Figure 4.5: Time resolved cryoTEM of 35:1 GOx@ZIF-8 at a.) 1 min, b.) 10 min, c.) 30 min and d.) 1 hour. e.) Lattice resolution cryoTEM image of 35:1 and corresponding selective area fourier transform of f.) pink region and g.) orange region from image. h.) SEM of 35:1 GOx@ZIF-8 after water washes.

4.3 Discussion

Enzyme folding and activities studies emphasize the importance of the biological relationship between structure and function when designing a successful biocomposite. As GOx is resistant to unfolding by zinc, it can remain in an active conformation and exhibit activity in ZIF-8 (Figure 4.3a). CAT, however, is not resistant to unfolding by zinc, and therefore, no active CAT@ZIF-8 complex can be formed. Considering these results, we hypothesize that enzymes must be resistant to unfolding in prenucleation clusters to be active in MOF biocomposites.

One way to prevent metal-induced unfolding from occurring is by using a hydrophilic ligand. Previous studies and our own work have shown CAT to remain active in MAF-7 (Figure C9),[13] which we believe is attributed to the ability of the more hydrophilic ligand to stabilize an

active protein conformation. While CAT exhibited activity when incubated with both HmTz or HmIM, we hypothesize that HmTz, with an additional nitrogen group, will exhibit enhanced binding strength to the protein complex, while the two nitrogen groups in HmIm are more likely to bind to zinc. Supporting this hypothesis, the solution of HmTz and catalase becomes turbid rapidly, indicating large aggregates, whereas the solution of HmIm and catalase remains clear (Figure C5). Importantly, these CAT/HmTz complexes still retain activity, meaning that significant catalase denaturation is not occurring like in the presence of zinc (Figure 2c). We suggest that these strong protein/HmTz complexes stabilize catalase in a more active conformation and protect it against denaturation by zinc. Additionally, previous studies have demonstrated that the addition of hydrophilic groups to organic ligands can influence the restoration of the active protein conformation. These studies have shown that hydrophilic groups facilitate hydration effects within MOF pores, which reduce chelation interactions between the metal and the protein, thereby preventing unfolding.[26]

The understanding of how each individual MOF precursor affects enzyme folding and orientation in initial complexes is indeed crucial when initially designing a biocomposite. This knowledge helps in determining the appropriate enzyme/MOF precursor pairing for a specific application. By studying the interactions between the enzyme and different MOF precursors, researchers can identify compatible combinations that promote favorable enzyme folding and orientation within the MOF framework. However, in some cases, a desired enzyme/MOF precursor pairing may be inherently incompatible. In such situations, extra steps can be employed to induce an active enzyme conformation. One such method involves the use of ultrasound. Ultrasound waves can be applied to the enzyme prior to immobilization, effectively facilitating the attainment of the active enzyme conformation. This temporary conformational change induced by ultrasound

can be "locked" into place by subsequently adding MOF precursors.[27] Whatever the case, all techniques and enzyme@MOF synthesis processes must consider the effect of MOF precursors on the stability of the enzyme in prenucleation clusters. However, this is only the first step in ensuring enzyme@MOF activity.

In a recent study that encapsulated GOx in amorphous MOFs (aMOFs), the authors found the aMOFs facilitates high enzymatic activity based on the large defects and interconnected mesopores, allowing access to substrate by enzymes inside of the composite.[17] While defects are present in all aMOFs in this study, the particles are 5x smaller (~20 nm) than the aMOFs in the previously mentioned study (100 nm). As GOx has an average length of ~6 nm and the aMOFs are only ~20 nm, a large surface of the enzyme is likely to be exposed to the particle surface and accessible to substrate.[28] Furthermore, even if the enzyme is located within the interior of the aMOF, the substrate would have a lower diffusion barrier to overcome the short path to the enzyme.[16] Although it is not quite clear how ZIF-C forms through the in situ cryoTEM studies, it is believed that it is formed through aggregation and then rearrangement of the amorphous particles. While the inclusion of ZIF-C, a polymorph that has mostly been reported in solvothermal synthesis,[20] in biomimetically mineralized catalase and glucose oxidase ZIF-8 composites is a novel result, we hypothesize that the ZIF-C composites are not active, and activity comes from aMOFs present in the sample. Previous studies have shown that ZIF-C is not porous to N_2, making it unlikely that the composite is porous to glucose, the substrate of GOx, which is larger and more polar.[13] Thus, we believe the smaller size of the aMOFs, coupled with the disordered structure, to be major factors in driving the high activity for this system, and the ZIF-C samples to be much less relevant in conferring activity.

We believe such amorphous characteristics to also influence the activity of the 35:1 GOx@ZIF-8 biocomposite. Irregular crystals observed through TEM are hypothesized to have remained polycrystalline with coordination defects within them. As the size of glucose (~10 Å) is much larger than the 3.4 Å window typically observed in ZIF-8 (sod),[15,25,29] such defects are required for accessibility of enzymes to substrate. Furthermore, it is expected that while some enzymes will be located on the crystal surface either within or near the defects, that other enzymes will be located within the interior of the highly crystalline crystals and inaccessible to substrate. By increasing the enzyme loading concentration, we can expect to have an increase in amorphous character and defects in the crystal resulting in greater activity.[15,19] Furthermore, such a system is expected to have some enzymatic activity because of the defects, but not as high as the free enzyme or at 4:1 GOx@ZIF-8 biocomposites. This is supported by our enzymatic assay results, which show low but present activity for the 35:1 GOx@ZIF-8 sample (Figure 4.2a).

While outside of the scope of this study, another factor that could influence the activity of 35:1 GOx@ZIF-8 is the orientation of the enzymes located within or near the defects. A study by Pan et al used electron paramagnetic resonance spectroscopy to investigate the orientation of enzymes within MOF surfaces.[9] While these enzymes were not immobilized on to the MOF in a similar mechanism, the idea of being able to control the orientation and exposure of enzymes to substrates would allow enhanced selectivity of substrates of varying sizes.

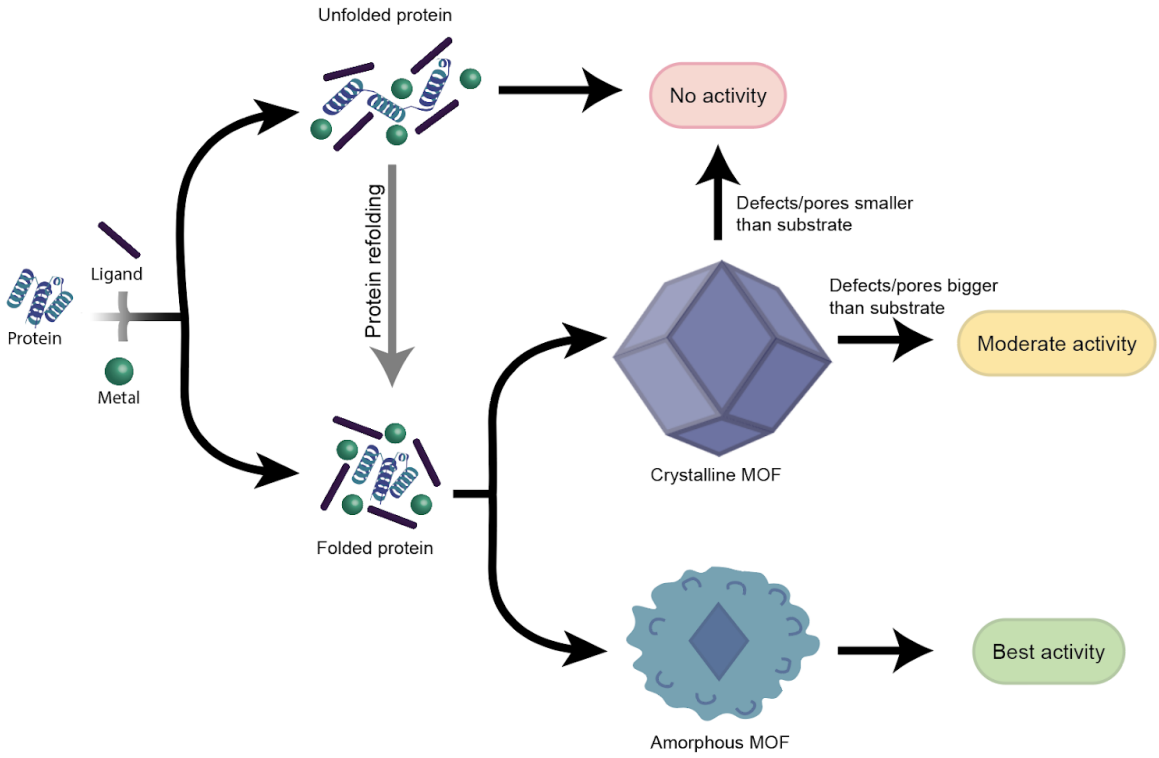

Figure 4.6: Proposed guide of the steps facilitating biocomposites with varying enzymatic activity. Initial protein folding in prenucleation clusters is the first step in determining whether a system will have enzymatic activity. From there, final physical properties such as extent of crystallinity and defects in the MOF will determine the catalytic performance of the system.

4.4 Conclusions

This work provides insight into a guide that should be followed when designing high performance biocomposites (Figure 4.6). While no one MOF is suitable to immobilize every enzyme, we have shown that studying the folding and activity of the enzymes in stable clusters with each MOF precursor could be a key initial screening towards pairing of metal ions and ligands to a given enzyme. Once precursors pass the initial screening with MOF precursors, the MOF design can then be redirected towards manipulating the crystal formation mechanism so that the final physical properties of the crystal align with the desired applications. We aim that providing

this step-by-step guide and relating our findings to other supported studies will lead to exponential growth in the design and use of high-performance protein-MOFs composites. However, to synthesize enzyme@MOFs, more should be known about the biomolecule and the effects of different precursors on enzyme folding. Future studies should take a more enzyme-oriented approach to enzyme@MOF synthesis, focusing on the real-time folding of biomolecules in prenucleation clusters and the structural changes that take place once an enzyme is encapsulated into a MOF.

4.5 Experimental

Materials

2-methylimidazole, zinc acetate dihydrate, tetrasodium ethylenediaminetetraacetic acid, and bovine liver catalase were purchased from Sigma Aldrich. Glucose oxidase from *A.Niger,* concentrated sulfuric acid, and potassium acetate were purchased from VWR International. Horseradish peroxidase, methanol, dimethyl sulfoxide, and 30% hydrogen peroxide were obtained from ThermoFisher. 3-Methyl-1H-1,2,4-triazole and 3,3',5,5' tetramethylbenzidine were purchased from TCI chemicals. Zinc nitrate dihydrate, xylenol orange, sodium phosphate dibasic anhydrous, phosphate buffered saline 10x, and ferrous ammonium sulfate were purchased from Strem Chemicals, Abcam, Chem-Impex International, Boston Bioproducts, and EMD Serono respectively.

GOx@ZIF-8 and Cat@ZIF-8 Synthesis

Individual solutions of 2-methylimidazole (HMIM) (2800 mM and 320 mM, 0.750 mL), zinc acetate (Zn) (40 mM), and enzyme (5 mg/ml, variable volume) were prepared in Milli-Q water (18 MΩ). For the high HmIm:Zn conditions (35:1), the more concentrated solution of HmIm was

used to achieve a final HmIm: Zn concentration ratio of 700:20 mM. For low HmIm: Zn conditions (4:1), the less concentrated solution of HmIm was used to achieve a final HmIm: Zn concentration ratio of 160:20 mM. The final enzyme concentration in each solution was 1.25 mg/ml. To synthesize the bio-MOF composite, 750 µL of HmIm solution was added to 750µL of enzyme solution, after which 1.5 mL of zinc solution was added in a glass vial, and the reaction was aged for 24 hours without stirring. After 24 hours, the precipitate was retrieved by centrifuging the reaction at 10,000 rpm. While the supernatant was separated and stored for EE% measurements, the precipitates were washed 3x with either water or methanol prior to further characterization.

Enzymatic activity of Catalase

The Ferrous Oxidation-Xylenol Orange (FOX) assay was used to measure the enzymatic activity of both Catalase and CAT@ZIF-8 systems. The FOX reagent was made using a solution of methanol (180 mL), Milli-Q water (20 mL), and Sulfuric acid 98% (278 µL). After stirring to ensure the solution was homogeneous, ferrous ammonium sulfate (19.6 mg) and then xylenol orange (15.2 mg) were added in their solid forms to the solution and allowed to stir for one hour to ensure complete dissolution. Solutions of Catalase and CAT@ZIF-8 systems were diluted to 0.01 mg/ml in 1x phosphate buffered saline (PBS), to a final volume of 2 mL. To initiate the reaction, 10 µL of 30% hydrogen peroxide was added to 2 mL of CAT or CAT@ZIF-8 system while stirring (320 rpm). Aliquots of the reaction mixture (50 uL) were taken, first at 15 seconds after the beginning of the reaction, then every 30 seconds, and added to 950 µL of FOX reagent. The absorbance of the samples were then measured at 560 nm using a Nanodrop absorption spectrophotometer, and plotted using the matplotlib, pandas, scipy, and numpy python libraries in an author-written python script.

Enzymatic activity of Glucose Oxidase

An enzymatic assay based on the oxidation of tetramethylbenzidine (TMB) by horseradish peroxidase (HRP) was employed to measure the activity of Glucose Oxidase (GOx). First, a phosphate-citrate buffer was prepared by dissolving sodium phosphate dibasic anhydrous (8.15 mg/mL) and citric acid monohydrate (9.60 mg/mL) into nanopure water under vigorous stirring to ensure complete dissolution. Then, a solution of TMB (0.1 mg/mL) was prepared in this buffer by first dissolving TMB (10 mg) into dimethyl sulfoxide (10 mL), stirring to fully dissolve the indicator. This solution was then diluted 10x in the previously synthesized phosphate-citrate buffer. A solution of HRP (5 mg/mL) was then prepared in this TMB buffer, and diluted 100x with more TMB buffer to a final concentration of 0.05 mg/mL. EE% measurements were used to dilute each bio-MOF composite to 2 mL of 0.015 mg/ml GOx in PBS, based on the assumption that all GOx not present in the supernatant was present in the final bio-MOF composite. 200 μL of this bio-MOF PBS solution were added to 400 μL of the HRP/TMB solution in a plastic cuvette, and then 200 μL of a 10 mM aqueous glucose solution were added to start the reaction. The reaction was measured at 650 nm every 15 seconds over 300 seconds in a Nanodrop UV-Visible spectrophotometer using the "kinetics" mode. Results were plotted using the pandas and matplotlib.pyplot python libraries in an author-written python script.

Circular dichroism

Solutions of enzymes and enzymes with MOF precursors were made at a concentration of 0.25 mg/mL, and placed into a 1 mL quartz cuvette. For the catalase measurements, three separate measurements were made on a Chirascan Circular Dichroism Spectrometer. Glucose Oxidase Circular Dichroism data was collected using a Jasco J-810 circular dichroism spectrometer. Results

were smoothed and plotted using the pandas, numpy, scipy and matplotlib python modules respectively in an author-written python script.

TEM

Dry-state TEM samples were prepared by diluting each sample 10X in nanopure water. Samples were then pipetted onto either 400 Mesh Carbon grids from TedPella or Quantifoil R2/2 Holey Carbon from Electron Microscopy Sciences. A Joel-2100 TEM equipped with a Schottyky type field emission gun was used to image samples. Serial EM software was used to obtain samples using a Gatan Oneview camera.

CryoTEM

CryoTEM samples were pipetted onto 400 Mesh Carbon grids from TedPella or Quantifoil R2/2 Holey Carbon from Electron Microscopy Sciences. Prior to sample application, the grids underwent glow discharge for 70 seconds to enhance grid hydrophilicity and spreading of sample. Time-resolved samples were taken at 1 minute, 30 minutes, and 1 hour were samples and centrifuged for 5 seconds where the supernatants were then vitrified using an Automatic Plunge Freezer ME GP2 (Leica Microsystems) at each timepoint. The plunger was set to 95% humidity in the sample chamber and blotted for 2.5 s prior to auto-plunging into liquid propane. A Joel-2100 TEM equipped with a Schottyky type field emission gun was used to image samples. Serial EM software was used to obtain samples using Gatan Oneview and Gatan K3 cameras.

SEM

Samples (10 uL) were pipetted onto 1 mm glass slides. Prior imaging, samples were coated with 5-10 nm Iridium (Quorum Q150T) to combat charging effects. A Magellan 400 XRH system was used to obtain secondary electrons images while operating at an accelerating voltage of 5 kV.

Intrinsic Tryptophan Fluorescence

Intrinsic Tryptophan Fluorescence was performed on the MOF washing supernatant–in a manner similar to earlier published works on protein-MOFs–to determine encapsulation efficiency (EE%).[10, 11] First, supernatants were diluted 10x in EDTA-PBS, which was prepared by making a 16.88 mg/mL solution of ethylenediaminetetraacetate tetrasodium salt (EDTA) in phosphate buffered saline (PBS). This diluted supernatant was measured using a Cary-60 UV-Visible Fluorimeter, exciting at 280 nm and measuring the fluorescence at 340 nm. The EE% was determined by referencing measured values to the slope of a previously prepared calibration curve (**SI plot**). To determine the red-shifting or blue-shifting of the tryptophan residues of the protein within the MOF, the MOFs were first dissolved in water, and diluted to a variable concentration which would not overload the fluorometer detector. A Cary-60 UV-Visible Fluorometer was used to excite the MOF composite at 280 nm, and the fluorescence values from 300-400 nm were measured, with the λ_{max} being used to establish either a red or blue shift.

Powder X-ray Diffraction

Samples were first dried in a vacuum oven with heating turned off to ensure proper dehydration of the bio-MOF composite. Depending on the specific sample being run, 3.9 mg of a Zirconium (IV) oxide standard was added to each sample before grinding. These samples were crushed into a fine powder using a mortar and pestle, then placed on a zero-background crystal attachment and diffracted using a Rigaku Ultima III X-ray diffractometer in Bragg-Brentano mode, measuring from 5-50 2θ at variable scan speeds. The data was plotted using the matplotlib, numpy, and pandas python libraries in an author-written python script.

4.6 References

(1) Lee, M.-R.; Baek, K.-H.; Jin, H. J.; Jung, Y.-G.; Shin, I. Targeted Enzyme-Responsive Drug Carriers: Studies on the Delivery of a Combination of Drugs. *Angewandte Chemie International Edition* **2004**, *43* (13), 1675–1678. https://doi.org/10.1002/anie.200353204.

(2) Cao, Z.; Li, W.; Liu, R.; Li, X.; Li, H.; Liu, L.; Chen, Y.; Lv, C.; Liu, Y. PH- and Enzyme-Triggered Drug Release as an Important Process in the Design of Anti-Tumor Drug Delivery Systems. *Biomedicine & Pharmacotherapy* **2019**, *118*, 109340. https://doi.org/10.1016/j.biopha.2019.109340.

(3) Karigar, C. S.; Rao, S. S. Role of Microbial Enzymes in the Bioremediation of Pollutants: A Review. *Enzyme Res* **2011**, *2011*, 805187. https://doi.org/10.4061/2011/805187.

(4) Chiranjeevi, P.; Bulut, M.; Breugelmans, T.; Patil, S. A.; Pant, D. Current Trends in Enzymatic Electrosynthesis for CO2 Reduction. *Current Opinion in Green and Sustainable Chemistry* **2019**, *16*, 65–70. https://doi.org/10.1016/j.cogsc.2019.02.007.

(5) Lawson, H. D.; Walton, S. P.; Chan, C. Metal–Organic Frameworks for Drug Delivery: A Design Perspective. *ACS Appl. Mater. Interfaces* **2021**, *13* (6), 7004–7020. https://doi.org/10.1021/acsami.1c01089.

(6) Zheng, H.; Zhang, Y.; Liu, L.; Wan, W.; Guo, P.; Nyström, A. M.; Zou, X. One-Pot Synthesis of Metal–Organic Frameworks with Encapsulated Target Molecules and Their Applications for Controlled Drug Delivery. *J. Am. Chem. Soc.* **2016**, *138* (3), 962–968. https://doi.org/10.1021/jacs.5b11720.

(7) Liang, K.; Ricco, R.; Doherty, C. M.; Styles, M. J.; Bell, S.; Kirby, N.; Mudie, S.; Haylock, D.; Hill, A. J.; Doonan, C. J.; Falcaro, P. Biomimetic Mineralization of Metal-Organic Frameworks as Protective Coatings for Biomacromolecules. *Nature Communications* **2015**, *6* (1), 7240. https://doi.org/10.1038/ncomms8240.

(8) Furukawa, H.; Cordova, K. E.; O'Keeffe, M.; Yaghi, O. M. The Chemistry and Applications of Metal-Organic Frameworks. *Science* **2013**, *341* (6149). https://doi.org/10.1126/science.1230444.

(9) Pan, Y.; Li, H.; Farmakes, J.; Xiao, F.; Chen, B.; Ma, S.; Yang, Z. How Do Enzymes Orient When Trapped on Metal–Organic Framework (MOF) Surfaces? *J. Am. Chem. Soc.* **2018**, *140* (47), 16032–16036. https://doi.org/10.1021/jacs.8b09257.

(10) Wang, X.; Lan, P. C.; Ma, S. Metal–Organic Frameworks for Enzyme Immobilization: Beyond Host Matrix Materials. *ACS Cent. Sci.* **2020**. https://doi.org/10.1021/acscentsci.0c00687.

(11) Fernando, D.; Mathesh, M.; Cai, J.; Yang, W. In Situ Immobilization of Multi-Enzymes for Enhanced Substrate Channeling of Enzyme Cascade Reactions: A Nanoarchitectonics Approach by Directed Metal–Organic Frameworks. *Langmuir* **2023**, *39* (22), 7979–7985. https://doi.org/10.1021/acs.langmuir.3c00879.

(12) Carpenter, B. P.; Talosig, A. R.; Mulvey, J. T.; Merham, J. G.; Esquivel, J.; Rose, B.; Ogata, A. F.; Fishman, D. A.; Patterson, J. P. Role of Molecular Modification and Protein Folding in the Nucleation and Growth of Protein–Metal–Organic Frameworks. *Chem. Mater.* **2022**, *34* (18), 8336–8344. https://doi.org/10.1021/acs.chemmater.2c01903.

(13) Liang, W.; Xu, H.; Carraro, F.; Maddigan, N. K.; Li, Q.; Bell, S. G.; Huang, D. M.; Tarzia, A.; Solomon, M. B.; Amenitsch, H.; Vaccari, L.; Sumby, C. J.; Falcaro, P.; Doonan, C. J. Enhanced Activity of Enzymes Encapsulated in Hydrophilic Metal–Organic Frameworks. *J. Am. Chem. Soc.* **2019**, *141* (6), 2348–2355. https://doi.org/10.1021/jacs.8b10302.

(14) Carraro, F.; Velásquez-Hernández, M. de J.; Astria, E.; Liang, W.; Twight, L.; Parise, C.; Ge, M.; Huang, Z.; Ricco, R.; Zou, X.; Villanova, L.; Kappe, C. O.; Doonan, C.; Falcaro, P. Phase

Dependent Encapsulation and Release Profile of ZIF-Based Biocomposites. *Chem. Sci.* **2020**, *11* (13), 3397–3404. https://doi.org/10.1039/C9SC05433B.
(15) Tong, L.; Huang, S.; Shen, Y.; Liu, S.; Ma, X.; Zhu, F.; Chen, G.; Ouyang, G. Atomically Unveiling the Structure-Activity Relationship of Biomacromolecule-Metal-Organic Frameworks Symbiotic Crystal. *Nat Commun* **2022**, *13* (1), 951. https://doi.org/10.1038/s41467-022-28615-y.
(16) Li, P.; Moon, S.-Y.; Guelta, M. A.; Lin, L.; Gómez-Gualdrón, D. A.; Snurr, R. Q.; Harvey, S. P.; Hupp, J. T.; Farha, O. K. Nanosizing a Metal–Organic Framework Enzyme Carrier for Accelerating Nerve Agent Hydrolysis. *ACS Nano* **2016**, *10* (10), 9174–9182. https://doi.org/10.1021/acsnano.6b04996.
(17) Wu, X.; Yue, H.; Zhang, Y.; Gao, X.; Li, X.; Wang, L.; Cao, Y.; Hou, M.; An, H.; Zhang, L.; Li, S.; Ma, J.; Lin, H.; Fu, Y.; Gu, H.; Lou, W.; Wei, W.; Zare, R. N.; Ge, J. Packaging and Delivering Enzymes by Amorphous Metal-Organic Frameworks. *Nat Commun* **2019**, *10* (1), 5165. https://doi.org/10.1038/s41467-019-13153-x.
(18) *ZIF-C as non-viral delivery system for CRISPR/Cas9 mediated hTERT knockdown in cancer cells | Materials Science | ChemRxiv | Cambridge Open Engage*. https://chemrxiv.org/engage/chemrxiv/article-details/6114a3d918911d63d0dec8c4 (accessed 2023-07-05).
(19) Ogata, A. F.; Rakowski, A. M.; Carpenter, B. P.; Fishman, D. A.; Merham, J. G.; Hurst, P. J.; Patterson, J. P. Direct Observation of Amorphous Precursor Phases in the Nucleation of Protein–Metal–Organic Frameworks. *J. Am. Chem. Soc.* **2020**, *142* (3), 1433–1442. https://doi.org/10.1021/jacs.9b11371.
(20) Maddigan, N. K.; Tarzia, A.; Huang, D. M.; Sumby, C. J.; Bell, S. G.; Falcaro, P.; Doonan, C. J. Protein Surface Functionalisation as a General Strategy for Facilitating Biomimetic Mineralisation of ZIF-8. *Chem. Sci.* **2018**, *9* (18), 4217–4223. https://doi.org/10.1039/C8SC00825F.
(21) Basnayake, S. A.; Su, J.; Zou, X.; Balkus, K. J. Carbonate-Based Zeolitic Imidazolate Framework for Highly Selective CO2 Capture. *Inorg Chem* **2015**, *54* (4), 1816–1821. https://doi.org/10.1021/ic5027174.
(22) Sumida, K.; Rogow, D. L.; Mason, J. A.; McDonald, T. M.; Bloch, E. D.; Herm, Z. R.; Bae, T.-H.; Long, J. R. Carbon Dioxide Capture in Metal–Organic Frameworks. *Chem. Rev.* **2012**, *112* (2), 724–781. https://doi.org/10.1021/cr2003272.
(23) Stillman, M. Biological Inorganic Chemistry. Structure and Reactivity. Edited by Ivano Bertini, Harry B. Gray, Edward I. Stiefel and Joan S. Valentine. *Angewandte Chemie International Edition* **2007**, *46* (46), 8741–8742. https://doi.org/10.1002/anie.200785504.
(24) Palma, G. D.; Geels, S.; Carpenter, B. P.; Talosig, R. A.; Chen, C.; Marangoni, F.; Patterson, J. P. Cyclodextrin Metal–Organic Framework-Based Protein Biocomposites. *Biomater. Sci.* **2022**, *10* (23), 6749–6754. https://doi.org/10.1039/D2BM01240E.
(25) Park, K. S.; Ni, Z.; Côté, A. P.; Choi, J. Y.; Huang, R.; Uribe-Romo, F. J.; Chae, H. K.; O'Keeffe, M.; Yaghi, O. M. Exceptional Chemical and Thermal Stability of Zeolitic Imidazolate Frameworks. *Proceedings of the National Academy of Sciences* **2006**, *103* (27), 10186–10191. https://doi.org/10.1073/pnas.0602439103.
(26) Zhang, H.; Lv, Y.; Tan, T.; van der Spoel, D. Atomistic Simulation of Protein Encapsulation in Metal–Organic Frameworks. *J. Phys. Chem. B* **2016**, *120* (3), 477–484. https://doi.org/10.1021/acs.jpcb.5b10437.
(27) Liang, J.; Bin Zulkifli, M. Y.; Yong, J.; Du, Z.; Ao, Z.; Rawal, A.; Scott, J. A.; Harmer, J. R.; Wang, J.; Liang, K. Locking the Ultrasound-Induced Active Conformation of Metalloenzymes in

Metal–Organic Frameworks. *J. Am. Chem. Soc.* **2022**, *144* (39), 17865–17875. https://doi.org/10.1021/jacs.2c06471.
(28) Libertino, S.; Aiello, V.; Scandurra, A.; Renis, M.; Sinatra, F. Immobilization of the Enzyme Glucose Oxidase on Both Bulk and Porous SiO2 Surfaces. *Sensors (Basel)* **2008**, *8* (9), 5637–5648. https://doi.org/10.3390/s8095637.
(29) Schwarz, T. M.; Dietrich, C. A.; Ott, J.; Weikum, E. M.; Lawitzki, R.; Solodenko, H.; Hadjixenophontos, E.; Gault, B.; Kästner, J.; Schmitz, G.; Stender, P. 3D Sub-Nanometer Analysis of Glucose in an Aqueous Solution by Cryo-Atom Probe Tomography. *Sci Rep* **2021**, *11* (1), 11607. https://doi.org/10.1038/s41598-021-90862-8.

Chapter 5.

Incorporation of Novel Proteins into Metal-Organic Frameworks

5.1 Introduction

Metal-organic frameworks (MOFs) have become a highly versatile class of materials with enhanced properties, making them a popular choice for a large scope of applications such as drug delivery and catalysis.[1–4] This versatility emerges as a result of the tunable chemical compositions and structural topologies, which further enables the integration of different guest molecules such as proteins.[5–7] Furthermore, MOFs can serve as a method for protein immobilization as the structural parameters can modify the protein loading efficiency, protection properties, and substrates selectivity.[6,8–10] Using the mechanistic and structural insight of protein@MOFs obtained from previous chapters in this thesis, two novel proteins, SARS-CoV-2 main protease (M^{pro}) and Nanoluciferase (Nanoluc), are integrated into a MOF, zeolitic imidazolate framework-8 (ZIF-8) systems for the first time.

During the severe acute respiratory syndrome coronavirus-2 (SARS-CoV-2) Pandemic,[11] the science community made extensive efforts in designing clinical drugs to alleviate the virus. One avenue is focusing on the inhibition of a protease key to the virus's life cycle and replication, M^{pro}. Through inhibition of M^{pro}, replication and symptoms of the virus could be minimized.[12] For such an approach to be successful, insight into the inhibition mechanisms of the protease with proposed drugs is required.[13] Encapsulation of M^{pro} into MOFs could enhance the stability and recyclability of a protease, enabling more efficient studies of the structure and inhibition mechanisms of the protease.

Additionally, Nanoluc is an engineered luciferase that reacts with a substrate to produce light.[14] Such an enzyme has high demands in the biomedical field as it has been engineered to exhibit even greater luminescence than the wild type, making it a desirable enzyme for applications in molecular imaging and cellular assays. While NanoLuc has greater stability than the wild type,

it still has limited shelf life and recyclability. Here, we immobilize NanoLuc into ZIF-8 as immobilization could potentially provide the protein enhanced stability and lead to next-generation imaging probes with longer lifetimes.

The incorporation of M^{pro} and NanoLuc into ZIF-8 is investigated with Fourier transform-infrared (FTIR) spectroscopy and fluorescence spectroscopy. Preliminary activity measurements of NanoLuc biocomposites were also performed. Additionally, the morphology and topology of the biocomposites were examined with transmission electron microscopy (TEM), scanning electron microscopy (SEM) and powder x-ray diffraction (PXRD). Such studies provide insight into how novel proteins affect the formation of ZIF-8 crystals and how to tailor the synthetic parameters to create optimized biocomposites.

5.2 Results and Discussion

Protein Incorporation and Activity Studies

M^{pro} biocomposites were synthesized through a combination separate stock solutions of protein (1 mg/ml), 2-methylimidazole (HmIm)(320 mM, 1400 mM, and 2800 mM), and zinc acetate (40 mM) in nanopure water. The stock solutions were combined to result in final composite systems with HmIm:Zn ratios of 2:1, 9:1, and 35:1. Biocomposite solutions were aged for 24 hours where they were then centrifuged at 10,000 rpm and washed 3x with nanopure water. Fourier transform-infrared spectroscopy (FTIR) was utilized to confirm the incorporation of protein using the C=O stretch at 1,660 cm^{-1} (Amide I)(Figure 5.1a). Additionally, peaks attributed to ZIF polymorphs can be observed in the spectra of all biocomposites at 1145, 1175, 1308, 1419, 1458, and 1580 cm^{-1}.[15] Intrinsic tryptophan fluorescence was performed on 2:1 and 9:1 M^{pro}@ZIF-8 and show a shift in $\boldsymbol{\lambda}_{max}$ from ~330 nm with M^{pro} to ~340 nm when encapsulated (Figure 5.1b). A red

shift, or increase in wavelength, indicates outward unfolding of the protein, indicating potential activity inhibition. Following these findings, difficulties with protease expression occurred preventing activity assays.

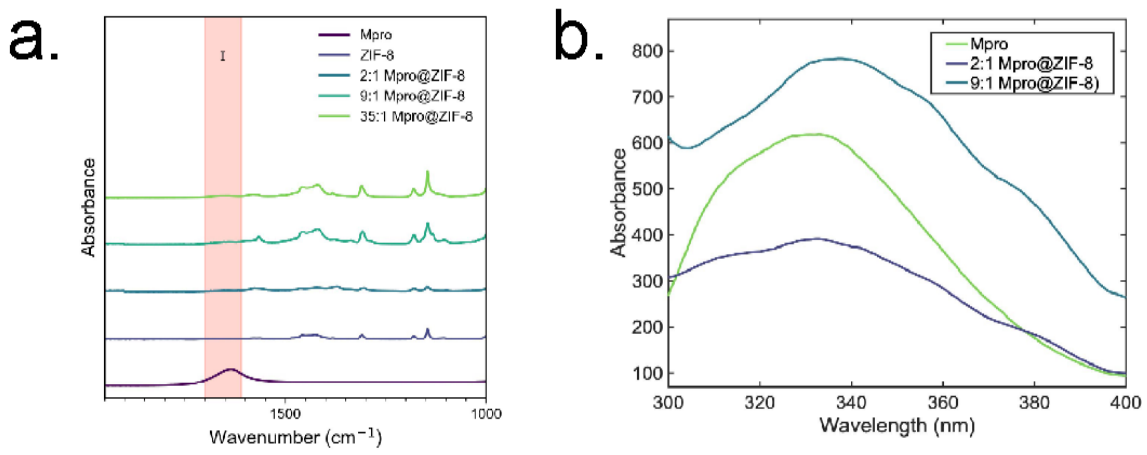

Figure 5.1: a.) FTIR spectra of M^{pro}@ZIF-8 biocomposites. b.) Intrinsic tryptophan fluorescence of M^{pro} and select M^{pro} composites.

NanoLuc biocomposites were synthesized through a combination of separate stock solutions of protein (48 ug/mL), 2-methylimidazole (HmIm)(320 mM, 1400 mM, and 2800 mM), and zinc acetate (40 mM) in nanopure water. The stock solutions were combined to result in final composite systems with HmIm:Zn ratios of 4:1, 17.5:1, and 35:1. Biocomposite solutions were aged for 24 hours where they were then centrifuged at 10,000 rpm and washed 3x with nanopure water. At 4:1, no precipitation was observed within 48 hours of aging. While ZIF-8 crystal formation is not favorable at 4:1 conditions without biomolecules, such a result is surprising as NanoLuc has an isoelectric point of 4.9, so it was expected to concentrate MOF precursors and enable crystal formation.[6,16,17] However, as only very low concentrations of protein are used during

the synthesis due to limited yield of protein during expression, we believe that higher concentrations of protein are required for NanoLuc to enable crystallization of ZIF-8 (sod).[18]

Fourier transform-infrared spectroscopy (FTIR) was utilized to confirm the incorporation of the protein in the remaining biocomposites using the C=O stretch at 1,660 cm^{-1} (Amide I)(Figure 5.2a). Additionally, peaks attributed to ZIF polymorphs can be observed in the spectra of all biocomposites at 1145, 1175, 1308, 1419, 1458, and 1580 cm^{-1}.[15] In preparation for activity assays, the encapsulation efficiency was determined for each MOF where it was found that 17.5:1 synthetic conditions facilitate an EE% of 100% whereas 35:1 synthetic conditions averaged an EE% of 60% (Figure 5.2b). Such a result is expected as biomolecules have shown to play a greater role in crystal formation at lower HmIm:Zn conditions resulting in greater EE%.[8,18,19] NanoLuc and the biocomposites were diluted to a normalized concentration where the substrate, furimazine, was added to initiate a reaction. While free NanoLuc exhibited activity, no signs of activity were observed for the biocomposites (Figure 5.2c). Further inspection on the total luminescence throughout the reaction revealed the biocomposites to have similar, but slightly higher, activity than the buffer background (Figure 5.2d).

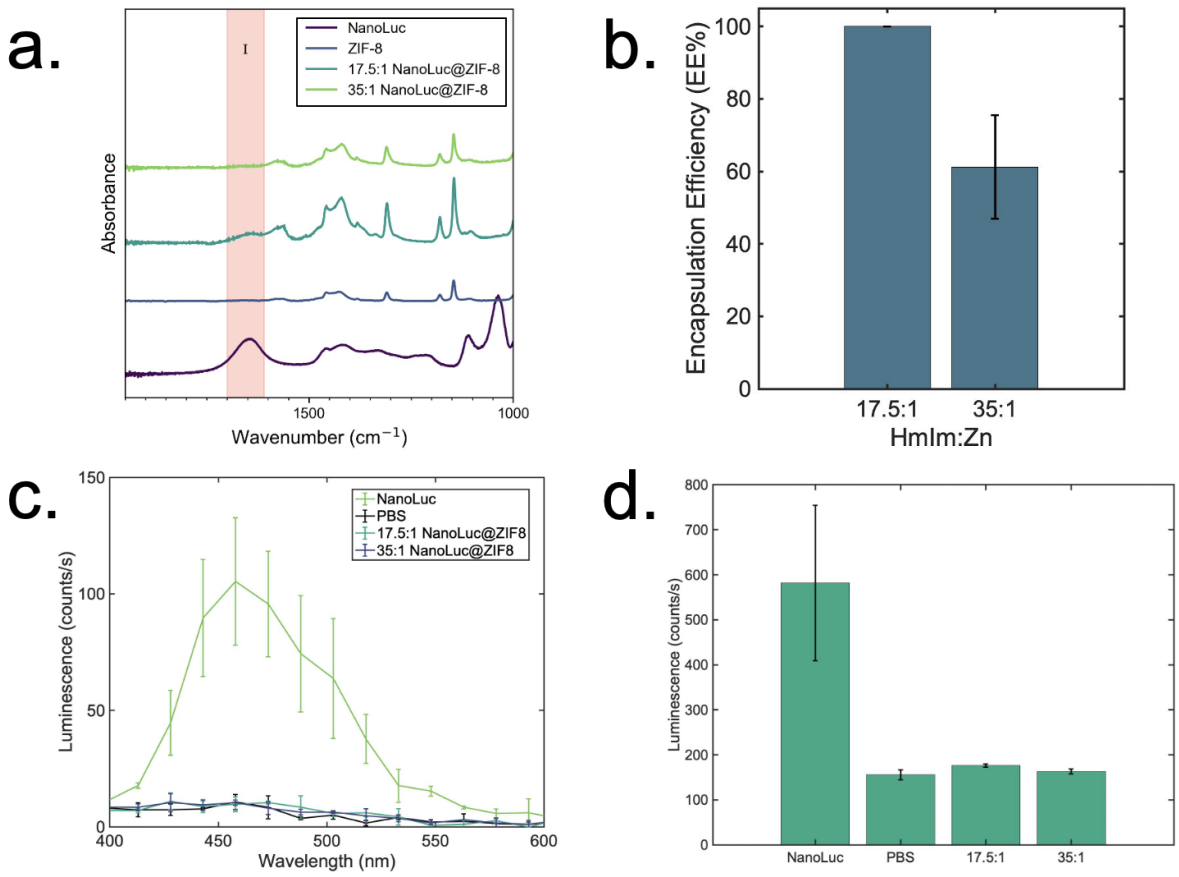

Figure 5.2: a.) FTIR spectra of NanoLuc@ZIF-8 composites. b.) Encapsulation efficiency of NanoLuc@ZIF-8 biocomposites. c.) Activity profiles of NanoLuc (green), PBS (black), 17.5:1 NanoLuc@ZIF-8 (turquoise), and 35:1 (violet). d) Total luminescence (counts/s) of NanoLuc, PBS, 17.5:1, and 35:1 NanoLuc@ZIF-8 from duration of activity measurements.

Morphological studies

M^{pro} was integrated into ZIF-8 biocomposites at HmIM:Zn ratios of 2:1, 9:1, and 35:1 to provide insight into the formation and final morphology when synthetic conditions are varied. Differences in the final size and shape of each biocomposite could be observed. At 2:1 synthetic conditions, spherical composites (> 500 nm) consisting of smaller aggregated particles (~10-20 nm) could be observed along with large polygons with some of the polygons appearing to consist of 2D layers (Figure 5.3a). At 9:1, well-defined, 2D structures are observed to be stacked in some regions and to be disordered in other regions (Figure 5.3b). These 2D structures aggregate to form

large, irregular 3D decussations (Figure D2b). Small particles (~10-20 nm) are also present throughout the structures with the largest concentration around the edges of the 2D structures. At 35:1, irregular structures are observed in addition to large flower-like structures consisting of 2D stacked sheets (Figure 5.3c, Figure D2c). Small particles (~10-20 nm) are dispersed throughout the sample. While such biocomposite structures with M^{pro} had not previously been observed at these synthetic conditions in the Patterson lab, a study by Chen et al reported crystals with similar decussation morphology as the 9:1 M^{pro}@ZIF-8 through addition of γ-poly-L-glutamic acid (PLGA) into a ZIF-8 system.[20] As PLGA is able to drive such architectures through modification of the surface charge of the biomolecule, it is hypothesized that components within the buffer of M^{pro}, including Tween-20, dithiothretol, and glycerol, are modifying the surface of M^{pro} similarly. To prove this theory, future experiments are needed where M^{pro} undergoes a buffer exchange in pure water to ensure the surface of M^{pro} is not modified.

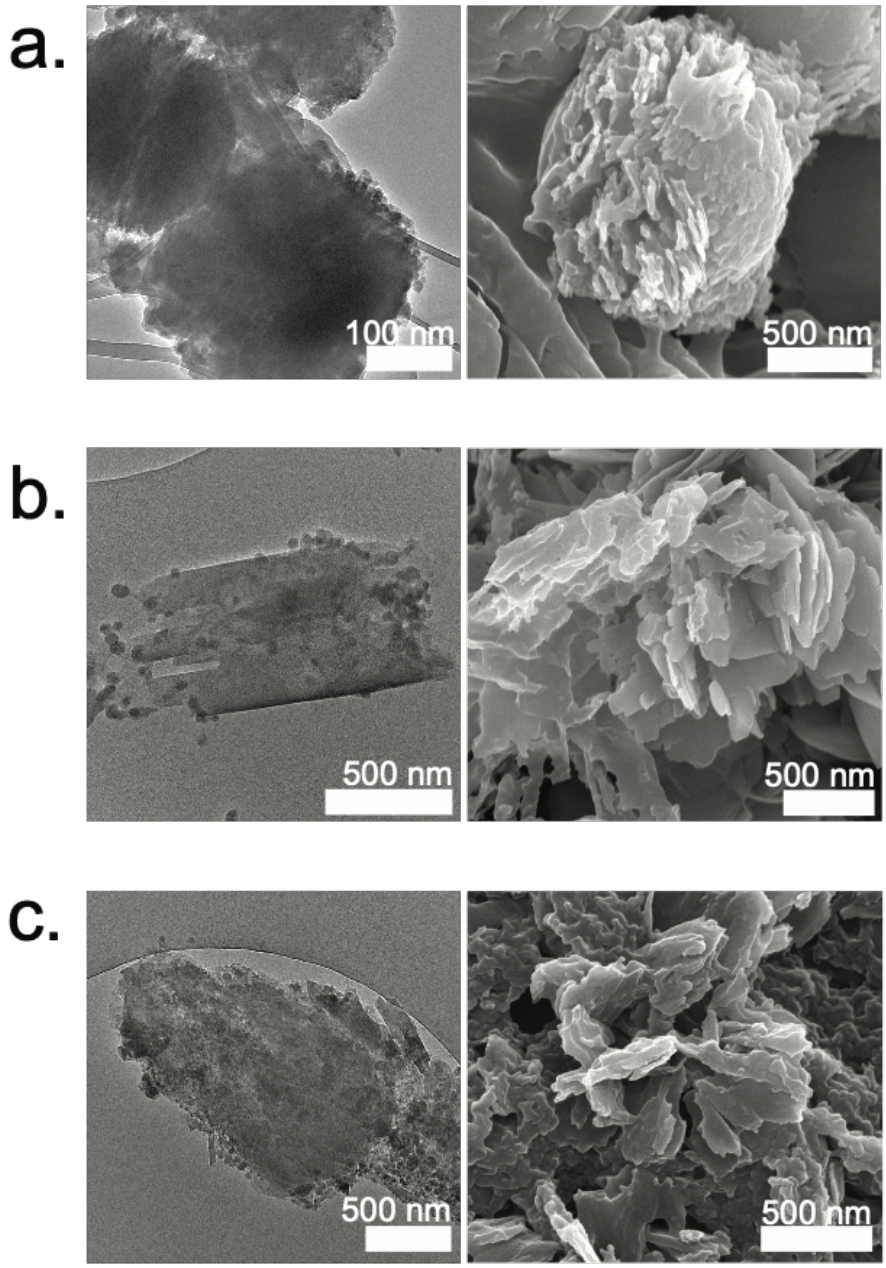

Figure 5.3: TEM (left) and SEM (right) images of M^{pro}@ZIF-8 biocomposites at HmIm:Zn ratios of a)2:1, b) 9:1, and c) 35:1.

Nanoluc

NanoLuc was integrated into ZIF-8 biocomposites at HmIM:Zn ratios of 4:1, 17.5:1, and 35:1 to provide insight into the formation and final morphology of NanoLuc biocomposites when

synthetic conditions are varied. At 17.5:1 and 35:1 synthetic conditions (Figure 5.4), precipitation occurred where TEM revealed each condition to share crystals (2 μm) with rhombic dodecahedral morphology. The crystals appear highly crystalline without obvious signs of pore or defect formation. As supported by Chapter 4 in this thesis and in other reportings,[8] such a finding is notable due to defects being essential for substrates to access immobilized proteins. Thus, the lack of activity within the biocomposites is hypothesized to be because of the lack of defects in the biocomposites. Additionally, both crystals also share small particles (~10-20 nm) which can be observed along the edges of each crystal. If proteins are located within the small particles, it is hypothesized that they are not in an active conformation to perform catalysis. Typically, at 17.5:1 synthetic conditions without biomolecule, a mixture of rhombic dodecahedron and flat sheets can be observed,[19] which indicates NanoLuc, while is not able to induce crystallization at low HmIm:Zn ratios (4:1), is able to control the crystallization at 17.5:1 to achieve crystals with solely rhombic dodecahedron morphology. This provides a promising result for future experiments as biocomposites that occur through such a mechanism are capable of inducing defects within a crystal by tuning of the protein concentration.[18]

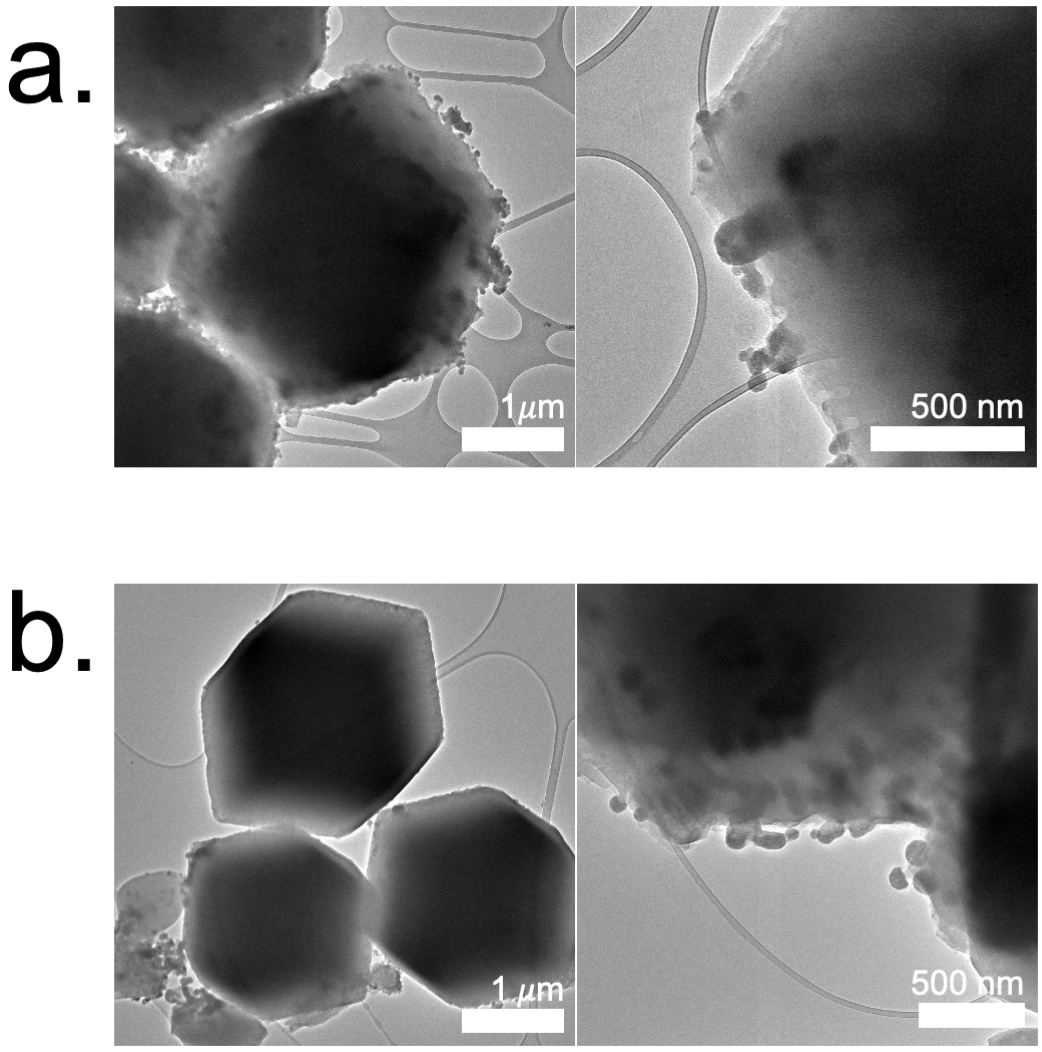

Figure 5.4: TEM images of Nanoluc@ZIF-8 biocomposites at HmIm:Zn ratios of a)17.5:1, and b) 35:1.

Structural Topological Studies

While proteins can induce formation of crystals with varying morphology, proteins can also influence the connectivity and symmetry of the metals and ligands within the crystal resulting in varying crystal structures. As previously mentioned, at low HmIM:Zn conditions, 2D sheet-like morphologies corresponding to diamondoid (dia) topologies are produced.[18,19] Crystals with (dia) topologies are considered thermodynamic products and typically take >24 hours to crystallize.[21]

By increasing the HmIM:Zn conditions or through introduction of a biomolecule, rhombic dodecahedron morphologies corresponding to sodalite (sod) topologies are produced. Sod is considered a kinetic product and forms rapidly within a few hours. An intermediate product to sod is ZIF-L which exhibits some connectivity characteristics of sod topology but differs in its cavity size.[22] In addition to sodalite and ZIF-L topologies, incorporation of a biomolecule can also favor the formation of ZIF-C, which incorporates CO_2.[15]

At 2:1 synthetic conditions for M^{pro}@ZIF-8, an unknown phase (indicated by the peak at 10°) and ZIF-C topology is observed (Figure 5.5).[15] At 4:1 synthetic conditions, a peak at 7.3° appears which is characteristic of the (011) plane in sod topology. Another peak is observed on the left shoulder of the peak at 7.3° indicating the sample is a mixture of sod and ZIF-L. As the ratio of HmIM:Zn increases, the samples increase in ZIF-L topology. Such results are consistent with the morphological findings as ZIF-L topologies have been reported to have 2D sheet morphologies.[22,23] Additionally, the XRD pattern at 9:1 M^{pro}@ZIF-8 aligns perfectly with the pattern provided when ZIF-8 was synthesized with 60 mg of PLGA,[20] further suggesting that the surface charge on M^{pro}, either naturally or artificially from the buffer, plays a role in the final structural topology.

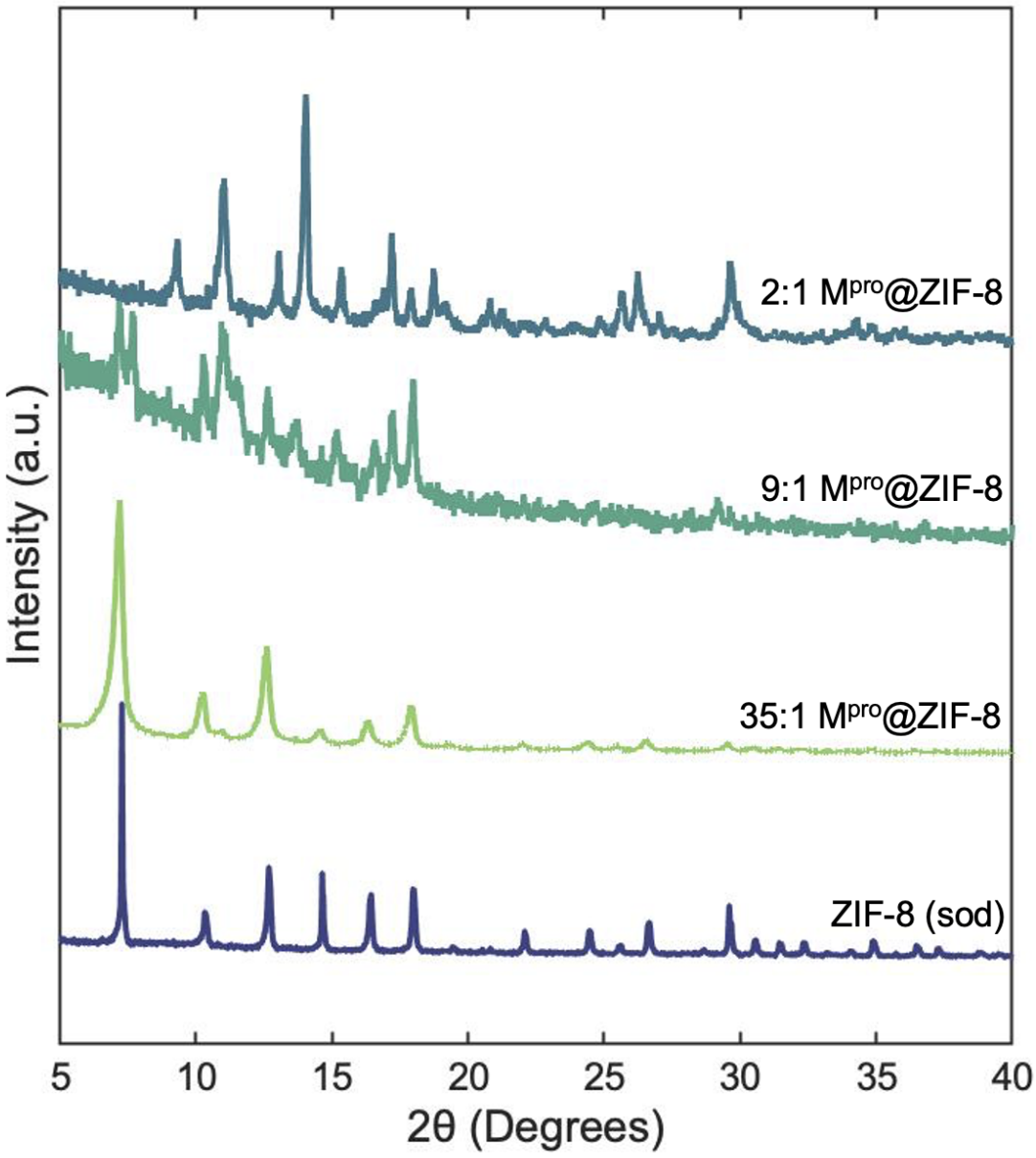

Figure 5.5: PXRD pattern of M^{pro}@ZIF-8 biocomposites at HmIM:Zn synthetic ratios of 2:1 (teal), 9:1 (turquoise), and 35:1 (green) after 3x water washes.

5.3 Conclusions

MOFs serve as a promising platform for immobilization of novel proteins for biomedical applications. The diverse topological and morphological properties of MOFs combined with the

unique properties of each novel protein have the potential to revolutionize treatments for SAR-COV-2 and improve in-vivo imaging technology. While results from this study show exciting potential, further research is required in understanding the structure function relationship between each protein and composite. More specifically, future studies will focus on activity and inhibition mechanisms of M^{pro} in ZIF-8. Additionally, from a nucleation and growth perspective, mechanistic studies will be performed to understand how M^{pro} facilitates the growth of such a diverse landscape of structural topologies. Future studies for NanoLuc will focus on optimizing synthetic conditions to promote larger defects and pores that would enable accessibility of substrate to enzyme.

5.4 Experimental Methods

Materials

2-methylimidazole and zinc acetate dihydrate were purchased from Sigma Aldrich.

M^{pro} Expression

Performed by the Martin Research Laboratory**,** Luria Broth Miller media was prepared and autoclaved in 2L flasks. To each flask, Ampicillin (1 ml) was added to a final concentration of 100 µg/ml and inoculated with M^{pro} starter culture. The cultures were grown to OD600 = 0.8 at 37°C, 230 rpm and expression was by adding 500 µL of IPTG (1M) to a final concentration of 500 µM. Cultures were grown for 4 h at 37°C and then harvest cells by centrifugation at 4C, 10,000 g for 35 min. Cell pellets were frozen in liquid nitrogen and stored at -80°C until cell lysis. The cells were then resuspended in 20 mL of Buffer A (20mM Tris pH 7.8, 150 mM NaCl, 5 mM Imidazole). Cells were lysed on ice with 12 cycles of sonification (5 s on, 25 s off per cycle and 40% amplitude). The cell extract was clarified by centrifuging at 30,000 g for 35 minutes at 4 C and

filtered through a 0.45 μm syringe filter. Proteases were purified via Ni affinity chromatography ((2 x 5 ml HiTrap-His in series).

NanoLuc Protein expression and purification

Performed by the Prescher Research Laboratory**,** NanoLuc was expressed and purified as previously described.[24]

M^{pro}@ZIF-8 and Nanoluc@ZIF-8 Synthesis

M^{pro} (1 mg/ml, 0.1 mL) was combined with individual solutions of 2-methylimidazole (HMIM) (2800 mM and 320 mM, 0.1 mL). Zinc acetate (Zn) (40 mM, 0.2 mL) solutions were then prepared and added to each protein/HmIm mixture to achieve final HmIm:Zn ratios of 4:1 and 35:1. Additional systems at 2:1 and 9:1 were made by combining M^{pro} (1 mg/ml, 0.1 mL) with individual solutions of 2-methylimidazole (HmIM) (1400 mM and 320 mM, 0.1 mL) followed by addition of zinc acetate (40 mM, 0.4 mL). Nanoluc (48 ug/ml, 0.05 mL) was combined with individual solutions of 2-methylimidazole (HmIm) (2800 mM and 1400 mM, 0.05 mL). Zinc acetate (Zn) (40 mM, 0.1 mL) solutions were then prepared and added to each protein/HmIm mixture to achieve final HmIm:Zn ratios of 17.5:1 and 35:1. M^{pro} and NanoLuc biocomposite reactions were aged for 24 hours without stirring. The precipitates were retrieved by centrifuging the reaction at 10,000 rpm where the initial supernatant was separated and stored for EE% measurements. The biocomposite precipitates were washed 3x with water.

General Bioluminescence Imaging

All analyses were performed by the Prescher Research Laboratory in black 96-well plates (Grenier Bio-One). Furimazine (FRZ, Promega) was added to all samples using a 1:100 dilution of the commercial stock. Plates were imaged in a dark, light-proof chamber using an IVIS Lumina (PerkinElmer) CCD camera chilled to –90 °C. The stage was kept at 37 °C during imaging and the camera was controlled using Living Image software. Exposure times were set to 30 s, and binning levels were set to medium. Regions of interest were selected for quantification and total flux values were analyzed using Living Image software. All data was exported to Microsoft Excel or PRISM (GraphPad) for further analysis.

NanoLuc activity assays

All assays were performed the Prescher Research Laboratory in black 96-well plates. NanoLuc and NanoLuc@ZIF-8 samples (1 nM, 100 μL) were imaged immediately after addition of furimazine (2 μL of commercial stock, Promega). Luminescence scans were performed on a TECAN Spark Microplate Reader (398–653 nm, bandwidth = 25, step value = 15, 1 s integration). All data was exported to Microsoft Excel or PRISM (GraphPad) for further analysis.

Transmission Electron Microscopy (TEM)

Pellets of each MOF were diluted 10x in nanopure water to obtain an ideal concentration for TEM imaging. Each sample was then pipetted (5 uL) onto either 400 Mesh Carbon grids from TedPella or Quantifoil R2/2 Holey Carbon from Electron Microscopy Sciences. Samples were imaged with a Joel-2100 TEM that was equipped with a Schottyky type field emission gun and a Gatan Oneview camera.

Scanning Electron Microscopy (SEM)

Samples (10 uL) were pipetted onto 1 mm glass slides. Once dry, samples were coated with 5 nm Iridium (Quorum Q150T) to reduce charging effects. Images were collected using a Magellan 400 XRH system while operating at an accelerating voltage of 5 kV.

Powder X-ray Diffraction (PXRD)

Samples were prepared by drying MOF precipitants in a vacuum oven. Samples were then crushed into a fine powder using a mortar and pestle and placed onto a zero-background crystal attachment. Patterns were obtained using a Rigaku Ultima III X-ray diffractometer in Bragg-Brentano mode.

Fourier Transform Infrared Spectroscopy (FTIR)

Samples were prepared by drying MOF precipitants in a vacuum. Samples were then analyzed with a Jasco V-670 spectrometer using the attenuated total reflection method. Spectras were obtained at a 150 scan resolution.

Bradford Assay

The standard calibration curve was achieved using BSA (2.5-25 µg/ml) solutions. The protein solutions (150 µL) were combined with Bradford reagent (150 µL). To determine encapsulation efficiency of each biocomposite, the initial supernatents (150 µL) from the biocomposites were taken and then combined with Bradford reagent (150 µL). Protein solutions and supernatants were incubated with Bradford reagent at room temperature for ~10 minutes.

Absorbance measurements were taken of each sample at 595 nm. EE% were determined based on the standard calibration curve.

5.5 References

(1) Furukawa, H.; Cordova, K. E.; O'Keeffe, M.; Yaghi, O. M. The Chemistry and Applications of Metal-Organic Frameworks. *Science* **2013**, *341* (6149), 1230444. https://doi.org/10.1126/science.1230444.

(2) Silva, P.; Vilela, S. M. F.; Tomé, J. P. C.; Paz, F. A. A. Multifunctional Metal–Organic Frameworks: From Academia to Industrial Applications. *Chem. Soc. Rev.* **2015**, *44* (19), 6774–6803. https://doi.org/10.1039/C5CS00307E.

(3) Lawson, H. D.; Walton, S. P.; Chan, C. Metal–Organic Frameworks for Drug Delivery: A Design Perspective. *ACS Appl. Mater. Interfaces* **2021**, *13* (6), 7004–7020. https://doi.org/10.1021/acsami.1c01089.

(4) Horcajada, P.; Serre, C.; Vallet-Regí, M.; Sebban, M.; Taulelle, F.; Férey, G. Metal–Organic Frameworks as Efficient Materials for Drug Delivery. *Angewandte Chemie International Edition* **2006**, *45* (36), 5974–5978. https://doi.org/10.1002/anie.200601878.

(5) Park, K. S.; Ni, Z.; Côté, A. P.; Choi, J. Y.; Huang, R.; Uribe-Romo, F. J.; Chae, H. K.; O'Keeffe, M.; Yaghi, O. M. Exceptional Chemical and Thermal Stability of Zeolitic Imidazolate Frameworks. *Proceedings of the National Academy of Sciences* **2006**, *103* (27), 10186–10191. https://doi.org/10.1073/pnas.0602439103.

(6) Liang, K.; Ricco, R.; Doherty, C. M.; Styles, M. J.; Bell, S.; Kirby, N.; Mudie, S.; Haylock, D.; Hill, A. J.; Doonan, C. J.; Falcaro, P. Biomimetic Mineralization of Metal-Organic Frameworks as Protective Coatings for Biomacromolecules. *Nature Communications* **2015**, *6* (1), 7240. https://doi.org/10.1038/ncomms8240.

(7) Van Vleet, M. J.; Weng, T.; Li, X.; Schmidt, J. R. In Situ, Time-Resolved, and Mechanistic Studies of Metal–Organic Framework Nucleation and Growth. *Chem. Rev.* **2018**, *118* (7), 3681–3721. https://doi.org/10.1021/acs.chemrev.7b00582.

(8) Tong, L.; Huang, S.; Shen, Y.; Liu, S.; Ma, X.; Zhu, F.; Chen, G.; Ouyang, G. Atomically Unveiling the Structure-Activity Relationship of Biomacromolecule-Metal-Organic Frameworks Symbiotic Crystal. *Nat Commun* **2022**, *13* (1), 951. https://doi.org/10.1038/s41467-022-28615-y.

(9) Fernando, D.; Mathesh, M.; Cai, J.; Yang, W. In Situ Immobilization of Multi-Enzymes for Enhanced Substrate Channeling of Enzyme Cascade Reactions: A Nanoarchitectonics Approach by Directed Metal–Organic Frameworks. *Langmuir* **2023**, *39* (22), 7979–7985. https://doi.org/10.1021/acs.langmuir.3c00879.

(10) Pan, Y.; Li, H.; Farmakes, J.; Xiao, F.; Chen, B.; Ma, S.; Yang, Z. How Do Enzymes Orient When Trapped on Metal–Organic Framework (MOF) Surfaces? *J. Am. Chem. Soc.* **2018**, *140* (47), 16032–16036. https://doi.org/10.1021/jacs.8b09257.

(11) Wu, F.; Zhao, S.; Yu, B.; Chen, Y.-M.; Wang, W.; Song, Z.-G.; Hu, Y.; Tao, Z.-W.; Tian, J.-H.; Pei, Y.-Y.; Yuan, M.-L.; Zhang, Y.-L.; Dai, F.-H.; Liu, Y.; Wang, Q.-M.; Zheng, J.-J.; Xu, L.; Holmes, E. C.; Zhang, Y.-Z. A New Coronavirus Associated with Human Respiratory Disease in China. *Nature* **2020**, *579* (7798), 265–269. https://doi.org/10.1038/s41586-020-2008-3.

(12) Cross, T. J.; Takahashi, G. R.; Diessner, E. M.; Crosby, M. G.; Farahmand, V.; Zhuang, S.; Butts, C. T.; Martin, R. W. Sequence Characterization and Molecular Modeling of Clinically Relevant Variants of the SARS-CoV-2 Main Protease. *Biochemistry* **2020**, *59* (39), 3741–3756. https://doi.org/10.1021/acs.biochem.0c00462.
(13) Antonopoulou, I.; Sapountzaki, E.; Rova, U.; Christakopoulos, P. Inhibition of the Main Protease of SARS-CoV-2 (Mpro) by Repurposing/Designing Drug-like Substances and Utilizing Nature's Toolbox of Bioactive Compounds. *Computational and Structural Biotechnology Journal* **2022**, *20*, 1306–1344. https://doi.org/10.1016/j.csbj.2022.03.009.
(14) *NanoLuc: A Small Luciferase Is Brightening Up the Field of Bioluminescence | Bioconjugate Chemistry*. https://pubs.acs.org/doi/10.1021/acs.bioconjchem.6b00112 (accessed 2023-07-13).
(15) Carraro, F.; Velásquez-Hernández, M. de J.; Astria, E.; Liang, W.; Twight, L.; Parise, C.; Ge, M.; Huang, Z.; Ricco, R.; Zou, X.; Villanova, L.; Kappe, C. O.; Doonan, C.; Falcaro, P. Phase Dependent Encapsulation and Release Profile of ZIF-Based Biocomposites. *Chem. Sci.* **2020**, *11* (13), 3397–3404. https://doi.org/10.1039/C9SC05433B.
(16) Li, E.; Brennan, C. K.; Ramirez, A.; Tucker, J. A.; Butkovich, N.; Meli, V. S.; Ionkina, A. A.; Nelson, E. L.; Prescher, J. A.; Wang, S.-W. Macromolecular Assembly of Bioluminescent Protein Nanoparticles for Enhanced Imaging. *Materials Today Bio* **2022**, *17*, 100455. https://doi.org/10.1016/j.mtbio.2022.100455.
(17) Maddigan, N. K.; Tarzia, A.; Huang, D. M.; Sumby, C. J.; Bell, S. G.; Falcaro, P.; Doonan, C. J. Protein Surface Functionalisation as a General Strategy for Facilitating Biomimetic Mineralisation of ZIF-8. *Chem. Sci.* **2018**, *9* (18), 4217–4223. https://doi.org/10.1039/C8SC00825F.
(18) Ogata, A. F.; Rakowski, A. M.; Carpenter, B. P.; Fishman, D. A.; Merham, J. G.; Hurst, P. J.; Patterson, J. P. Direct Observation of Amorphous Precursor Phases in the Nucleation of Protein–Metal–Organic Frameworks. *J. Am. Chem. Soc.* **2020**, *142* (3), 1433–1442. https://doi.org/10.1021/jacs.9b11371.
(19) Carpenter, B. P.; Talosig, A. R.; Mulvey, J. T.; Merham, J. G.; Esquivel, J.; Rose, B.; Ogata, A. F.; Fishman, D. A.; Patterson, J. P. Role of Molecular Modification and Protein Folding in the Nucleation and Growth of Protein–Metal–Organic Frameworks. *Chem. Mater.* **2022**, *34* (18), 8336–8344. https://doi.org/10.1021/acs.chemmater.2c01903.
(20) Chen, G.; Huang, S.; Kou, X.; Zhu, F.; Ouyang, G. Embedding Functional Biomacromolecules within Peptide-Directed Metal–Organic Framework (MOF) Nanoarchitectures Enables Activity Enhancement. *Angewandte Chemie International Edition* **2020**, *59* (33), 13947–13954. https://doi.org/10.1002/anie.202005529.
(21) Katsenis, A. D.; Puškarić, A.; Štrukil, V.; Mottillo, C.; Julien, P. A.; Užarević, K.; Pham, M.-H.; Do, T.-O.; Kimber, S. A. J.; Lazić, P.; Magdysyuk, O.; Dinnebier, R. E.; Halasz, I.; Friščić, T. In Situ X-Ray Diffraction Monitoring of a Mechanochemical Reaction Reveals a Unique Topology Metal-Organic Framework. *Nature Communications* **2015**, *6* (1), 6662. https://doi.org/10.1038/ncomms7662.
(22) Deacon, A.; Briquet, L.; Malankowska, M.; Massingberd-Mundy, F.; Rudić, S.; Hyde, T. l; Cavaye, H.; Coronas, J.; Poulston, S.; Johnson, T. Understanding the ZIF-L to ZIF-8 Transformation from Fundamentals to Fully Costed Kilogram-Scale Production. *Commun Chem* **2022**, *5* (1), 1–10. https://doi.org/10.1038/s42004-021-00613-z.
(23) Chen, R.; Yao, J.; Gu, Q.; Smeets, S.; Baerlocher, C.; Gu, H.; Zhu, D.; Morris, W.; Yaghi, O. M.; Wang, H. A Two-Dimensional Zeolitic Imidazolate Framework with a Cushion-Shaped Cavity for CO2 Adsorption. *Chem Commun (Camb)* **2013**, *49* (82), 9500–9502. https://doi.org/10.1039/c3cc44342f.

(24) Ng, K. K.; Reinert, Z. E.; Corver, J.; Resurreccion, D.; Hensbergen, P. J.; Prescher, J. A. A Bioluminescent Sensor for Rapid Detection of PPEP-1, a Clostridioides Difficile Biomarker. *Sensors* **2021**, *21* (22), 7485. https://doi.org/10.3390/s21227485.

Chapter 6.

Conclusion

Chapter 6: Conclusion

6.1 Outlook and Future Directions

This dissertation presents compelling progress in MOF crystallization, providing new mechanistic insights into how proteins dictate MOF formation. By combining fundamental nucleation and growth theories with experiments, this research has advanced our understanding of the mechanisms underlying the evolution of prenucleation species into bulk crystals.

Chapter 2 introduces time-resolved cryoTEM studies performed on ZIF-8 and BSA@ZIF-8, revealing nonclassical nucleation mechanisms.[1] ZIF-8 was discovered to form through a dissolution-recrystallization of amorphous particles. Meanwhile, BSA@ZIF-8 formed simultaneously through the dissolution recrystallization of amorphous particles and through solid-state transformation of amorphous particles as confirmed through high-resolution cryoTEM. With continuous advancements into the temporal and spatial resolution of instrumentation, deeper insights into nucleation and crystal growth, at both the molecular and bulk scales, are anticipated. Additionally, as we continue to develop high-throughput characterization methods, such as with the recent development of high-throughput TEM,[2] the size in which data sets can be generated will advance, allowing translatable findings to a greater range of systems.

Chapter 3 details the discovery of how protein folding can influence the stability of amorphous phases in MOF growth, and consequently, the overall rate, extent, and mechanisms of of crystallization.[3] As with FITC-BSA@ZIF-8, the molecular modification unfolded the protein, which promoted a mixture of both crystalline and amorphous products to be formed. Future work includes enhancing methodology and instrumentation to differentiate the multiple phases that frequently form simultaneously during crystallization. This would enable intermediate and final

phase(s) that contain the protein to be distinguished so that we can better understand how (location, orientation etc.) the enzyme is incorporated into each phase.

Chapter 4 constructs a roadmap to engineering high-performance MOFs, using key themes from the literature studies combined with our own studies using catalytically active enzymes, GOx and CAT.[4,5] This guide initially considers protein folding with the MOF precursors as proper protein folding is key to ensuring that activity is preserved. Once a protein is paired with MOF precursors that stabilize its most active conformation, focus can be shifted towards directing a formation mechanism that yields a crystal with desired physical properties for an application. For example, mechanisms that facilitate crystals with high crystallinity are ideal for storage and shelf-life purposes, but crystals with less crystallinity and/or more defects often enable higher catalytic activity due to easier accessibility of enzymes to substrates in solution.

To demonstrate the generalizability of the findings, **Chapter 5** extends concepts learned from previous chapters to novel MOF systems, M^{pro}@ZIF-8 and NanoLuc@ZIF-8. Encapsulation of both proteins into ZIF-8 was successfully achieved, with Mpro@ZIF-8 exhibiting a range of structural topologies not observed under previous synthetic conditions. Future studies for M^{pro}@ZIF-8 will investigate the mechanisms facilitating these topologies. Additionally, no activity could be observed for NanoLuc@ZIF-8, so future studies will focus on optimizing the synthetic conditions, specifically through defect formation and topology, to enable activity.

As we are excited for the future of MOF crystallization, this dissertation emphasizes on the importance of relying heavily on nucleation and growth fundamentals to tap into the unexplored design space and engineer MOFs with enhanced performances.

6.2 References

(1) Ogata, A. F.; Rakowski, A. M.; Carpenter, B. P.; Fishman, D. A.; Merham, J. G.; Hurst, P. J.; Patterson, J. P. Direct Observation of Amorphous Precursor Phases in the Nucleation of Protein–Metal–Organic Frameworks. *J. Am. Chem. Soc.* **2020**, *142* (3), 1433–1442. https://doi.org/10.1021/jacs.9b11371.
(2) Gong, X.; Gnanasekaran, K.; Ma, K.; Forman, C. J.; Wang, X.; Su, S.; Farha, O. K.; Gianneschi, N. C. Rapid Generation of Metal–Organic Framework Phase Diagrams by High-Throughput Transmission Electron Microscopy. *J. Am. Chem. Soc.* **2022**, *144* (15), 6674–6680. https://doi.org/10.1021/jacs.2c01095.
(3) Carpenter, B. P.; Talosig, A. R.; Mulvey, J. T.; Merham, J. G.; Esquivel, J.; Rose, B.; Ogata, A. F.; Fishman, D. A.; Patterson, J. P. Role of Molecular Modification and Protein Folding in the Nucleation and Growth of Protein–Metal–Organic Frameworks. *Chem. Mater.* **2022**, *34* (18), 8336–8344. https://doi.org/10.1021/acs.chemmater.2c01903.
(4) Tong, L.; Huang, S.; Shen, Y.; Liu, S.; Ma, X.; Zhu, F.; Chen, G.; Ouyang, G. Atomically Unveiling the Structure-Activity Relationship of Biomacromolecule-Metal-Organic Frameworks Symbiotic Crystal. *Nat Commun* **2022**, *13* (1), 951. https://doi.org/10.1038/s41467-022-28615-y.
(5) Wu, X.; Yue, H.; Zhang, Y.; Gao, X.; Li, X.; Wang, L.; Cao, Y.; Hou, M.; An, H.; Zhang, L.; Li, S.; Ma, J.; Lin, H.; Fu, Y.; Gu, H.; Lou, W.; Wei, W.; Zare, R. N.; Ge, J. Packaging and Delivering Enzymes by Amorphous Metal-Organic Frameworks. *Nat Commun* **2019**, *10* (1), 5165. https://doi.org/10.1038/s41467-019-13153-x.

Appendix A:

Supplementary Information for Chapter 2.

This work appears in the following publication and has been re-formatted for this thesis:

Ogata, A.F.; Rakowski A.M.; Carpenter B.P. Fishman, D.A.; Merham, J.G.; Hurst, P.J.; Patterson, J.P. Direct Observation of Amorphous Precursor Phases in the Nucleation of Protein-Metal-Organic Frameworks. *J. Am. Chem. Soc*, 2020. 142 (3), 1433-1442.

Appendix A: Supporting Information for Chapter 2

A.1 Supplemental Methods:

Particle Picking

Particles were picked by qualitative assessment from each picture in Fiji, ImageJ to determine their coordinates for later analysis. A representative image shown Figure A9a shows the chosen particles that were then aligned into a stack.

Stack Alignment

Stack alignment of the chosen particles was carried out by a normalized cross-correlation method as implemented in the HyperSpy library Signal Class.14 All particles were overlaid, and each were translated until the best shift matrix was found for the entire stack. This produced an 'average particle' picture (APP) for Line Profile analysis.

Line Profile method:

Eight lines were overlaid on the APP and centered in the middle 5 pixels thick as represented in Figure A5b. The lines were truncated from both edges to be equal in length to the shortest line. To circumvent artifacts and noise, the longer lines were truncated from both edges to be equal in length to the shortest line. The particle is fully contained inside the shortest line while all other data is classified as background. Lines are put in a 2D grid and averaged along the pixel position. The resulting one-dimensional list is the final line profile of the particle.

A.2 Supplemental Tables

Table A1: HmIm : 2-methylimidazole, Zn : Zinc acetate, BSA : bovine serum albumin, GOX : glucose oxidase, ZIF-8 : zeolitic framework 8, sod: sodalite, dia : diamondoid, FBSA: fluorescein-tagged BSA

Ratio (HmIm:Zn)	Protein + concentration	Crystal product	Protein encapsulation	ref
10 mM : 5 mM **2:1**	Lipase (100 mg)	ZIF-8 (sod)	Not reported	1
80 mM : 20 mM **4:1**	BSA 0.025 mg/mL	ZIF-8 (sod)	homogenous	2
25 mM : 25 mM **1:1**	CytC 0.025 mg/mL	ZIF-8 (sod)	homogenous	3-4
1.9 mM : 0.096 mM **20:1**	GOx 2.3 mg/mL	ZIF-8 (dia)	Not reported	5
1040 mM : 26 mM **40:1**	GOX 0.45 mg/mL HRP 0.68 mg/mL	ZIF-8 (sod)	GOX- localized to outer region HRP- localized to inside region	6
2.835 mM : 0.0045 mM **630 : 1**	BSA 0.5 mg/mL	ZIF-8 (sod)	Not reported	7
700 mM : 10 mM **70:1**	GOX 0.1 mg/ mL	ZIF-8 (sod)	homogeneous	8 9
160 mM : 20 mM **8:1**	Tobacco mosaic virus 2-10 mg/mL	ZIF-8 (sod)	Surface-localized	10
666 mM : 41 mM **16 :1**	Catalase 0.83 mg/mL	ZIF-8 (dia)	Localized to outer regions	11
640 mM : 40 mM **16:1**	FBSA 0.33 mg/mL	ZIF-8 (sod)	Surface-localized	12
80 mM : 20 mM **4:1** **40:1** 80 mM : 2 mM	Lipase 4 – 9 mg/mL	4:1 unknown peaks 40:1 ZIF-8 (sod)	Not reported	13
700 mM : 20 mM **35:1**	**BSA** **5 mg/mL**	**ZIF-8 (sod)**	**Surface-localized**	**This work**

Table A2: HmIm: 2-methylimidazolate, Zn : Zinc acetate, ZIF-8 : zeolitic framework 8, sod: sodalite, dia : diamondoid

Ratio HmIm:Zn (mM : mM)	HmIm : Zn	Protein concentration	Final Product
5400:2	270:1	0 mg/mL	ZIF-8 (sod)
2000:20	100:1	0 mg/mL	ZIF-8 (sod)
700:20	35:1	0 mg/mL	ZIF-8 (sod)
200:20	10:1	0 mg/mL	ZIF-8 (dia)
80:20	4:1	0 mg/mL	ZIF-8 (dia)
350:10	35:1	0 mg/mL	ZIF-8 (sod) and amorphous material
140:4	35:1	0 mg/mL	ZIF-8 (sod) and amorphous material
70:2	35:1	0 mg/mL	No crystallization
80:20	4:1	5 mg/mL	ZIF-8 (sod) and amorphous material
80:20	4:1	0.5 mg/mL	ZIF-8 (sod), ZIF-8 (dia) and amorphous material
700:20	**35:1**	**5 mg/mL**	**ZIF-8 (sod)**
700:20	35:1	0.5 mg/mL	ZIF-8 (sod)
700:20	35:1	0.05 mg/mL	ZIF-8 (sod)

A.3 Supplemental Figures

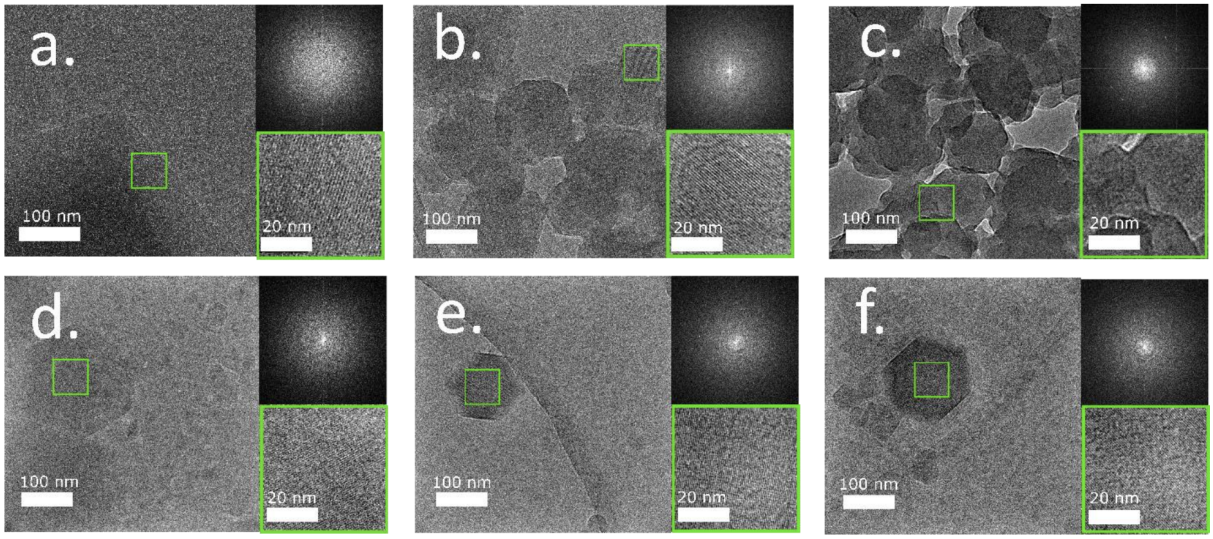

Figure A1: Lattice-resolution TEM and cryoTEM micrographs. (a-c) Drystate TEM images of (a) ZIF-8 and (b,c) BSA-ZIF-8 after 24 hrs reaction time. (d-e) cryoTEM images of ZIF-8 crystallization solutions vitrified at 4 hrs reaction time. Top inset of fast Fourier transform and bottom inset of ABS filtered region outlined in green box showing lattice fringes.

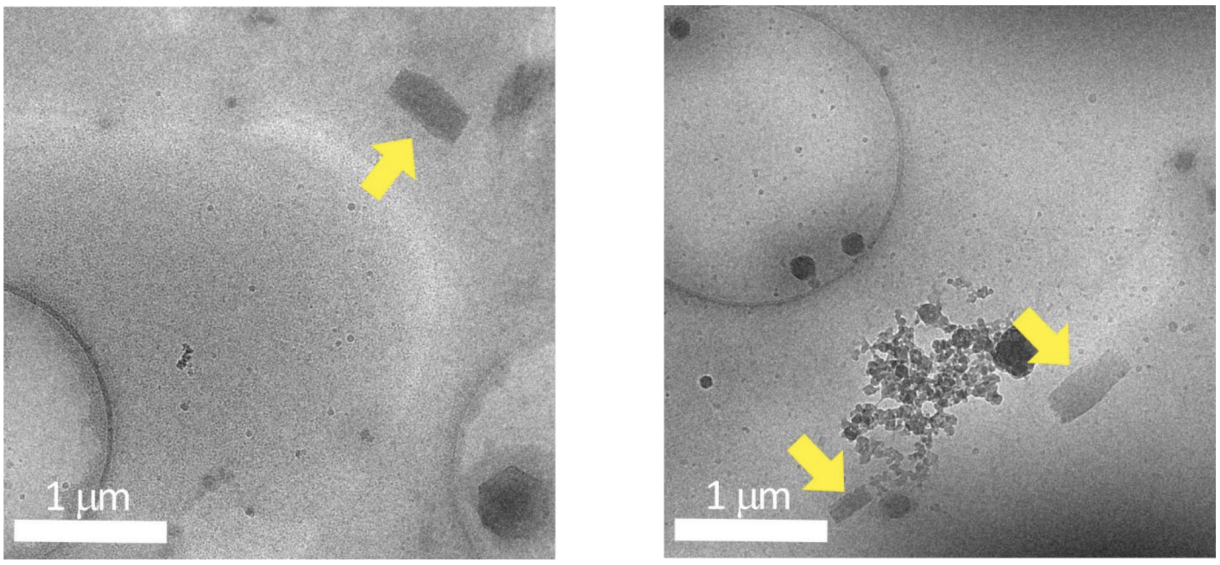

Figure A2. CryoTEM images of ZIF-8 crystallization solutions at 4 hrs aging. Yellow arrows pointing to 2D sheet-like structures observed randomly across samples.

A.4 Discussion

Crystallization through dissolution-recrystallization of amorphous particles explains the many polymorphs that exist for ZIF-8 in aqueous systems. Here, dissolution rates for amorphous particles may similarly depend on particle size, affecting the composition of the corresponding bulk amorphous phase. Therefore, any heterogenous distribution of amorphous particles can result in multiple microenvironments of different supersaturation levels within a single sample. We demonstrate this phenomenon through the observation of 2D structures which coexist throughout ZIF-8 and BSA-ZIF-8 formation but show no direct role in ZIF-8 formation (Figure 2A). We therefore propose that more than one crystalline phase can nucleate within a single sample, resulting in 2D structures and ZIF-8; however, there is no evidence that 2D structures are an intermediate for ZIF-8 formation.

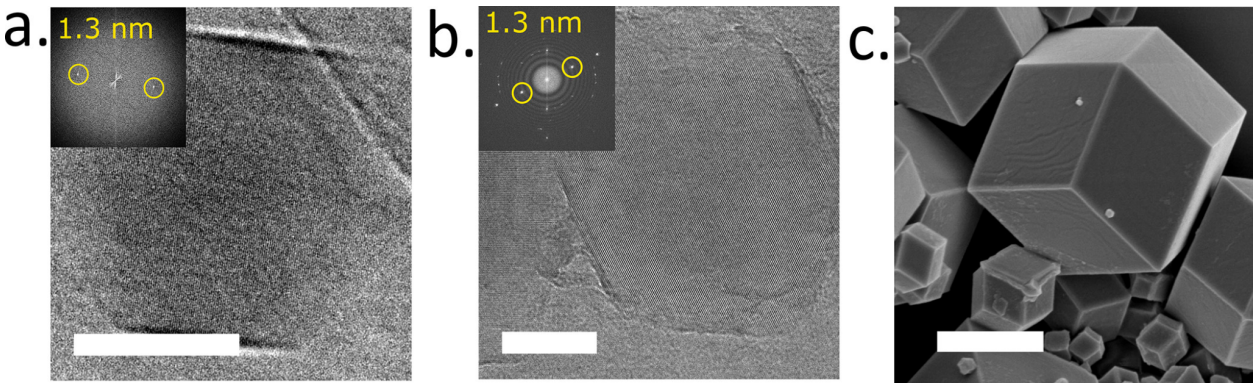

Figure A3. Characterization of final ZIF-8 crystals. (a) CryoTEM of ZIF-8 crystallization solutions at 4 h showing a single crystal. Scale bar, 200 nm. (b) Dry-state TEM micrograph of final ZIF-8 product. Scale bar, 200 nm. (c) SEM of final ZIF-8 products. Scale bar, 1 µm. Images are processed using an average background subtraction filter. Insets in panels a and b are fast Fourier transform from unfiltered images indicating crystallinity.

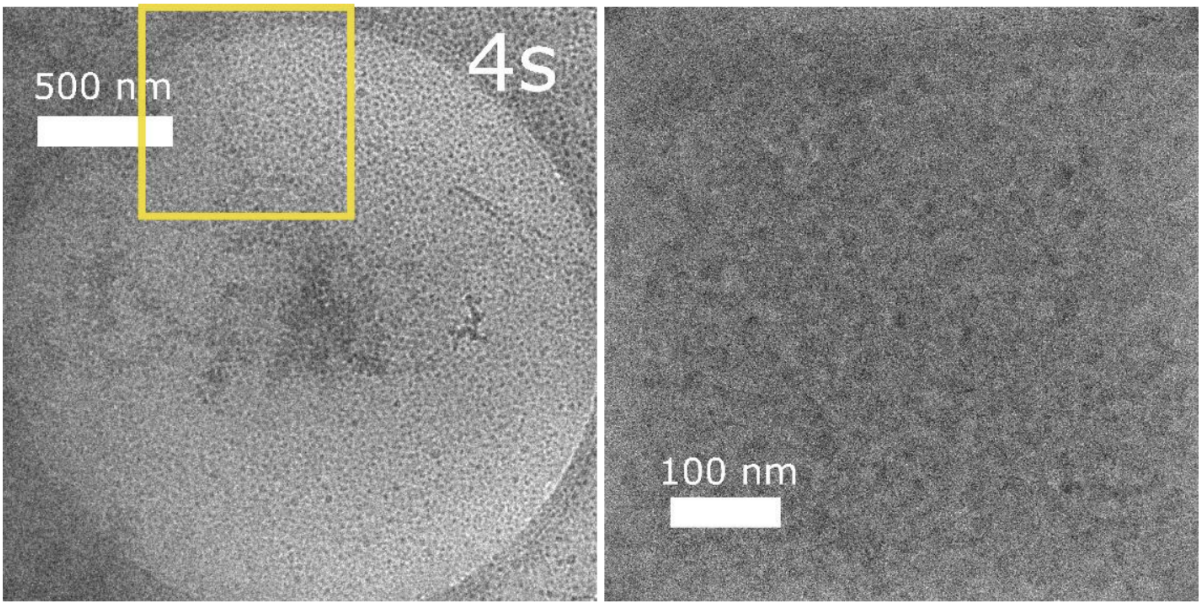

Figure A4. Representative CryoTEM images of nucleation and growth process of BSA-ZIF-8 in water at low (left) and high (right) magnification. At 4s reaction time, amorphous particles and the amorphous bulk phase were observed simultaneously with the formation of a protein-induced amorphous phase

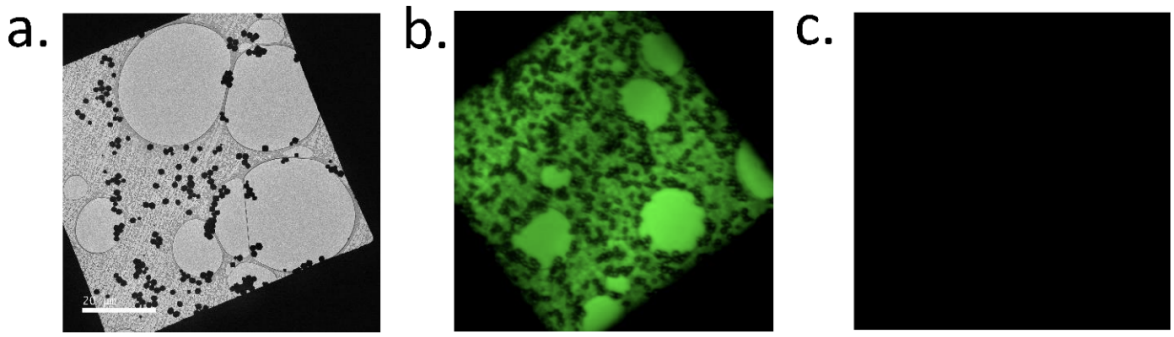

Figure A5. TEM and all-optical microscopy of ZIF-8 crystals. ZIF-8 synthesis was carried out as described in the full methods section. The final precipitate was then centrifuged, resuspended in a 5 mg/mL solution of fluorescein-isothiocyanate conjugated BSA and incubated for 24 hrs. Samples were then washed twice by centrifugation and resuspended in water. Analysis by (a)TEM and (b) optical transmission images show ZIF-8 crystals 2 – 3 μm in size dispersed on a lacey carbon grid. (c) Fluorescence microscopy images for grid of unlabeled protein and were obtained for identical experimental conditions to other fluorescence data

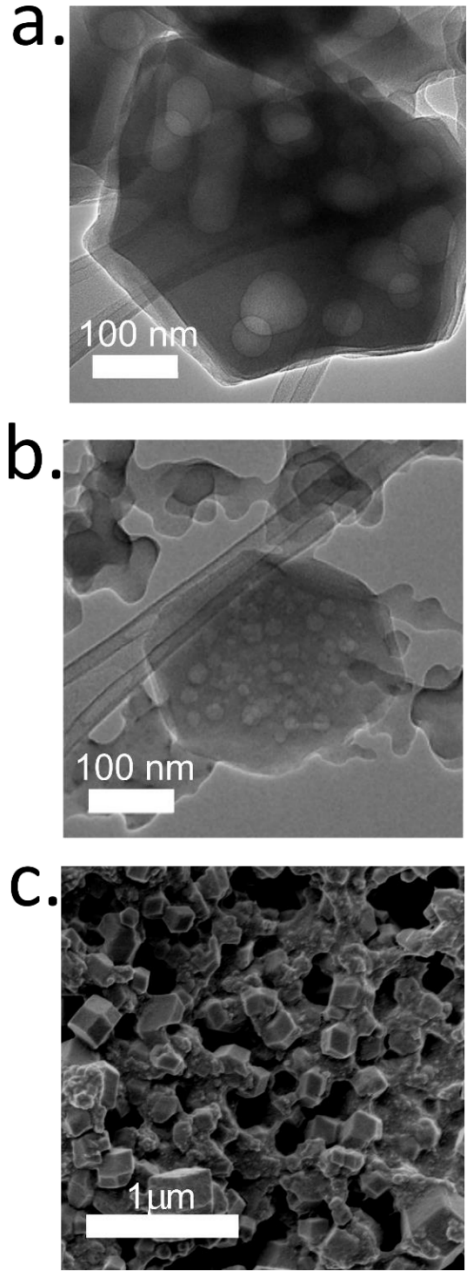

Figure A6: (a) TEM of BSA-ZIF-8 at a HmIm:Zn ratio of 4:1 with 5 mg/mL of BSA after 24 hrs reaction time. (b) TEM and (SEM) of BSA-ZIF-8 at a HmIm:Zn ratio of 4:1 with 0.5 mg/mL of BSA after 24 hrs reaction time. A large network of amorphous material covered all samples. This amorphous material showed to be very beam sensitive and shrunk in size upon contact with the electron beam during TEM imaging.

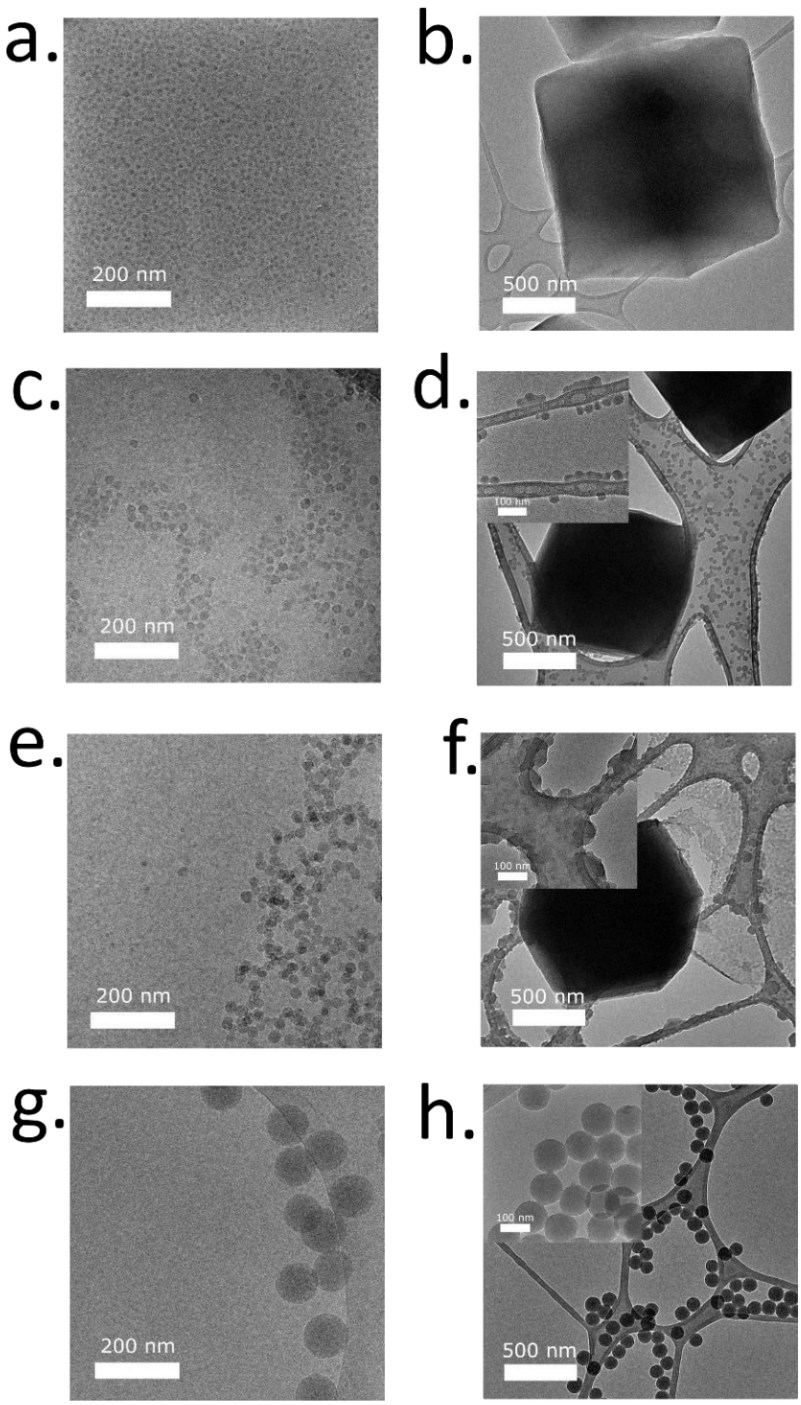

Figure A7. (a,c,e,g) cryoTEM of crystallization solution after 1 min. (b,d,f,h) Drystate TEM of crystallization solution after 24 hrs. Each solution prepared by the following HmIm : Zn ratios, (a,e) 700 mM : 20 mM (b,f) 350 mM : 10 mM (c,g) 140 mM : 4 mM (d,h) 70 mM : 2 mM. Amorphous particles observed by cryoTEM increase in size as the whole concentration of ZIF precursors decreases. After 24 hrs, samples b-h show both ZIF8 crystals and amorphous material that is attributed to the amorphous particles damaged under high

vacuum conditions. Sample h contains no ZIF-8 crystals after 24 hrs and amorphous particles observed by cryoTEM remain stable under high vacuum conditions.

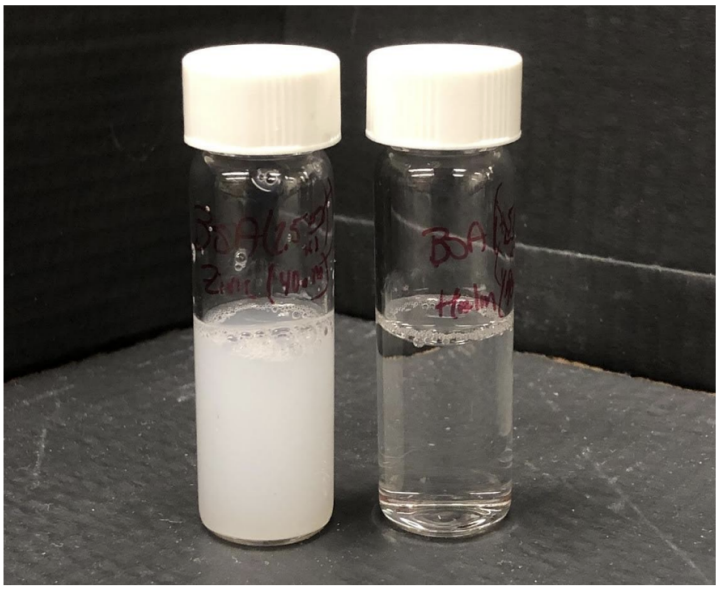

Figure A8. Photo of solutions consisted of 5 mg/mL BSA mixed with (left) Zn at 20 mM and (right) HmIm at 700 mM solutions upon addition of protein.

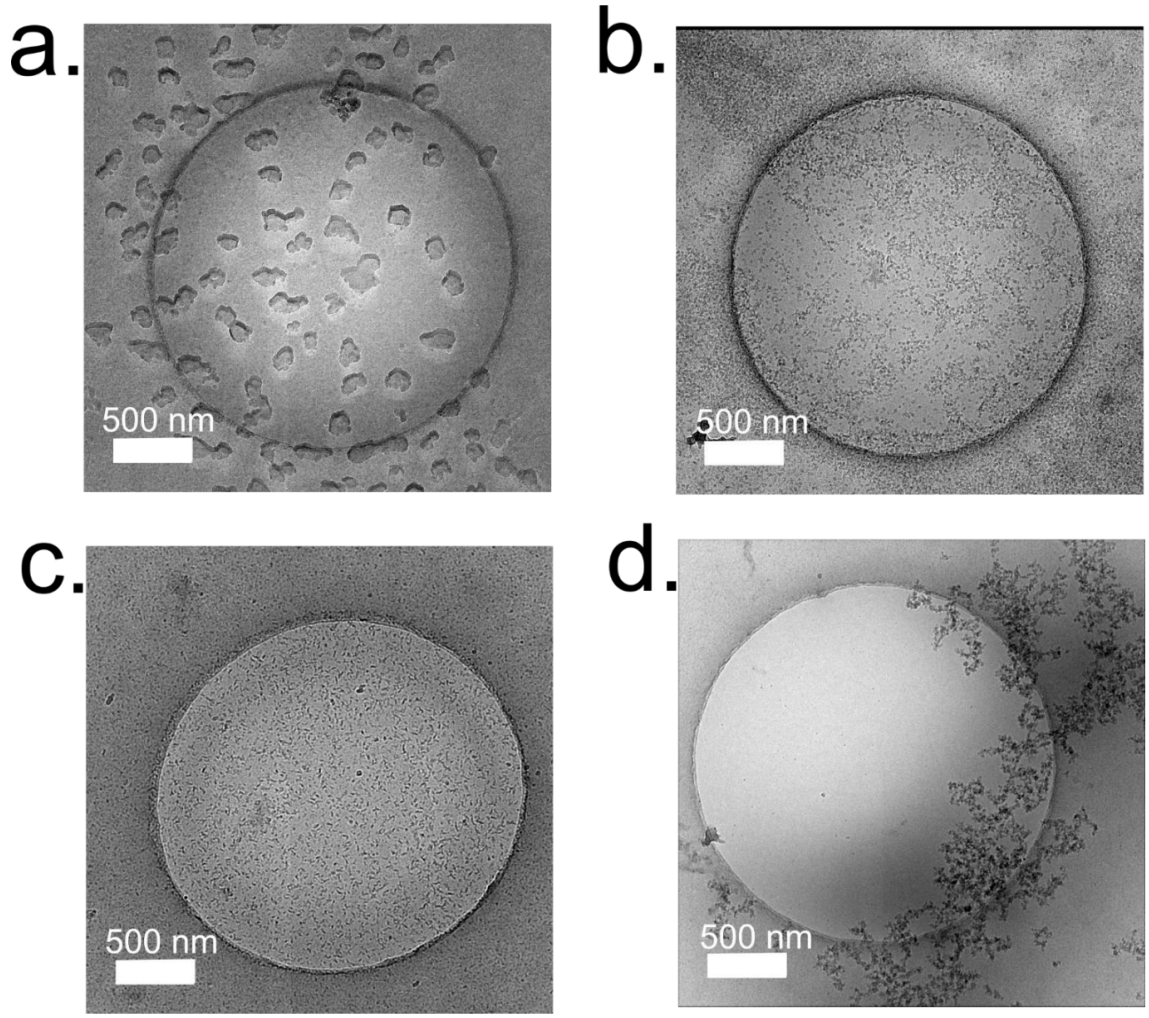

Figure A9. CryoTEM micrographs of (a) lipase-HmIm, (b) lipase-Zn, (c) pepsin-HmIm, and (d) pepsin-Zn solutions. Protein/Zn solutions were prepared by adding protein into a solution of zinc acetate for a final concentration of 5 mg/mL protein in a zinc acetate aqeous solution (40 mM, 1mL. Protein/HmIm solutions were prepared by adding protein into a solution of 2-methylimidazole for a final concentration of 5mg/mL protein in a 2-methylimidazole aqueous solution (1400 mL, 1mL) and subsequently mixed with a separate solution of zinc acetate (40 mM, 1 mL). Each biomolecule/precursor pair produces a unique secondary structure and aggregation of these structures.

A.6 Supplementary References

1. He, H.; Han, H.; Shi, H.; Tian, Y.; Sun, F.; Song, Y.; Li, Q.; Zhu, G., Construction of Thermophilic Lipase-Embedded Metal-Organic Frameworks via Biomimetic Mineralization: A Biocatalyst for Ester Hydrolysis and Kinetic Resolution. ACS Appl Mater Interfaces 2016, 8 (37), 24517-24.
2. Min, H.; Wang, J.; Qi, Y.; Zhang, Y.; Han, X.; Xu, Y.; Xu, J.; Li, Y.; Chen, L.; Cheng, K.; Liu,

G.; Yang, N.; Li, Y.; Nie, G., Biomimetic Metal-Organic Framework Nanoparticles for Cooperative Combination of Antiangiogenesis and Photodynamic Therapy for Enhanced Efficacy. Adv Mater 2019, 31 (15), e1808200.
3. Lyu, F.; Zhang, Y.; Zare, R. N.; Ge, J.; Liu, Z., One-pot synthesis of protein-embedded metalorganic frameworks with enhanced biological activities. Nano Lett 2014, 14 (10), 5761-5. 4. Zhang, C.; Wang, X.; Hou, M.; Li, X.; Wu, X.; Ge, J., Immobilization on Metal-Organic Framework Engenders High Sensitivity for Enzymatic Electrochemical Detection. ACS Appl Mater Interfaces 2017, 9 (16), 13831-13836.
5. Wang, Q.; Zhang, X.; Huang, L.; Zhang, Z.; Dong, S., GOx@ZIF-8(NiPd) Nanoflower: An Artificial Enzyme System for Tandem Catalysis. Angew Chem Int Ed Engl 2017, 56 (50), 16082-16085.
6. Wu, X.; Ge, J.; Yang, C.; Hou, M.; Liu, Z., Facile synthesis of multiple enzyme-containing metalorganic frameworks in a biomolecule-friendly environment. Chem Commun (Camb) 2015, 51 (69), 13408-11.
7. Chen, T. T.; Yi, J. T.; Zhao, Y. Y.; Chu, X., Biomineralized Metal-Organic Framework Nanoparticles Enable Intracellular Delivery and Endo-Lysosomal Release of Native Active Proteins. J Am Chem Soc 2018, 140 (31), 9912-9920.
8. Chen, W. H.; Luo, G. F.; Vazquez-Gonzalez, M.; Cazelles, R.; Sohn, Y. S.; Nechushtai, R.; Mandel, Y.; Willner, I., Glucose-Responsive Metal-Organic-Framework Nanoparticles Act as "Smart" Sense-andTreat Carriers. ACS Nano 2018, 12 (8), 7538-7545.
9. Chen, W.-H.; Vázquez-González, M.; Zoabi, A.; Abu-Reziq, R.; Willner, I., Biocatalytic cascades driven by enzymes encapsulated in metal–organic framework nanoparticles. Nature Catalysis 2018, 1 (9), 689-695.
10. Li, S.; Dharmarwardana, M.; Welch, R. P.; Benjamin, C. E.; Shamir, A. M.; Nielsen, S. O.; Gassensmith, J. J., Investigation of Controlled Growth of Metal-Organic Frameworks on Anisotropic Virus Particles. ACS Appl Mater Interfaces 2018, 10 (21), 18161-18169.
11. Cui, J.; Feng, Y.; Lin, T.; Tan, Z.; Zhong, C.; Jia, S., Mesoporous Metal-Organic Framework with Well-Defined Cruciate Flower-Like Morphology for Enzyme Immobilization. ACS Appl Mater Interfaces 2017, 9 (12), 10587-10594.
12. Liang, W.; Ricco, R.; Maddigan, N. K.; Dickinson, R. P.; Xu, H.; Li, Q.; Sumby, C. J.; Bell, S. G.; Falcaro, P.; Doonan, C. J., Control of Structure Topology and Spatial Distribution of Biomacromolecules in Protein@ZIF-8 Biocomposites. Chemistry of Materials 2018, 30 (3), 1069-1077.
13. Pitzalis, F.; Carucci, C.; Naseri, M.; Fotouhi, L.; Magner, E.; Salis, A., Lipase Encapsulation onto ZIF-8: A Comparison between Biocatalysts Obtained at Low and High Zinc/2-Methylimidazole Molar Ratio in Aqueous Medium. ChemCatChem 2018, 10 (7), 1578-1585.

Appendix B:

Supplementary Information for Chapter 3.

This work appears in the following publication and has been re-formatted for this thesis:
Carpenter, B.P.; Talosig, A.R.; Mulvey, J.T.; Merham, J.G.; Esquivel, J.; Rose, B.; Ogata, A.F.; Fishman, D.A.; Patterson, J.P. Role of Molecular Modification and Protein Folding in the Nucleation and Growth of Protein-Metal-Organic Frameworks. Chem Mater. 2022, 24 (18), 8336-8344.

B.1 Supplementary Figures

Protein Characterization

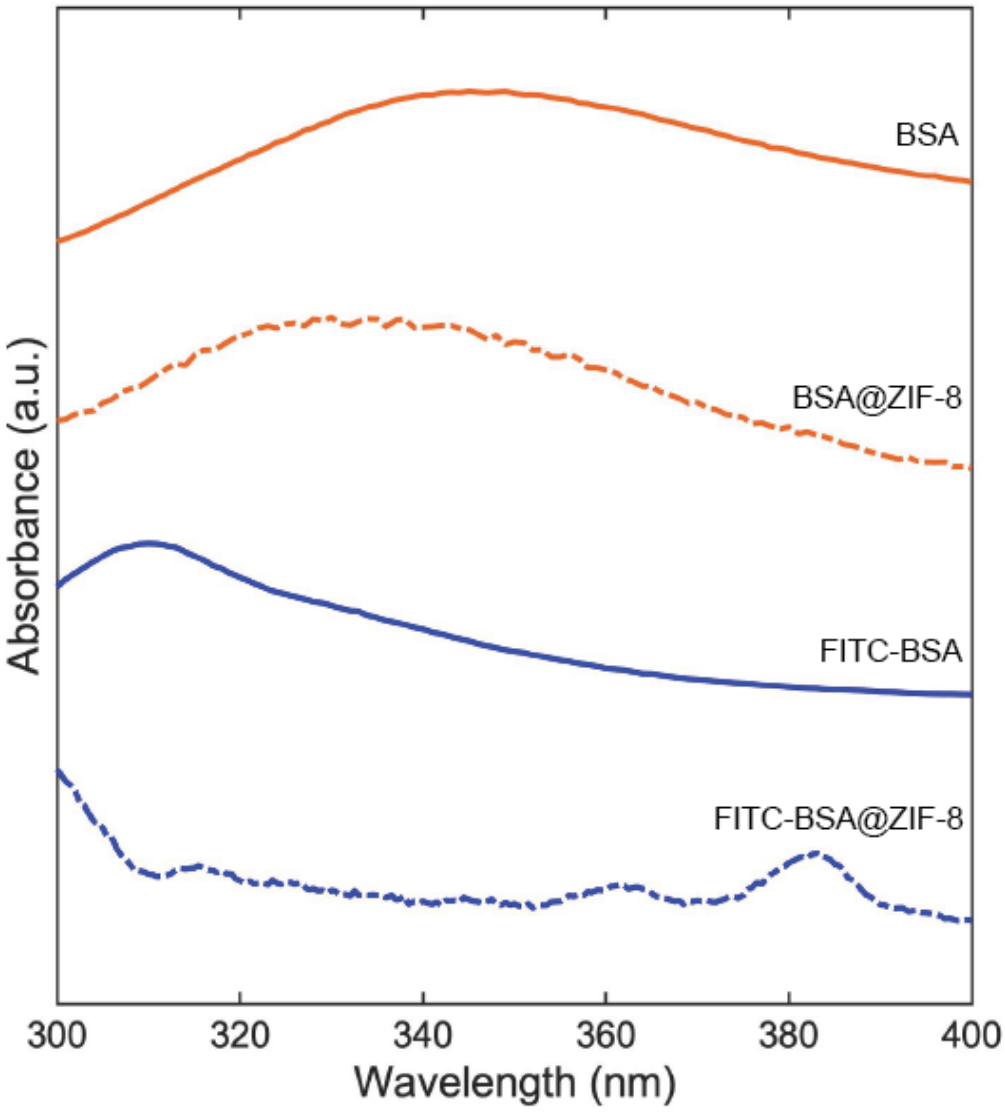

Figure B1: Intrinsic tryptophan fluorescence spectra of BSA (orange, solid), BSA@ZIF-8 (orange, dashed), FITC-BSA (blue, solid), and FITC-BSA@ZIF-8. Samples were excited at 280 nm and the emission was analyzed from 300-400 nm.

Crystal structure analysis

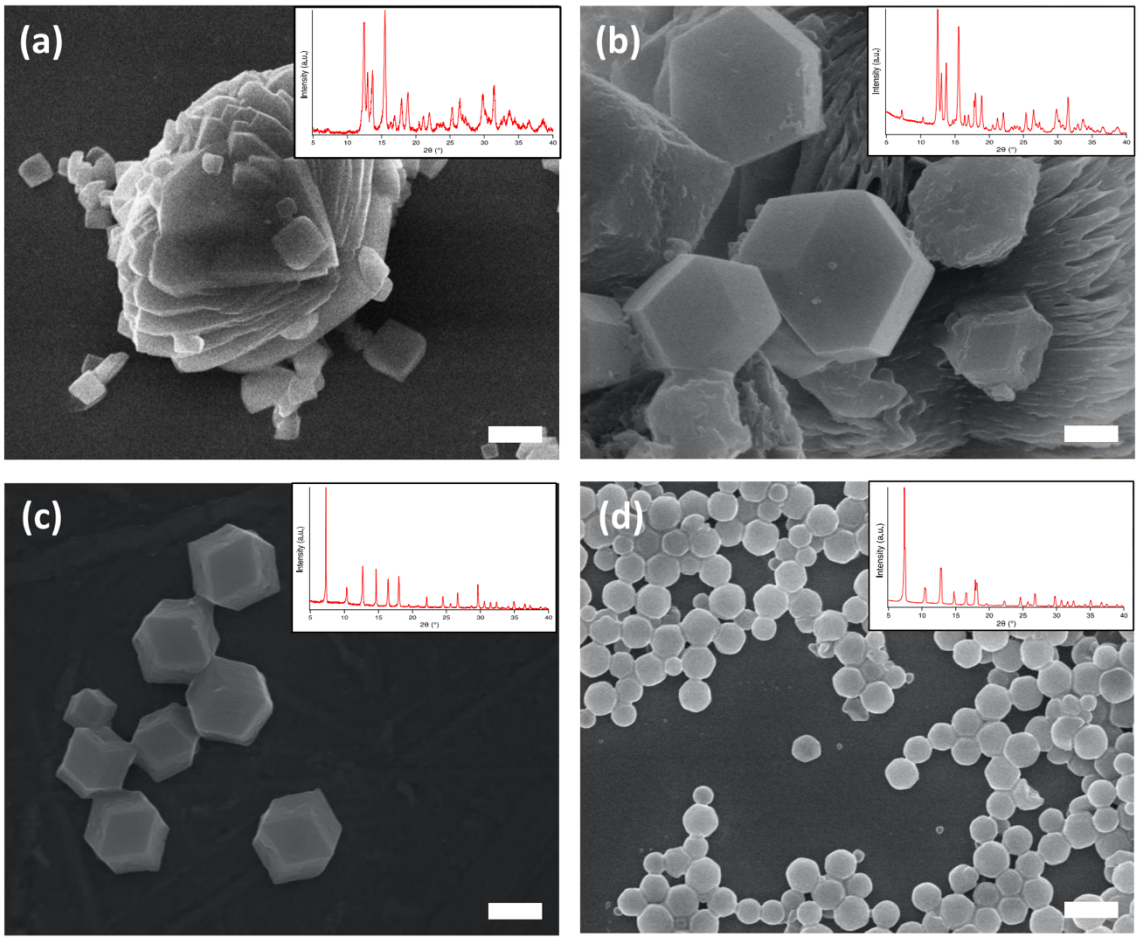

Figure B2: SEM images of ZIF-8 at (a) 4:1 (b) 17.5:1 (c) 35:1 (d) 70:1. At 4:1, ZIF-8(dia) is exclusively seen whereas at 17.5:1, a mixture of ZIF-8(dia) and ZIF-8(sod) is seen. At 35:1 and 70:1, only ZIF-8 sod is present. Scale bar is 1 µm.

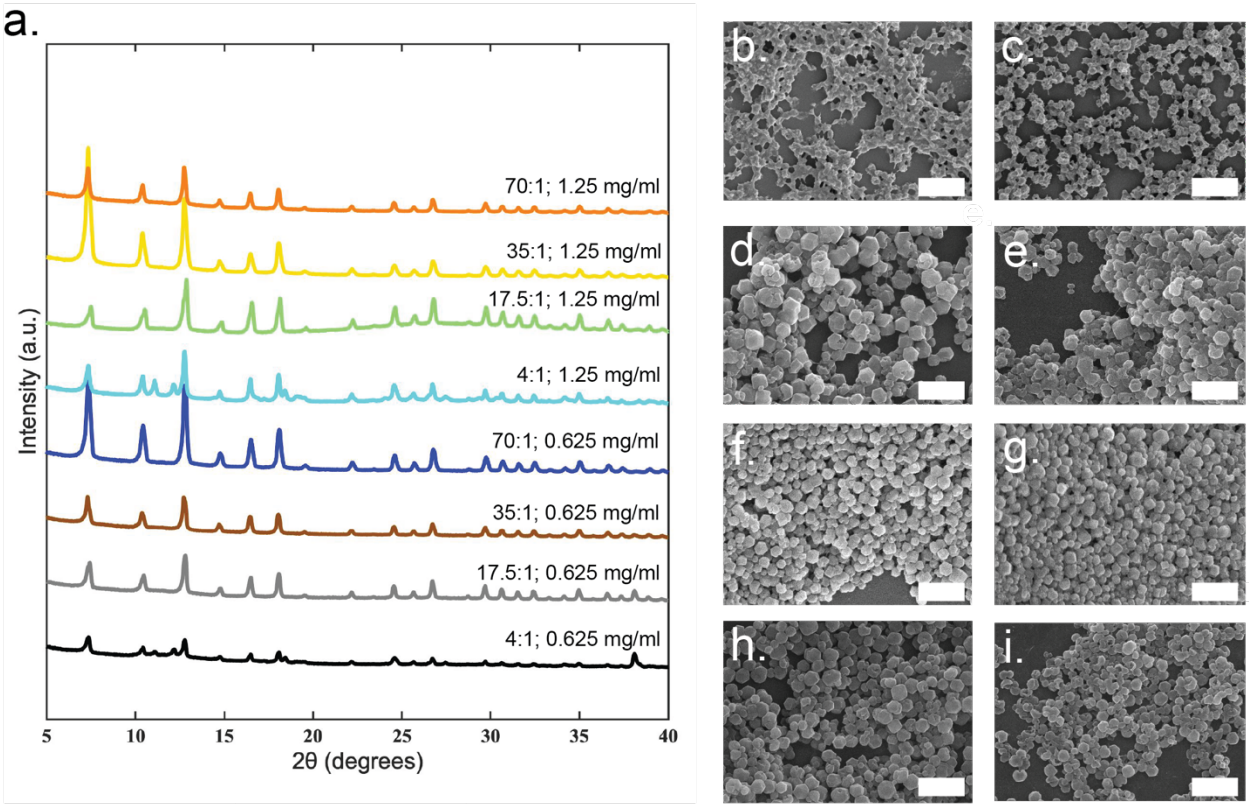

Figure B3: (a.) PXRD patterns of BSA@ZIF-8 at varying HmIm:Zn ratios and at final BSA concentrations of either 1.25 mg/ml or 0.625 mg/ml. SEM images of BSA-ZIF-8 with final protein concentrations of 1.25 mg/ml BSA at HmIm:Zn ratios of (b) 4:1 (d) 17.5:1 (f) 35:1 (h) 70:1, and 0.625 mg/ml BSA at HmIm:Zn ratios of (c) 4:1 (e) 17.5:1 (g) 35:1 (i) 70:1. Scale bar is 1 µm.

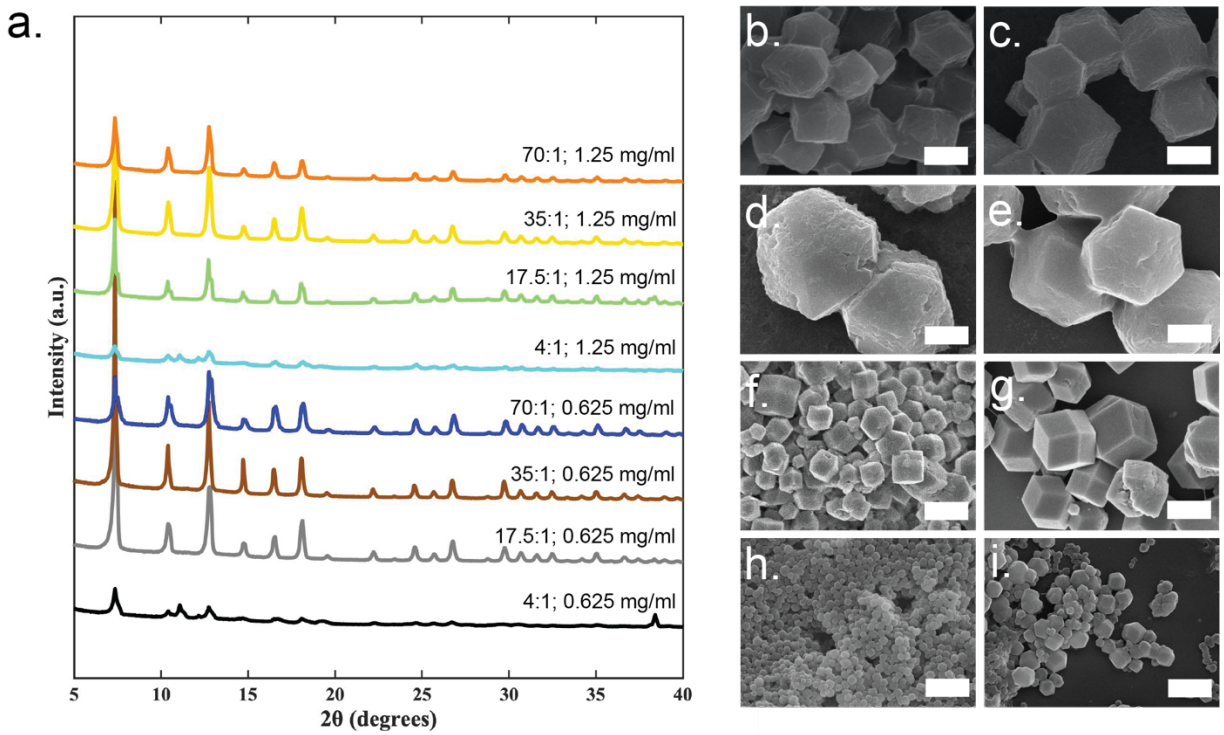

Figure B4: (a.) PXRD patterns of FITC-BSA@ZIF-8 at varying HmIm:Zn ratios and at final FITC-BSA concentrations of either 1.25 mg/ml or 0.625 mg/ml. SEM images of FITC-BSA@ZIF-8 crystals with final protein concentrations of 1.25 mg/ml FITC-BSA at HmIm:Zn ratios of (b) 4:1 (d) 17.5:1 (f) 35:1 (h) 70:1, and with final protein concentrations of 0.625 mg/ml FITC-BSA at HmIm:Zn ratios of (c) 4:1 (e) 17.5:1 (g) 35:1 (i) 70:1. Scale bar is 1 µm.

Crystal Size analysis

SEM was used to determine crystal diameter by averaging the length of ~50-100 crystals per sample using Fiji, ImageJ (Figure S5). From the analysis, crystals sizes were binned into groups of 250 nm and plotted with Prism.

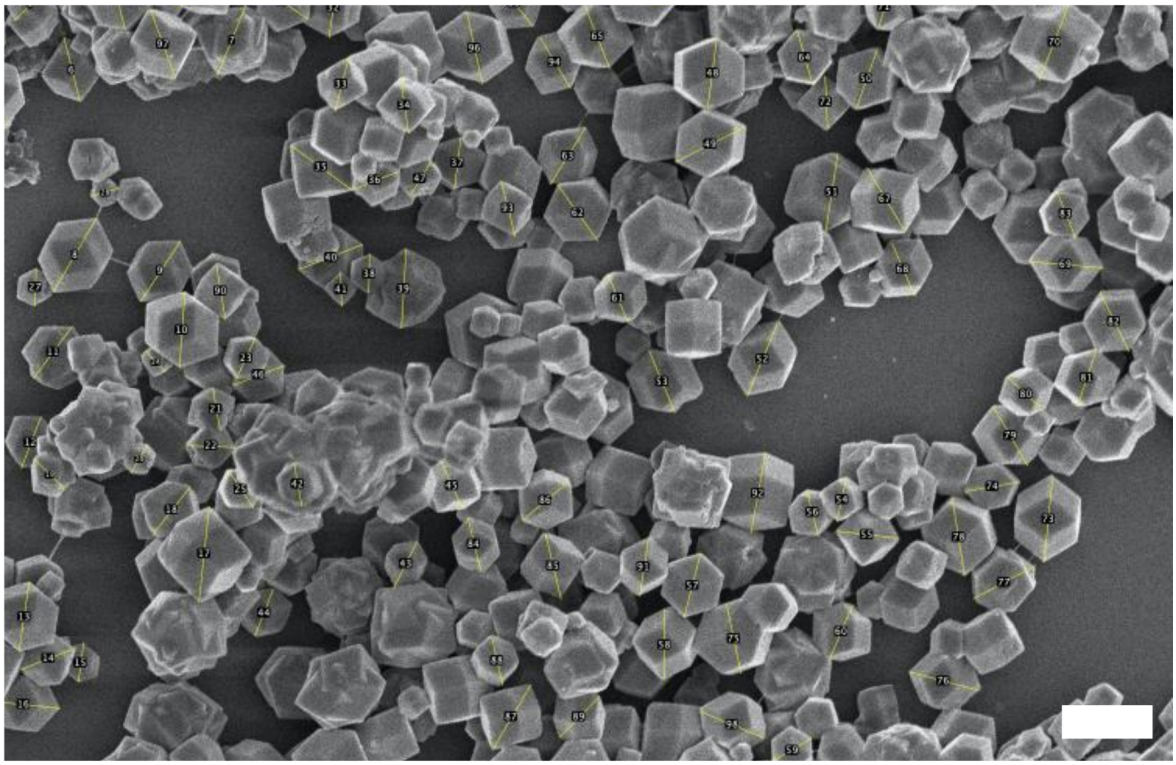

Figure B5: SEM image (scale bar 2 µm) of FITC-BSA-ZIF-8 at protein concentration of 0.625 mg/ml at 35 : 1 (HmIm : Zn). Numbered yellow lines indicate the diameter of the crystal measured using Fiji, ImageJ.

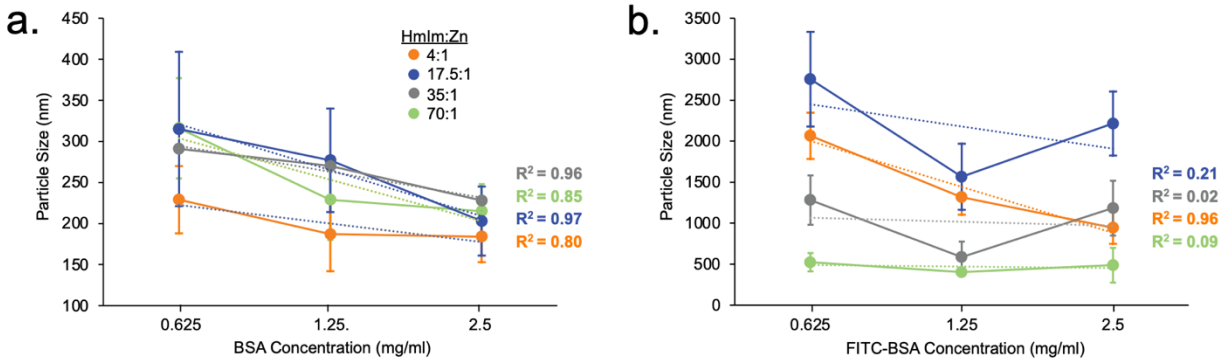

Figure B6: Plots of protein concentration versus size (nm) for (a) BSA-ZIF-8 crystals and (b) FITC-BSA-ZIF-8 crystals. The following HmIm:Zn were plotted for each sample: 4:1 (orange), 17.5:1 (blue), 35:1 (grey), 70:1(green). Results demonstrate that for BSA-ZIF-8, the size for each HmIm:Zn decreases with increasing protein concentration. However, no trends could be observed for the FITC-BSA-ZIF-8 systems.

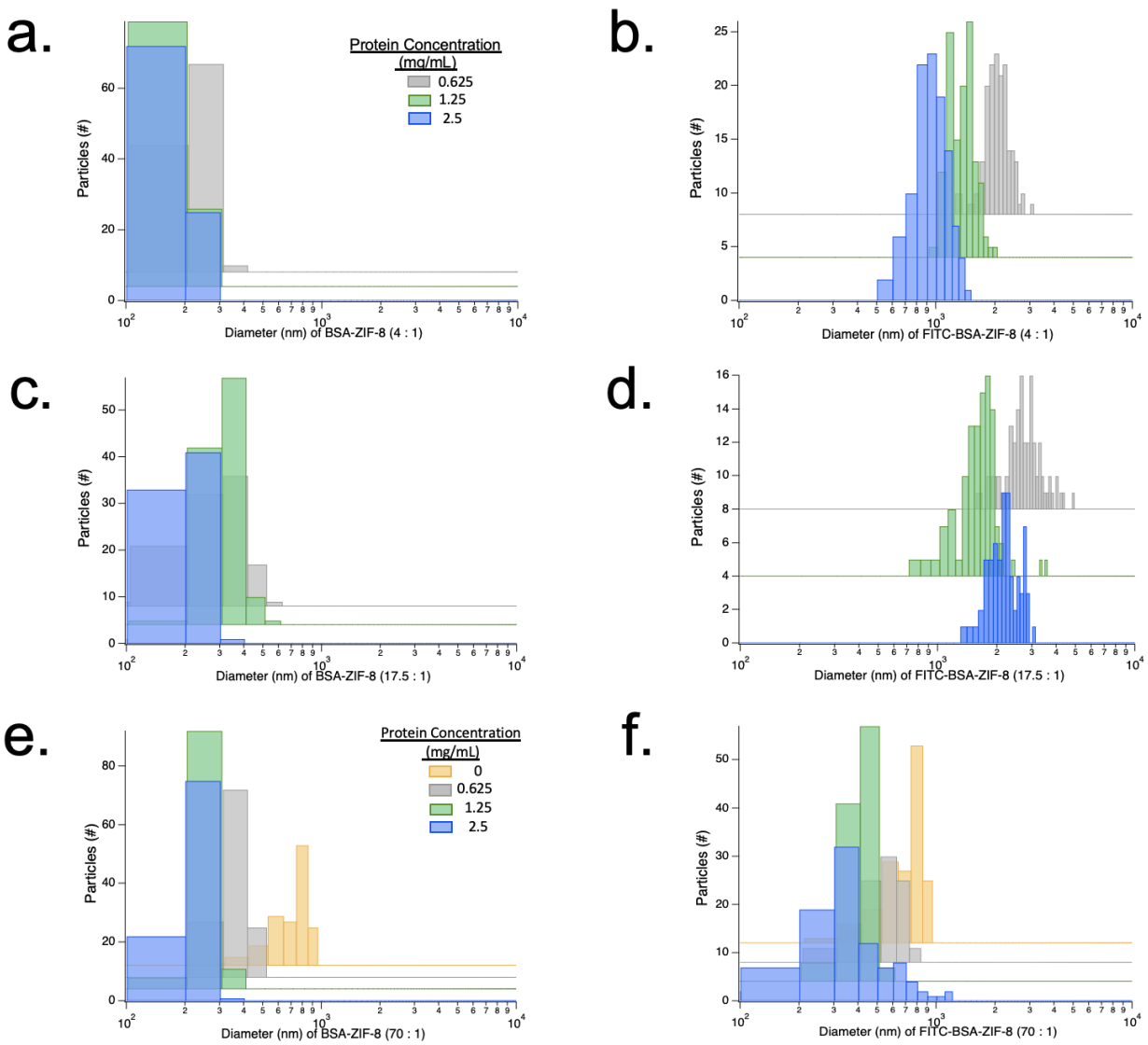

Figure B7: Histogram of size measurements from crystals in SEM images of (a) BSA-ZIF-8 at 4:1 (b) FITC-BSA-ZIF8 at 4:1 (c) BSA-ZIF-8 at 17.5:1 (d) FITC-BSA-ZIF-8 at 17.5:1 and (e) BSA-ZIF-8 at 70:1 (f) FITC-BSA-ZIF-8 70:1 using protein concentrations of 0.625 mg/ml (grey), 1.25 mg/ml (green), and 2.5 mg/ml (blue). Yellow bars in 70:1 systems indicate crystals without protein.

Crystal Morphology

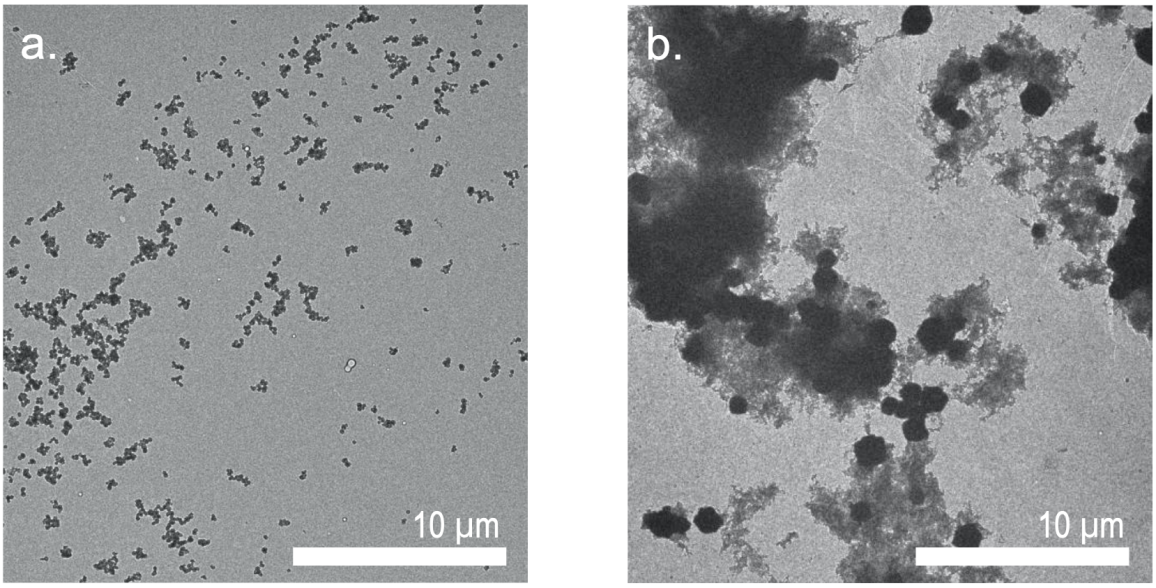

Figure B8: TEM images taken of low magnification of (a) BSA-ZIF-8 and (b) FITC-BSA-ZIF-8. The systems were at 35:1 (HmIm:Zn) with final protein concentrations of 2.5 mg/ml. Samples were washed 3x in water, 1x in methanol, and diluted 10x in methanol Images were taken at low magnification to capture a broad area of sample and validate that our findings are consistent throughout the sample.

Protein Incorporation and Encapsulation Efficiency

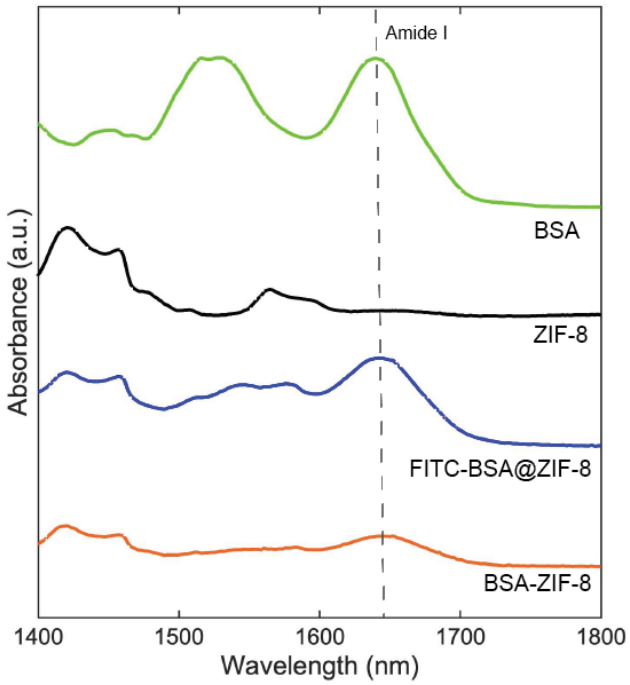

Figure B9: FT-IR spectra of BSA(green), ZIF-8 (black), FITC-BSA@ZIF-8 (blue), and BSA@ZIF-8 (orange). The protein@MOFs were centrifuged for 10 minutes at 10,000 rpm and washed with water 3x. Samples washed with water were compared to samples that were washed with an additional time with 1x SDS buffer, but little to no difference could be observed in the protein@MOF spectra.

B.2 Supplemental Methods

When measuring intrinsic tryptophan fluorescence of a MOF supernatant, excess HmIm and Zinc ions are likely in solution coordinating with remaining protein. Such coordination would alter the fluorescent intensity compared to the isolated protein. HmIm can influence fluorescence intensity based on two factors: pH and BSA/HmIm interactions.[1,2] When dissolved in water, HmIm alters the pH by making it more basic due to HmIm having a pka ~8.[3] This change in the pH for the protein environment is not desirable since the protein can undergo conformational change causing varying fluorescent intensities. However, diluting the supernatants in phosphate

buffer (pH 6.7) alleviates this change in pH, assuring that BSA is in the same protein conformation for each measurement.

To address the influence of BSA/HmIm interactions, fluorescent controls were made using each protein/HmIm condition for the 4:1, 17.5:1, 35:1, and 70:1 systems, excluding the zinc. For each control, BSA (10 mg/ml 5mg/ml, 2.5 mg/ml, 1.25 mg/ml, 0.625 mg/ml, 500 uL), HmIm (5600 mM, 2800 mM, 1400 mM, and 3200 mM, 500 uL, and water (1 ml) were combined and then diluted by 10 in phosphate buffer to give final final protein concentrations of 0.25 mg/ml, 0.125 mg/ml, 0.0625 mg/ml, 0.312 mg/ml and 0.0156 mg/ml and final HmIm concentrations of 140 mM, 70 mM, and 35 mM and 8 mM. Each system was measured by exciting at 280 nm and measuring the emission at 340 nm. It was reported that as the HmIm concentration decreases, the slope of the curve increases (Figure B10). The encapsulation efficiencies for each system were calculated using each calibration curve – one with protein and HmIm and the other with protein only. However, the results between the two calculations only varied by 0-8% due to low protein concentrations in supernatant resulting in lower intensities. For each of the calibration curves, with and without HmIm, the lower protein concentration ranges appear very close together, which explains the similar EE% calculated with both curves. This method potentially would not have worked as well if higher protein concentrations/intensities had been recorded for the supernatants. Thus, the EE% were recorded in the main text based on the protein only calibration curve.

To prevent protein-zinc binding interactions from altering the fluorescent measurements, EDTA was added to sequester zinc ions. Controls were made by first incubating BSA and zinc together in a solution containing BSA (2.5 mg/ml, 500 uL), zinc acetate (40 mM), and water (500 uL). Once incubated for ~30 min, 0.2 uL of the solution was added to separate vials containing 2.8 mL of phosphate buffer with various concentrations of EDTA (0 mM, 10 mM, 20 mM, 45 mM,

and 90 mM). It was found that at EDTA concentrations greater than or equal to 20 mM, the fluorescent intensity plateaus (Figure B11a). Upon addition of BSA (2.5 mg/ml, 0.5 mL), Zinc Acetate (40 mM, 1 mL), and water (0.5 mL), the solution becomes turbid due formation of BSA/Zinc aggregates (Figure B11b). Upon addition of 90 mM EDTA, the solution becomes clear due to the metal chelator sequestering the metal ions from BSA.

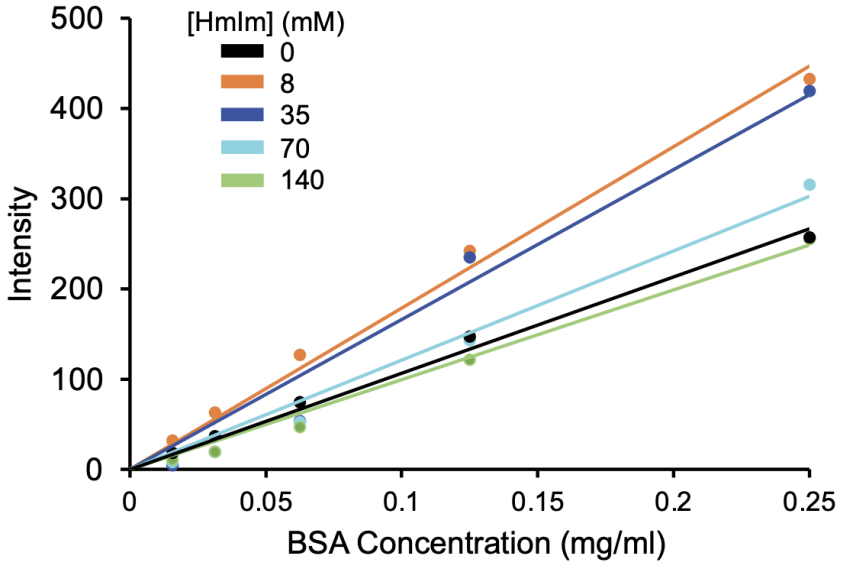

Figure B10: HmIm fluorescent control using protein concentrations of 0.25 mg/ml, 0.125 mg/ml, 0.0625 mg/ml, 0.312 mg/ml and 0.0156 mg/ml with HmIm concentrations of 0 mM (black), 8 mM (orange), 35 mM (yellow), 70 mM (blue), and 140 mM (green).

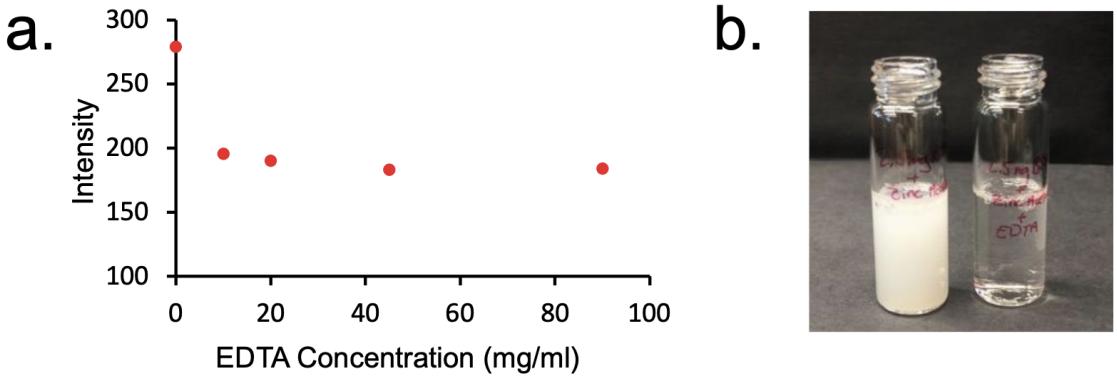

Figure B11: (a) Fluorescent measurements of addition of EDTA (0 mM, 10 mM, 20 mM, 45 mM, and 90 mM, 2.8 mL) to solution of BSA/Zinc solution (0.2 mL). (b). Image of BSA/Zinc solution before (left) and after (right) addition of EDTA (90 mM).

Calibration Curves

A BSA calibration curve was made using the following protein concentrations in phosphate buffer (pH 6.7) with 80 mM EDTA: 0.25 mg/ml, 0.125 mg/ml, 0.0625 mg/ml, 0.03125 mg/ml, and 0.0156 mg/ml. Triplicates of each system were made and measured with Cary Eclipse Spectrophotometer using an excitation of 280 nm and emission of 340 nm (Figure B12a). Supernatants of each MOF system were diluted by 10-fold in the Phosphate/EDTA solution and compared to the standard calibration curve.

FITC-BSA calibration curves were made using the following protein concentrations: 0.025 mg/ml, 0.0125 mg/ml, 0.00625 mg/ml, 0.003125 mg/ml, and 0.00156 mg/ml. Triplicates of each concentration were made and measured using an excitation of 494 nm and emission of 520 nm (Figure B12b). Supernatants of FITC-BSA-ZIF-8 systems were diluted by 100-fold in phosphate buffer (pH 6.7) and compared to the standard calibration curve.

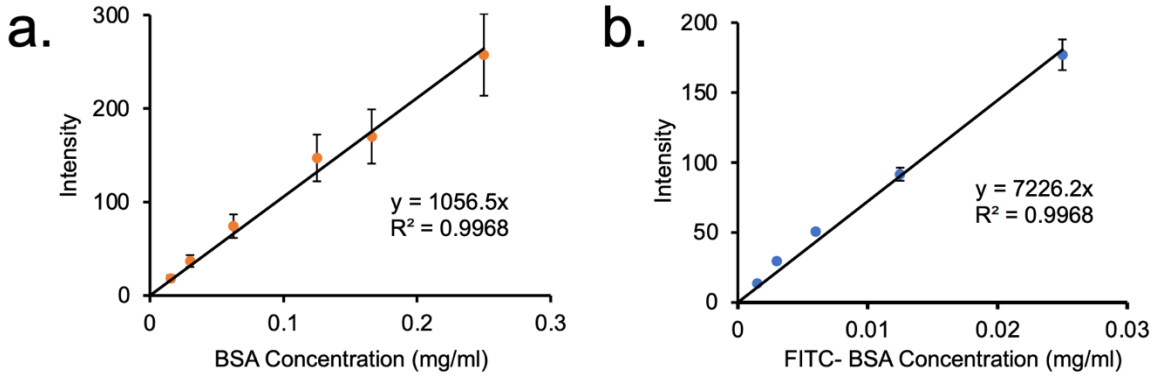

Figure B12: Tryptophan fluorescence standard calibration curve for (a) BSA and (b) FITC-BSA. Triplicate measurements of separate protein stocks were taken for each protein

concentration and averaged. Each data point represents an average of three runs with the error bars indicating the standard deviation of the three runs.

Bradford Assay

To validate the EE% results from intrinsic tryptophan fluorescence, the Bradford reagent is utilized. The Bradford reagent used was a ready-made solution from Sigma Aldrich containing Coomassie Blue G-250. To make the standard calibration curve, Bradford reagent (3 mL) was added to 100 μL of protein solution (0.1mg/mL, 0.425 mg/mL, 0.75 mg/mL, 1.05 mg/mL, and 1.4 mg/mL) and inverted gently to mix. The samples were incubated at room temperature for 10 minutes. In disposable cuvettes, the absorbances of the protein samples were taken at 595 nm using UV-Vis on a Nanodrop 2000C (Figure B4). The supernatants (100 μL) from BSA -ZIF-8 systems (4:1, 17.5: 1, 35:1, and 70:1) were then mixed with Bradford reagent (3 mL)) and measured with absorbance. EE% were calculated based on the standard calibration (Figure B13). Results from the measurements were then compared to the fluorescent method (Figure B14).

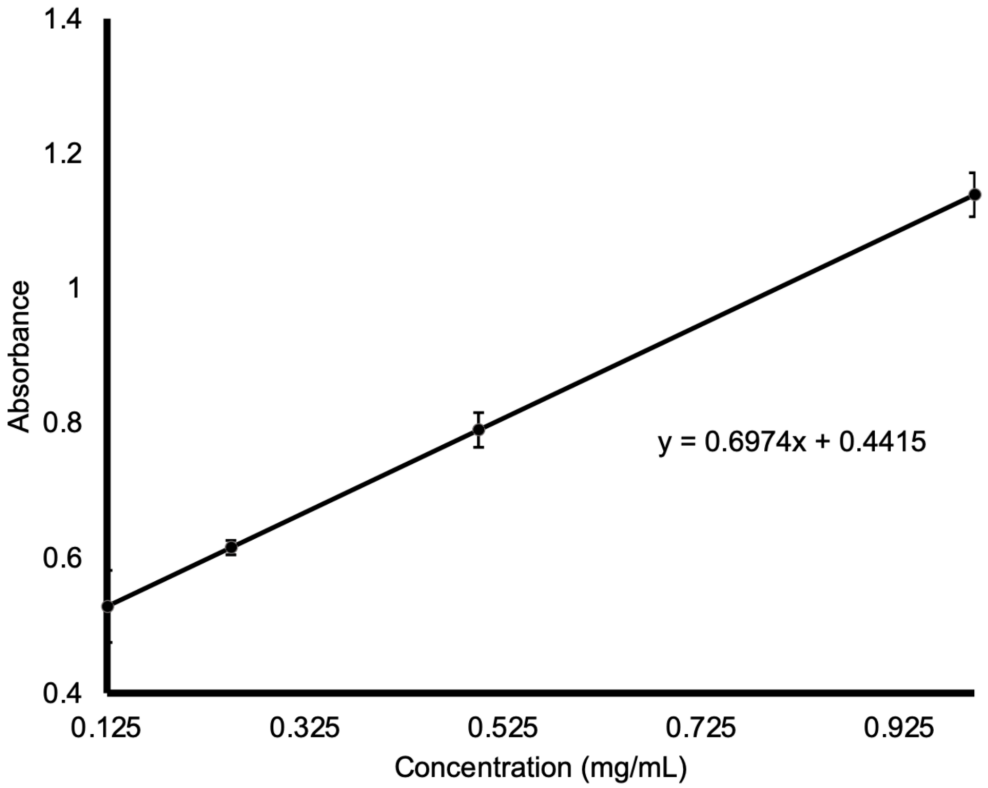

Figure B13: Bradford assay standard calibration curve for BSA.

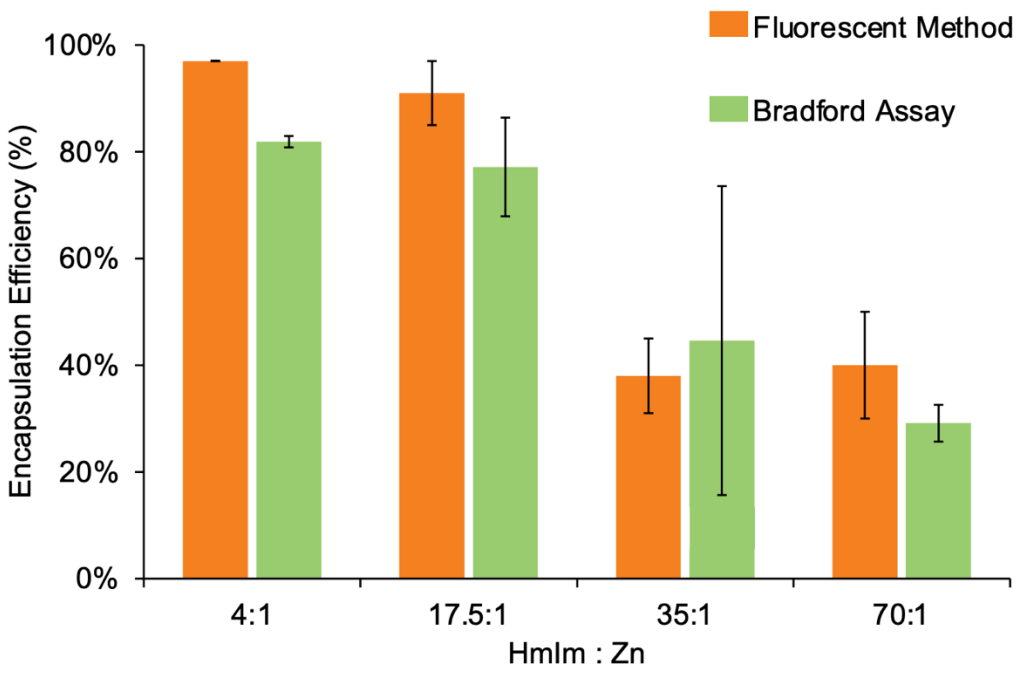

Figure B14: EE% method comparison of protein@MOF supernatants using the Bradford assay (orange) and the fluorescent method (blue).

In situ XRD analysis

Instantaneous peaks or valleys can be caused by low signal to noise, so a sliding-window Gaussian weighted mean was applied to each XRD region where the mean signal was used to smooth the data (eq 1). A standard deviation of 3 data points was used. The same trends can be seen in both the raw and smoothed data shown in Figure A15.

$$S_s = \text{signal convolution } (S_r, k_{gauss}) \quad (1)$$

where S_s: Gaussian smoothed mean signal
Sr: Raw mean signal
k_{gauss}: 1D normalized Gaussian kernel

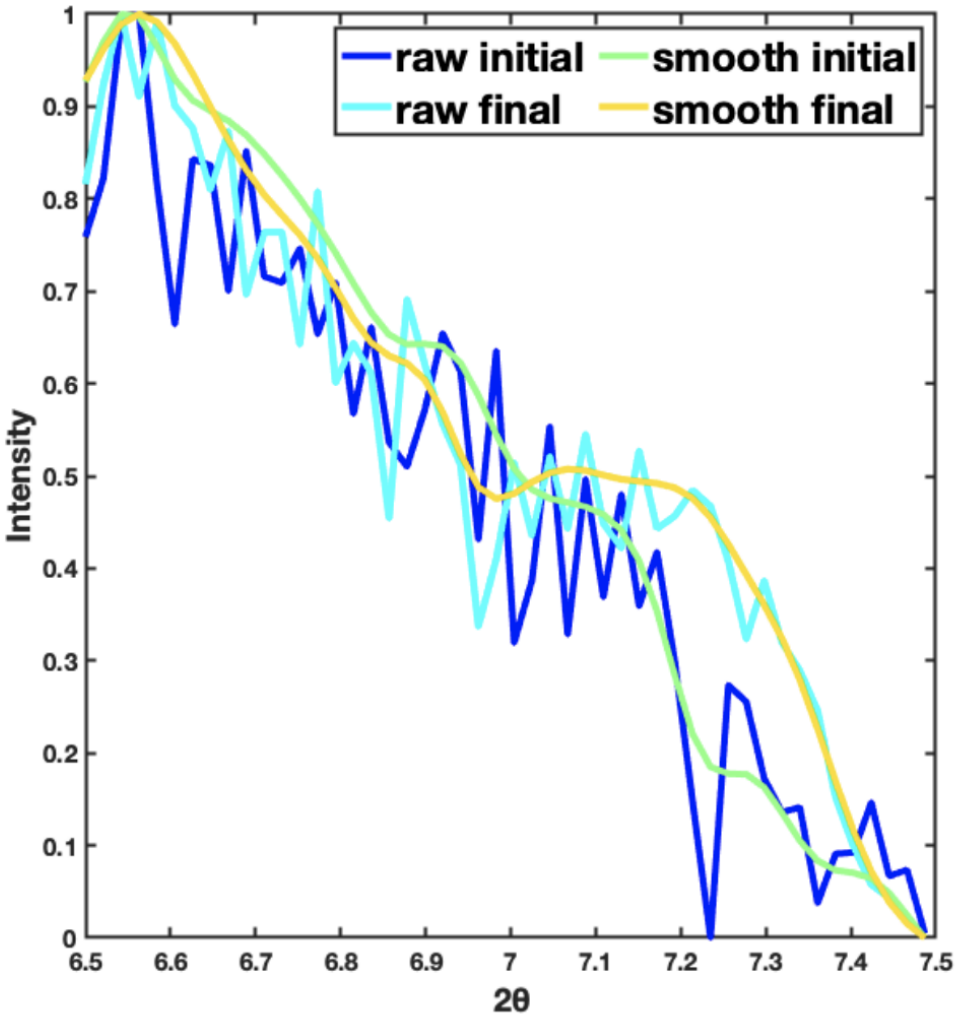

Figure B15: In situ XRD Data of FITC-BSA@ZIF-8 at initial (0 mins) and final (450 minutes) timepoints. Raw data has been plotted for the initial (purple) and final (blue) XRD patterns. Smoothed data has also been plotted for the initial (green) and final (yellow) XRD patterns.

Particle Size Analysis

Particles were manually picked and overlaid using the same method as Ogata et.al.[4] The sizes of the particles were then calculated using a full-width-half-max algorithm to determine the size between multiple particles in a consistent manner.

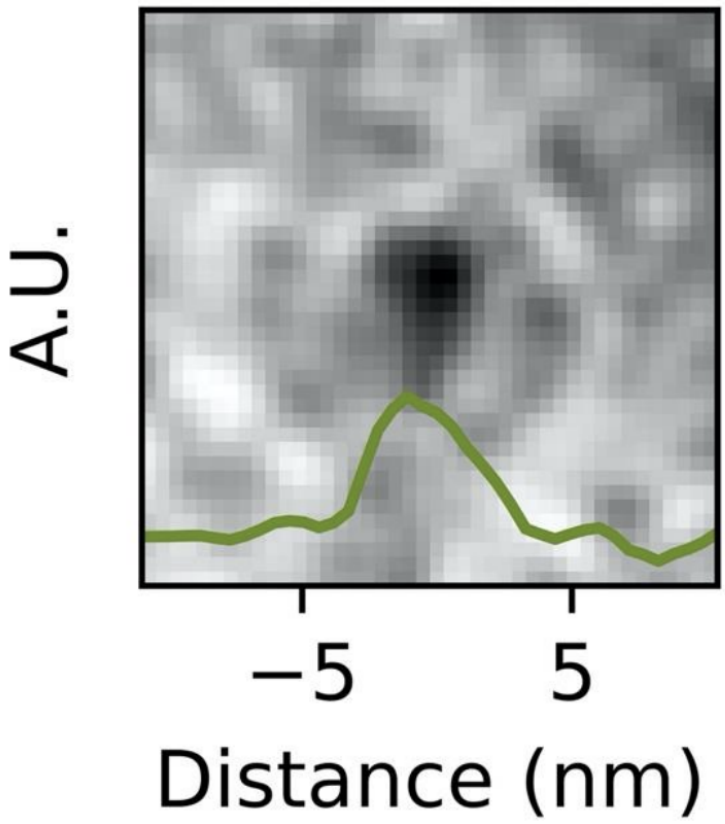

Figure B16: Size Analysis of particles in cryoTEM image at 1hr of 35:1 FITC-BSA@ZIF-8 with final protein concentration of 2.5 mg/ml.

Partially Unfolded Protein Analysis

BSA was unfolded by aging a 10 mg/ml BSA solution in water at room temperature for 6 months.

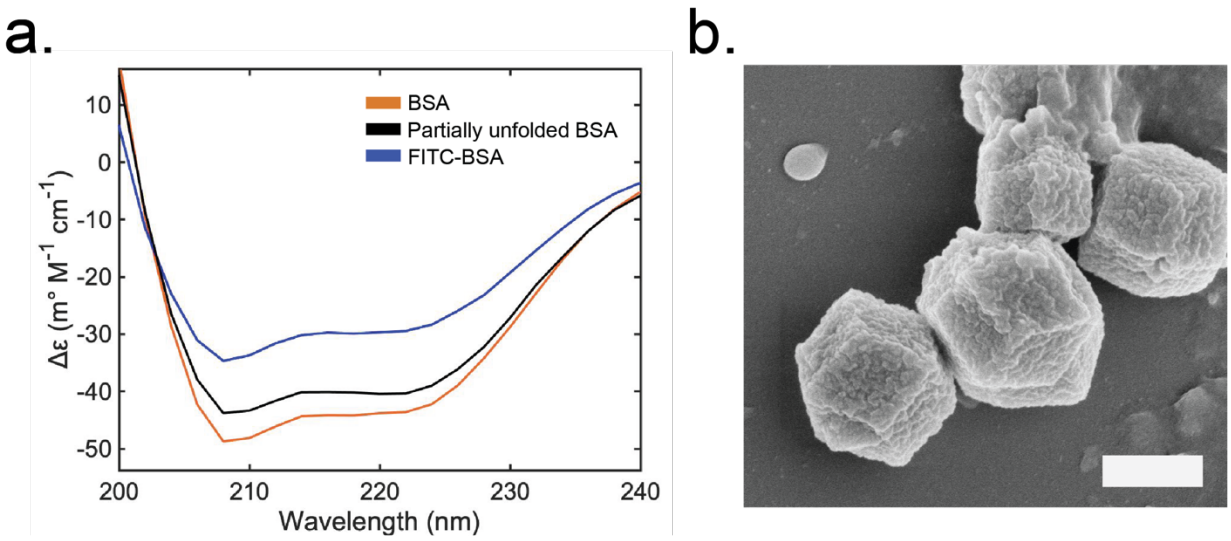

Figure B17: a.) Circular dichroism of BSA (orange), partially unfolded BSA (black), and FITC-BSA (blue). SEM image of partially unfolded BSA encapsulated in 35:1 ZIF-8 at final protein concentrations of 2.5 mg/ml. Scale bar is 500 nm.

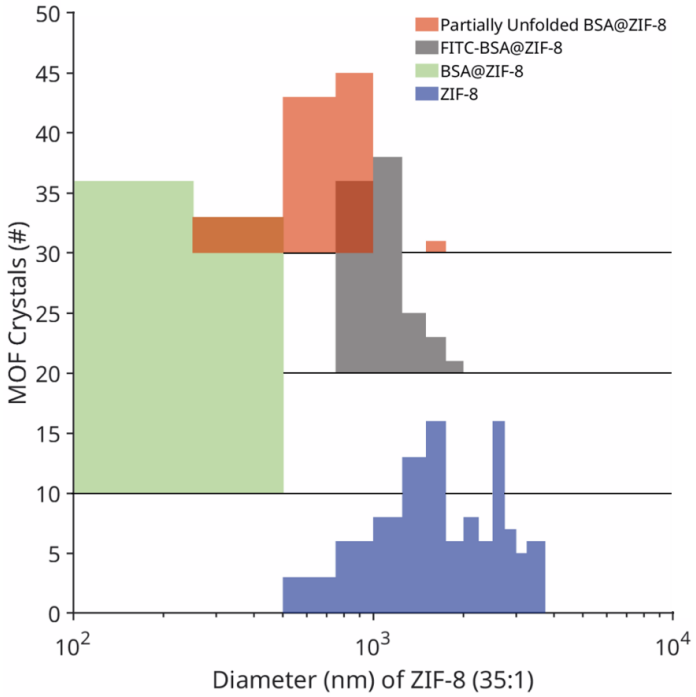

Figure B18: Size histogram of the particle sizes of partially unfolded BSA in ZIF-8 (orange), FITC-BSA-ZIF-8 (gray), BSA@ZIF-8 (green), and ZIF-8 (blue). MOFs were synthesized at HmIm:Zn ratio of 35:1 with a final protein concentration of 2.5 mg/ml.

B.3 Supplemental Figures Continued

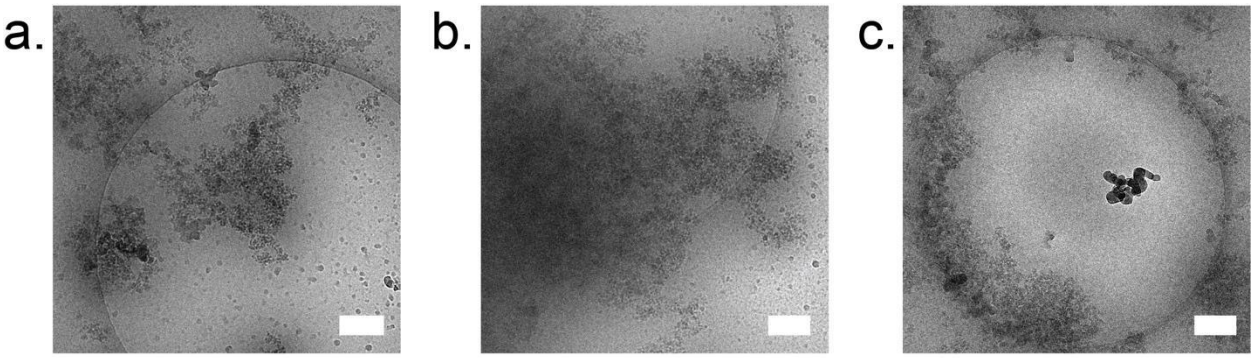

Figure B19: CryoTEM images of FITC-BSA@ZIF-8 at 1 minute when at HmIm:Zn ratio of 35:1 and final protein concentration of 2.5 mg/ml. The scale bars for (a.) and (b.) are 100 nm, and the scale bar for (c.) is 200 nm.

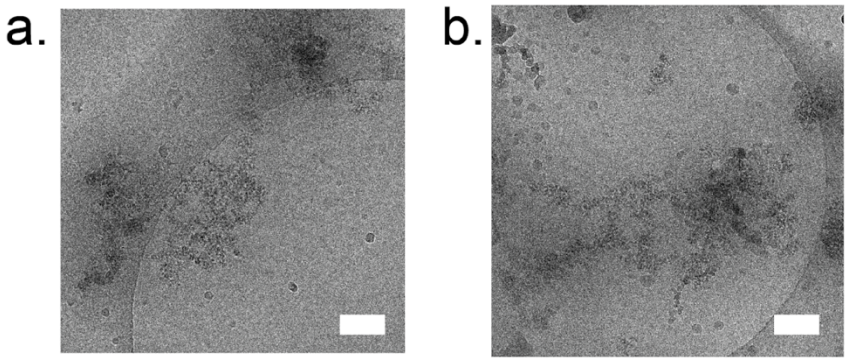

Figure B20: CryoTEM images of FITC-BSA@ZIF-8 at 5 minutes when at HmIm:Zn ratio of 35:1 and final protein concentration of 2.5 mg/ml. The scale bar is 100 nm.

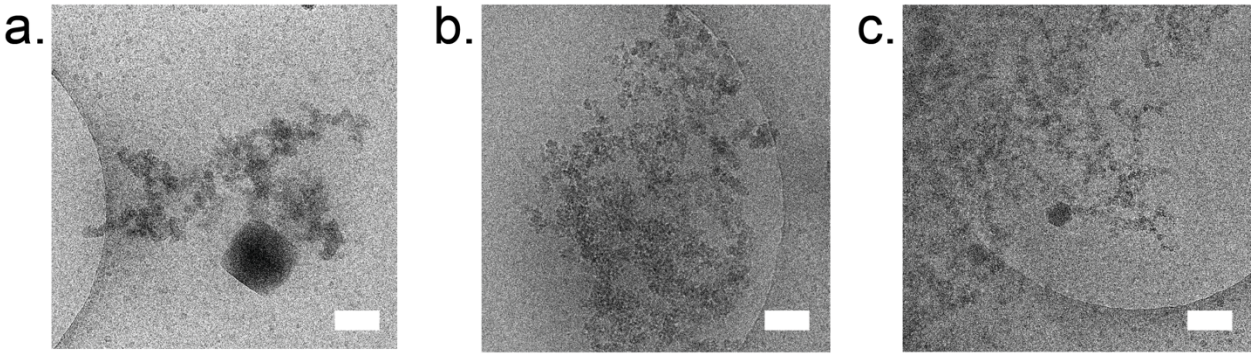

Figure B21: CryoTEM images of FITC-BSA@ZIF-8 at 30 minutes when at HmIm:Zn ratio of 35:1 and final protein concentration of 2.5 mg/ml. The scale bar is 100 nm.

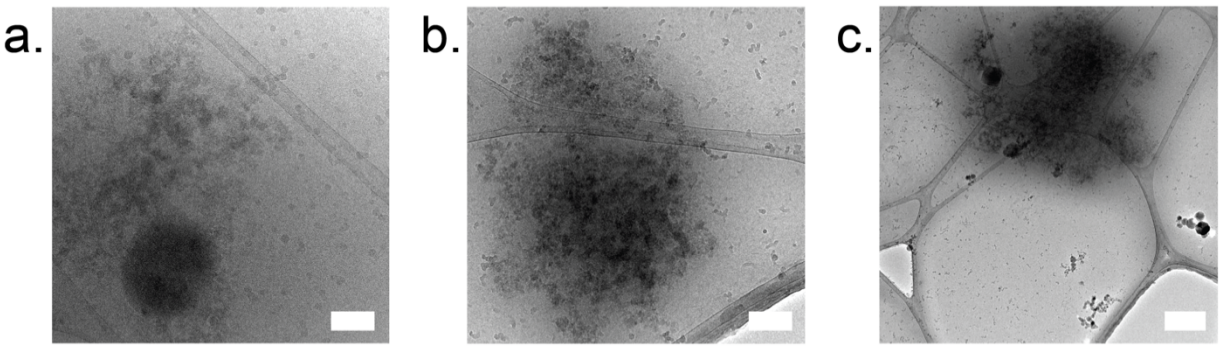

Figure B22: CryoTEM images of FITC-BSA@ZIF-8 at 1 hour when at HmIm:Zn ratio of 35:1 and final protein concentration of 2.5 mg/ml. The scale bars for (a.) and (b.) are at 100 n,m and the scale bar for (c.) is at 1 µm.

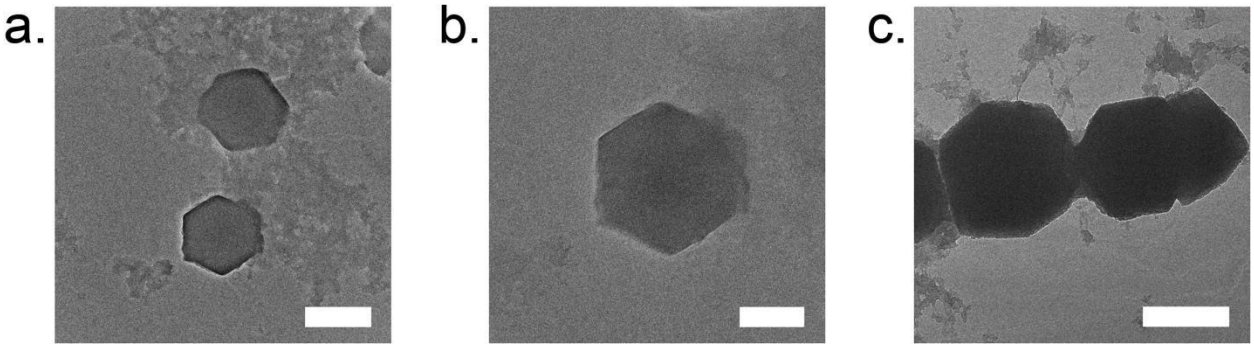

Figure B23: Dry state TEM of FITC-BSA@ZIF-8 after 24-hour synthesis and 3x washes with water. Scale bar for (a.) is 500 nm, and the scale bar for (b.) and (c.) is at 1 µm.

B.4 Supplemental References:

(1) Liao, S.-M.; Du, Q.-S.; Meng, J.-Z.; Pang, Z.-W.; Huang, R.-B. The Multiple Roles of Histidine in Protein Interactions. *Chem Cent J* **2013**, *7*, 44. https://doi.org/10.1186/1752-153X-7-44.
(2) Guckeisen, T.; Hosseinpour, S.; Peukert, W. Effect of PH and Urea on the Proteins Secondary Structure at the Water/Air Interface and in Solution. *Journal of Colloid and Interface Science* **2021**, *590*, 38–49. https://doi.org/10.1016/j.jcis.2021.01.015.

(3) Lenarcik, B.; Ojczenasz, P. The Influence of the Size and Position of the Alkyl Groups in Alkylimidazole Molecules on Their Acid-Base Properties. *Journal of Heterocyclic Chemistry* **2002**, *39* (2), 287–290. https://doi.org/10.1002/jhet.5570390206.
(4) Ogata, A. F.; Rakowski, A. M.; Carpenter, B. P.; Fishman, D. A.; Merham, J. G.; Hurst, P. J.; Patterson, J. P. Direct Observation of Amorphous Precursor Phases in the Nucleation of Protein–Metal–Organic Frameworks. *J. Am. Chem. Soc.* **2020**, *142* (3), 1433–1442. https://doi.org/10.1021/jacs.9b11371.

Appendix C:

Supplementary Information for Chapter 4.

Appendix C: Supplementary Information for Chapter 4

C.1 Supplementary Figures

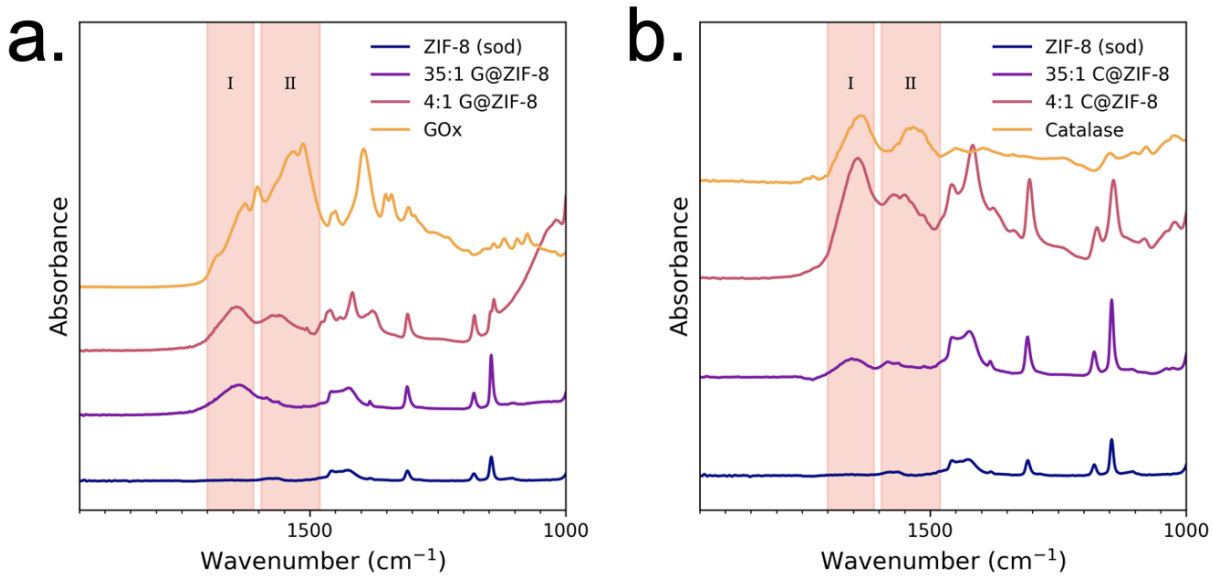

Figure C1: FTIR spectra of enzymes (yellow) and enzyme MOFs at 4:1 (pink) and 35:1 (purple) synthetic conditions for a.) GOx and b.) Catalase. FTIR of ZIF-8 without enzymes (blue) is also included. Enzyme@ZIF-8 samples were washed 3x with water and the precipitant was analyzed with Jasco V-670 spectrometer. Data was plotted using the pandas and matplotlib pyplot python libraries, used in an author-written python script. Amide I and amide II peaks are highlighted indicating incorporation of enzymes in each biocomposite.

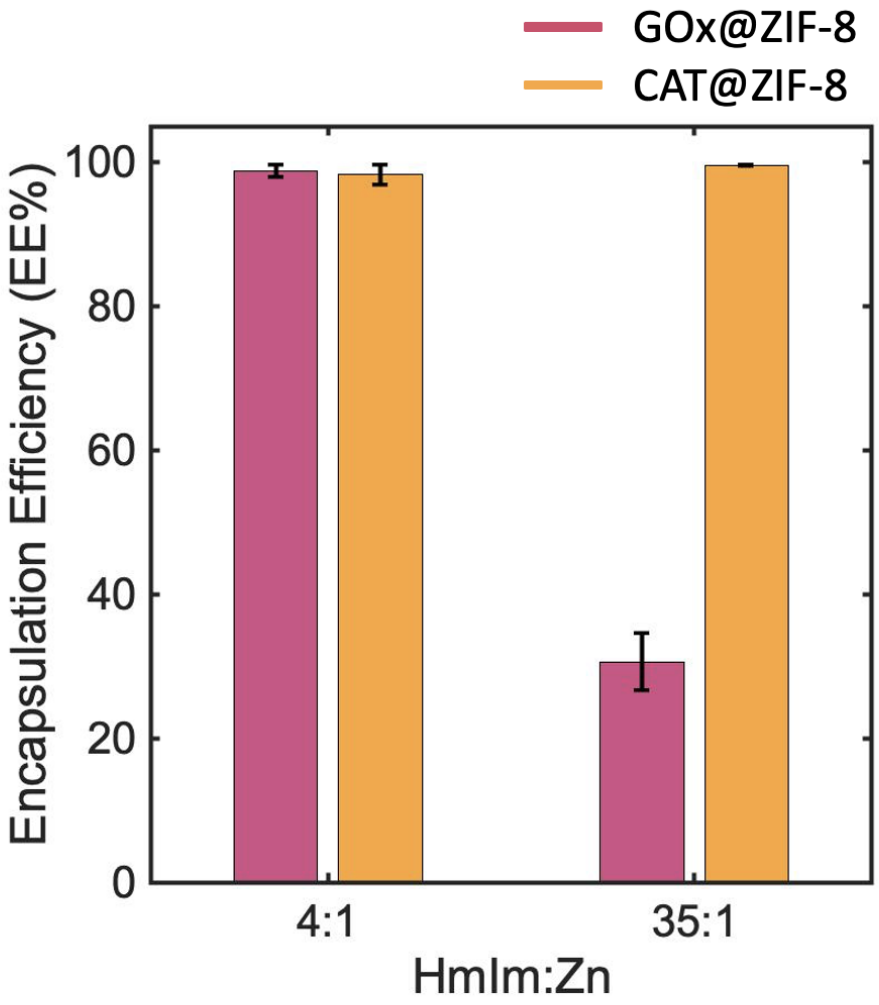

Figure C2: Encapsulation efficiency of a.) GOx@ZIF-8 and b.) CAT@ZIF-8 at 4:1 and 35:1 ratios of HmIM:Zn. Calculations were determined using a standard calibration curve of each protein concentration using intrinsic tryptophan fluorescence while following a previously published manuscript.

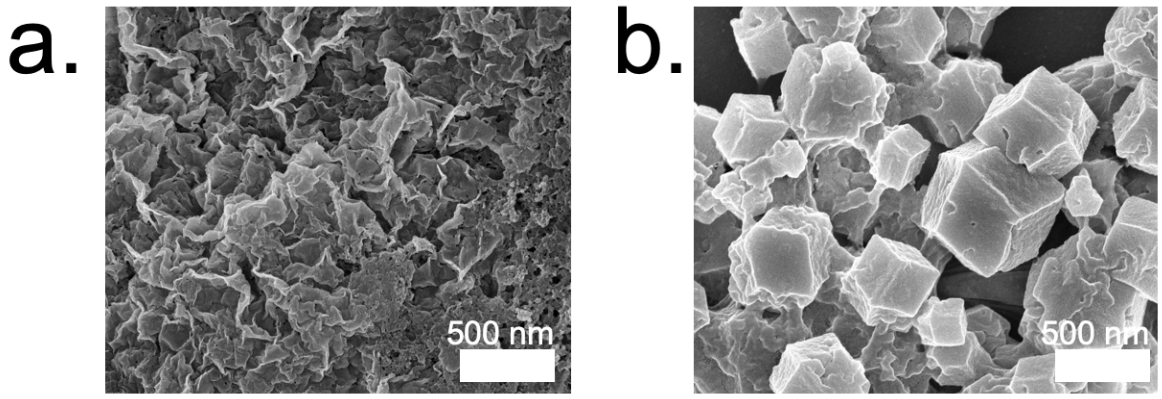

Figure C3: SEM images of CAT@ZIF-8 samples when synthesized at HmIm:Zn ratios of a.) 4:1 and b.) 35:1.

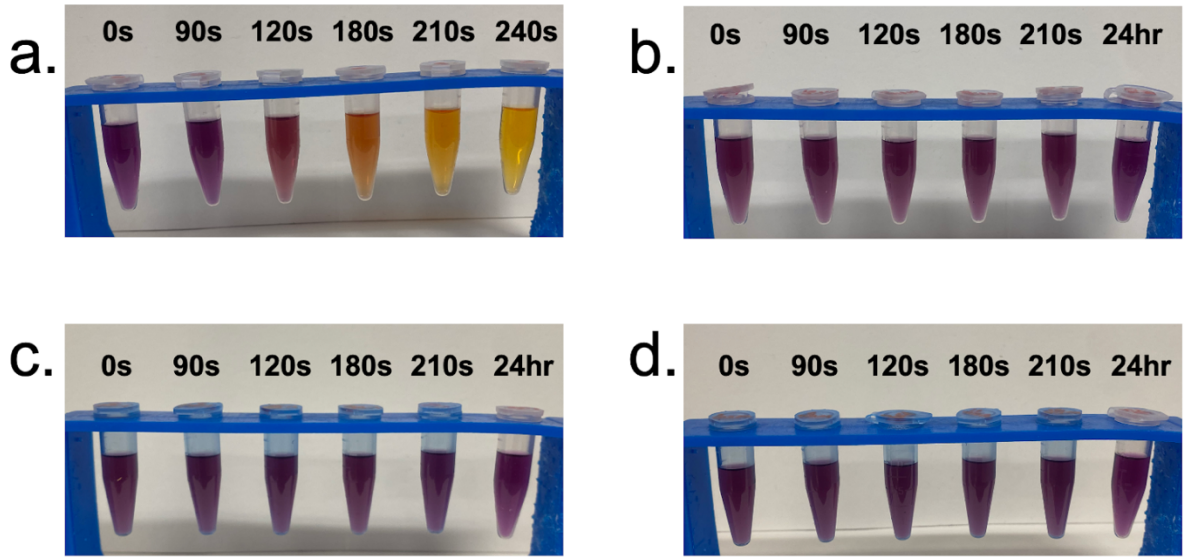

Figure C4: Images from the reaction of a.) CAT, b.) 4:1 CAT@ZIF-8 after 3x washes with water and c.) 3x washes with methanol, and d.) 35:1 CAT@ZIF-8 with hydrogen peroxide once aliquots of the reaction were added to the FOX regent. Aliquots were taken at 0s, 90s, 120s, 180s, 210s, and 240s for CAT. Aliquots after 24 hours were taken for CAT@ZIF-8 system; however, no change in regent could be observed.

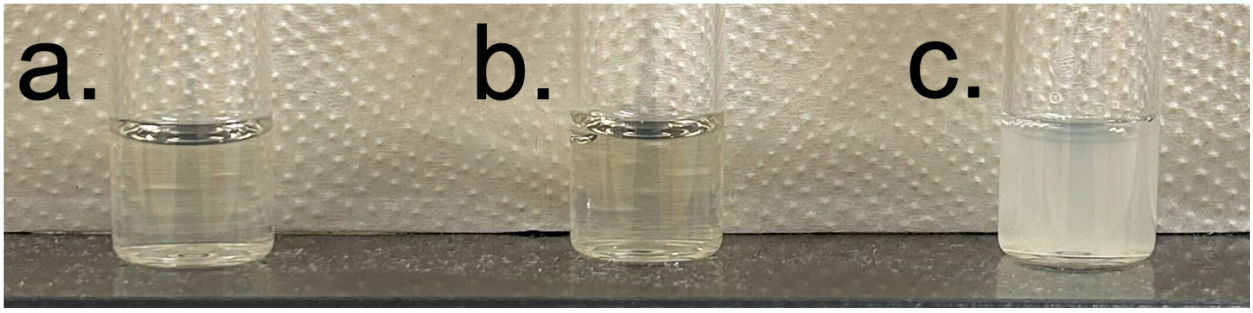

Figure C5: Images of water solutions of a.) CAT, b.) CAT and HmIm, and c.) CAT and HmTz at final concentrations of CAT of 2.5 mg/ml and ligand of 120 mM.

Crystal Size Analysis

CryoTEM and TEM were used to determine crystal diameters by averaging the length of ~50 crystals per sample using Fiji, ImageJ (Figure SX). Crystal sizes were then binned into groups of 5 nm and plotted, using the matplotlib pyplot python library in an author-written python script.

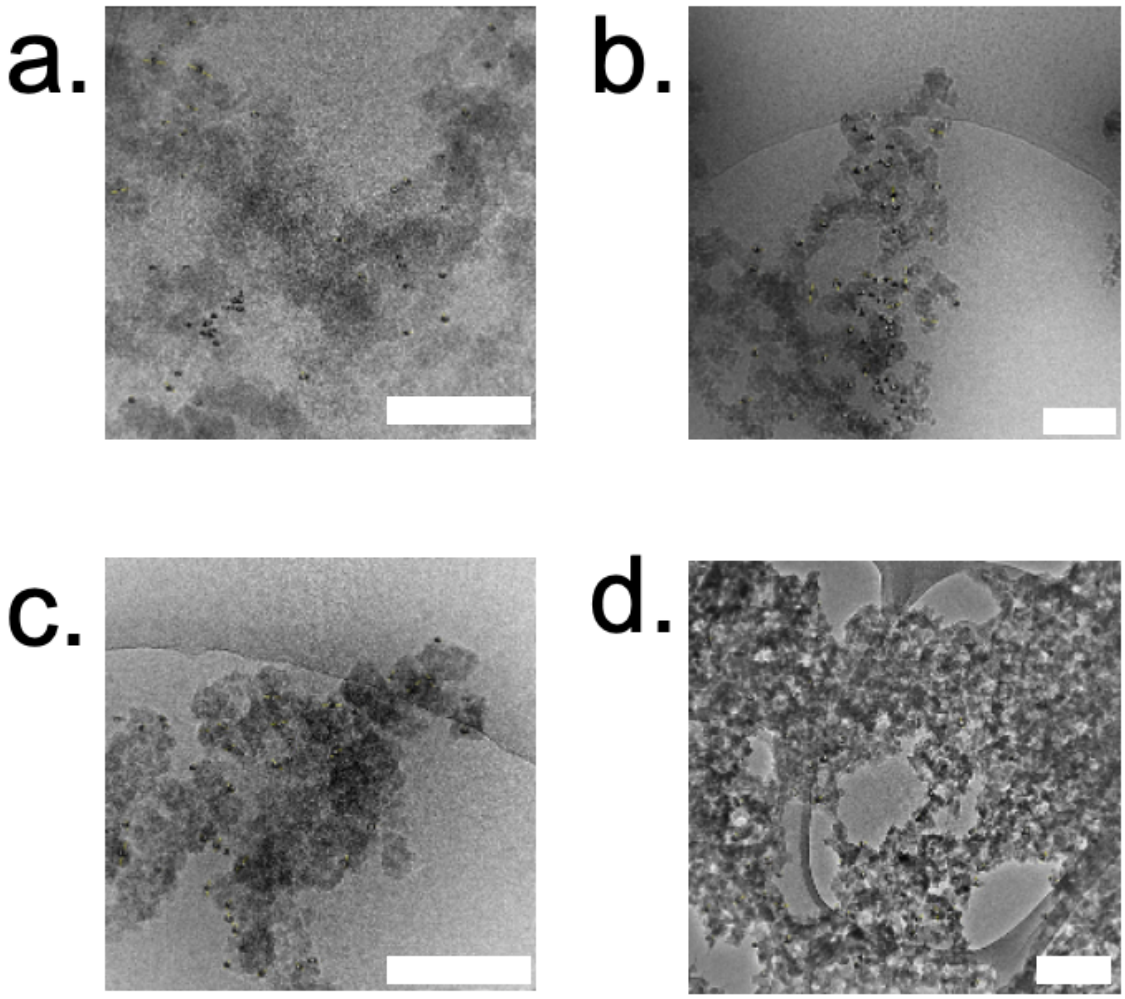

Figure C6: CryoTEM (scale bar 200 nm) of 4:1 GOx@ZIF-8 at (a) 1 min (b) 30 min and (c.) 1 hour and dry-state TEM of 4:1 GOx@ZIF-8 at 24 hours. The measured crystals are marked by numbered yellow lines.

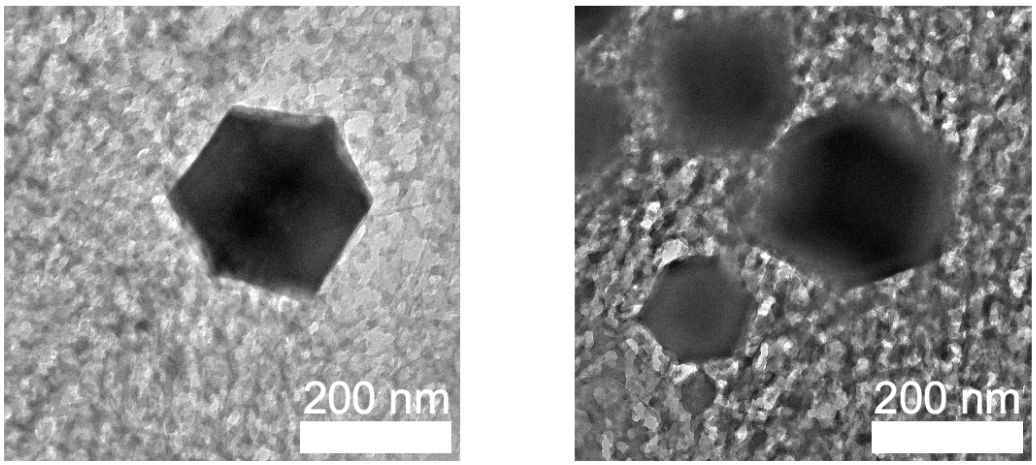

Figure C7: Dry-state TEM images of 35:1 GOx@ZIF-8 at 1 hour. Images show classic rhombic dodecahedron crystals surrounded by dense particulate phase.

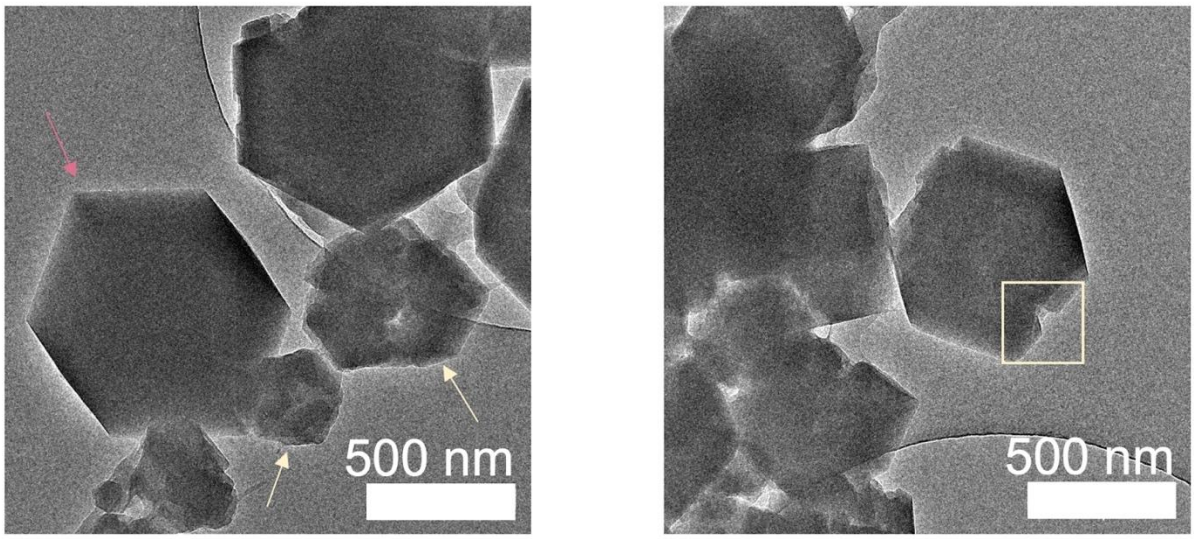

Figure C8: Dry-state TEM images of 35:1 GOx@ZIF-8 after 24 hours with water washes. Pink arrow indicates monocrystalline biocomposite. Yellow arrow points to disordered biocomposites that are hypothesized to be polycrystalline. Yellow box indicates a large defect in the crystal.

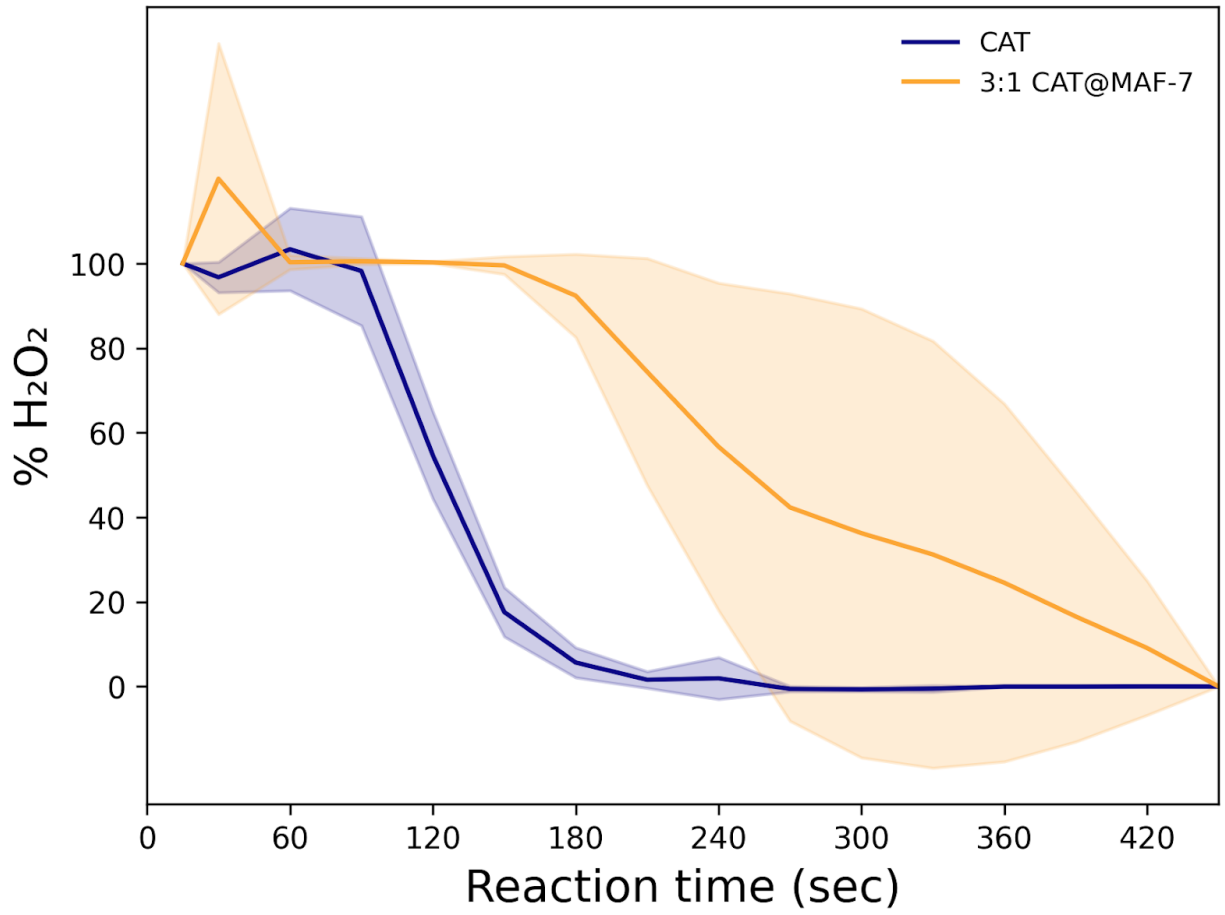

Figure C9: Enzymatic assay of 3:1 Catalase@MAF-7 composite, showing activity is present in the composite. Image was plotted without smoothing using pandas and pyplot libraries in an author-written python script.

Appendix D:

Supplementary Information for Chapter 5.

Appendix D: Supplementary Information for Chapter 5

D.1: Supplementary Figures

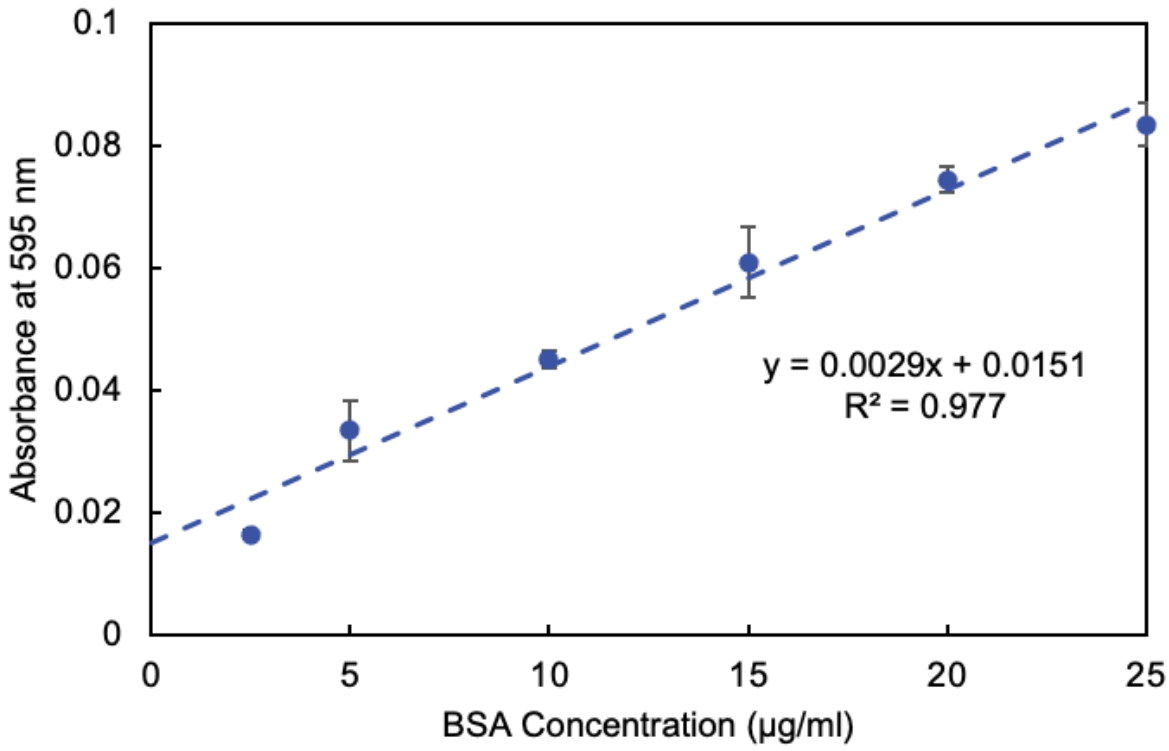

Figure D1: Standard Calibration Curve of BSA using the Bradford Assay. Measurements were taken in duplicates with the standard error indicated by black bars.

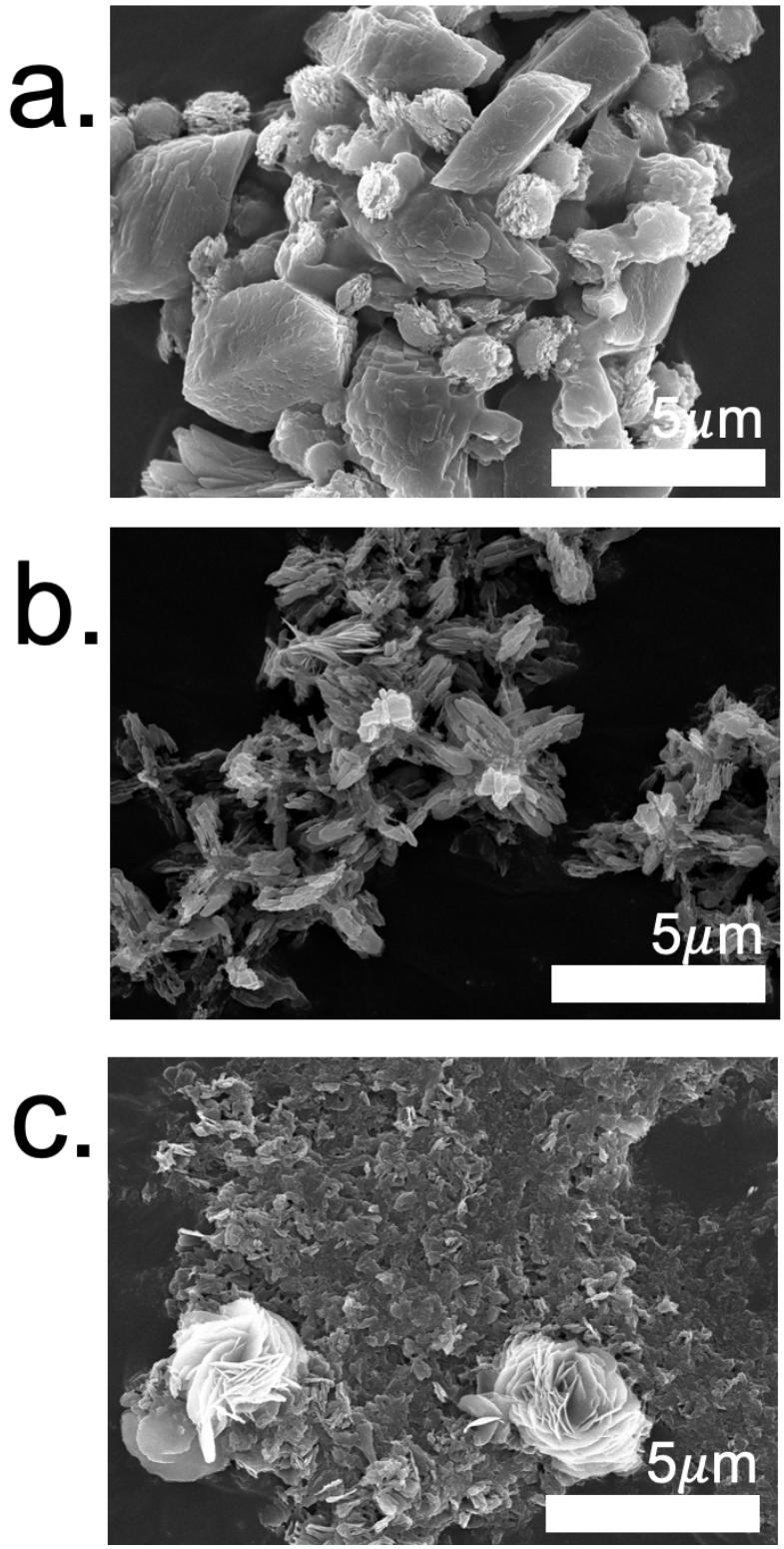

Figure D2: SEM of M^{pro}@ZIF-8 at HmIm:Zn ratios of a) 2:1, b) 9:1, and c) 35:1.